National Technical University of Athens
School of Naval Architecture and Marine Engineering
Ship Hydrodynamics Division
Laboratory for Ship and Marine Hydrodynamics

Calculation of the Hydrodynamic Resistance of Appendages on Conventional Vessels

PhD Thesis

Stylianos P. Polyzos

Supervisor: Professor George D. Tzabiras

Athens, March 2017

(This page intentionally left blank)

National Technical University of Athens
School of Naval Architecture and Marine Engineering
Ship Hydrodynamics Division
Laboratory for Ship and Marine Hydrodynamics

Calculation of the Hydrodynamic Resistance of

Appendages on Conventional Vessels

PhD Thesis

Stylianos P. Polyzos

Examination Committee:

1. G. Tzabiras (Supervisor)*
   Professor, NTUA, School of Naval Architecture and Marine Engineering

2. G. Politis*
   Professor, NTUA, School of Naval Architecture and Marine Engineering

3. G. Triantafyllou*
   Professor, NTUA, School of Naval Architecture and Marine Engineering

4. K. Belibasakis
   Ass. Professor, NTUA, School of Naval Architecture and Marine Engineering

5. A. Dimas
   Professor, University of Patras, School of Engineering, Dept. of Civil Engineering

6. G. Grigoropoulos
   Professor, NTUA, School of Naval Architecture and Marine Engineering

7. S. Voutsinas
   Professor, NTUA, School of Mechanical Engineering

* Member of the Advisory Committee

Athens, March 2017

(This page intentionally left blank)

Dedicated to
Chrysa

(This page intentionally left blank)

ABSTRACT

The present thesis deals with the numerical formulation, programming and validation of a method for solving the viscous flow problem around the appendages on conventional vessels. The proposed method is based on the overlapping blocks approach, part of the Finite Volume family of methods.

The proposed method is based upon and expands the LSMH method for solving the resistance and propulsion "bare" hull problem at model and full scale. The LSMH method solves the Reynold's Averaged Navier-Stokes (RANS) in conjunction with the two equations k-ε or k-ω-SST turbulence models. Introduced in this thesis is the use of Total Variation Diminishing differencing scheme with Minmod limiter function. The use of this higher-order scheme aims at increasing the accuracy of the method.

The coupled momentum and mass continuity equations are solved in a staggered grid arrangement, by means of the SIMPLE algorithm. The propeller action is modeled via the classical actuator disk method, taking into account both axial and tangential body forces.

The flow around the hull is modeled using structured body fitted grids, comprising orthogonal curvilinear 2-D O-type grids, generated by means of the conformal mapping technique. The method is now expanded so that up to three grid blocks may be employed, namely a C-O-type around the bow, an H-O-type around the mid and stern of the ship and finally an H-H-type abaft the transom stern of ships. Using the new arrangement, the method can more accurately predict the resistance of ships with "full" lines near the bow and also predict the effect of a "wetted" transom stern.

In the original LSMH software, the free surface is calculated either via a surface tracking RANS based method or via a surface tracking potential flow method. A novel hybrid method is proposed in this thesis. In this new method, the free surface calculated by means of the potential solver is corrected via a surface tracking RANS method. The correction is applied only at the aft half and the wake of the ship while boundary conditions on the free surface are specially treated, in order to avoid convergence problems. The proposed method is validated by comparing the calculated free surface for two ship designs with experimental data.

A new method for solving the flow problem around the appendages is then proposed. The method is based on the Overlapping Grid Block approach, where the flow around each component of the ship appendages is solved using a separate grid block. The blocks overlap and information is passed-on from one block to the other through the boundary conditions of the later. A method for the parametric representation of ship appendages is presented in this thesis. Then, the method for generating the individual grid blocks is presented in detail along with the proposed method for the exchange of flow variables between blocks.

The LSMH RANS solver is modified to handle the new blocks and the exchange of flow variables according to the overlapping block approach. The ability of the method to solve the flow past individual blocks is then demonstrated through a number of numerical tests for each of the individual blocks.

The new software, the result of the research carried out in this thesis, is used to solve the resistance and propulsion problem for the "Dyne" tanker. Calculations are performed at both model and full scale and for both the "bare" hull and the case of the ship with the rudder. The model scale calculations include symmetric and asymmetric flow calculations, as well as calculations with wall functions and near wall treatment instead.

The rudder of the "Dyne" tanker is modeled using a separate grid block. A grid independence test is performed, in order to determine the required grid size for the rudder block. Also a series of tests is presented, to evaluate the effectiveness of the overlapping block setup. Finally resistance and propulsion calculations are performed for the ship with the rudder, at model and full scale. All numerical results are compared with the available experimental data

Key words: Computational Fluid Dynamics, Marine Hydrodynamics, Numerical Towing Tank, Ship Propulsion, Ship Appendages, Total Variation Diminishing, Surface Tracking, Overlapping Blocks.

ACKNOWLEGMENTS

(This page intentionally left blank)

CONTENTS

(This page intentionally left blank)

CHAPTER 1   INTRODUCTION

(This page intentionally left blank)

1   Introduction

The development of high performance computer systems and of powerful computational methods have allowed researchers and engineering to attempt to numerically solve quite complex flow problems. The quest for more accurate solutions on more complex problems is an ongoing one and there are many problems yet to be solved. Furthermore several schools of thoughts have appeared, with regard to the method of solving a particular problem. Consequently, several numerical methods have been developed, approaching similar problems in different ways, each having its distinct advantages and disadvantages.

In this quest for greater accuracy, the Total Variation Diminishing schemes for the convection terms were examined and an implementation using the Minmod limiter fiction is introduced to the LSMH RANS solver.

A unique problem in the marine hydrodynamics is the presence of the free surface. Anyone body in motion, near the interface of two fluids of different density, called the free surface, generates a system of gravity waves on the interface of the two fluids. This wave system, travels at the same speed as the body and in order to be sustained, an amount of energy is required. That energy forms the wave making portion of the total resistance that the body has to overcome. The shape of the wave system depends on the speed of the body and the geometry of the problem, i.e. the shape of the body, its distance from the fluid interface etc. The shape of the wave system dictates the amount of the wave making resistance; hence the accurate calculation of the free surface is crucial for the prediction of the resistance characteristics of ships. Moreover in a computational approach to the resistance problem, the free surface is one of the boundaries of the computational domain, hence affecting the numerical solution.

Most commercial CFD software employ some sort of Surface Capturing method, for the calculation of the free surface. In that approach two fluids are considered, water and air, and a separate system of differential equations is solved in order to calculate the fraction of each finite volume that is occupied by each fluid. Consequently the numerical grid extends up to the main deck, or even above and very fine meshed are required near the free surface. On the other hand, the grid does not have to be modified as the free surface is calculated.

A more traditional approach is that of Surface Tracking. In these methods the free surface is considered as a boundary surface. During an iterative procedure, this boundary is free to deform until the kinematic and dynamic conditions are both satisfied. The main drawback of the Surface Tracking methods is that during this iterative procedure, the numerical grid has to be modified, at least partially, in order to conform to the free surface. Also these methods cannot simulate wave breaking, spray or deck wetting. On the other hand the Surface Tracking methods can more accurately predict the free surface and consequently they are more suited for resistance or propulsion calculations.

The LSMH software follows the Surface Tracking approach. In an attempt to increase the efficiency of the LSMH method, a novel hybrid method is introduced in this thesis. The free surface is initially calculated by considering the flow inviscid and

irrotational, a potential flow. Then the free surface is corrected at the aft half of the ship and at the wake, using a RANS surface tracking method. The new hybrid method combines the accuracy of the RANS approach with the efficiency of the potential.

The CFD methods that are based on the finite volume approach require the use of a numerical grid. This grid divides the computational domain into the finite volumes. There are two main categories of numerical grids, the structured and the unstructured grids. A structured grid comprises hexahedral volumes, arranged in rows and columns. Each volume is fully defined by its numbering, i.e. the values of its I,J,K indexes. The neighboring volumes can be identified immediately by adding or subtracting one to the respective index. The matrix of the resulting system of linear equations is banded and only the non-zero bands need to be calculated and stored onto the computer memory. Furthermore by applying the appropriate method the grid lines can be made perpendicular at their intersection, at least in one plane. When that is achieved, a local curvilinear coordinate system is devised for each volume and the speed components are always parallel to the local axis. As a result the corresponding equations are simplified, leading to faster convergence of the problem.

When structured grids are employed, complex shapes are very difficult if not impossible to model. To overcome this, two methods have been developed. The first uses blocks of structured grids that in pairs have common boundaries. The main drawback of this method is that generating grids with predefined boundaries is usually difficult. Furthermore in the case of a geometrical alteration, for example when testing various angles of attack for the rudder, it is possible that more than one block has to be modified.

A second method is to use overlapping blocks of structured grids. In this case a separate grid block is generated for each component and the momentum and turbulence model equations are solved independently for each block. In the case of a ship with appendages, there may be one or more blocks for the hull and one or more blocks for each appendage. The transfer of information between blocks is accompliced by using part of the solution of one block as the boundary condition for those boundaries of other blocks that lie within the first one. This implies that the grid blocks must overlap.

In the overlapping grid method each block is easier to generate, since there is no need of sharing boundaries. The only extra effort required is in the bookkeeping of which volume lends boundary conditions to whom. In the case of boundaries moving relative to each other, the grid blocks remain unaltered and only the tables that prescribe the transfer of information have to be recalculated. The above scheme is has successfully been employed in various complex problems of aerodynamics and hydrodynamics.

The second category of numerical grids is the unstructured grids. An unstructured grid comprises volumes of arbitrary shape. Consequently indexing is also arbitrary. As a result the matrix of the system of linear equations is scarce but not banded. Consequently a larger portion of it has to be stored, resulting in greater memory usage. Unstructured grid methods are considered more versatile and easier to adapt for complex shapes and are employed for various problems of fluid mechanics, though numerical efficiency and computer memory requirements have been reported to be compromised.

After an extensive bibliographic research, it was decided that the overlapping blocks approach would be adopted in an effort to solve the flow problem around the appendages of ships. In order to realize this approach, first the software for generating the appropriate grid blocks should be created. Furthermore the existing LSMH RANS solver would have to be modified, to handle the overlapping blocks. Each block should be orthogonal curvilinear in the uv-directions.

1.1 Literature Survey

1.1.1 Total Variation Diminishing Schemes

In order to increase the accuracy of the Finite Volume method, it is necessary to use a higher-order differencing scheme, in terms of the Taylor series truncation error. Higher-order schemes can cause instability of the convergence though.

Through the study of gas-dynamics problems it was concluded that a desirable characteristic for a stable higher-order scheme is the preserving of monotonicity. A scheme is preserving monotonicity when (i) it does not create new local extremes, (ii) it does not lower the value of a local minimum and (iii) it does not increase the value of a local maximum, in other words when a scheme does not generate new oscillations of the solution.

The property of preserving the monotonicity affects the Total Variation (TV) of the discrete solution, specifically, in order for a scheme to preserve monotonicity, the total variation must not increase (Lien & Leschziner, 1994). Consequently a differencing scheme that is monotonicity preserving, causes the reduction of the total variation as the algorithm progresses, hence the name Total Variation Diminishing.

The main idea is to combine the the upwind, linear-upwind and central differencing schemes, in such a way that the resulting scheme is TVD and second-order in accuracy. To achieve that, a function that limits the convection flux is introduced, called a Flux Limiter Function. Several limiter functions have been proposed are and TVD schemes in their current form are the result of the contributions of many researchers (Van Leer, 1974, 1977a, 1977b & 1979, Sweby, 1984 and Roe, 1985).

1.1.2 Free Surface Calculation Methods

Regarding the problem of the free surface calculation, most commercial CFD software nowadays employ some sort of Surface Capturing method. These methods, now more than 10 years old, solve a separate system of differential equations in order to calculate the fraction of each finite volume that is occupied by water (Carrica et al., 2006 and Queutey & Visonneau, 2007)

These methods can give answers to complex multi-phase problems (Albadawia et al., 2014). They are also quite efficient for maneuvering and sea-keeping calculations (Carrica et al., 2006, Carrica et al., 2007, Araki et al., 2012, Shi et al., 2012, Stern et al., 2015, Irkal et al., 2016).

The more traditional Surface Tracking methods consider the free surface as a boundary surface that during an iterative procedure is free to deform, until the kinematic and dynamic conditions are both satisfied (Tzabiras & Ventikos, 1991, Tzabiras, 1997c, Tzabiras, 1997d, Tzabiras, 1995f).

The Surface Tracking methods have proven very accurate, in calculating the free surface and thus are more suited for resistance or propulsion calculations (Papakonstantinou & Tzabiras, 2002, Wilson et al., 2006). On the other hand, since the numerical grid needs to adapt to the changing free surface, they are rarely used for maneuvering or sea-keeping calculations (Wilson et al., 2006)

A different approach to a Surface Tracking method is to consider the flow inviscid and irrotational. Then, the potential flow problem can be solved using the classical formulation of Hess & Smith (1966) and the free surface can be calculated at a fraction of the computational cost of the previous methods. The potential approach is very effective in predicting the wave pattern around ships (Tzabiras, 2008) except near the stern and at the wake of the ship where the effect of viscosity becomes very important.

1.1.3 Methods for Solving the Flow around Ship Appendages

The hydrodynamic resistance of ship appendages can be quite significant, especially in the case of fast vessels with multiple propeller, such as passenger ferries, cruise ship or naval vessels. Various empirical (Lewis, 1988.) or experimental (Jang et al., 2009) methods have been proposed but as the hydrodynamic efficiency becomes more important, the need for a computational method that accurately calculate the resistance of appendages becomes greater. The invention of hydrodynamic devices that aim at improving the efficiency of ships, further increases the need for such numerical tools (Rhee & Kim, 2008, Park et al., 2015)

Most commercial CFD software nowadays, adopt an unstructured grid approach. One of the earliest attempts at solving the appendages problem was the PhD thesis of Pinar (1997). In his thesis, Pinard employed an unstructured grid in order to solve the problem of a twin screw vessel. In his work the propeller shafts and the V-brackets were modeled but not the rudder.

Three year later, Simonsen in his PhD thesis (2000) attempted to solve the hull, propeller and rudder interaction problem using a multi-block approach. In his work, the free surface was not calculated and propeller was modeled using an actuator disk.

Since then, there have been many publications on the subject of ship appendages, mainly using unstructured grids (Deng et al., 2006, Visonneau et al., 2006a, Visonneau et al., 2006b, Zorn et al., 2009).

The multi-block or overset grids approach was also further developed with the introduction of dynamic overset grids and sliding grids. These methods attempt to solve even the more complex problem of the propeller operation (Shen et al., 2015).

Though widely used, the unstructured grid approach has been reported to be compromising in terms of numerical efficiency and computer memory requirements (Steger, 1991).

1.1.4 Methods for Overlapping Grid Blocks

Another approach to the problem of ship appendages is that of the overlapping structured grid blocks. In this method, a separate grid block is generated for each component and the momentum and turbulence model equations are solved independently for each block. This approach was first introduced for aerodynamic problems (Dougherty et al., 1985, Steger & Benek, 1987).

Since the momentum and turbulence model equations are solved independently for each block, special care is required in order to ensure the continuity of mass. In that front many methods have been published (Steger, 1991, Wang, 1995, Lilek et al., 1997, Brezzi et al., 2001, Djomehri & Biswas, 2003, Zhang et al., 2008, Brounswig et al., 2009).

Nowadays the overlapping block approach is widely used in the field of aerodynamics, for airplane wings (Badcock et al., 2000, Tarhan & Oktay, 2002, Desquesnes et al., 2006, Jinsheng et al., 2006, Chicheportiche & Gloerfelt, 2012), wind turbines (Lia et al., 2012, Nini et al., 2014, Li et al., 2015) or even for the flow past helicopter rotors (Chan, 2009).

The overlapping block approach is also in use in the field of marine hydrodynamics both for resistance and propulsion problems (Lin et al., 1995, Campana et al., 2006, Regnstrom & Bathfield, 2006, Kim et al., 2007, Carrica et al., 2010, Zaghia et al., 2015) and for maneuvering and seakeeping problems (Simonsen & Stern, 2005, Carrica et al., 2007, Panahi & Shafieefar, 2010, Stern et al., 2015).

In most cases, a Cartesian coordinate system is employed on each of the grid blocks. The use of a curvilinear coordinate system though, in conjunction with an orthogonal curvilinear grid, is known to increase the accuracy of the numerical solution (Tzabiras et al., 1986, Tzabiras, et al., 1989). There are examples of use of orthogonal curvilinear grids blocks in an overlapping block arrangement (Salcudean, et al., 1996, Talukdar, et al., 2005, Anwera, et al., 2009, Borazjani, et al., 2013) but there is no reference in the literature of such a setup for marine hydrodynamics and especially for the problem of ship appendages.

1.2   The LSMH Method for Solving the Flow around Ships

Since 1983 (Tzabiras & Loukakis, 1983), Computational Fluid Dynamic methods have been in development at the Laboratory for Ship and Marine Hydrodynamics of the National Technical University of Athens, with the main focus point being the Numerical Towing Tank. In that front, several software have been developed in-house, to solve the resistance and propulsion problems of ships, in model and full scale.

The LSMH software solves the Reynold's Averaged Navier-Stokes (RANS) equations by employing a Finite Volume method. Turbulence is modeled by employing several models with k-ε and k-ω-SST being more commonly used. The coupled momentum and mass continuity equations are solved in a staggered grid arrangement, by means of the almost universally adopted SIMPLE (Semi-Implicit

Method for Pressure Linked Equations) algorithm devised by Patankar & Spalding (Patankar, 1980).

For the propulsion calculations, the propeller is modeled by employing the classical actuator disk method (Tzabiras, 1996a, 1997a and 2004). The effect of the propeller operation on the flow is simulated by means of body forces, introduced in the source term of momentum equations. These forces act both in the axial and the tangential direction, the later causing the flow to swirl.

The employed numerical grid is a structured body fitted arrangement, comprising 2-D sections normal to the ship longitudinal axis. On each section an orthogonal curvilinear O-type grid is generated by means of the conformal mapping technique (Tzabiras et al. 1986, Tzabiras, 2004), that also conforms to the free surface. In the third direction, the grid is non-orthogonal Cartesian, hence the 3-D grid is partially orthogonal, H-O-type, presenting significant advantages in terms of accuracy and convergence (Tzabiras et al., 1986). Conformal mapping is also used for the geometrical representation of the hull (Tzabiras, 1998).

The free surface can be calculated either via a surface tracking RANS based method (Tzabiras, 2004) or via a surface tracking potential flow method (Tzabiras, 1997b, 2004). The later being significantly faster and also providing the boundary conditions at the external boundary of the ship grid block required by the RANS solver. The drawback of the potential flow approach is the reduced accuracy of the method near the stern of ship, especially in the case of ships with a transom stern.

The present PhD thesis is based upon and expands the CFD software developed at LSMH. The main targets of this thesis are to:

- Increase the accuracy of the employed finite volume method, through the implementation of stable higher order differencing schemes. In that front, the Total Variation Diminishing scheme in conjunction with the Minmod Limiter function is introduced.

- Increase the accuracy of the resistance predictions for ships characterized by full lines at the bow area and also ships with a "wetted" transom stern. The above are achieved through the implementation of a three grid blocks arrangement, a C-O-type around the bow, an H-O-type around the mid and stern of the ship and finally an H-H-type abaft the transom stern.

- Increase the efficiency of the method for the calculation of the free-surface. A novel hybrid method is introduced, where a potential solver provides the initial free surface that is then corrected using a RANS based surface tracking method. The correction is applied only at the aft half and the wake of the ship while boundary conditions on the free surface are specially treated, to avoid convergence problems.

- Develop a method for the parametric representation of ship appendages and create the software for the generation of the grid blocks around the components of the appendages. The grid blocks are orthogonal curvilinear in the uv-directions thus increasing the accuracy of the method.

- Modify the LSMH RANS solver to handle the new blocks and the exchange of flow variables according to the overlapping block approach.

- Develop the method for the exchange of flow variables between the blocks. Fast and accurate exchange of flow variables is key in an overlapping block method.

- Validate the overlapping grid method, by comparing available experimental data with numerical calculations, in the case of a ship with rudder. The validation should concern both the resistance and the propulsion problem, at model and full scale.

1.3 Thesis Outline

The present thesis includes seven chapters, including the introduction and the conclusions. The contents of each chapter are summarized below.

In Chapter 1, the introductory chapter of this thesis, an overview of the scientific literature is presented, concerning CFD methods for solving the viscous flow problem around ships as well as methods for overlapping grid blocks. Then the features of the CFD software developed in LSMH-NTUA are outlined, along with new components proposed in this thesis.

In Chapter 2, an overview of the Finite Volume method is presented. Included in this overview are the governing equations in Cartesian and Curvilinear coordinates along with the modeling of turbulence. Regarding turbulence, the two equations k-ε and k-ω-SST models are presented. Then, the finite volume formulation is explained including the pressure correction algorithm, the boundary conditions and the Total Variation Diminishing differencing scheme with Minmod limiter function, introduced in the LSMH software as part of this thesis. The method for the geometrical representation of the hull is also presented in Chapter 2, along with the method for generating the numerical grid. Introduced in this thesis is the use of up to three grid blocks around the hull, including a C-O-type around the bow, a classical H-O-type around the mid and stern of the ship and finally an H-H-type abaft the transom stern of ships. Finally in Chapter 2, the actuator disk method is presented along with the method for solving the ship self-propulsion problem.

In Chapter 3, three alternative methods for calculating the free surface are presented. First the direct method is explained where only the RANS equations are solved and the free surface is calculated using a surface tracking iterative procedure. An alternative surface tracking method is then explained, where the flow is considered inviscid and irrotational and the potential flow problem is solved. Finally in Chapter 3 a new hybrid method is proposed. In this new method the free surface calculated by means of the potential solver is corrected via a surface tracking RANS method. The correction is applied only at the aft half and the wake of the ship. Boundary conditions on the free surface are specially treated, in order to avoid convergence problems near the area where the method of calculation changes. In order to validate the new method, numerical tests are performed for two ship designs and the results are compared with experimental data.

In Chapter 4, the proposed method for solving the flow problem around the appendages of ships is presented. The method is based on the Overlapping Grid Block approach, where the flow around each component of the ship appendages is solved using a separate grid block. In order to obtain the solution for the overall flow problem, the blocks overlap and information is passed-on from one block to the other through the boundary conditions of the later. In Chapter 4 the proposed method is explained in detail. Also presented are the methods for generating the individual blocks along with a general method for 2-D orthogonal curvilinear grid sections. All grid blocks are orthogonal curvilinear in the uv-directions whine in the w-direction, they are non-orthogonal Cartesian. Finally in this chapter the proposed method for the exchange of flow variables between blocks is detailed.

In Chapter 5, the ability of the method to solve the flow past individual blocks is demonstrated. Specifically, for each of the ship appendages components, the results of a number of numerical tests are presented. These results also demonstrate the required total number of grid nodes in cases of ships with complex appendages.

In Chapter 6, results of the proposed method are presented for the "Dyne" tanker, a model extensively tested both in the towing tank and the wind tunnel, in order to provide a comprehensive data set for the validation of CFD methods. Using the proposed hybrid method the free surface was calculated in model scale and compared with available experimental data. Then, resistance and propulsion calculations were performed in model and full scale, for the "bare" hull. The model scale calculations include symmetric and asymmetric flow calculations, as well as calculations with wall functions and near wall treatment.

The "Dyne" tanker rudder was modeled using a separate grid block. In Chapter 6, a grid independence test for the rudder block is presented. Also presented is a series of tests to evaluate the effectiveness of the overlapping block setup. Finally resistance and propulsion calculations were performed for the ship with the rudder, in model and full scale. All numerical results are compared with the available experimental data.

In Chapter 7, the methods and results presented herein are discussed and the conclusions drawn are summarized. Also presented are the journal publications and conference papers that have, thus far, resulted from the research carried out in this thesis. Finally several suggestions are made with regard to future research based upon this thesis.

All software presented in this thesis are realized in Fortran programming language. The new software is based upon and incorporates software created at the Laboratory for Ship and Marine Hydrodynamics of the National Technical University of Athens.

CHAPTER 2   THE METHOD FOR SOLVING THE FLOW AROUND A SHIP

(This page intentionally left blank)

2.1   The Governing Equations

2.1.1   The Navier-Stokes Equations

In the case of the flow of water past the appendages of a conventional ship, the flow field is described by the well-known Navier-Stokes equations (N-S equations, in sort). The N-S equations arise from the application of the Newton's second law to fluid motion and assume that the fluid is a continuum, i.e. it is infinitively divisible, isotropic and that the stress in the fluid is the sum of a diffusing viscous term and a pressure term. In 3-D Cartesian coordinates the N-S equations may be expressed as:

$$\rho\left(\frac{\partial u_1}{\partial t} + u_1\frac{\partial u_1}{\partial x_1} + u_2\frac{\partial u_1}{\partial x_2} + u_3\frac{\partial u_1}{\partial x_3}\right) = -\frac{\partial(p + \rho gz)}{\partial x_1} + \mu\left(\frac{\partial^2 u_1}{\partial x_1^2} + \frac{\partial^2 u_1}{\partial x_2^2} + \frac{\partial^2 u_1}{\partial x_3^2}\right)$$

$$\rho\left(\frac{\partial u_2}{\partial t} + u_1\frac{\partial u_2}{\partial x_1} + u_2\frac{\partial u_2}{\partial x_2} + u_3\frac{\partial u_2}{\partial x_3}\right) = -\frac{\partial(p + \rho gz)}{\partial x_2} + \mu\left(\frac{\partial^2 u_2}{\partial x_1^2} + \frac{\partial^2 u_2}{\partial x_2^2} + \frac{\partial^2 u_2}{\partial x_3^2}\right)$$

$$\rho\left(\frac{\partial u_3}{\partial t} + u_1\frac{\partial u_3}{\partial x_1} + u_2\frac{\partial u_3}{\partial x_2} + u_3\frac{\partial u_3}{\partial x_3}\right) = -\frac{\partial(p + \rho gz)}{\partial x_3} + \mu\left(\frac{\partial^2 u_3}{\partial x_1^2} + \frac{\partial^2 u_3}{\partial x_2^2} + \frac{\partial^2 u_3}{\partial x_3^2}\right)$$

$$(2.1.1)$$

where (u_1, u_2, u_3) the three velocity components, parallel to the (x_1, x_2, x_3) axis, p the pressure, ρ the density and μ the dynamic viscosity. In conservation form the N-S equations are:

$$\frac{\partial \rho \cdot \Phi}{\partial t} + \text{div}(\rho \cdot \Phi \cdot \mathbf{U}) = \mu \cdot \nabla^2\Phi + S_\Phi \qquad (2.1.2)$$

where $\mathbf{U}$ is the velocity vector and Φ one of the three velocity components (u_1, u_2, u_3). The N-S equations are a statement of the balance of momentum and for the flow to be fully described, more information is needed in the form of boundary conditions, conservation of mass, balance of energy and an equation of state. In the case of Marine Hydrodynamics and when cavitation is ignored, only the boundary conditions and an equation expressing the conservation of mass are required. In 3-D Cartesian coordinates the conservation of mass may be expressed through the continuity equation as:

$$\frac{\partial \rho}{\partial t} + \frac{\partial \rho u_1}{\partial x_1} + \frac{\partial \rho u_2}{\partial x_2} + \frac{\partial \rho u_3}{\partial x_3} = 0 \quad (2.1.3)$$

Or in conservation form:

$$\frac{\partial \rho}{\partial t} + \nabla \cdot (\rho \cdot \mathbf{U}) = 0 \quad (2.1.4)$$

The N-S equations may be further simplified by the fact that water is incompressible hence all time and space derivatives of density are equal to zero:

$$\frac{\partial u_1}{\partial t} + u_1\frac{\partial u_1}{\partial x_1} + u_2\frac{\partial u_1}{\partial x_2} + u_3\frac{\partial u_1}{\partial x_3} = -\frac{1}{\rho}\frac{\partial(p + \rho gz)}{\partial x_1} + \nu\left(\frac{\partial^2 u_1}{\partial x_1^2} + \frac{\partial^2 u_1}{\partial x_2^2} + \frac{\partial^2 u_1}{\partial x_3^2}\right)$$

$$\frac{\partial u_2}{\partial t} + u_1\frac{\partial u_2}{\partial x_1} + u_2\frac{\partial u_2}{\partial x_2} + u_3\frac{\partial u_2}{\partial x_3} = -\frac{1}{\rho}\frac{\partial(p+\rho gz)}{\partial x_2} + \nu\left(\frac{\partial^2 u_2}{\partial x_1{}^2} + \frac{\partial^2 u_2}{\partial x_2{}^2} + \frac{\partial^2 u_2}{\partial x_3{}^2}\right)$$

$$\frac{\partial u_3}{\partial t} + u_1\frac{\partial u_3}{\partial x_1} + u_2\frac{\partial u_3}{\partial x_2} + u_3\frac{\partial u_3}{\partial x_3} = -\frac{1}{\rho}\frac{\partial(p+\rho gz)}{\partial x_3} + \nu\left(\frac{\partial^2 u_3}{\partial x_1{}^2} + \frac{\partial^2 u_3}{\partial x_2{}^2} + \frac{\partial^2 u_3}{\partial x_3{}^2}\right)$$

$$(2.1.5)$$

where $\nu=\mu/\rho$ the kinematic viscosity. In conservation form:

$$\frac{\partial\Phi}{\partial t} + \mathrm{div}(\Phi\cdot\mathbf{U}) = \nu\cdot\nabla^2\Phi + S_\Phi \qquad (2.1.6)$$

The equation for the conservation of mass becomes:

$$\frac{\partial u_1}{\partial x_1} + \frac{\partial u_2}{\partial x_2} + \frac{\partial u_3}{\partial x_3} = 0 \quad (2.1.7)$$

Or in conservation form:

$$\nabla\cdot\mathbf{U} = 0 \qquad (2.1.8)$$

The N-S equations along with the continuity equation form a system of four equations with four unknown quantities, the velocity components and pressure. Using the appropriate boundary conditions this system can be solved numerically.

2.1.2   Curvilinear Coordinates

When numerically solving the strongly coupled momentum and continuity equations for a flow around bodies of arbitrary geometry, the use of a Cartesian coordinate system can lead to significant accuracy and convergence problems. On the other hand the use of a local curvilinear coordinate system in conjunction with a curvilinear orthogonal grid, i.e. a grid where the grid lines are perpendicular at their intersection, is beneficial both in terms of accuracy and convergence (Tzabiras, 1986).

The generation of a 3-D orthogonal curvilinear grid is quite difficult though. Similar accuracy can be achieved, through the use of successive 2-D orthogonal curvilinear grids that when combined, form a partially orthogonal 3-D grid. Then at every point of the grid, a local curvilinear coordinate system is devised with the two curvilinear directions laying on the 2-D section, while in the third direction the grid is non-orthogonal and a Cartesian coordinate system is employed. In such a hybrid curvilinear (x_1, x_2-directions) and Cartesian (x_3-direction) coordinate system, the Reynolds averaged Navier-Stokes equations can be written as (Tzabiras, 1996):

$$C(u_1) = -\frac{1}{h_1}\frac{\partial p^*}{\partial x_1} + \rho u_2{}^2 k_{21} - \rho u_1 u_2 k_{12} + (\sigma_{11} - \sigma_{22})k_{21} + 2\sigma_{12}k_{12}$$

$$+\frac{1}{h_1}\frac{\partial\sigma_{11}}{\partial x_1} + \frac{1}{h_2}\frac{\partial\sigma_{12}}{\partial x_2} + \frac{1}{h_3}\frac{\partial\sigma_{13}}{\partial x_3}$$

$$C(u_2) = -\frac{1}{h_2}\frac{\partial p^*}{\partial x_2} + \rho u_1{}^2 k_{12} - \rho u_1 u_2 k_{21} + (\sigma_{22} - \sigma_{21})k_{12} + 2\sigma_{21}k_{21}$$

$$+\frac{1}{h_2}\frac{\partial\sigma_{22}}{\partial x_2} + \frac{1}{h_1}\frac{\partial\sigma_{12}}{\partial x_1} + \frac{1}{h_3}\frac{\partial\sigma_{23}}{\partial x_3}$$

$$C(u_3) = -\frac{1}{h_3}\frac{\partial p^*}{\partial x_3} + (\sigma_{13} - \sigma_{23})k_{12} + \frac{1}{h_3}\frac{\partial \sigma_{33}}{\partial x_3} + \frac{1}{h_2}\frac{\partial \sigma_{23}}{\partial x_2} + \frac{1}{h_1}\frac{\partial \sigma_{13}}{\partial x_1}$$

(2.1.09)

where $C(u_i)$ is the convection term:

$$C(u_i) = \frac{\rho}{h_1 h_2}\left[\frac{\partial h_2 u_1 u_i}{\partial x_1} + \frac{\partial h_1 u_2 u_i}{\partial x_2} + \frac{\partial u_3 u_i}{\partial x_3}\right] \qquad (2.1.10)$$

In the above equations, h_1, h_2 and $h_3{=}1$ are the grid metrics and k_{12}, k_{21} the curvatures. The stress tensor σ_{ij} includes the viscous stresses and the double velocity correlations and can is expressed as:

$$\sigma_{11} = 2\mu_e\left[\frac{1}{h_1}\frac{\partial u_1}{\partial x_1} + u_2 k_{12}\right] = 2\mu_e e_{11}$$

$$\sigma_{22} = 2\mu_e\left[\frac{1}{h_2}\frac{\partial u_2}{\partial x_2} + u_1 k_{21}\right] = 2\mu_e e_{22}$$

$$\sigma_{33} = 2\mu_e\frac{\partial u_3}{\partial x_3} = 2\mu_e e_{33}$$

$$\sigma_{12} = \mu_e\left[\frac{1}{h_1}\frac{\partial u_2}{\partial x_1} + \frac{1}{h_2}\frac{\partial u_1}{\partial x_2} - u_2 k_{21} - u_1 k_{12}\right] = \mu_e e_{12}$$

$$\sigma_{13} = \mu_e\left[\frac{1}{h_1}\frac{\partial u_3}{\partial x_2} + \frac{\partial u_1}{\partial x_3}\right] = \mu_e e_{13}$$

$$\sigma_{23} = \mu_e\left[\frac{1}{h_2}\frac{\partial u_3}{\partial x_2} + \frac{\partial u_2}{\partial x_3}\right] = \mu_e e_{23}$$

(2.1.11)

On (2.1.09) p^* is equal to $p+\rho gh$, where h the vertical distance from a reference level.

2.2   Turbulence Modeling

2.2.1   The Reynolds Averaged Navier-Stokes Equations

The flow past a ship is usually characterized by a high Reynold's number, in the order of 10^9 while for scaled down experiments the Reynold's number is in the region of 10^6. Consequently the flow in both cases is turbulent. Turbulence is the time-dependent chaotic behavior of a flow, were both velocity and pressure fluctuate intensely in terms of time and in terms of space. Although the N-S equations are believed to accurately describe the turbulent behavior of fluid flows, in practice the direct solution of the time-dependent N-S in the case of a turbulent flow is extremely difficult. The problem arises from the very small time-step required to capture the time fluctuation of the flow in conjunction with the very fine space discretization required to capture the smallest flow structures. Several attempts have been made in the past to numerically solve the N-S equations in turbulent flow cases but even with modern super-computers this approach has been proven impractical. Instead in most practical applications the Reynolds-averaged Navier-Stokes (RANS, in sort) method is employed in conjunction with a turbulence model.

The idea behind the RANS equations is that of the Reynolds decomposition, where each flow characteristic Φ at a given time, may be decomposed into its time-averaged portion $\overline{\Phi}$ and a fluctuating quantity Φ':

$$\Phi(\mathbf{x}, t) = \overline{\Phi}(\mathbf{x}) + \Phi'(\mathbf{x}, t) \quad (2.2.1)$$

where $\mathbf{x} = (x_1, x_2, x_3)$ the position vector. The time-averaged portion is defined as:

$$\overline{\Phi}(\mathbf{x}) = \frac{1}{t_2 - t_1} \int_{t_1}^{t_2} \Phi(\mathbf{x}, t) \, dt \quad (2.2.2)$$

where the time interval for the integration $\delta t = t_2 - t_1$, is significantly larger than the time scale of turbulence. Expression (2.2.1) is introduced to the N-S equations that are then integrated in time. It is important to note that the time-average of the fluctuating quantity of Φ is equal to zero. Consequently the Reynolds-averaged Navier-Stokes, in Cartesian coordinates, become:

$$\overline{u_1}\frac{\partial \overline{u_1}}{\partial x_1} + \overline{u_2}\frac{\partial \overline{u_1}}{\partial x_2} + \overline{u_3}\frac{\partial \overline{u_1}}{\partial x_3} = -\frac{1}{\rho}\frac{\partial}{\partial x_1}(p + \rho g z) + \nu\left(\frac{\partial^2 \overline{u_1}}{\partial x_1^2} + \frac{\partial^2 \overline{u_1}}{\partial x_2^2} + \frac{\partial^2 \overline{u_1}}{\partial x_3^2}\right)$$

$$+ \frac{\partial}{\partial x_1}\left(-\overline{u_1'^2}\right) + \frac{\partial}{\partial x_2}\left(-\overline{u_1'u_2'}\right) + \frac{\partial}{\partial x_3}\left(-\overline{u_1'u_3'}\right)$$

$$\overline{u_1}\frac{\partial \overline{v}}{\partial x_1} + \overline{u_2}\frac{\partial \overline{v}}{\partial x_2} + \overline{u_3}\frac{\partial \overline{v}}{\partial x_3} = -\frac{1}{\rho}\frac{\partial}{\partial x_2}(p + \rho g z) + \nu\left(\frac{\partial^2 \overline{u_2}}{\partial x_1^2} + \frac{\partial^2 \overline{u_2}}{\partial x_2^2} + \frac{\partial^2 \overline{u_2}}{\partial x_3^2}\right)$$

$$+ \frac{\partial}{\partial x_1}\left(-\overline{u_1'u_2'}\right) + \frac{\partial}{\partial x_2}\left(-\overline{u_2'^2}\right) + \frac{\partial}{\partial x_3}\left(-\overline{u_2'u_3'}\right)$$

$$\overline{u_1}\frac{\partial \overline{w}}{\partial x_1} + \overline{u_2}\frac{\partial \overline{w}}{\partial x_2} + \overline{u_3}\frac{\partial \overline{w}}{\partial x_3} = -\frac{1}{\rho}\frac{\partial}{\partial x_3}(p + \rho g z) + \nu\left(\frac{\partial^2 \overline{u_3}}{\partial x_1^2} + \frac{\partial^2 \overline{u_3}}{\partial x_2^2} + \frac{\partial^2 \overline{u_3}}{\partial x_3^2}\right)$$

$$+ \frac{\partial}{\partial x_1}\left(-\overline{u_1'u_3'}\right) + \frac{\partial}{\partial x_2}\left(-\overline{u_2'u_3'}\right) + \frac{\partial}{\partial x_3}\left(-\overline{u_3'^2}\right) \quad (2.2.3)$$

The equation for the conservation of mass becomes:

$$\left(\frac{\partial \overline{u_1}}{\partial x_1} + \frac{\partial \overline{u_2}}{\partial x_2} + \frac{\partial \overline{u_3}}{\partial x_3}\right) = 0 \qquad (2.2.4)$$

Or in conservation form:

$$\frac{\partial \Phi}{\partial t} + \text{div}(\Phi \cdot \overline{U}) = \nu \cdot \nabla^2 \Phi - \left[\frac{\partial}{\partial x_i}\left(\overline{u_i'\varphi'}\right)\right] + S_\Phi \qquad (2.2.5)$$

$$\text{div}(\overline{U}) = 0 \qquad (2.2.6)$$

The resulting system of equations resembles the original N-S plus continuity equations where instead of the pressure and the velocity components, the new unknown quantities are the respective mean values. Rather inconveniently a total of six new unknown quantities appear at the right hand side of the RANS equations, called Reynolds stresses. The new quantities require a further six equations in order for the problem to be solved. The new equations can be obtained by multiplying the N-S equations with one of the fluctuating quantity and then by calculating the time average of the product (Tzabiras, 1998). Unfortunately in doing so, we obtain six new equations in which twenty-two new unknown quantities appear. The above is the well-known closure problem.

Many different models attempting to circumvent the closure problem have been proposed in the literature. A large class of turbulence models is based upon the Boussinesq approximation where the Reynolds stresses can be expressed as:

$$-\overline{u_i'u_j'} = \nu_t\left(\frac{\partial \overline{u_i}}{\partial x_j} + \frac{\partial \overline{u_j}}{\partial x_i}\right) - \frac{1}{\rho}\frac{2}{3}k\delta_{ij} \qquad (2.2.7)$$

where ν_t the eddy viscosity, δ_{ij} the Kronecker delta and k the turbulent kinetic energy:

$$k = \frac{1}{2}\left(\overline{u_1'^2} + \overline{u_2'^2} + \overline{u_3'^2}\right) \qquad (2.2.8)$$

The eddy viscosity ν_t, is a scalar object, dependent of the flow field and in the general case, different for each of the Reynolds stresses. Boussinesq introduced the approximation that eddy viscosity is isotropic and consequently is a function of the position vector only.

In the curvilinear coordinates of paragraph 2.1, the RANS equations become:

$$C(u_i) = -\frac{1}{h_i}\frac{\partial p}{\partial x_i} + \rho u_j^2 K_{ji} + \rho u_l^2 K_{li} - \rho u_i u_j K_{ij} - \rho u_i u_l K_{il}$$

$$+\left(\sigma_{ii} - \sigma_{jj}\right)K_{ji} + \left(\sigma_{ii} - \sigma_{ll}\right)K_{li} + \sigma_{ij}\left(2K_{ij} + K_{lj}\right) + \sigma_{il}\left(2K_{il} + K_{jl}\right)$$

$$+\frac{1}{h_i}\frac{\partial \sigma_{ii}}{\partial x_i} + \frac{1}{h_j}\frac{\partial \sigma_{ij}}{\partial x_j} + \frac{1}{h_l}\frac{\partial \sigma_{il}}{\partial x_l} \qquad (2.2.9)$$

where u_i, u_j, u_l, stand for the mean values of the velocity components, and $C(\Phi)$ is the sum of the convective terms:

$$C(\Phi) = \frac{\rho}{h_i h_j h_l}\left[\frac{\partial(h_j h_l u_i \Phi)}{\partial x_i} + \frac{\partial(h_i h_l u_j \Phi)}{\partial x_j} + \frac{\partial(h_i h_j u_l \Phi)}{\partial x_l}\right] \qquad (2.2.10)$$

In the above equations, h_i, h_j, h_l are the grid metrics and K_{mn} the curvatures:

$$K_{mn} = \frac{1}{h_m h_n} \frac{\partial h_m}{\partial x_n}, m \neq n \qquad (2.2.11)$$

The stress tensor σ_{ij} is related linearly to the deformation tensor e_{ij} according to:

$$\sigma_{ii} = 2\mu_e e_{ii} = 2\mu_e \left[\frac{1}{h_i} \frac{\partial u_i}{\partial x_i} + u_j K_{ij} + u_l K_{il} \right] \quad (2.2.12a)$$

$$\sigma_{ij} = \mu_e e_{ij} = \mu_e \left[\frac{h_j}{h_i} \frac{\partial}{\partial x_i} \left(\frac{u_j}{h_j} \right) + \frac{h_i}{h_j} \frac{\partial}{\partial x_j} \left(\frac{u_i}{h_i} \right) \right] \qquad (2.2.12b)$$

Where the effective viscosity μ_e is calculated as the sum of the dynamic viscosity μ and the eddy viscosity μ_t:

$$\mu_e = \mu + \mu_t = \mu + \rho \cdot \nu_t \qquad (2.2.13)$$

2.2.2 The Two-Equation k-ε Model

One of the most commonly used turbulence models is the classical k-ε (kappa-epsilon) model (Launder and Spalding, 1974). The k-ε model is based upon the Boussinesq approximation, meaning that eddy viscosity is isotropic. According to the k-ε model, eddy viscosity is calculated by the following equation:

$$\nu_t = f_\mu C_\mu \frac{k^2}{\varepsilon} \quad (2.2.14)$$

where ε the turbulent dissipation:

$$\varepsilon = \nu \left[\frac{\partial u_i'}{\partial x_j} \left(\frac{\partial u_i'}{\partial x_j} + \frac{\partial u_j'}{\partial x_i} \right) \right] \qquad (2.2.15)$$

Turbulent kinetic energy and turbulent dissipation are calculated by solving the corresponding transport equations:

$$\frac{Dk}{Dt} = \frac{\partial}{\partial x_j} \left(\nu_t \frac{\partial k}{\partial x_j} \right) + G - (\varepsilon + D) \qquad (2.2.16)$$

$$\frac{D\varepsilon}{Dt} = \frac{\partial}{\partial x_j} \left(\frac{\nu_t}{\sigma_\varepsilon} \frac{\partial \varepsilon}{\partial x_j} \right) + C_1 f_1 G \frac{\varepsilon}{k} - C_2 f_2 \frac{\varepsilon^2}{k} + E \qquad (2.2.17)$$

where G is the source of turbulent kinetic energy:

$$G = \nu_t \left[\left(\frac{\partial \overline{u_1}}{\partial x_2} + \frac{\partial \overline{u_2}}{\partial x_1} \right)^2 + \left(\frac{\partial \overline{u_2}}{\partial x_3} + \frac{\partial \overline{u_3}}{\partial x_2} \right)^2 + \left(\frac{\partial \overline{u_1}}{\partial x_3} + \frac{\partial \overline{u_3}}{\partial x_1} \right)^2 + \left(\frac{\partial \overline{u_1}}{\partial x_1} \right)^2 + \left(\frac{\partial \overline{u_2}}{\partial x_2} \right)^2 + \left(\frac{\partial \overline{u_3}}{\partial x_3} \right)^2 \right]$$
$$(2.2.18)$$

The rest of the values appearing in equations (2.2.16) and (2.2.17) are adjustable constants, deriving from experimental studies according to the various flavors of the model proposed in the literature (table 2.2.1).

The RANS equations along with the time-averaged continuity equation and the k and ε transport equations, form a system of six equations with six unknown quantities. This system replaces the original four-equation system.

Table 2.2.1. Flavors of the k-ε model.

	Turbulence Model		
	Standard	Launder-Sharma	Lam-Bremhorst
C_μ	0.09		
C_1	1.44		
C_2	1.92		
σ_ε	2.20		
f_μ	1.	$\exp\left[-3.4/\left(1+\frac{R_T}{50}\right)^2\right]$	$[1.-\exp(-0.0165 \cdot R_y)]^2 \cdot \left(1.+\frac{20.5}{R_T}\right)$
f_1	1.	1	$1.+\left(0.05/f_\mu\right)^3$
f_2	1.	$1.-0.3 \cdot \exp\left[-R_T{}^2\right]$	$1.-\exp\left[-R_T{}^2\right]$
D	0.	$2.\cdot \nu \cdot \left(\partial\sqrt{k}/\partial x_2\right)^2$	0.
E	0.	$2.\cdot \nu \cdot \nu_t \cdot (\partial^2 U/\partial x_2{}^2)^2$	0.

In the curvilinear coordinates of paragraph 2.1, using the Standard model, the transport equations (2.2.16) and (2.2.17) become:

$$C(k) = \frac{1}{h_i h_j h_l}\left[\frac{\partial}{\partial x_i}\left(\mu_t \frac{h_j h_l}{h_i}\frac{\partial k}{\partial x_i}\right) + \frac{\partial}{\partial x_j}\left(\mu_t \frac{h_i h_l}{h_j}\frac{\partial k}{\partial x_j}\right) + \frac{\partial}{\partial x_l}\left(\mu_t \frac{h_i h_j}{h_l}\frac{\partial k}{\partial x_l}\right)\right] + G - \rho\varepsilon \quad (2.2.19)$$

$$C(\varepsilon) = \frac{1}{h_i h_j h_l}\left[\frac{\partial}{\partial x_i}\left(\frac{\mu_t}{\sigma_\varepsilon}\frac{h_j h_l}{h_i}\frac{\partial \varepsilon}{\partial x_i}\right) + \frac{\partial}{\partial x_j}\left(\frac{\mu_t}{\sigma_\varepsilon}\frac{h_i h_l}{h_j}\frac{\partial \varepsilon}{\partial x_j}\right) + \frac{\partial}{\partial x_3}\left(\frac{\mu_t}{\sigma_\varepsilon}\frac{h_i h_j}{h_l}\frac{\partial \varepsilon}{\partial x_l}\right)\right] + C_1 G\frac{\varepsilon}{k} - C_2\rho\frac{\varepsilon^2}{k}$$
$$(2.2.20)$$

where h_i, h_j, h_l are the grid metrics, μ_t the eddy viscosity and the source of turbulent kinetic energy is:

$$G = 2\mu_t\left[e_{ii}{}^2 + e_{jj}{}^2 + e_{ll}{}^2 + \frac{1}{2}\left(e_{ij}{}^2 + e_{jl}{}^2 + e_{il}{}^2\right)\right] \quad (2.2.21)$$

The RANS equations along with the continuity equation and the k and ε equations, form a system of six equations with six unknown quantities, the three velocity components, the pressure and the turbulent kinetic energy and its dissipation rate.

2.2.3   The Two-Equation k-ω-SST Model

The k-ω-SST (Shear stress transport) model is another widely used two-equation model also based upon the Boussinesq approximation. This model divides the domain into two regions, the outer where the k-ε model is applied and the inner where the k-ω model is applied. The expression for the effective viscosity μ_e is the same as in the k-ε model (equation 2.2.13) only this time eddy viscosity is a function of k and ω, the latter being the specific rate of dissipation of the turbulence kinetic energy k. The transport equations for k and ω can be written in the general form:

$$C(\Phi) = \frac{1}{h_i h_j h_l}\left[\frac{\partial}{\partial x_i}\left(\sigma_\Phi \mu_t \frac{h_j h_l}{h_i}\frac{\partial \Phi}{\partial x_i}\right) + \frac{\partial}{\partial x_j}\left(\sigma_\Phi \mu_t \frac{h_i h_l}{h_j}\frac{\partial \Phi}{\partial x_j}\right) + \frac{\partial}{\partial x_l}\left(\sigma_\Phi \mu_t \frac{h_i h_j}{h_l}\frac{\partial \Phi}{\partial x_l}\right)\right] + S_\Phi$$
$$(2.2.22)$$

where

$$\Phi = k \text{ or } \omega$$

$$S_k = G - \beta^* \cdot \rho \cdot \omega \cdot k$$

$$S_\omega = \frac{\gamma}{\nu_t} G - \beta \cdot \rho \cdot \omega^2 + 2 \cdot \rho \cdot (1 - F_1) \frac{\sigma_{\omega 2}}{\omega} \frac{1}{h_j^2} \frac{\partial k}{\partial x_j} \frac{\partial \omega}{\partial x_j}$$

$$(2.2.23)$$

The constants of the model are:

$$\alpha_1 = 0.31, \beta^* = 0.09, \kappa = 0.41$$

<u>Internal k-ω model (φ$_1$)</u> $$\sigma_{k1} = 0.5, \sigma_{\omega 1} = 0.500, \beta_1 = 0.075$$

$$\gamma_1 = \frac{\beta_1}{\beta^*} - \frac{\sigma_{\omega 1}\kappa^2}{\sqrt{\beta^*}} = 0.553$$

<u>Internal k-ε model (φ$_2$)</u> $$\sigma_{k2} = 0.85, \sigma_{\omega 2} = 0.500, \beta_2 = 0.0828$$

$$\gamma_2 = \frac{\beta_2}{\beta^*} - \frac{\sigma_{\omega 2}\kappa^2}{\sqrt{\beta^*}} = 0.44$$

The constants σ_k, σ_ω, β, γ in the unified transport equations (2.2.22) are linear combinations of the internal and external regions:

$$\varphi = F_1 \cdot \varphi_1 + (1 - F_1) \cdot \varphi_2 \quad (2.2.24)$$

In (2.2.24) F_1 is a blending function given through:

$$F_1 = \tanh(\text{arg}_1{}^4), \quad \text{arg}_1 = \min\left\{\max\left[2\frac{\sqrt{k}}{0.09 \cdot y \cdot \omega}; \frac{500v}{y^2 \omega}\right]; \frac{4 \cdot \rho \cdot \sigma_{\omega 2} \cdot k}{CD_{k\omega}y^2}\right\}$$

where y is the distance from the solid boundary and

$$CD_{k\omega} = \max\left[2 \cdot \rho \cdot \sigma_{\omega 2} \frac{1}{\omega} \frac{1}{h_j^2} \frac{\partial k}{\partial x_j} \frac{\partial \omega}{\partial x_j}; 10^{-20}\right]$$

The eddy viscosity is calculated from the following expression:

$$\nu_t = a_1 \cdot k / \max[a_1 \cdot \omega; |\text{rot}(\vec{c})|F_2] \quad (2.2.25)$$

where the function F_2 is calculated as:

$$F_2 = \tanh(\text{arg}_2{}^2), \quad \text{arg}_2 = \max\left[2\frac{\sqrt{k}}{0.09 \cdot y \cdot \omega}; \frac{500v}{y^2 \omega}\right] \quad (2.2.26)$$

The above formulation is adopted near the solid boundaries. In the wake or the regions far from the solid boundary, turbulence is modeled using only the k-ε model, i.e. $F_1 = F_2 = 0$. The source of turbulent kinetic energy is calculated through the eddy viscosity and the deformation tensor, in the same way as in the k-ε model:

$$G = 2\mu_t \left[e_{ii}{}^2 + e_{jj}{}^2 + e_{ll}{}^2 + \frac{1}{2}(e_{ij}{}^2 + e_{jl}{}^2 + e_{il}{}^2)\right] \quad (2.2.27)$$

2.3 The Finite Volume Method

2.3.1 Introduction

The Navier-Stokes equations, or indeed the RANS equations, are non-linear partial differential equations that cannot be solved directly; rather a numerical method is required. Amongst the many methods that are capable of solving such equations, the Finite Volume method is the most widely used in the area of Computational Hydrodynamics. In the Finite Volume method, the computational domain is divided via a grid mesh, into a number of discrete finite volumes, also known as Control Volumes. Each volume is characterized by a single point, usually its center. Then, the equations governing the flow are integrated over each volume and by employing the divergence theorem, the integrals that contain a divergence term are converted to surface integrals. These terms are evaluated as fluxes on the boundary surface of each volume. The fluxes are themselves evaluated from the values on the center points of the neighboring volumes by adopting a differencing scheme. In figure 2.3.1 a finite volume is presented (shaded area) along with the coordinates system (x_1, x_2, x_3), the center of the finite volume (P), the centers of the neighboring volumes (West - W, East - E, North - N, South - S, Upstream - U, Downstream - D) and the center of the faces (w, e, n, s, u, d).
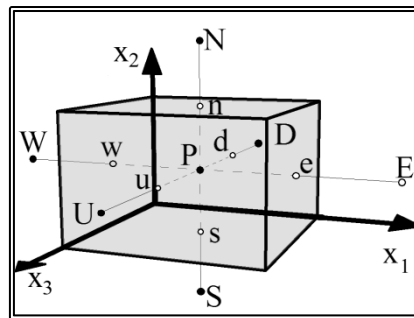
Figure 2.3.1 Definition of a 3-D finite volume

As an example of the method, let us consider the simpler problem of the 2-D steady-state laminar flow of an incompressible fluid. Let's also consider the numerical grid as an orthogonal grid with grid spacing Δx and Δy in the x_1 and x_2 directions respectively (figure 2.3.2).
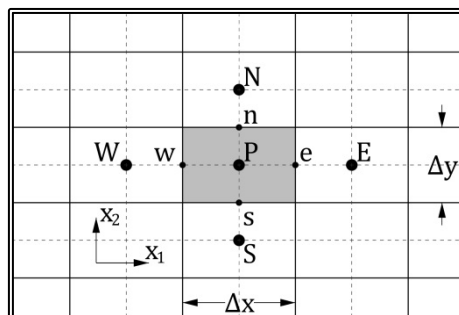
Figure 2.3.2 Definition of a 2-D finite volume

The Navier-Stokes equations as well as the continuity equation can be written in Cartesian coordinates as:

$$\text{div}(\vec{u}) = 0 \quad \Rightarrow \quad \frac{\partial u_1}{\partial x_1} + \frac{\partial u_2}{\partial x_2} = 0 \quad (2.3.1)$$

$$\text{div}(\vec{u} \cdot \Phi) = \text{div}[\nu \cdot \mathbf{grad}(\Phi)] + S_\Phi \quad (2.3.2)$$

where Φ is scalar representing one of the two velocity components u_1, u_2. The left hand side of (2.3.2) is the convection term; while on the right hand side, the first term is the diffusion term and the last term is the source term:

$$S_\Phi = -\frac{1}{\rho} \cdot \frac{\partial p^*}{\partial x_\Phi} + \frac{\partial}{\partial x_1}\left(\nu \cdot \frac{\partial u_1}{\partial x_\Phi}\right) + \frac{\partial}{\partial x_2}\left(\nu \cdot \frac{\partial u_2}{\partial x_\Phi}\right) \qquad (2.3.3)$$

We first integrate the equations over each volume and then apply the divergence theorem:

$$\int_{CV} \text{div}(\vec{a})dV = \int_A \vec{n} \cdot \vec{a}\,dA \quad (2.3.4)$$

In the case of the 2-D orthogonal grid the faces of each volume are always parallel to one of the axis of the Cartesian coordinate system and as a result the continuity equation becomes:

$$\int_{CV} \text{div}(\vec{u})dV = \int_A \vec{n} \cdot \vec{u}\,dA = 0 \qquad (2.3.5)$$

$$\int_e \vec{i} \cdot \vec{u}\,dy + \int_w (-\vec{i}) \cdot \vec{u}\,dy + \int_n \vec{j} \cdot \vec{u}\,dx + \int_s (-\vec{j}) \cdot \vec{u}\,dx = 0 \Rightarrow$$

$$\int_e u_1\,dy - \int_w u_1\,dy + \int_n u_2\,dx - \int_s u_2\,dx = 0 \Rightarrow$$

$$\left(\overline{u_1}|_e \cdot \int_e dy\right) - \left(\overline{u_1}|_w \cdot \int_w dy\right) + \left(\overline{u_2}|_n \cdot \int_n dx\right) - \left(\overline{u_2}|_s \cdot \int_s dx\right) = 0 \Rightarrow$$

$$\overline{u_{1e}} \cdot A_e - \overline{u_{1w}} \cdot A_w + \overline{u_{2n}} \cdot A_n - \overline{u_{2s}} \cdot A_s = 0 \Rightarrow$$

$$C_e - C_w + C_n - C_s = 0 \qquad (2.3.6)$$

where e, w, n, s, denote the four faces of the finite volume, i, j are the unit vectors parallel to the x_1 and x_2 axes respectively, A_* is the area of the (*) face (where (*) is e, w, n or s) and C_* is the flux through the (*) face. Similarly the Navier-Stokes equation becomes:

$$\int_{CV} \text{div}(\Phi \cdot \vec{u})dV = \int_{CV} \nu \cdot \text{div}(\mathbf{grad}\Phi)dV + \int_{CV} S_\Phi dV$$

$$\int_A \vec{n} \cdot \vec{u} \cdot \Phi\,dA = \int_A \nu \cdot \vec{n} \cdot \mathbf{grad}(\Phi)\,dA + \int_{CV} S_\Phi dV \Rightarrow I_1 = I_2 + I_3 \qquad (2.3.7)$$

Regarding the convection term:

$$I_1 = \int_{CV} \text{div}(\Phi \cdot \vec{u})\,dV = \int_A \vec{n} \cdot \vec{u} \cdot \Phi\,dA \Rightarrow$$

$$I_1 = \int_e \vec{\mathbf{i}} \cdot \vec{\mathbf{u}} \cdot \Phi \, dy + \int_w (-\vec{\mathbf{i}}) \cdot \vec{\mathbf{u}} \cdot \Phi \, dy + \int_n \vec{\mathbf{j}} \cdot \vec{\mathbf{u}} \cdot \Phi \, dx + \int_s (-\vec{\mathbf{j}}) \cdot \vec{\mathbf{u}} \cdot \Phi \, dx \Rightarrow$$

$$I_1 = \int_e u_1 \cdot \Phi \, dy - \int_w u_1 \cdot \Phi \, dy + \int_n u_2 \cdot \Phi \, dx - \int_s u_2 \cdot \Phi \, dx \Rightarrow$$

$$I_1 = \left(\overline{u_1 \cdot \Phi}|_e \cdot \int_e dy \right) - \left(\overline{u_1 \cdot \Phi}|_w \cdot \int_w dy \right)$$

$$+ \left(\overline{u_2 \cdot \Phi}|_n \cdot \int_n dx \right) - \left(\overline{u_2 \cdot \Phi}|_s \cdot \int_s dx \right) \Rightarrow$$

$$I_1 \approx u_{1e} \cdot \Phi_e \cdot A_e - u_{1w} \cdot \Phi_w \cdot A_w + u_{2n} \cdot \Phi_n \cdot A_n - u_{2s} \cdot \Phi_s \cdot A_s \Rightarrow$$

$$I_1 = \Phi_e \cdot C_e - \Phi_w \cdot C_w + \Phi_n \cdot C_n - \Phi_s \cdot C_s \quad (2.3.8)$$

where Φ_* is the mean value of the scalar Φ on the (*) face.

The diffusion term becomes:

$$I_2 = \int_{CV} \text{div}[v \cdot \text{grad}(\Phi)] \, dV = \int_A v \cdot \vec{\mathbf{n}} \cdot \text{grad}(\Phi) \, dA \Rightarrow$$

$$I_2 = \int_e v \cdot \vec{\mathbf{i}} \cdot \mathbf{grad}(\Phi) \, dy + \int_w v \cdot (-\vec{\mathbf{i}}) \cdot \mathbf{grad}(\Phi) \, dy$$

$$+ \int_n v \cdot \vec{\mathbf{j}} \cdot \mathbf{grad}(\Phi) \, dx + \int_s v \cdot (-\vec{\mathbf{j}}) \cdot \mathbf{grad}(\Phi) \, dx \Rightarrow$$

$$I_2 = \int_e v \cdot \frac{\partial \Phi}{\partial x} \, dy - \int_w v \cdot \frac{\partial \Phi}{\partial x} \, dy + \int_n v \cdot \frac{\partial \Phi}{\partial y} \, dx - \int_s v \cdot \frac{\partial \Phi}{\partial y} \, dx \Rightarrow$$

$$I_2 = \left(v \cdot \overline{\frac{\partial \Phi}{\partial x}}\Big|_e \cdot \int_e dy \right) - \left(v \cdot \overline{\frac{\partial \Phi}{\partial x}}\Big|_w \cdot \int_w dy \right)$$

$$+ \left(v \cdot \overline{\frac{\partial \Phi}{\partial y}}\Big|_n \cdot \int_n dx \right) - \left(v \cdot \overline{\frac{\partial \Phi}{\partial y}}\Big|_s \cdot \int_s dx \right) \Rightarrow$$

$$I_2 \approx v \cdot \frac{\Phi_E - \Phi_P}{\delta x_{PE}} \cdot A_e - v \cdot \frac{\Phi_P - \Phi_W}{\delta x_{WP}} \cdot A_w + v \cdot \frac{\Phi_N - \Phi_P}{\delta y_{PN}} \cdot A_n - v \cdot \frac{\Phi_P - \Phi_S}{\delta y_{SP}} \cdot A_s \Rightarrow$$

$$I_2 = v \cdot \frac{\Phi_E - \Phi_P}{\delta x_{PE}} \cdot \delta y_{ns} - v \cdot \frac{\Phi_P - \Phi_W}{\delta x_{WP}} \cdot \delta y_{ns}$$

$$+ v \cdot \frac{\Phi_N - \Phi_P}{\delta y_{PN}} \cdot \delta x_{ew} - v \cdot \frac{\Phi_P - \Phi_S}{\delta y_{SP}} \cdot \delta x_{ew} \Rightarrow$$

$$I_2 = \Phi_E \cdot \frac{v \cdot \delta y_{ns}}{\delta x_{PE}} + \Phi_W \cdot \frac{v \cdot \delta y_{ns}}{\delta x_{WP}} + \Phi_N \cdot \frac{v \cdot \delta x_{ew}}{\delta y_{PN}} + \Phi_S \cdot \frac{v \cdot \delta x_{ew}}{\delta y_{SP}}$$

$$- \Phi_P \cdot \left(\frac{v \cdot \delta y_{ns}}{\delta x_{PE}} + \frac{v \cdot \delta y_{ns}}{\delta x_{WP}} + \frac{v \cdot \delta x_{ew}}{\delta y_{PN}} + \frac{v \cdot \delta x_{ew}}{\delta y_{SP}} \right) \quad (2.3.9)$$

where Φ_P is the mean value of the scalar over the finite volume, Φ_* with (*) equal to E, W, N, S the mean value of the scalar Φ over the (*) neighboring finite volume. Also

δx_{ew} and δy_{ns} are the finite volume length and height and δx_{PE}, δy_{WP}, δy_{PN} and δy_{SP} the distance of the P node from the E, W, N, S, neighboring nodes respectively.

The source term for the u_1 velocity becomes:

$$I_3 = \int_{CV} \left[-\frac{1}{\rho} \cdot \frac{\partial p^*}{\partial x_\Phi} + \frac{\partial}{\partial x}\left(v \cdot \frac{\partial u_1}{\partial x_\Phi}\right) + \frac{\partial}{\partial y}\left(v \cdot \frac{\partial u_2}{\partial x_\Phi}\right) \right] dV \Rightarrow$$

$$I_3 = \int_{CV} \left[-\frac{1}{\rho} \cdot \frac{\partial p^*}{\partial x} + \frac{\partial}{\partial x}\left(v \cdot \frac{\partial u_1}{\partial x}\right) + \frac{\partial}{\partial y}\left(v \cdot \frac{\partial u_2}{\partial x}\right) \right] dV = I_{31} + I_{32}$$

$$I_{31} = \int_{CV} -\frac{1}{\rho} \cdot \frac{\partial p^*}{\partial x} \, dV = -\frac{1}{\rho} \cdot \overline{\left[\frac{\partial p}{\partial x}\right]} \int_{CV} dV \approx -\frac{1}{\rho} \cdot \frac{P_e - P_w}{\delta x_{ew}} \cdot \delta x_{ew} \cdot \delta y_{ns} = \frac{P_w - P_e}{\rho} \cdot \delta y_{ns}$$

$$(2.3.10)$$

where p_e and p_w are the mean values of pressure p over the e, w faces.

$$I_{32} = \int_{CV} \left[\frac{\partial}{\partial x}\left(v \cdot \frac{\partial u_1}{\partial x}\right) + \frac{\partial}{\partial y}\left(v \cdot \frac{\partial u_2}{\partial x}\right) \right] dV \Rightarrow$$

$$I_{32} = \int_e v \cdot \frac{\partial u_1}{\partial x} \, dy - \int_w v \cdot \frac{\partial u_1}{\partial x} \, dy + \int_n v \cdot \frac{\partial u_2}{\partial x} dx - \int_s v \cdot \frac{\partial u_2}{\partial x} \, dx \Rightarrow$$

$$I_{32} = \left(v \cdot \overline{\frac{\partial u_1}{\partial x}}\bigg|_e \cdot \int_e dy \right) - \left(v \cdot \overline{\frac{\partial u_1}{\partial x}}\bigg|_w \cdot \int_w dy \right)$$

$$+ \left(v \cdot \overline{\frac{\partial u_2}{\partial x}}\bigg|_n \cdot \int_n dx \right) - \left(v \cdot \overline{\frac{\partial u_2}{\partial x}}\bigg|_s \cdot \int_s dx \right)$$

$$I_{32} \approx v \cdot \frac{u_{1E} - u_{1P}}{\delta x_{PE}} \cdot A_e - v \cdot \frac{u_{1P} - u_{1W}}{\delta x_{WP}} \cdot A_w$$

$$+ v \cdot \frac{u_{2ne} - u_{2nw}}{\delta x_{ew}} \cdot A_n - v \cdot \frac{u_{2se} - u_{2sw}}{\delta x_{ew}} \cdot A_s \Rightarrow$$

$$I_{32} = v \cdot \frac{u_{1E} - u_{1P}}{\delta x_{PE}} \cdot \delta y_{ns} - v \cdot \frac{u_{1P} - u_{1W}}{\delta x_{WP}} \cdot \delta y_{ns}$$

$$+ v \cdot \frac{u_{2ne} - u_{2nw}}{\delta x_{ew}} \cdot \delta x_{ew} - v \cdot \frac{u_{2se} - u_{2sw}}{\delta x_{ew}} \cdot \delta x_{ew} \Rightarrow$$

$$I_{32} = \Phi_E \cdot \frac{v \cdot \delta y_{ns}}{\delta x_{PE}} + \Phi_W \cdot \frac{v \cdot \delta y_{ns}}{\delta x_{WP}} - \Phi_P \cdot \left(\frac{v \cdot \delta y_{ns}}{\delta x_{PE}} + \frac{v \cdot \delta y_{ns}}{\delta x_{WP}} \right)$$

$$+ v \cdot (u_{2ne} - u_{2nw} - u_{2se} + u_{2sw}) \quad (2.3.11)$$

where u_{2ne}, u_{2nw}, u_{2se}, and u_{2sw} are the values of u_2 velocity at the north-east (ne), north-west (nw), south-east (se) and south-west (sw) corners of the finite volume. A similar formulation can be obtained for the source term for the u_2 velocity.

The above analysis results in an expression for the N-S equation that contains the values of the unknown scalar quantity Φ on the center of each finite volume. Also appearing are the mean values of the scalar Φ on the volume faces. In order to calculate the values on the faces, some differencing scheme is applied and yet again

the values on the faces are expressed through the values of Φ on the center of the finite volumes.

Finally, by subtracting the continuity equation from the convection term and then properly arranging the terms so that only Φ_P appears on the left-hand side and all other terms are on the right-hand side, one can arrive at the typical formulation for a system of linear equations:

$$A_P * \Phi_P = A_E * \Phi_E + A_W * \Phi_W + A_N * \Phi_N + A_S * \Phi_S + S_\Phi \quad (2.3.12)$$

where

$$A_P = A_E + A_W + A_N + A_S$$

2.3.2   The Differencing Scheme

In the previous paragraph the formulation for the convection term, equation 2.3.8, contains the mean values of the scalar Φ on each face of the finite volume yet the values for the scalar Φ are calculated on the center of each volume. Consequently a differencing scheme must be employed in order to calculate the values on the volume faces from the values at the volume centers. Theoretically if one could use an infinite number of grid nodes, the solution obtained by the finite volume method would be the exact solution, regardless of the differencing scheme. In practice, only a relatively small number of nodes can be used, a fact that can lead to numerical instabilities that in turn can hamper the convergence of the method. The differencing scheme plays a very important role in the convergence of the method and in order to ensure the convergence, the differencing scheme must be characterized by (Demirdzic et al., 1987):

➢ Conservativeness
➢ Boundedness
➢ Transportiveness

A scheme is conservative when it ensures the continuity of Φ throughout the computational domain. That can be achieved if the flux of Φ exiting one finite volume through one of its faces, is always equal to the flux of Φ entering the neighboring volume through their common face.

A condition that is sufficient for the convergence of an iterative method for solving partial differential equations in the form of equation 2.3.12, is that:

$$\frac{\sum|A_i|}{|A_P'|} \begin{cases} \leq 1 \text{ , on all nodes} \\ < 1 \text{ , on at least one node} \end{cases}, i = E, W, N, S, U, D \quad (2.3.13)$$

where

$$A_P' = A_P - S_\Phi$$

If the above is true then it is said that the matrix of the linear system has a strong main diagonal. A differencing scheme that results in a matrix with a strong main diagonal is characterized by boundedness.

For a convection-diffusion flow one can define the non-dimensional Péclet number:

$$Pe = \frac{convection\ transport\ rate}{diffusion\ transport\ rate}$$

Péclet number is a measure of the relative importance of convection and diffusion in a flow. When $Pe \to 0$, there is pure diffusion while $Pe \to \infty$ corresponds to pure convection. A differencing scheme that relates the direction of transport of a flow characteristic, to the direction of the flow and to the Péclet number, is characterized by transportiveness.

Another important characteristic of a differencing scheme is its accuracy measured through the Taylor series truncation error. A scheme characterized by higher accuracy is desirable, since for a given grid size the results will be more accurate, or else, for a desired level of accuracy, a coarser grid is required.

Many differencing schemes have been proposed in the literature with different accuracy levels and not all of them being characterized by conservativeness, boundedness and transportiveness. In the following a brief overview of the most common schemes will be presented.

The simplest scheme one can devise is to use at a face the value calculated on the center of one of the finite volumes that are either side of the face, depending on the sign of the flux through that face. This scheme is called the Upwind Differencing Scheme (UD). In the case of a 1-D flow (figure 2.3.3) and for the east face of a finite volume the UD scheme can be written as:

$$\left.\begin{array}{l} \Phi_e = \Phi_P \ , \ C_e > 0 \\ \Phi_e = \Phi_E \ , \ C_e < 0 \end{array}\right\} \ (2.3.14)$$

The Upwind Differencing scheme is conservative since Φ_e for the finite volume P is always equal to Φ_w for the neighboring E node. Also this scheme is characterized by boundedness since its contribution to A_P is always positive and is also characterized by transportiveness since the sign of the flux is affecting the transport of Φ.
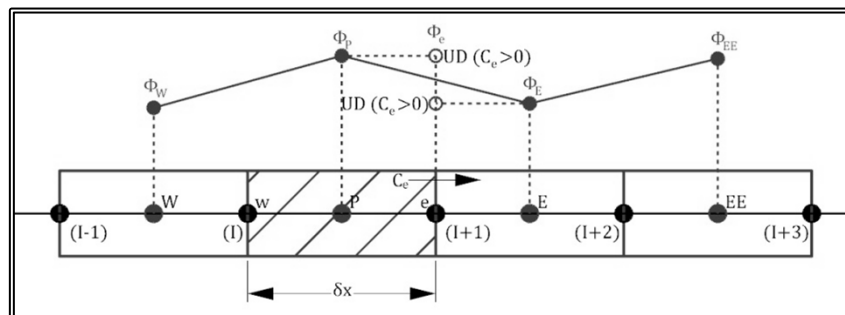
Figure 2.3.3 Definition of the Upwind Differencing Scheme

In terms of the Taylor series truncation error, the Upwind Differencing scheme is a zero-order scheme. Another disadvantage of the Upwind Differencing scheme is that it reduces the variation of the transported value resulting in a form of artificial diffusion. On the other hand, in flows with a strong mean flow such as the flow past a ship, the use of the Upwind Differencing scheme in the direction parallel to the mean flow, results in adequate accuracy with the minimum computational cost.

A first order, in accuracy, scheme that can be considered an expansion of the previous is the Linear Upwind Scheme (LUD). In this scheme the value of Φ on a face is effectively the linear extrapolation of the values on two successive grid nodes that are either on one side of the face or the other, depending on the sign of the flux through that face. In the case of a 1-D flow (figure 2.3.4) and for the east face of a finite volume the LUD scheme can be written as:

$$\left.\begin{array}{l} \Phi_e = \Phi_P + \dfrac{\Phi_P - \Phi_W}{2} \ , \ C_e > 0 \\[2mm] \Phi_e = \Phi_E - \dfrac{\Phi_{EE} - \Phi_E}{2} \ , \ C_e < 0 \end{array}\right\} \qquad (2.3.15)$$

The Linear Upwind Differencing scheme is conservative and is characterized by transportiveness just as the zero-order Upwind Scheme. On the other hand it is not always characterized by boundedness and can cause instabilities to the iterative solution.
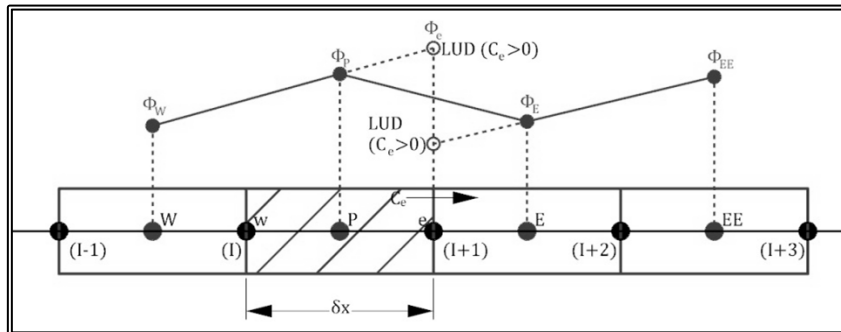
Figure 2.3.4 Definition of the Linear Upwind Differencing Scheme

Another simple scheme and perhaps the one that immediately springs into mind, is the Central Differencing scheme (CD). In this scheme the value of Φ on a face is calculated as effectively the linear interpolation amongst the values on the two grid nodes that are on either side of the face. In the case of a 1-D flow (figure 2.3.5) and for the east face of a finite volume the CD scheme can be written as:

$$\Phi_e = \Phi_P + \dfrac{\Phi_E - \Phi_P}{2} \quad (2.3.16)$$

The Central Differencing scheme is second order in terms of the Taylor series truncation error. It is also conservative but is not always characterized by boundedness. Furthermore it is not characterized by transportiveness so it is unsuitable to model convection flows.
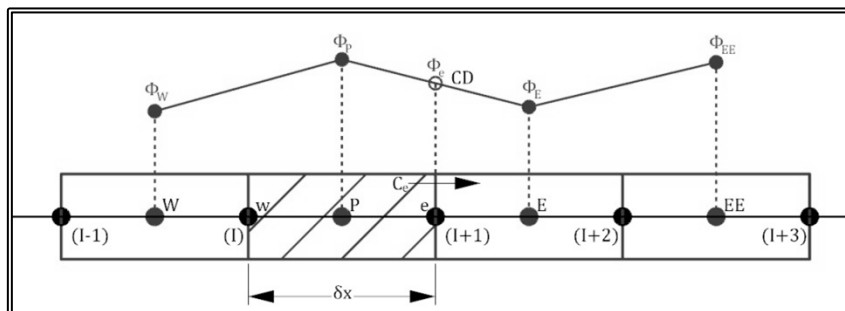
Figure 2.3.5 Definition of the Central Differencing Scheme

2.3.3 Total Variation Diminishing Schemes

From the above paragraph it is concluded that all three simple differencing schemes have considerable drawbacks that in many cases makes their use impractical. Many other differencing schemes have been proposed in the literature, some of them of third or higher order of accuracy. Due to their particular characteristics and drawbacks, no single scheme has been widely adopted. The main concern with the higher-order schemes is the stability of convergence. To combine the accuracy of the higher-order schemes with the stability of lower-order ones, bounded schemes called Total Variation Diminishing (TVD) schemes were developed. TVD schemes are second or higher –order and to avoid instabilities, they introduce artificial diffusion or they increase the contribution of the upstream flow characteristics. Initially, the TVD schemes were developed for solving gas-dynamics problems and were called Flux Corrected Transport (FCT) schemes. The TVD schemes in their current form are the result of the contributions of many researchers (Van Leer, 1974, 1977a, 1977b & 1979, Sweby, 1984 and Roe, 1985)

Based on the analysis of the previous paragraph for a 1-D flow, the value of Φ at the east face and for a positive flux can be calculated as:

Upwind Differencing (UD):

$$\Phi_e = \Phi_P$$

Linear Upwind Differencing (LUD):

$$\Phi_e = \Phi_P + \frac{\Phi_P - \Phi_W}{2}$$

Central Differencing (CD):

$$\Phi_e = \Phi_P + \frac{1}{2}(\Phi_E - \Phi_P)$$

Let us consider the general scheme:

$$\Phi_e = \Phi_P + \frac{1}{2}\psi(r)(\Phi_E - \Phi_P) \qquad (2.3.17)$$

$$r = \left(\frac{\Phi_P - \Phi_W}{\Phi_E - \Phi_P}\right) \ (2.3.18)$$

where r is effectively the ratio of the derivatives of Φ on either side of the e-face. It can be easily deducted that depending on the form of $\psi(r)$, the general scheme of equation 2.3.17 becomes one of the three simple schemes:

$$\psi(r) = 0 \rightarrow \text{Upwind Differencing.}$$

$$\psi(r) = 1 \rightarrow \text{Central Differencing.}$$

$$\psi(r) = r \rightarrow \text{Linear Upwind Differencing.}$$

In figure 2.3.6 the form of $\psi(r)$ is presented for the three schemes. The flux through the e-face is considered positive.
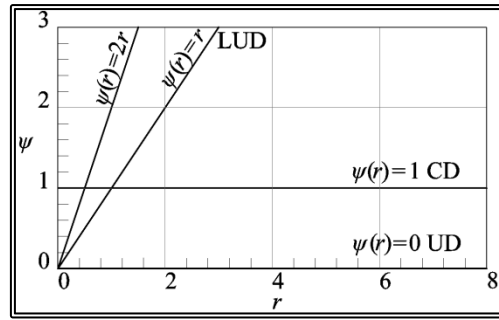
Figure 2.3.6 r – ψ diagram.

Through the study of gas-dynamics problems it was concluded that a desirable characteristic for a stable higher-order scheme is the preserving of monotonicity. A scheme is preserving monotonicity when (i) it does not create new local extremes, (ii) it does not lower the value of a local minimum and (iii) it does not increase the value of a local maximum, in other words when a scheme does not generate new oscillations of the solution.

The property of preserving the monotonicity affects the Total Variation (TV) of the discrete solution. For example, the Total Variation of the solution of figure 2.3.7 is defined as (Lien & Leschziner, 1994):

$$TV(\Phi) = |\Phi_2 - \Phi_1| + |\Phi_3 - \Phi_2| + |\Phi_4 - \Phi_3| + |\Phi_5 - \Phi_4|$$

$$TV(\Phi) = |\Phi_3 - \Phi_1| + |\Phi_5 - \Phi_3| \quad (2.3.19)$$
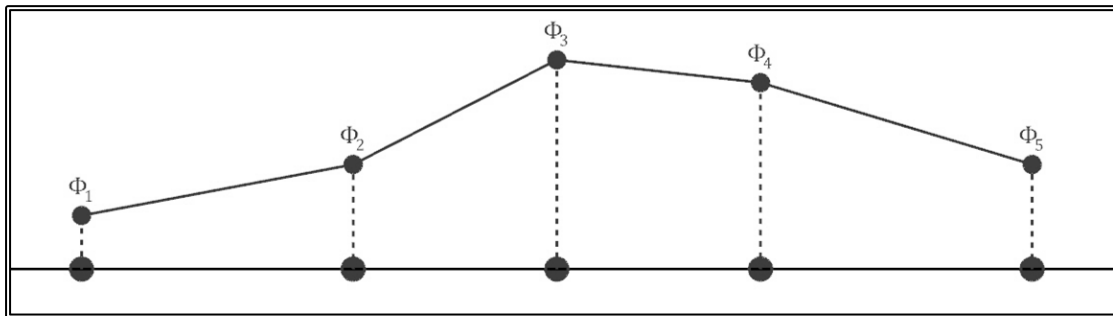
Figure 2.3.7 An example of a discrete solution.

In order for a scheme to preserve monotonicity, the total variation must not increase. Consequently a differencing scheme that is monotonicity preserving, causes the reduction of the total variation as the algorithm progresses, hence the name Total Variation Diminishing.

Sweby (1984) was able to proove that the necessary and sufficient conditions for a differencing scheme to be TVD are:

$$\psi(r) \leq 2r \text{, for } 0 < r < 1 \text{ and}$$

$$\psi(r) \leq 2 \text{, for } r \geq 1.$$

In figure 2.3.8 the TVD region of the r – ψ diagram is presented.
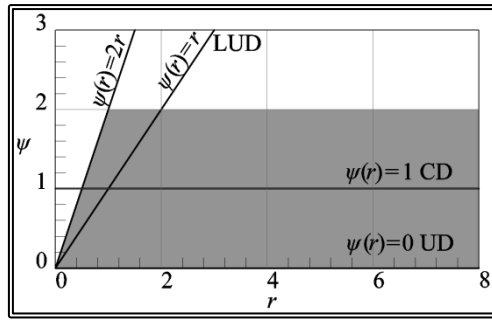
Figure 2.3.8 r – ψ diagram, the TVD region (shaded).

Regarding the differencing schemes of the previous paragraph, we can notice that:

> ➢ The Upwind Differencing scheme is always TVD,
> ➢ The Linear Upwind Differencing scheme is TVD for r ≤ 2 and that
> ➢ The Central Differencing scheme TVD for r ≥ 0.5.

The main idea now is to modify one of the above schemes in order for the ψ(r) function to remain in the TVD region. The ψ(r) function has to limit the convection flux. For that reason such a ψ(r) function is called a Flux Limiter Function.

Sweby introduced a further condition for a TVD scheme to also be second-order in accuracy: The limiter function of a second-order scheme must cross the (1,1) point of the r – ψ diagram.

On figure 2.3.7 we can observe that the ψ(r) functions for the central and the linear upwind differencing schemes, do indeed cross the (1,1) point.

Sweby was also able to prove that the range of the second-order TVD schemes is bounded by the central and the linear upwind differencing schemes:

$$r \leq \psi(r) \leq 1, \text{ for } 0 < r < 1 \text{ and}$$

$$1 \leq \psi(r) \leq r, \text{ for } r \geq 1 .$$

Consequently every weighted average of the central and the linear upwind differencing scheme, that remains within the TVD region of the r – ψ diagram is a second-order scheme.

Finally Sweby proposed the notion of symmetry of a limiter function:

$$\frac{\psi(r)}{r} = \psi\left(1/r\right) \quad (2.3.20)$$

He was able to prove that a function that is symmetrical in the above sense ensures that the flux is calculated in a uniform way, both in the upstream and the downstream direction.

On table 2.3.1, some of the many limiter functions that have been proposed, are presented while the same functions are graphically presented on figure 2.3.9.

Table 2.3.1 Second-order limiter functions.

	Limiter function $\psi(r)$
Van Leer (1974)	$\psi(r) = \dfrac{r + \lvert r \rvert}{1 + r}$
Min-Mod (Roe, 1985)	$\psi(r) = \begin{cases} \min(r; 1) & , r > 0 \\ 0 & , r \le 0 \end{cases}$
SUPERBEE (Roe, 1985)	$\psi(r) = \max[0; \min(2r; 1), \min(r; 2)]$
Sweby (1984)	$\psi(r) = \max[0; \min(\beta \cdot r; 1); \min(r; \beta)]$
QUICK	$\psi(r) = \max[0; \min(2r; (3 + r)/4; 2)]$
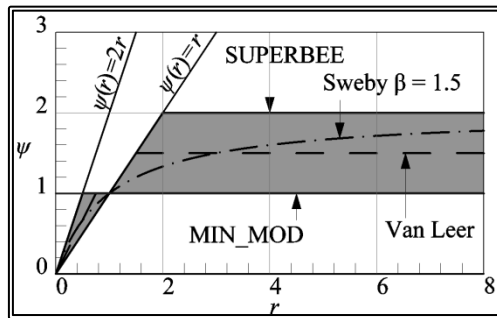
Figure 2.3.9. $r - \psi$ diagram, second-order TVD region (shaded) and limiter functions.

After an extensive bibliographical research, the Min-mod limiter function was selected for implementation with the existing RANS finite volume solver developed at LSMH. The Min-mod limiter function follows the lower limit of the TVD region for second-order schemes. The main advantage of this function is the fact for a given value of r, the TVD scheme becomes one of the three schemes presented in the previous paragraph. Consequently this method has virtually the same computational cost as each of the three schemes. The above characteristic is depicted in figure 2.3.10.
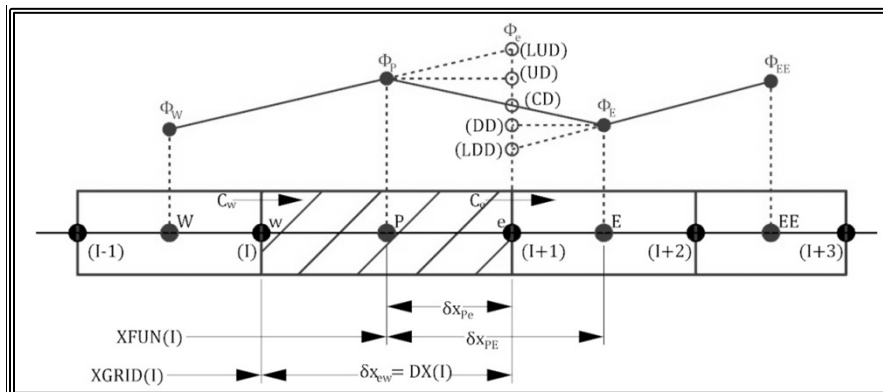
Figure 2.3.10. Calculation of Φ_e using the Min-Mod limiter function, r < 0: upwind differencing; 0 < r < 1: linear upwind differencing; r ≥ 1: central differencing.

As part of the present study, the TVD scheme in conjunction with the Min-mod limiter function was expanded for use in 3-D non-uniform curvilinear grids and was successfully applied for calculating the convection term in two (Tzabiras et al. 2009b) and three dimensions (Tzabiras et al. 2009a),(Tzabiras & Kontogiannis, 2009).

2.3.4 Boundary Conditions

In order to solve the transport equations, due to their elliptic nature, boundary conditions are required throughout the boundary of the computational domain. For an external flow problem, characterized by a velocity vector **U∞**, we can define four sections of the boundary (figure 2.3.11), namely:

- West (W), the upstream, or inlet boundary
- North (N), the external boundary
- East (E), the downstream or outlet boundary and
- South (S), the solid boundary or the surface of the body (or bodies)
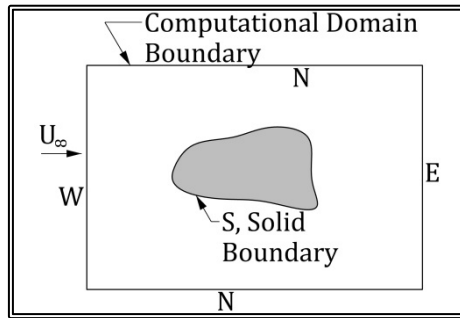
Figure 2.3.11 Definition of the computational domain boundary.

On each section of the boundaries, a condition for each flow variable Φ (u_1, u_2, u_3, p, k, ε) must be provided. These boundary conditions can be of two types:

$$\text{Dirichlet:} \Phi = f$$

$$\text{Neumann:} \frac{\partial \Phi}{\partial n} = f \qquad (2.3.21)$$

where n is the direction perpendicular to the boundary.

Each section of the boundary is handled in a deferent manner. The inlet and external boundaries are placed far enough from the body, so that the flow is laminar and the conditions may be calculated by means of simplified models. A first approach is to consider the boundaries so far from the body, that the flow is almost undisturbed. In that case, the boundary conditions are:

$$u_1 = \mathbf{U}_\infty \cdot \bar{\imath}$$

$$u_2 = \mathbf{U}_\infty \cdot \bar{\jmath}$$

$$u_3 = \mathbf{U}_\infty \cdot \bar{k}$$

$$p = p_{static}$$

$$k \ll, \varepsilon \ll \qquad (2.3.22)$$

Though far from the body, flow is considered laminar, the boundary condition for the turbulent kinetic energy k and the turbulent dissipation ε is a very small but non-zero value. This is done to avoid the possibility of divisions by zero.

The drawback of the above approach is that the boundary must be quite far from the body, thus increasing the computational cost. Another approach is to consider the two boundaries closer to the body but still well outside of the boundary layer. Outside the boundary layer, the effect of viscosity is negligible and the behavior of the flow resembles that of an inviscid flow. If we also consider the flow outside the boundary layer as irrotational, an assumption that is also in good agreement with the actual behavior of the flow, then we can obtain the boundary conditions by means of the potential theory. Using a surface panel methodology based on the classical method of Hess & Smith (1968) we can obtain the values for the velocity components and the pressure on every point of the computational domain. The boundary conditions then become:

$$u_1 = u_{1,potential}$$

$$u_2 = u_{2,potential}$$

$$u_3 = u_{3,potential}$$

$$p = p_{potential}$$

$$k \ll, \varepsilon \ll \qquad (2.3.23)$$

The situation with the outlet boundary is rather more complicated since it contains part of the wake. Inside the wake the flow is significantly affected by viscosity, consequently the potential theory does not apply. The adopted solution is to assume that at a distance from the body, the flow has "stabilized" and that the values of each flow variable, bar pressure, remain the same, or in other words the derivatives of all variables normal to the outlet boundary are equal to zero:

$$\frac{\partial u_1}{\partial n} = \frac{\partial u_2}{\partial n} = \frac{\partial u_3}{\partial n} = \frac{\partial k}{\partial n} = \frac{\partial \varepsilon}{\partial n} = 0 \qquad (2.3.24)$$

Regarding pressure, the value on the boundary is calculated by a linear extrapolation of the corresponding values on the two finite volumes nearest to the boundary, as calculated in the previous iteration.

On a solid boundary, that in the external flow case is considered stationary, the no-penetration condition applies:

$$u_n = 0 \qquad (2.3.25)$$

Furthermore for a viscous flow, the no-slip condition also applies:

$$u_t = 0 \qquad (2.3.26)$$

where u_n the velocity normal to the solid boundary and u_t the tangential velocity. As a result the boundary conditions on the solid boundary are:

$$u_1 = u_2 = u_3 = k = 0, \frac{\partial p}{\partial n} = 0 \qquad (2.3.27)$$

Regarding the turbulent dissipation ε, the boundary conditions depend on the turbulence model. When the k-ω-SST model is used, the boundary conditions for ε derive from a mixing length approximation.

This approach has two significant drawbacks, namely the k-ε model fails to predict the logarithmic velocity profile near the solid boundary and in any case, in order to model the flow within the viscous sub-layer, a very fine discretization is required. To circumvent both problems, the wall functions method (Launder and Spalding, 1974) was introduced. The wall functions consider the near-wall flow, a steady Couette flow. They then use empirical laws to model the near-wall region so that it is possible to express the mean velocity parallel to the wall u and turbulence quantities outside the viscous sub-layer in terms of the distance from the wall y_R and wall conditions such as the wall shear stress τ_w. Hence, the wall functions can be used to provide near-wall boundary conditions for the momentum and turbulence transport equations, rather than conditions at the wall itself, so that the flow inside the viscous sub-layer does not have to be solved. Experimental and dimensional analysis shows that the wall shear stress τ_w is related to the mean velocity parallel to the wall u, through the so-called logarithmic law of the wall:

$$u^+ = \frac{1}{\kappa}\ln(E \cdot y^+) \qquad (2.3.28)$$

where the wall-coordinate y^+ is given by:

$$y^+ = \frac{y_R}{\nu}\left(\frac{\tau_w}{\rho}\right)^{1/2} \qquad (2.3.29)$$

and

$$u^+ = \frac{u}{(\tau_w/\rho)^{1/2}} \qquad (2.3.30)$$

also κ=0.42 is the von Kármán constant and E=9.79 is a roughness parameter. The turbulent kinetic energy k is then:

$$k = C_\mu^{-1/2}\left(\frac{\tau_w}{\rho}\right) \qquad (2.3.31)$$

where C_μ=0.09, while the turbulent dissipation ε is:

$$\varepsilon = (\tau_w/\rho)^{3/2}/(\kappa \cdot y_R) \qquad (2.3.32)$$

finally:

$$\frac{\tau_w}{\rho} = \nu_t\frac{\partial u}{\partial y_R}, \frac{\partial u}{\partial y_R} = \frac{(\tau_w/\rho)^{1/2}}{\kappa \cdot y_R} \qquad (2.3.33)$$

The logarithmic law is valid in the region 40<y^+<200. By setting the first computational node inside the above region and by employing the wall functions method, one can obtain a full set of boundary condition for the near-wall region.

A special case of boundary conditions appears when one of the boundaries is a symmetry plane. Then the flux normal to the symmetry plane must be zero and the derivatives of all other variables normal to the symmetry plane must also be zero:

$$u_n = 0$$

$$\frac{\partial u_t}{\partial n} = \frac{\partial p}{\partial n} = \frac{\partial k}{\partial n} = \frac{\partial \varepsilon}{\partial n} = 0 \quad (2.3.34)$$

As mentioned in previous paragraphs, in the finite volume method, the values for the flow variables are calculated and stored on the center point of each finite volume. In order for the boundary conditions to be applied at the center points of the boundary volumes, it is necessary that the dimension normal to the boundary of these volumes is zero. In doing so, the center points are on the boundary itself. As an example, let us consider the 2-D case of an orthogonal NIxNJ grid where equi-J-lines are horizontal, parallel to the x_1 axis and equi-I-lines are vertical, parallel to the x_2 axis (figure 2.3.12). Let's also say that the value of the variable $\Phi(I,J)$ is stored at the center of the finite volume defined by the four grid nodes (I,J), (I+1,J) (I,J+1) and (I+1,J+1). Then the above formulation results in the I=1 and J=1 grid lines coinciding with the I=2 and J=2 lines respectively.
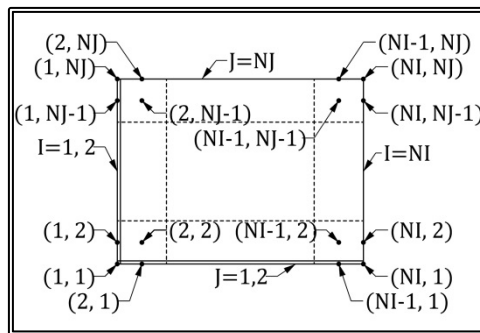
Figure 2.3.12 Definition of the boundary nodes on a 2-D H-type grid.

Another special case is that of o-type grids. As an example, let us consider the 2-D case of a cylindrical NIxNJ grid where equi-J-lines are circular, parallel to the θ-axis and equi-I-lines are radial, parallel to the r-axis (figure 2.3.13). In order to apply the boundary conditions correctly, the I=NI-1 line must coincide with the I=1 line while the I=NI line coincides with the I=2 line. In doing so, $\Phi(NI-1,J) = \Phi(1,J)$ and $\Phi(NI,J) = 0.5*[\Phi(1,J) + \Phi(2,J)]$.
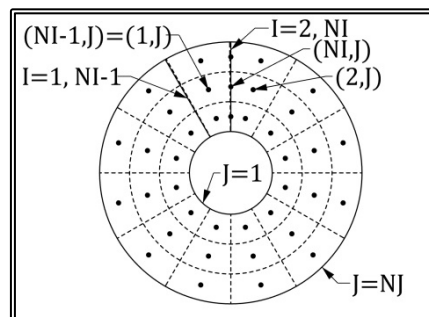
Figure 2.3.13 Definition of the boundary nodes on a 2-D o-type grid.

The above formulations refer to the boundary conditions for an external flow problem. In the case of the overlapping grid blocks, a special treatment of the boundary conditions is required in order to transfer the flow variables from one block to the next while ensuring the conservation of mass. This special treatment will be discussed in a following paragraph.

2.3.5 Pressure Correction Algorithm

The Navier-Stokes equations along with the continuity equation, form a system of four (in the 3-D case) non-linear partial differential equations with four unknown quantities, u_1, u_2, u_3 and p. Although the direct numerical solution of such a system is possible, this direct approach is used rarely and for special types of flow such as compressible flows. Regarding the Marine Hydrodynamics problems the SIMPLE (Semi-Implicit Method for Pressure Linked Equations) algorithm devised by Patankar & Spalding (Spalding, 1980) is almost universally adopted.

The SIMPLE algorithm is an iterative procedure where the transport equation for each of the velocity components is solved separately and then an equation for the correction of the pressure is solved in such a way that the corrected pressure satisfies continuity. More specifically, at an intermediate iteration, the distribution of pressure and the velocity components is considered known (from the previous iteration) and the transport equations for each velocity component are solved separately. The resulting new velocity distributions do not satisfy continuity since the pressure field used in the calculations is not exact. As an example let us consider the 2-D problem where at an intermediate step k of the iterative procedure, the linearized transport equations can be written as:

$$u_P = \frac{A_E}{A_P} u_E + \frac{A_W}{A_P} u_W + \frac{A_N}{A_P} u_N + \frac{A_S}{A_P} u_S + S_P \quad (2.3.35)$$

where the source S_P incorporates the integrated pressure terms:

$$D_u \delta p = \frac{\delta s}{A_P} \delta p \quad (2.3.36)$$

where the term δs is a geometrical dimension. A change of u_P, due to a change in the pressure field δp, can be approximated as:

$$\delta u_P \approx D_u \delta p \quad (2.3.37)$$

That is the sum of the $A_i * u_i$ terms is neglected. The new velocity field (u_1*, u_2*) that results from the above change in the pressure field, can be written as:

$$u_1{}^* = u_1 + \delta u_1 \approx u_1 + D_{u_1} \delta p_1$$

$$u_2{}^* = u_2 + \delta u_2 \approx u_2 + D_{u_2} \delta p_2 \quad (2.3.38)$$

where δp_1 and δp_2 correspond to the pressure change along the x_1 and x_2 directions respectively. We then demand that the new velocity field satisfies the continuity equation:

$$u_{1e}{}^* \cdot \delta x_{2e} - u_{1w}{}^* \cdot \delta x_{2w} + u_{2n}{}^* \cdot \delta x_{1n} - u_{2s}{}^* \cdot \delta x_{1s} = 0 \quad (2.3.39)$$

From equations (2.3.38) and (2.3.39) we obtain a new equation for the pressure correction:

$$D_{u_{1e}} \cdot \delta x_{2e} \cdot (\delta p_P - \delta p_E) - D_{u_{1w}} \cdot \delta x_{2w} \cdot (\delta p_W - \delta p_P) +$$

$$D_{u_{2n}} \cdot \delta x_{1n} \cdot (\delta p_P - \delta p_N) - D_{u_{2s}} \cdot \delta x_{1s} \cdot (\delta p_S - \delta p_P) = -S_m \quad (2.3.39)$$

or else:

$$A_P \delta p_P = A_E \delta p_E + A_W \delta p_W + A_N \delta p_N + A_S \delta p_S - S_m$$

$$A_P = A_E + A_W + A_N + A_S \qquad (2.3.40)$$

The term S_m in (2.3.39) and (2.3.40) is the integral over the finite volume, of the divergence of the original velocity field:

$$S_m = u_{1e} \cdot \delta x_{2e} - u_{1w} \cdot \delta x_{2w} + u_{2n} \cdot \delta x_{1n} - u_{2s} \cdot \delta x_{1s} \qquad (2.3.39)$$

By applying the above procedure for every finite volume, we arrive at a system of linear equations of the (2.3.40) form. The solution of this system is a correction field for the pressure δp and the corrected pressure field is:

$$p_k = p_{k-1} + \delta p \qquad (2.3.40)$$

where p_{k-1} is the original pressure field and p_k the corrected pressure field. The corrected pressure field will not satisfy the transport equations but it is used in the next iteration. The algorithm converges when the pressure correction becomes very small. The flow chart of the SIMPLE algorithm is presented in figure 2.3.14.
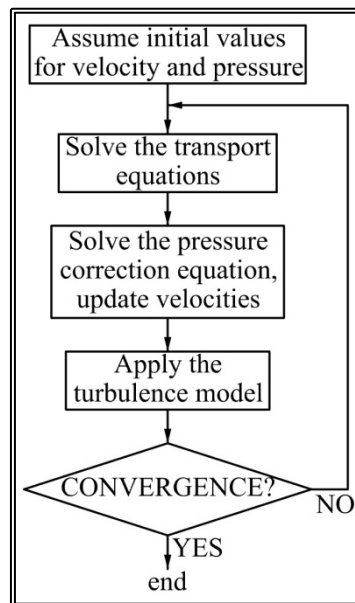
Figure 2.3.14 The SIMPLE algorithm flow chart.

The SIMPLE algorithm is usually combined with the staggered grid concept where the finite volumes for the pressure and the velocity components are different. Let us consider as an example the case of a 2-D orthogonal grid defined by (NIxNJ) grid nodes, where the equi-J-lines are parallel to the x_1-direction and the equi-I-lines parallel to the x_2-direction (figure 2.3.15). The pressure finite volume is defined by the grid nodes (I,J), (I+1,J), (I,J+1) and (I+1,J+1) (denoted by the crosses-hatch in the figure) and the pressure is calculated at the center of the volume. The u_1-velocity is stored at the mid-point of the (I,J), (I,J+1) grid nodes, while the u_2-velocity is stored at the mid-point of the (I,J), (I+1,J) grid nodes. The respective finite volumes differ from the pressure volume and are denoted in figure 2.3.15 with +45 degrees and -45 degrees line hatches respectively.
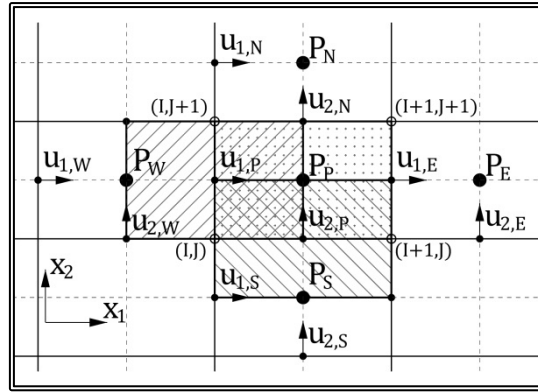
Figure 2.3.15 Definition of staggered grid arrangement.

Another concept used in order to increase the chance of convergence of the SIMPLE algorithm, is that of under-relaxation. The main idea of under-relaxation is that during an iterative solution, the renewed values of a variable result from a linear combination of the calculated value of the present step Φ_k and the value of the previous step Φ_{k-1}:

$$\Phi_k{}' = r \cdot \Phi_k + (1 - r) \cdot \Phi_{k-1} \qquad (2.3.41)$$

where $\Phi_k{}'$ is the new value and r is the under-relaxation factor with $0 \leq r \leq 1$. If r=1 then $\Phi_k{}'=\Phi_k$ while if r=0 then $\Phi_k{}'=\Phi_{k-1}$ consequently the smaller the value of r, the slowest the convergence. On the other hand the higher the value of r, the higher is also the chance that the iterative procedure will not converge.

The under-relaxation can be incorporated into the generation of the matrix of the system of linear equations:

$$A_P{}' = {A_P}\big/{r}$$

$$S_\Phi{}' = S_\Phi + (1 - r) \cdot A_P{}' \cdot \Phi_{k-1} \qquad (2.3.42)$$

The first of the two equations has the effect of making the main diagonal stronger, thus improving convergence. The value for the under-relaxation factor is different for each flow variable.

The use of the staggered grid arrangement is very important for the accuracy and convergence of the SIMPLE algorithm. Even so there are types of flow where for the convergence of the SIMPLE algorithm, very small values for the under-relaxation factors are required. Such flows are detached flows or flows characterized by high pressure gradients. The weakness of the SIMPLE algorithm is the simplification of the equation 2.3.37 where the effect of the sum of the $A_i{}^*u_i$ terms is neglected. In order to remedy the shortcomings of the SIMPLE algorithm, many variations have been proposed in the literature where the terms $A_i{}^*u_i$ are taken into account either directly or indirectly.

2.4 Geometrical Representation of the Hull

2.4.1 Introduction

In order to generate the numerical grids required by the finite volume method, the hull geometry needs to be represented. In the present work, the hull geometry is analytically represented through the coefficients of the conformal mapping of 2-D sections onto a unit circle. The conformal mapping is also employed to generate the 2-D orthogonal curvilinear grids. Also the conformal mapping method is employed in the generation of the appendages grid blocks, in order to locate the intersections of the appendages with the hull surface and to calculate the locations of the grid nodes that lay on the hull. Finally the conformal mapping can be used to generate the 2-D grids on sections of the rudder grid block.

2.4.2 The Conformal Mapping Method

In the present work, the hull surface is represented by employing the well-known conformal mapping method, adopted by many of the CFD software developed at LSMH. In this method, the hull surface is described by a number of 2-D transverse sections. Each section is analytically represented by means of its conformal mapping onto the complex plane of the unit circle (Tzabiras & Kontogiannis, 2009).

The general conformal transformation that maps a ship-like section reads (Kerczek, 1969):

$$z = c_0 + c_{-1}\zeta + \sum_{n=1}^{N} c_n \zeta^{-n} \quad (2.4.1)$$

where ζ is the complex plane of the unit circle and z the section plane. If the curve is symmetric with respect to the y-axis, figure 2.4.1, coefficients c_n reduce to the real α_n and the real and imaginary parts of z in equation (2.4.1) are expanded as:

$$x = \alpha_{-1}\cos\varphi + \sum_{n=1}^{N} \alpha_n \cos(-n\varphi)$$

$$y = \alpha_0 + \alpha_{-1}\sin\varphi + \sum_{n=1}^{N} \alpha_n \sin(-n\varphi) \quad (2.4.2)$$
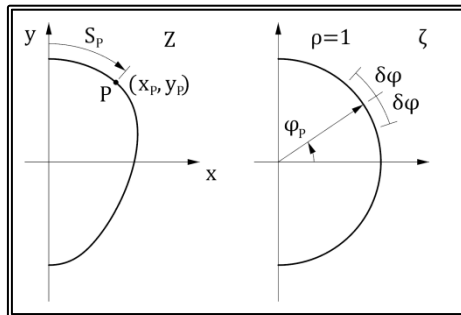
Figure 2.4.1 Transformation of a ship section on the unit circle (Tzabiras & Kontogiannis, 2009).

In equation 2.4.2, φ stands for the argument of point (x, y) on the circle plane, while the coefficients α_n can be calculated (Tzabiras, Dimas & Loukakis, 1986), either through the integrals:

$$a_0^{(1)} = \frac{1}{2\pi} \int_0^{2\pi} x(\varphi)d\varphi$$

$$a_{-1}^{(1)} + a_1^{(1)} = \frac{1}{\pi} \int_0^{2\pi} x(\varphi)\cos(\varphi)d\varphi$$

$$a_n^{(1)} = \frac{1}{\pi} \int_0^{2\pi} x(\varphi)\cos(\varphi)d\varphi, n > 2 \quad (2.4.3a)$$

or the integrals:

$$a_0^{(2)} = \frac{1}{2\pi} \int_0^{2\pi} y(\varphi)d\varphi$$

$$a_{-1}^{(2)} + a_1^{(2)} = \frac{1}{\pi} \int_0^{2\pi} y(\varphi)\sin(\varphi)d\varphi$$

$$a_n^{(2)} = \frac{1}{\pi} \int_0^{2\pi} y(\varphi)\sin(\varphi)d\varphi, n > 2 \quad (2.4.3b)$$

Equations 2.4.3a and 2.4.3b show that coefficients α_{-1}, α_0, ... , α_n can be calculated analytically in two ways, both resulting in equal values for N→∞. However, since a finite number N is used, the calculation of integrals (2.4.3a) and (2.4.3b) results in different values for $\alpha_n^{(1)}$ and $\alpha_n^{(2)}$ and the effectiveness of each approach depends on the section shape. In order to find an optimum representation of an arbitrary 2-D section, a linear relation between the two approximations is assumed to hold:

$$a_n = ra_n^{(1)} + (1 - r)a_n^{(2)}, n = -1, ..., N \quad (2.4.4)$$

The weight factor r is defined by minimizing the total error:

$$E_t = \sum_P [(x_P - x_{aP})^2 + (y_P - y_{aP})^2] \quad (2.4.5)$$

Where P is the number of (x_P, y_P) data points that describe the section contour and (x_{aP}, y_{aP}) the corresponding analytical expressions through equation 2.4.2. By introducing r, the above expressions become:

$$x_{aP} = \left[ra_{-1}^{(1)} + (1 - r)a_{-1}^{(2)}\right]\cos\varphi_P + \sum_{n=1}^{N} [ra_n^{(1)} + (1 - r)a_n^{(2)}]\cos(-n\varphi_P)$$

$$y_{aP} = \left[ra_0^{(1)} + (1 - r)a_0^{(2)}\right] + \left[ra_{-1}^{(1)} + (1 - r)a_{-1}^{(2)}\right]\sin\varphi_P$$

$$+ \sum_{n=1}^{N} [ra_n^{(1)} + (1 - r)a_n^{(2)}]\sin(-n\varphi_P)$$

$$(2.4.6)$$

Then, r is defined by solving the linear equation:

$$\frac{\partial E_t}{\partial r} = 0 \quad (2.4.7)$$

It should be noted that the coefficients α_1 and α_{-1} are uniquely defined from the linear system which is derived by evaluating the second integral of (2.4.3a) and (2.4.3b). As the number of coefficients increases, the weight factor r changes. The general trend is that for H >> B, r→0 while for B >> H, r →1, where B is the beam and H the draft of the section.

For a particular section, the iterative procedure proposed by von Kerczek (1969) is followed, i.e. calculations start with four coefficients and proceed by increasing their number up to a user-defined value N or until the total error becomes smaller than a certain limit. Anyhow, the evaluation of integrals (2.4.3a) and (2.4.3b) requires the calculation of angles φ_P, i.e. the arguments of points P on the circle plane. In the original work of von Kerczek and Tuck (1969) the angle φ_P was defined by finding the minimum distance between the particular point and the analytical representation, by increasing φ monotonically. However, this procedure fails when applied in complex sections and results to irregular representations (Kerczek, 1969, Tzabiras et al., 1995). To overcome the problem, an improvement has been introduced, where φ_P is calculated via a two-step procedure. In the first step, φ_P is assumed to be a function of S_P where S is the contour integral of the section, calculated by:

$$S_P = S_{P-1} + \sqrt{(x_P - x_{P-1})^2 + (y_P - y_{P-1})^2} \qquad (2.4.8)$$

Next, introducing a set of known angles φ_i, the values of S_i are computed analytically through the conformal representation. Then, the angles φ_P are defined by linear or cubic-spline interpolation of the corresponding length (equation 2.4.8) with respect to S_i, (Tzabiras, 1996b). The distribution of φ_i depends on the variation of curvature along the section, i.e. points are concentrated in concave regions. This method has proven to be stable and quite fast but, since it is based on the approximation of S_P through the data points, it may produce inaccurate representations in regions of high curvature. Therefore, it is applied only in the intermediate steps, while in the last iteration (maximum N) a second procedure is followed where φ_P is calculated by finding the minimum distance of P from the analytic representation of the section in the range [φ_P-$\delta\varphi$, φ_P+$\delta\varphi$] i.e. not monotonically, where $\delta\varphi \approx 0.1\pi$ (figure 2.4.1).

The above procedure is followed for both bulbous bow sections and general sections which may be symmetrical only in y-axis (including asymmetric sterns, Tzabiras, 1996b). For normal ship sections that are also symmetrical in x, the general transformation (eq. 2.4.3) becomes:

$$z = \sum_{n=1}^{N} a_n \zeta^{3-2n} \qquad (2.4.9)$$

However, in normal ship sections the section contour cuts usually the x-axis at non-orthogonal angles. This problem has been raised in (Kerczek, 1983) by applying first a Karman-Trefftz transformation. Consequently a two-step transformation has to be applied. Although this method has been used successfully (Tzabiras, 1997a) it may produce irregularities when sections are interpolated because it is very sensitive on the calculation of the intersection angle. This is why the original approximation is employed, taking also into account that any probable deviations are restricted locally at the upper part of the ship, located above the free surface. Besides, substantial improvement can be achieved by using an adequate number of data points in this region.

A typical example showing the effectiveness of the proposed approach is presented in figure 2.4.2 for a ship hull with a bulbous bow and a stern skeg. The bulb was approximated with 20 coefficients, the hull just after the bulb with 150, while 60 coefficients were used in the remaining part. The input points were 100 in each section while the calculated values of r ranged between 0.7 and 0.9 along the hull's normal sections.
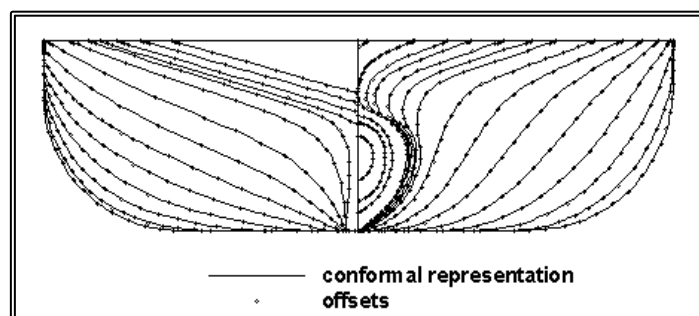
Figure 2.4.2 Conformal Mapping Representation of ship sections. (Tzabiras & Kontogiannis, 2009).

2.4.3   Interpolation of Sections

The representation of the hull geometry is achieved through a relative small number of sections, the data stations (figure 2.4.2). On the other hand, for the finite volume method, quite fine grids are required. Moreover, the plane of a 2-D grid section may not even be parallel to the data stations. It is essential therefore, to be able to accurately and efficiently generate intermediate transverse sections. In all relevant methods, the general approach is to calculate the coefficients of any desired section by interpolating among those obtained for the original data. The first attempt (Kerczek, & Tuck, 1969) was based on a polynomial interpolation. However, the developed procedure was unsuccessful and the use of cubic splines was found to be very accurate (Kerczek, 1983). For complex ship hulls exhibiting rapid longitudinal variation of geometry, an effective alternative is to apply a simple cubic interpolation on subsequent stations (Tzabiras, 1997a). An example is shown in figure 2.4.3 where a stern section with skeg is produced by interpolating the coefficients among the four neighboring sections. The resulting section fits very well the real offsets. However, the aforementioned methods have been unsuccessful at bulbous bows or sterns, where any interpolation among the data sections produces quite irregular representations, as shown in figure 2.4.4. In this figure, seven sections were used initially at the bow part and 150 mapping coefficients were adopted.

Obviously, both the cubic and the spline interpolations fail to generate the intermediate section. To address the problem, a new procedure has been developed which, first, generates data points on the required transverse plane by using cubic interpolation among the points at four neighboring stations. The latter are calculated by the transformation of points defined introducing an equal angle spacing on the unit cycle. Then, the resulting contour is transformed according to the conformal mapping technique described above and the coefficients are stored. The corresponding representation of the intermediate station is adequately close to the real offsets (figure 2.4.4).
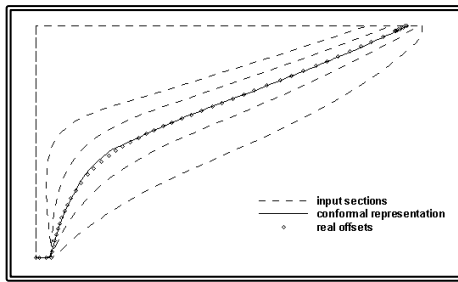
Figure 2.4.3 Interpolation of sterns sections, through interpolation of the coefficients (Tzabiras & Kontogiannis, 2009).
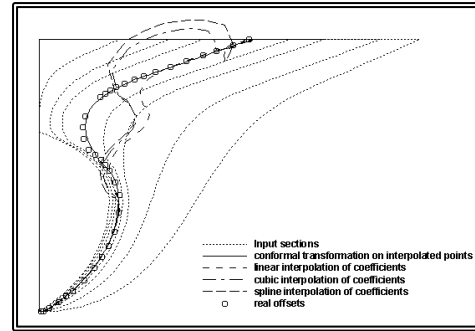
Figure 2.4.4 Comparison of four interpolation methods (Tzabiras & Kontogiannis, 2009).

2.4.3 The Conformal Mapping of Doubly Connected Regions

The conformal mapping method described above cannot handle sections, where part of it is a line segment laying on y-axis, such as the bulbous bow or the stern with a hub. For such a doubly connected region, a sequence of transformations has to be applied in order to obtain a set of conformal mapping coefficients, describing the hole of the section. Initially, the sections on the hull and the bulb are transformed independently and the mapping coefficients are calculated. Then, the following steps are performed, (figure 2.4.5):

1. (TR1) Using the inverse transformation ζ^{-1}, the section is transformed onto the unit circle (AB).
2. (TR2) Applying $w = z + 1/z$, the unit circle is transformed to the line-segment (AB).
3. (TR3) The bulb section is transformed to the unit circle (CD) on plane z' by applying the general transformation (2.4.2), while the bow section remains a line-segment (AB).
4. (TR4) Under the mapping $w'' = z'' + 1/z''$ the unit circle is transformed onto the line-segment (CD).
5. (TR5) With the final inverse mapping $(z'' + 1/z'')^{-1} = w'$ onto the final unit circle on z'', the mapping of the original end-points A, B, C, D are defined.

Then, a continuous grid on the ship transverse plane may be generated by adopting the mapping of the original section, including the vertical line segments, onto the final unit circle.
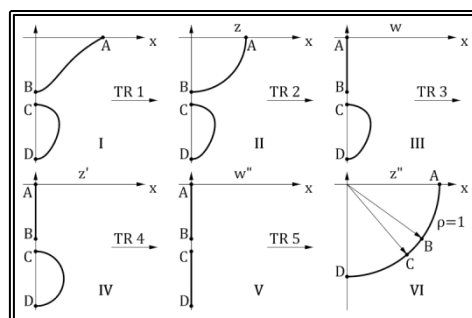
Figure 2.4.5 Transformation procedure for doubly connected domains (Tzabiras & Kontogiannis, 2009).

2.5   The Numerical Grid

2.5.1   Introduction

The Finite Volume method requires the subdivision of the computational domain into small volumes, the finite volumes. This subdivision is achieved by means of a numerical grid. When a curvilinear orthogonal grid is employed and the transport equations are expressed in a local curvilinear coordinate system, there are significant advantages in terms of accuracy and convergence (Tzabiras, 1986). The generation of a 3-D orthogonal curvilinear grid is quite difficult but similar accuracy can be achieved through the use of successive 2-D orthogonal curvilinear grids that combined form a partially orthogonal 3-D grid. Then at every point of the grid, a local curvilinear coordinate system is devised with the two curvilinear directions laying on the 2-D section, while in the third direction the grid is non-orthogonal and a Cartesian coordinate system is employed (figure 2.5.1).
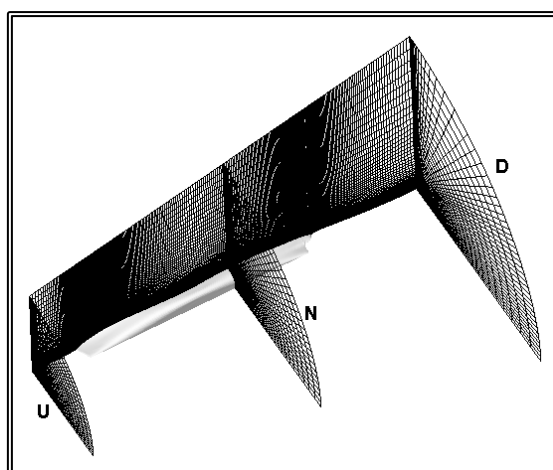
Figure 2.5.1 Typical partially orthogonal curvilinear H-O-type grid, around a ship hull, comprising 2-D orthogonal grids, normal to the longitudinal axis (Tzabiras, 2004).

The use of a single grid presents some limitations with regards to modeling bulbous bows or ships with a "wet" transom stern. In the present work, three grid blocks are generated around the hull of the ship. If the examined hull has a bulbous bow, a C-O-type grid is generated and Block (I) is defined. Block (I) covers the bow of the ship and extends up to around midship. The mid and stern parts of the ship are covered by an H-O-type grid block (II). If there is a transom stern, an H-H-type grid block (III) is introduced, covering the wake part of the computational domain. If there exists no bulbous bow, Block (I) is deleted and Block (II) covers the length of the ship and extends upstream the bow, in order for the inflow boundary conditions to be applied. If the stern of the ship is of cruiser type, or the transom is always considered to be "dry", grid Block (III) is deleted. In that case, Block (II) extends downstream the stern, in order for the outflow conditions to be applied. In any case, the mesh generation is based on the conformal mapping of simple or doubly connected regions as described by Tzabiras & Kontogiannis (2011), with each block comprising planar sections and on each section a 2-D grid is generated as described in the following.

2.5.2 The Conformal Mapping Method for 2-D Grids

On a planar section of the hull, a 2-D grid is generated by employing the conformal mapping approach. Fist, the section is analytically represented in terms of the coefficients of the conformal mapping to a unit circle (paragraph 2.4.2). Then a, orthogonal curvilinear grid is generated around the unit circle, on ζ-plane, comprising homocentric circles and radii. Since the employed mapping is conformal, the inverse mapping is also conformal. Consequently, the grid nodes that result from the inverse mapping of the ζ-plane nodes form an orthogonal curvilinear grid on the original z-plane (figure 2.5.2). The distribution of nodes on both radial and peripheral directions is variable. When the distribution is prescribed on the z-plane, the corresponding radii and angles are calculated through the direct mapping.
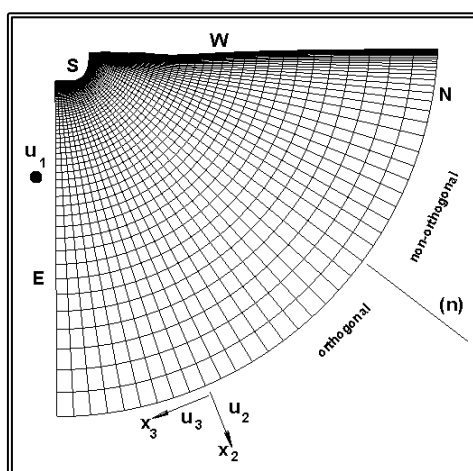
Figure 2.5.2 2-D partially orthogonal O-type grid, around a ship section, using the conformal mapping technique (Tzabiras, 2004).

In the presented method, the grid is generated having as input only the South edge (figure 2.5.2). In the case of a ship moving through water, the grid must also conform to shape of the free-surface. In order to achieve that, the 2-D domain is subdivided into two regions, separated by the line (n) (figure 2.5.2). The grid covering the lower region is generated according to the above paragraph. The grid covering the other region, the one between the free-surface and line (n) is generated as follows. The grid lines parallel to the x_3-direction are generated as before while the other set of lines is deformed, in order to follow the shape of the free-surface.

Consequently to upper part of the grid is non-orthogonal but the grid preserves two advantageous properties that are associated to the local orthogonal curvilinear reference-system on the transverse section, whose x_3 lines coincide always with the respective grid lines. The first property refers to the simplified expressions that link the u_3-velocity components with the corresponding pressure gradients (rapidly varying girth-wise), as well as to the diffusion terms in x_3-direction. The second is associated with the same advantages in both x_2 and x_3-directions of the orthogonal part of the grid that covers regions of high curvature, where intense flow changes occur.

It is worthy to note here that this type of grid generation is quite fast and requires negligible CPU time with respect to the time required to solve the Navier-Stokes equations under a specified free-surface. The time-consuming work is to perform an

initial transformation of specified sections, required to calculate and tabulate the corresponding conformal mapping coefficients.

Since the distribution of grid nodes can be prescribed, in the case of a doubly connected region, the grid lines may intersect the original section on the corner points A, B, C, D (figure 1.4.5). An example of a 2-D grid generated around a doubly connected stern section is shown in figure 2.5.3.
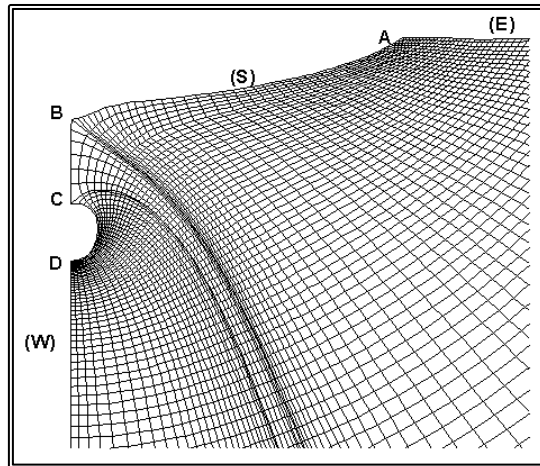
Figure 2.5.3 2-D partially orthogonal O-type grid, around a doubly connected section, using the conformal mapping technique (Tzabiras & Kontogiannis, 2009).

The above method can also be employed to generate 2-D orthogonal curvilinear grids around other objects, such as hydrofoil sections. The procedure is the same, with the section contour being mapped into a unit circle and then the 2-D grid being generated by the inverse mapping of a cylindrical grid around the unit circle. In figure 2.5.4, the conformal mapping of such a section is presented, while in figure 2.5.5, the resulting 2-D grid is presented.
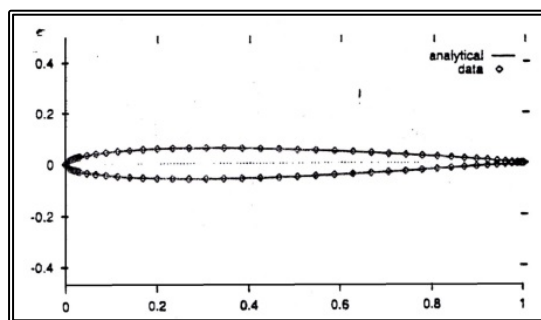
Figure 2.5.4 Conformal mapping of a hydrofoil section (Tzabiras, 1998).
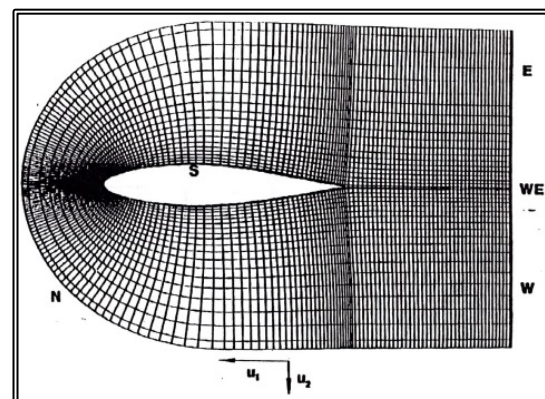
Figure 2.5.5 2-D partially orthogonal C-type grid, around a hydrofoil section, using the conformal mapping technique (Tzabiras, 1998).

2.5.3 The Bow Grid Block

In the case of a ship with a bulbous bow, a C-O-type grid block is generated around the bow and part of the midship. The 3-D grid comprises planar 2-D grids. The planes are arranged in a fan-type fashion around the bow, while they become normal to the longitudinal axis throughout the rest of the block's length (figures 2.5.6, 2.5.7). On each section a 2-D partially orthogonal curvilinear grid is generated, according to the method of paragraph 2.5.2. Near the free-surface, the lines of the 2-D grids deform, in order to follow the free-surface geometry.
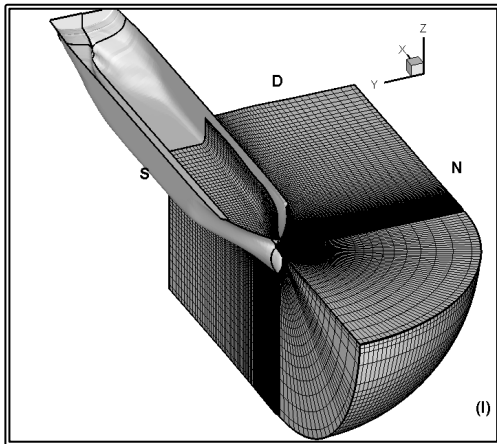
Figure 2.5.6 C-O-type grid, around a ship bow (Tzabiras & Psaras, 2014).
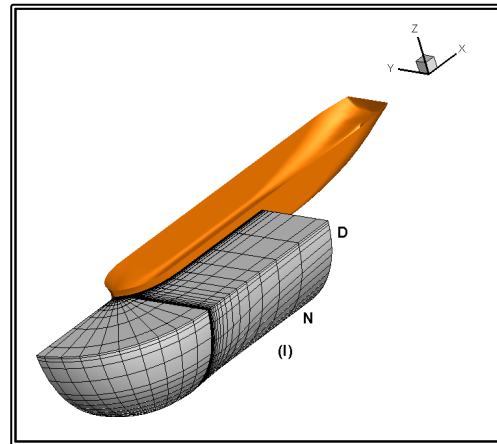
Figure 2.5.7 C-O-type grid, around a ship bow (Tzabiras & Polyzos, 2016).

2.5.4 The Grid Block around the Midship and Stern

The midship and stern regions of the ship are covered by an H-O-type grid block comprising planar 2-D grids normal to the longitudinal axis (figures 2.5.8, 2.5.9). On each section a 2-D partially orthogonal curvilinear grid is generated, according to the method of paragraph 2.5.2. Near the free-surface, the lines of the 2-D grids deform, in order to follow the free-surface geometry.
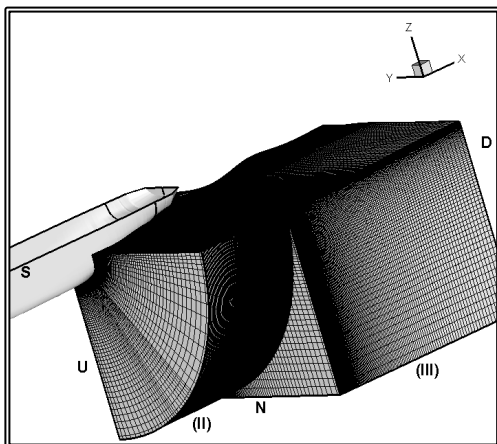
Figure 2.5.8 Combination of an H-O-type grid around the midship and stern and an H-H-type grid at the wake (Tzabiras & Psaras, 2014).
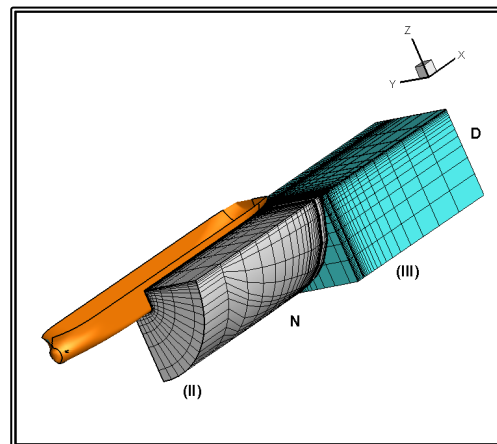
Figure 2.5.9 Combination of an H-O-type grid around the midship and stern and an H-H-type grid at the wake (Tzabiras & Polyzos, 2016).

2.5. THE NUMERICAL GRID

2.5.5   The Wake Grid Block

In the case of a ship with a transom stern, an H-H-type grid block is generated at the wake. The 3-D grid comprises planar 2-D grids normal to the longitudinal axis (figure 2.5.10). On each section a 2-D non- orthogonal grid is generated, conforming to the free-surface (figure 2.5.11). The grid block extends upstream the stern by a number of sections, in order for the flow information to be transferred bfrpm the stern grid block.
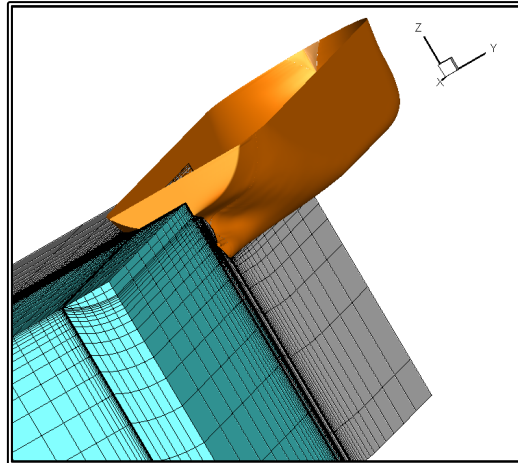
Figure 2.5.10 Combination of an H-O-type grid around the midship and stern and an H-H-type grid at the wake (Tzabiras & Polyzos, 2016).
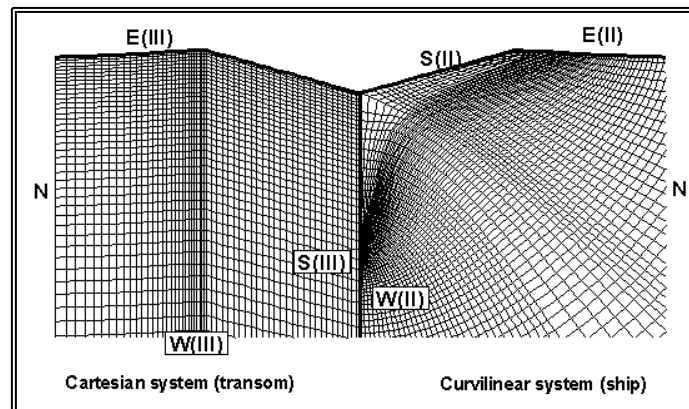
Figure 2.5.11 Comparison of an O-type orthogonal curvilinear grid on a stern section and an H-type non-orthogonal grid at the wake (Tzabiras & Kontogiannis, 2009).

[48]

2.6 The Actuator Disk Method

In the present, the propeller is modeled by employing the classical actuator disk method, where the propeller is considered as having an infinite number of blades, effectively becoming a disk. The effect of the propeller operation on the flow is simulated by means of a body force F_B, introduced in the source term of momentum equations for the control volumes which, lie within or intersect the sweep outline of the propeller. Consequently, the geometry of the propeller is taken into account.

According to the classical lifting line theory, the thrust T, generated by a propeller with an infinite number of blades, is:

$$T = C_1 \cdot \int_{r_h}^{r_t} \Gamma(r) \cdot r \cdot dr \qquad (2.6.1)$$

where r is the radius, r_t and r_h are the propeller tip and hub radii respectively and $\Gamma(r)$ is the circulation distribution along radius r of the blade. The torque Q required by the propeller is equal to:

$$Q = C_Q \cdot \int_{r_h}^{r_t} \Gamma(r) \cdot r \cdot dr \qquad (2.6.2)$$

The constants C_1 and C_Q are related to the propeller geometry.

According to the above formulation, the body forces acting in the axial direction, on a finite volume can be calculated as (Tzabiras, 2004):

$$F_{B,1} = C_1 \cdot E_P \cdot \Gamma(r) \qquad (2.6.3)$$

where E_P is the area of intersection of the finite volume with the propeller sweep outline. The C_1 constant can be calculated from the equation:

$$C_1 = F_L(\frac{x}{c(r)}, \frac{\delta x}{c(r)}) \cdot \frac{T}{2 \cdot \pi \cdot \int_{r_h}^{r_t} \Gamma(r) \cdot r \cdot dr} \qquad (2.6.4)$$

where δx is the length of the affected volume and c(r) is the projection of the propeller chord, at a radius r, to the longitudinal plane (figure 2.6.1). The parameter F_L is a function of the non-dimensional quantities $x/c(r)$ and $\delta x/c(r)$ that distributes the body force along x_1 according to a 2-D hydrofoil pressure distribution, resulting to a transfer of the major part of the thrust close to the leading edge (Tzabiras, 1997d).
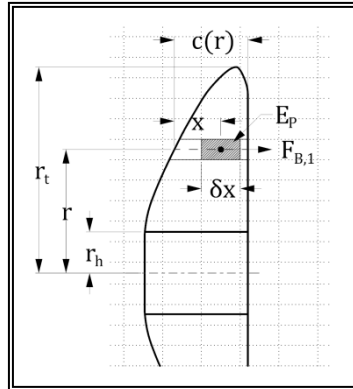
Figure 2.6.1 Definition of the Actuator Disk geometry.

The body forces acting in the other two directions, are:

$$F_{B,2} = C_2 \cdot E_P \cdot {}^{\Gamma(r)}/_r \quad (2.6.5a)$$

$$F_{B,3} = C_3 \cdot E_P \cdot {}^{\Gamma(r)}/_r \quad (2.6.6b)$$

where the constants C_2 and C_3 are proportional to the propeller torque Q and take into account the orientation of the examined velocity component with respect to the local curvilinear coordinate system.

The circulation distribution depends on the exact propeller geometry, and may be calculated by means of analytical models, such as lifting surface model. In the present work, a simplified circulation distribution is adopted, namely there are two options, circulation of constant amplitude, or a sinusoidal distribution with a maximum value at $(r_t + r_h)/2$ and zero values at r_t and r_h. The above approximation has been proven very effective in predicting the effect of the propeller operation on the flow around a ship (Tzabiras, 1996).

Given the thrust, torque and the shape of the circulation distribution, though not the actual values of the distribution, the constants C_1, C_2 and C_3 can be calculated and therefore, the body forces $F_{B,1}$, $F_{B,2}$ and $F_{B,3}$. In the case of a self-propelled ship though, i.e. a ship propelled under the action of the propeller thrust, without any other external force, the required thrust is not a priori known, since it is different to the calm water resistance. Also the torque is related to the efficiency of the propeller and can only be measured experimentally or calculated by means of advanced propeller models.

With regards to the thrust, an iterative procedure is adopted. Initially, the resistance problem is solved. Then, thrust is considered equal to the resistance and the body forces are calculated for given propeller geometry (tip and hub diameter, sweep outline), shape of circulation distribution and propeller efficiency. Then the flow problem is solved again, this time taking into account the body forces. The new flow field is different from the original and a new value for the resistance is calculated. The thrust is set equal to the new value for the resistance, the new body forces are calculated and the flow problem is solved once more. This procedure is repeated until the problem converges, i.e. the resistance and thrust become equal.

The effective wake fraction $1-w_E$ is estimated by solving the inverse problem: given the propeller thrust and the calculated propeller inflow at the ship's stern, the velocity at infinite is calculated by performing a numerical open water test (Tzabiras, 1996). Then, since the non-dimensional parameter K_T/J^2 is defined, the optimum propeller revolutions RPM and the required horsepower DHP are calculated using the polynomial expressions of the Wageningen B-Series. This procedure holds for both model and full scale computations and, therefore, no extrapolation assumptions are made.

CHAPTER 3   THE METHOD FOR CALCULATING THE FREE SURFACE

(This page intentionally left blank)

3.1 RANS Free Surface Calculations

A unique problem in the marine hydrodynamics is the calculation of the free surface. Anyone body in motion, near the interface of two fluids of different density, called the free surface, generates a system of gravity waves on the interface of the two fluids. This wave system, travels at the same speed as the body and in order to be sustained, an amount of energy is required. That energy forms the wave making portion of the total resistance that the body has to overcome. The shape of the wave system depends on the speed of the body and the geometry of the problem, i.e. the shape of the body, its distance from the fluid interface etc. The shape of the wave system dictates the amount of the wave making resistance; hence the accurate calculation of the free surface is crucial for the prediction of the resistance characteristics of ships. Moreover in a computational approach to the resistance problem, the free surface is one of the boundaries of the computational domain, hence affecting the numerical solution.

On the free-surface two conditions hold true. The Dynamic condition states that the total pressure p* on the free surface is equal to the sum of the ambient pressure, i.e. the atmospheric pressure in the case of the air to water interface, plus the hydrostatic pressure. The Kinematic condition states that the free surface should be a sharp boundary separating the two fluids and there should be no flux through this boundary. Consequently the velocity normal to the free surface is equal to zero.

Since the free surface is not a priori known, a surface tracking iterative procedure has been adopted (Tzabiras, 2004). The iterative procedure is based on successive steady-state steps, under constant ship speed. In this procedure, the dynamic boundary condition is always fulfilled in terms of the known total pressure on the free surface, $p^* = p_S + \rho g h$, where p_S is the ambient pressure ($p_S = 0$) and ($\rho g h$) the hydrostatic pressure. The kinematic condition is satisfied when convergence is achieved.

On an intermediate step, the free surface obtained in the previous step, is considered as a fixed boundary. The transport equations are solved by enforcing the dynamic condition on the free surface and the SIMPLE algorithm is allowed to converge, thus the velocity components on the free surface are obtained and the curvilinear velocity components are transformed on the Cartesian system (x, y, z), (figure 3.1.1). Then, the free surface is updated according to a Lagrangian-Eulerian approach, in two steps.

First, the free surface is updated following the local flow lines, in the Lagrangian sense. This is done in two alternative ways. The first way is to transfer a fluid particle α on the transverse plane K, to a new location b on plane K+1 (figure 3.1.1). Point b is calculated as follows. First the line that passes through points α and P′ and is parallel to the local velocity vector passing through P, is defined. Point P is the center of the pressure finite volume, located on plane K+1/2 and P′ is a point on the same vertical line as P. Point b is defined as the intersection of the α-P′ line with the K+1 plane. Points b form a new transverse cut of the free surface on plane K+1. Then, the new grid nodes on K+1, corresponding to the constant coordinate x_3-lines, are found by means of interpolation among points b.

Alternatively, the free surface is updated as follows. Following the local flow lines, a fluid particle P on the center of a pressure finite volume, on the transverse plane

K+1/2, is transferred to P′ in the Lagrangian sense, with the translation being equal to the product of the local velocity vector U and a time step δt (figure 3.1.2). The location of points P′ does not coincide with the transverse cuts of the original surface. Consequently the new grid nodes are the calculated by interpolations amongst points P′.
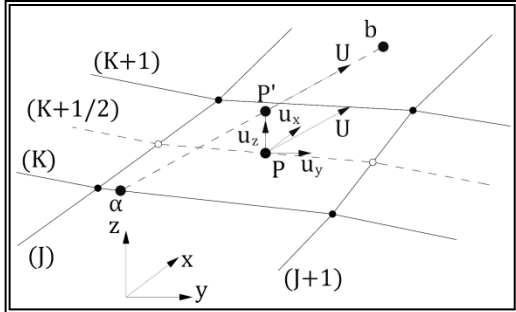
Figure 3.1.1 First correction of free surface.
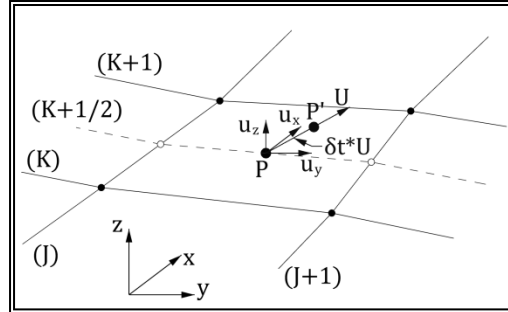
Figure 3.1.2 First correction of free surface using a time step δt.

The second correction is applied to all the finite volume faces that lay on the free surface, in order to satisfy locally the kinematic condition. In an integrated form, this condition is satisfied when the flux through the examined face becomes equal to zero. Approximately, this can be achieved moving the corner point C of face (ABCD) vertically by δz (C to C′), (figure 3.1.3). To be compatible with the convergence of the continuity equation, (ABCD) coincides with the north face of the free surface pressure control volume. The distance δz is calculated from the following equation:

$$u_x \cdot A_x + u_y \cdot A_y + u_z \cdot A_z = 0 \qquad (3.1.1)$$

where A_x, A_y and A_z are the projections of (AB′C′D) in the respective axes. The location of the B′ point is considered the result of the same translation for the neighboring face to the right of (ABCD).
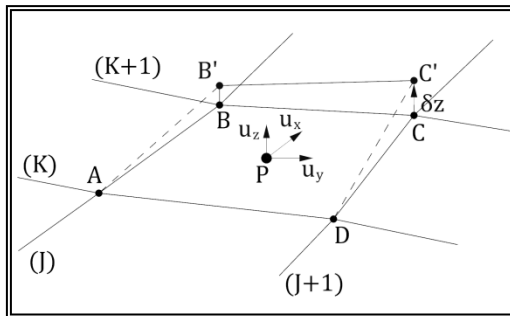
Figure 3.1.3 Second correction of free surface (Kinematic condition).

After the free surface is updated, the RANS problem is solved and the whole procedure is repeated until the kinematic boundary condition converges. The satisfaction of the kinematic boundary condition is tested through the mean value of the correction obtained from equation (3.1.1) $\overline{|\delta z|}$. Owing to the approximation of the free surface with quadrilateral panels, this value decreases as the problem converges but exhibits a limiting behavior. Therefore, convergence with respect to $\overline{|\delta z|}$ is satisfied, when it becomes lower than a suitable value depending on both the Froude number and the scale. By definition, the smaller the limiting value of $\overline{|\delta z|}$, the more accurate the solution.

3.2 Potential Flow Free Surface Calculations

The method of the previous paragraph can accurately predict the shape of the free surface. On the other hand is very expensive in terms of computational cost. A common approach when tackling complex problems in computational fluid dynamics is to attempt to simplify the physical modeling, whenever it can be done without compromising the accuracy of the method. In terms of the free surface, the flow can be approximated as inviscid and irrotational. In the following a numerical method for the calculation of the free surface, based on the classical formulation of Hess & Smith (1966) will be presented. The method adopts an iterative surface tracking procedure, similar to that of paragraph 3.1. The method can also calculate the wave making component of the ship resistance as well as the running sinkage and trim.

Once the free surface is calculated, it can be input to the RANS solver and the flow problem is solved under the surface, know considered a fixed boundary. Finally, since the flow field around the ship is solved, the method can provide the RANS solver with boundary conditions for the inflow and external boundaries.

3.2.1 The Potential Flow Problem

In this investigation, the fluid is considered incompressible, inviscid and irrotational. Let $\mathbf{U}$ denote the fluid velocity at any point, p the fluid pressure, ρ the fluid density, μ the dynamic and ν the kinematic viscosity. In the following, symbols in bold denote vectors. For an incompressible and inviscid fluid ρ is constant and $\mu = \nu = 0$, hence the general Navier-Stokes equations (3.2.1) reduce to the Eulerian equation of motion (3.2.2).

$$\left.\begin{aligned}
\frac{\partial \rho u_x}{\partial t} + \text{div}(\rho u_x \mathbf{U}) &= -\frac{\partial p}{\partial x} + \text{div}(\mu\, \text{grad} u_x) + S_{M_x} \\
\frac{\partial \rho u_y}{\partial t} + \text{div}(\rho u_y \mathbf{U}) &= -\frac{\partial p}{\partial y} + \text{div}(\mu\, \text{grad} u_y) + S_{M_y} \\
\frac{\partial \rho u_z}{\partial t} + \text{div}(\rho u_z \mathbf{U}) &= -\frac{\partial p}{\partial z} + \text{div}(\mu\, \text{grad} u_z) + S_{M_z}
\end{aligned}\right\} \qquad (3.2.1)$$

$$\left.\begin{aligned}
\frac{\partial u_x}{\partial t} + \text{div}(u_x \mathbf{U}) &= -\frac{1}{\rho}\frac{\partial p}{\partial x} \\
\frac{\partial u_y}{\partial t} + \text{div}(u_y \mathbf{U}) &= -\frac{1}{\rho}\frac{\partial p}{\partial y} \\
\frac{\partial u_z}{\partial t} + \text{div}(u_z \mathbf{U}) &= -\frac{1}{\rho}\frac{\partial p}{\partial z}
\end{aligned}\right\} \qquad (3.2.2a)$$

$$\frac{\partial \mathbf{U}}{\partial t} + (\mathbf{U}\cdot\text{grad})\mathbf{U} = -\frac{1}{\rho}\text{grad}p \qquad (3.2.2b)$$

The equation of continuity (3.2.4) simplifies to (3.2.5).

$$\frac{\partial \rho}{\partial t} + \text{div}(\rho \mathbf{U}) = 0 \qquad (3.2.4)$$

$$\text{div}(\mathbf{U}) = 0 \qquad (3.2.5)$$

In equations (3.2.1) and (3.2.2) all body forces (such as gravity) have been assumed to be conservative, and their potentials have been absorbed in the pressure. Equations (3.2.2) and (3.2.5) hold in the field of flow, that is, the region exterior to the boundary

surfaces, in our case, the immersed portion of the two hulls and the surrounding water surface.

In order to solve the above equations, certain boundary conditions must be added. The method adopted (Hess, 1966) can solve the direct problem of fluid dynamics. That is, the locations of all boundary surfaces are assumed known, possibly as functions of time, and the normal component of fluid velocity is prescribed on these boundaries. In our case though the boundaries are not a priori known, since neither the shape of the free surface, nor the attitude of the ship (running sinkage and trim) are known in advance. In order to overcome this problem, an iterative procedure is adopted where the shape of the free surface is assumed, then the potential flow field is calculated and the free surface is updated (see 3.2.4) (Tzabiras, 2008).

The boundary condition will be written for the entire boundary S as

$$\mathbf{U} \cdot \mathbf{n}|_{\mathbf{S}} = \mathbf{F} \quad (3.2.6)$$

where $\mathbf{n}$ is the unit outward normal vector at a point of S, and $\mathbf{F}=\mathbf{F(x,t)}$ is a known function of position on S and possibly also a known function of time. In our problem the boundaries at every step of the iterative procedure are considered static, hence

$$\mathbf{U} \cdot \mathbf{n}|_{\mathbf{S}} = 0 \quad (3.2.7)$$

Furthermore a regularity condition at infinity must be imposed.

The above equations define an incompressible and inviscid flow, but not a potential flow. In a potential flow the velocity vector is equal to the negative gradient of a scalar potential function, the velocity potential φ.

$$\mathbf{U} = -\nabla\varphi \quad (3.2.8)$$

From vector calculus it is known that the curl of a gradient is equal to zero:

$$\nabla \times \nabla\varphi = 0 \quad (3.2.8)$$

Subsequently the vorticity of a potential flow field is zero:

$$\nabla \times \mathbf{U} = 0 \quad (3.2.9)$$

This implies that a potential flow is an irrotational flow.

Here, a slightly more general class of flows will be considered, according to the formulation of Hess (1966). The velocity field $\mathbf{U}$ is expressed as the sum of two velocities:

$$\mathbf{U} = \mathbf{U}_\infty + \mathbf{u} \quad (3.2.10)$$

The vector $\mathbf{U}_\infty$ is the velocity of the onset flow, which is defined as the velocity field that would exist in the fluid if all boundaries ceased to exist, here is equal to the negative of the ship's speed. The vector $\mathbf{u}$ is the disturbance velocity field due to the presence of boundaries. The velocity $\mathbf{u}$ is assumed to be irrotational, but $\mathbf{U}_\infty$ is not so restricted. Accordingly, $\mathbf{u}$ may be expressed as the negative gradient of a potential function φ, that is,

$$\mathbf{u} = -\text{grad}\varphi \quad (3.2.11)$$

Since $\mathbf{U}_\infty$ is the velocity of an incompressible flow, it satisfies the continuity equation (3.2.5), and thus $\mathbf{u}$ does also; that is,

$$\text{div}(\mathbf{u}) = 0 \quad (3.2.12)$$

Using $\mathbf{u}$ from (3.2.11) in (3.2.12) we derive to the expected result: the potential φ satisfies Laplace equation:

$$\nabla^2\varphi = 0 \quad (3.2.13)$$

The boundary conditions on φ arise from (3.2.7), (3.2.10) and (3.2.11) in the form:

$$\text{grad}\varphi \cdot \mathbf{n}|_S = \left.\frac{\partial\varphi}{\partial\mathbf{n}}\right|_S = \mathbf{U}_\infty \cdot \mathbf{n}|_S \quad (3.2.14)$$

The regularity condition at infinity is:

$$|\text{grad}\varphi| \to 0 \quad (3.2.15)$$

Equations (3.2.13), (3.2.14), and (3.2.15) comprise a well-set problem for the potential φ, and it is this problem that the present method is designed to solve.

The onset flow $\mathbf{U}_\infty$ must be such that the disturbance velocity $\mathbf{u}$ is a potential flow. In our case $\mathbf{U}_\infty$ is also a potential flow and the above condition is obviously satisfied.

The essential simplicity of potential flow derives from the fact that the velocity field is determined by the equation of continuity (3.2.12) and the condition of irrotationality (3.2.11). Thus the equation of motion (3.2.2) is not used, and the velocity may be determined independently of the pressure.

Also time, t, enters only as a parameter in (3.2.14); therefore the instantaneous velocity is obtained from the instantaneous boundary condition; that is, all problems are essentially steady with respect to determination of the velocity. In our case, the equation of motion (3.2.2) can be integrated to give the Bernoulli's equation:

$$p - p_\infty = \frac{1}{2}\rho(|\mathbf{U}_\infty|^2 - |\mathbf{U}|^2) \quad (3.2.16)$$

(3.2.16) can be written in terms of the pressure coefficient C_P as

$$C_P = \frac{p-p_\infty}{\frac{1}{2}\rho|\mathbf{U}|^2} = 1 - \frac{|\mathbf{U}|^2}{|\mathbf{U}_\infty|^2} \quad (3.2.17)$$

where p_∞ (=0) is the pressure at infinity.

The potential theory can describe a variety of flow fields, although the neglect of viscosity, vorticity and compressibility must not invalidate the results.

The neglect of viscosity is justified except in regions of rapid variations of speed, such as boundary layers and at points in or very near regions of catastrophic separation, for example wakes. In those regions, vorticity is also known to be important; hence the potential flow theory fails to provide reasonable predictions of the flow. Obviously, drag forces are never predicted correctly.

The neglect of compressibility is justified for all flows where the local Mach number does not exceed a value of approximately one-half. In the case of flow around ships, the Mach number is sufficiently low.

In our case, the aim is firstly to calculate the pattern of the free surface around ships, secondly the wave component of the ships resistance and finally the running sinkage and trim. As for the free surface the potential theory is expected to provide good results except in areas were viscocity becomes very important such as the stern and wake of the ship. The wave resistance is considered to be equal to the calculated pressure resistance, since no other form of resistance (viscous pressure or frictional) can be predicted by means of the potential theory. Finally the sinakge and trim can be calculated by integrating the pressure on the hull.

3.2.2 The Hess & Smith Method for Potential Flows

The exact solution of the direct problem of potential flow can be approached in a variety of ways, all of which must finally become numerical in order to be solved on a computing machine. The present method is based on an integral equation for a source-density distribution on the surface of the hulls and water, about which the flow is being computed.

The problem considered is that defined by (3.2.13), (3.2.14), and (3.2.15). Consider a unit point source located at a point q whose Cartesian coordinates are x_q, y_q, z_q. At a point P whose coordinates are x, y, z the potential due to this source is

$$\varphi = \frac{1}{r(P,q)} \qquad (3.2.18)$$

where r(P, q) is the distance between P and q, namely,

$$r(P,q) = \sqrt{(x - x_q)^2 + (y - y_q)^2 + (z - z_q)^2} \qquad (3.2.19)$$

The designation "source" is employed in accordance with customary fluid dynamics usage. The potential (3.2.18) gives rise to a velocity radially outward in all directions from the point q, and thus the point q may be thought of as the location of a "source" of fluid.

According to the present method, the solution is built up of elementary potentials of the form (3.2.18). Each potential satisfies (3.2.13) and (3.2.15) at all points except the point q. Because of the linearity of the problem, the potential due to any ensemble of such sources or any continuous distribution of them that lies upon the boundary surface S satisfies equations (3.2.13) and (3.2.15) in the region exterior to S.

Consider a continuous source distribution on the surface S. If the local intensity of the distribution is σ(q), where the source point q is a general point of the surface S, then the potential of the distribution is

$$\varphi = \oiint_S \frac{\sigma(q)}{r(P,q)} dS \qquad (3.2.20)$$

It is shown (Kellogg, 1929), that under very general conditions the disturbance potential of a body in potential flow can indeed be represented in the form (3.2.20).

Regardless of the nature of the function σ(q), the disturbance potential as given by (3.2.20) satisfies two of the three equations of the direct problem of potential flow. The σ(q) function is then determined from the requirement that the potential must also satisfy the third equation, (3.2.14), which expresses the normal-velocity boundary condition on the surface S.

The disturbance potential as given by (3.2.20) is differentiated, and the boundary condition (3.2.14) applied to it by allowing the point P to approach a point p on the surface S. The result is the following integral equation for the source-density distribution σ(p):

$$2\pi\sigma(p) - \oiint_S \frac{\partial}{\partial n}\frac{1}{r(p,q)}\sigma(q)\,dS = \mathbf{n}(p) \cdot \mathbf{U}_\infty \quad (3.2.21)$$

In this equation, $\partial/\partial n$ denotes differentiation in the direction of the outward normal to the surface S at the point p, and the unit outward normal vector has been written $\mathbf{n}(p)$ to show explicitly its dependence on location. The solution of (3.2.21) is the central problem of the present method.

Equation (3.2.21) is a Fredholm integral equation of the second kind over the boundary surface S. The term $2\pi\sigma(p)$ arises from the delta function that is brought in by the limiting process of approaching the boundary surface. The kernel of the integral equation is the outward normal velocity at the point p due to a unit point source at the point q. This kernel depends only on the geometry of the surface S. The specific boundary conditions, that is, onset flow, enters (3.2.21) only on the right side.

The theory of the solution of (3.2.21) and fundamental existence and uniqueness theorems are beyond the scope of the present work and can be found in the potential flow literature.

The conditions under which a solution can be obtained are very general. For the problem of flow exterior to a given surface, S may consist of several disjoint surfaces. The right side is likewise practically unrestricted. Since only $\mathbf{U}_\infty$ enters (3.2.21), it is not essential that this velocity field be derivable from a potential function, although of course the disturbance velocity field must be a potential flow. Furthermore $\mathbf{U}_\infty$ may vary with position.

There is one restriction on (3.2.21). The existence proof requires that the prescribed boundary value, that is, the right side of (3.2.21), be a continuous function of position on the surface. Because of the presence of $\mathbf{n}(p)$, this means that the surface S must have a continuous normal vector, thus boundaries with corners are excluded from the existence proof. In practice, however, it has been found that the present method does give correct results near convex corners. For concave corners the method has difficulty, but concave corners are rarely encountered on ship hulls.

For a known boundary surface S, the kernel of (3.2.21) can be calculated in a straightforward manner, and the equation is a linear one for the unknown function σ.

Furthermore, for three-dimensional bodies, (3.2.21) is a two-dimensional integral equation. This feature accounts for the efficiency of the integral-equation methods since the dimensionality of the problem is reduced by one.

Equation (3.2.21) is an integral equation of the second kind, for which the unknown function appears outside the integral as well as inside. Numerically, integral equations of the second kind are rather easily tractable since the integral equation is approximated by a set of linear algebraic equations, and the presence of the term outside the integral insures that in general the diagonal entries of the resulting coefficient matrix will be much larger than any off-diagonal entries. This feature is very important numerically, since it ensures the stability of iterative matrix-solution methods.

The two terms on the left side of (3.2.21) have a simple interpretation. The term $2\pi\sigma(p)$ is the contribution to the outward normal velocity at a point p on the boundary of the source density in the immediate neighborhood of p. The integral term represents the contribution of the source density on the remainder of the boundary surface to the outward normal velocity at p.

3.2.3 The Numerical Method of Solution

The approach adopted consists of approximating (3.2.21) by a set of linear algebraic equations. This is accomplished in the following manner. The boundary surface S (hull and water surface) about which the flow is to be computed, is approximated by a number of surface elements or panels, whose characteristic dimensions are small compared to those of S. Obviously the water surface should extent to infinity. Since that is impossible in the present method, only a portion of the free surface, around the hulls, is modeled (figure 3.2.1). It should also be mentioned that since the problem is symmetric about x-axis, only one hull and one half of the water surface is modeled. Over each surface element the value of the surface source density is assumed constant. This reduces the problem of determining the continuous source density function σ to that of determining a finite number of values of σ, one for each of the surface elements.
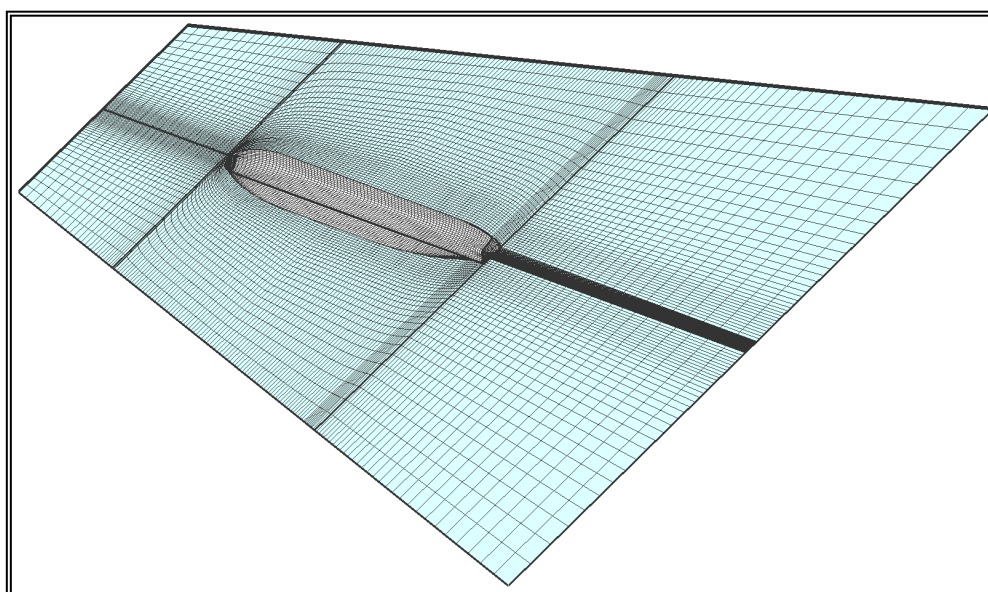
Figure 3.2.1 The computational domain.

The contribution of each element to the integral in (3.2.21) can be obtained by taking the constant but unknown value of σ on that element out of the integral and then

performing the indicated integration of known geometric quantities over the element. Requiring (3.2.21) to hold at one point of the approximate body surface, that is, requiring the normal velocity to take on its prescribed value at one point, gives a linear relation between the values of σ on the elements. On each element a control point is selected where (3.2.21) is required to hold. This gives a number of linear equations equal to the number of unknown values of σ. The coefficient matrix consists of the normal velocities induced by the elements at each other's control points for unit values of source density. Once the linear equations have been solved, flow velocities and potential may be calculated at any point by summing the contributions of the surface elements and that of the onset flow.

Usually, velocities and pressures on the body surface are of greatest interest. Because of the manner in which the solution has been formulated, these must be evaluated at the control points, that is, at the same points where the normal velocity was made to take its prescribed value.

The basic input to the computer program consists of the specification of the hull surface about which the flow is to be computed, the free water surface around the hull and the onset flow (a uniform stream). The hull and water surface are specified by means of the coordinates of a set of points distributed over both of them (see 2.3). Because the input points are used to form the approximating surface elements, their distribution and total number determine the accuracy of the resulting calculations.

The input points are associated in groups of four and used to form plane quadrilateral surface elements or elements. The plane of the element is equidistant from the four input points used to form it, and its unit normal vector **n** is the normalized cross-product of two "tangential" vectors each of which is obtained by subtracting the coordinates of two of the four input points. The corners of the quadrilateral are projections of the four input points into the plane of the element. In order to model surfaces that end at a single point (bow, bulb, stern hub or stern without transom), the program can use triangular elements, by simply joining two of the four corner points. This is only necessary for the last row of elements. figures 3.2.2 and 3.2.3 present the surface elements used on the hull and water surface for a low C_B and a high C_B ship respectively.
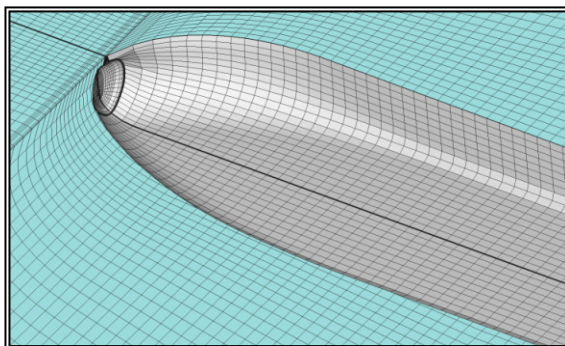
Figure 3.2.2 Panels on the hull and the water surface, for a high C_B ship.
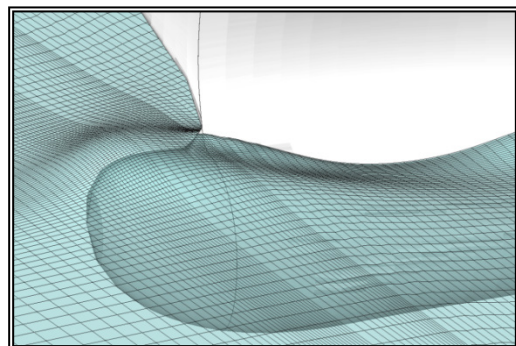
Figure 3.2.3 Panels on the water surface, for a low C_B ship.

On each element a control point is selected at which the normal velocity boundary condition is to be satisfied. The proper choice of the control point is not at all obvious. In this investigation, the location of the control point coincides with the location of

the point, where the tangential to the element speed becomes zero. The later point is called a Null point (Hess, 1966).

It should be emphasized that for all body geometries the surface elements are simply devices for effecting the numerical solution of the integral equation (3.2.21). They essentially define integration increments and normal directions at points of the surface and have no direct physical significance. It is only at the control points that the normal velocity assumes its prescribed value. For example, if the normal velocity is prescribed as zero, it is in general nonzero at all points of the element except the control point; that is, the element "leaks". At the edges of the elements the velocity approaches infinity because of the discontinuity of the source density and/or the discontinuity in slope. The computed flow has significance only at the control points themselves and at points off the body surface.

The accuracy of the calculation is determined by the number and distribution of the elements. In order to achieve a reasonable level of accuracy a total number of elements in the order of 5,000 would be sufficient. The present method though requires a significantly larger amount of elements on the free surface, in order to calculate its shape (see 3.2). In practice a total number of elements in the order of 20,000, is found to yield results of adequate accuracy.

In order to reduce the computational effort, the solution may start with a coarse grid which is successively refined to the maximum number of panels according to a sequel defined in the input data. Apart from the necessary geometrical interpolations, there is no difficulty to pass from the one grid resolution to another due to the steady-state decomposition which is followed.

Once the hull and water surfaces have been approximated by elements of the appropriate type, the elements are ordered sequentially and numbered from 1 to N, where N is the total number of elements. The exact order of the sequence is immaterial. It is simply a logical device for keeping track of the elements during the computational procedure. Reference will accordingly be made to the ith and the jth element, where the integers i and j denote the positions of the elements in the sequence.

Assume for the moment that the surface source density on the jth element has the constant value of unity. Denote by Φ_{ij} and $\mathbf{U}_{ij}$ the potential and velocity, respectively, that are induced at the control point of the ith element by a unit source density on the jth element. The formulas for the induced potential and velocity form the basis of the present method of flow calculation. They are obtained by integrating over the element in question the formulas for the potential and velocity induced by a unit point source and thus depend on the location of the point at which the potential and velocity are being evaluated and also on the geometry of the element. Since there is no restriction on the location of the control point of the ith element with respect to the jth element, the formulas for Φ_{ij} and $\mathbf{U}_{ij}$ are those for the potential and velocity induced by an element at an arbitrary point in space.

For the plane quadrilateral elements used, the unit-point-source formulas for potential and velocity can be integrated analytically over an element. This is most conveniently done by using a coordinate system in which the element itself lies in a coordinate plane, and thus coordinates of points and components of vectors must be transformed

between the reference coordinate system in which the body surface is input and an "element coordinate system" based on the element in question. The analytic integration over the element produces rather lengthy formulas, whose evaluation is time consuming. To conserve computing time, the effect of an element at points sufficiently far from the element is calculated approximately. This is accomplished by means of a multiple expansion. In fact, if the point in question is farther from the centroid of the element than four times the maximum dimension of the element, the quadrilateral source element may be replaced by a point source of the same total strength located at its centroid. With the accuracy criteria adopted, errors due to the use of the multiple expansion or point-source formulas are apparently small compared with those arising from the basic approximation of the body surface by plane elements having constant values of source density. The use of these alternative formulas therefore involves no loss of accuracy at all in the overall calculation.

When this phase of the calculation has been completed, the result consists of the NxN matrices Φ_{ij} and $\mathbf{U}_{ij}$ that give the potentials and velocities induced by the elements at each other's control points for a unit source density. The vector matrix $\mathbf{U}_{ij}$ is

$$\mathbf{U_{ij}} = X_{ij} \cdot \vec{i} + Y_{ij} \cdot \vec{j} + Z_{ij} \cdot \vec{k} \quad (3.2.22)$$

where i, j, k are the unit vectors along the axes of the reference coordinate system in which the body surface is input, and the scalar matrices X_{ij}, Y_{ij}, Z_{ij} are simply the components of $\mathbf{U}_{ij}$. The normal velocity induced at the control point of the ith element by a unit source density on the jth element is

$$A_{ij} = \mathbf{n_i} \cdot U_{ij} \quad (3.2.23)$$

where $\mathbf{n_i}$ is the unit normal vector to the ith element. The five matrices Φ_{ij}, X_{ij}, Y_{ij}, Z_{ij}, and A_{ij} do not necessarily have any zero entries. As mentioned above, the number of elements used is large enough for the handling of the amount of numerical data represented by these matrices to be a considerable problem.

It should be mentioned that the i=j case does not require special handling. Because the integration over an element is done analytically, problems of infinite integrands or principal-value integrals, fail to materialize. The velocity induced by an element at its own control point has a magnitude of 2π and is directed along the element's normal vector.

Above we calculated the matrix A_{ij}, whose entries are the normal velocities induced by the elements at each other's control points for unit values of source density. To obtain actual normal velocities, the entries of A_{ij} must be multiplied by the proper values of the source density σ. In particular, the quantity

$$\sum_{j=1}^{N} A_{ij} \cdot \sigma_j \quad (3.2.24)$$

is the normal velocity at the control point of the ith element due to the complete set of surface elements. Clearly, (3.2.24) is the approximation of the normal velocity associated with the disturbance potential of the body surface. To obtain the prescribed normal velocities at the control points of all elements, (3.2.24) must be set equal to the proper value as given by (3.2.14) for every value of i. The result is

$$\sum_{j=1}^{N} A_{ij} \cdot \sigma_j = -\mathbf{n_i} \cdot \mathbf{U}_{\infty,i} \quad i = 1,2,\ldots,N \qquad (3.2.25)$$

Equation (3.2.25) is a set of linear algebraic equations for the values of source density on the surface elements. This set of linear algebraic equations is the desired approximation of the integral equation (3.2.21). The method adopted for solving (3.2.21) is the iterative Gauss-Seidel.

Once the values of the source density σ_j have been obtained as the solution of (3.2.25), all other flow quantities of interest can be obtained by relatively rapid direct calculation. Flow quantities on the hull and water surfaces are computed only at the control points of the elements. Specifically, the potential and velocity at a control point on the surface are calculated from

$$\left.\begin{array}{l} \varphi_i = \sum_{j=1}^{N} \Phi_{ij} \cdot \sigma_j \\ \mathbf{U}_i = \sum_{j=1}^{N} \mathbf{V}_{ij} \cdot \sigma_j + \mathbf{U}_{\infty,i} \end{array}\right\} i = 1,2,\ldots,N \qquad (3.2.26)$$

The velocity $\mathbf{U_i}$ at each control point is given in terms of its components along the axes of the reference coordinate system in which the body is input.

$$\left.\begin{array}{l} u_{x,i} = \sum_{j=1}^{N} \mathbf{X}_{ij} \cdot \sigma_j + u_{\infty,x,i} \\ u_{y,i} = \sum_{j=1}^{N} \mathbf{Y}_{ij} \cdot \sigma_j + u_{\infty,y,i} \\ u_{z,i} = \sum_{j=1}^{N} \mathbf{Z}_{ij} \cdot \sigma_j + u_{\infty,z,i} \end{array}\right\} i = 1,2,\ldots,N \qquad (3.2.27)$$

Notice that σ is the perturbation potential due to the body surface, and $\mathbf{U_i}$, is the total velocity, including the effects of the onset flow. The components of $\mathbf{U_i}$ are used to compute velocity magnitude and then pressure coefficient from (3.2.17). Flow quantities may also be computed at points off the body surface.

The pressure at each control point may then be calculated from the Bernoulli's equation (3.2.16) while the local value of the pressure coefficient C_P can be calculated from (3.2.17).

3.2.4 The Free Surface Calculation

As mentioned in the previous paragraph, the potential solver used here, can attack only the direct problem of fluid dynamics, that is, the locations of all boundary surfaces are assumed known. In our case though the boundaries are not a priori known since neither the shape of the free surface nor the attitude of the ship (running sinkage and trim) are known in advance. In order to overcome this problem, an iterative procedure is adopted (Tzabiras, 2008).

Assuming that at an intermediate step the free-surface geometry is known, the panels on the hull and water surface are directly constructed by finding analytically the intersection of the free-surface and the transverse sections. The points on a transverse cut of the free surface are found by interpolation (spline or linear) following an exponential arrangement. Then, the potential problem is solved by setting the normal velocity on the control point of each panel equal to zero (kinematic condition, see 2.1). After the calculation of the panel sources, the velocity components u_x, u_y, u_z, are calculated on the control points of the surface panels and the total pressure p* is derived from the Bernoulli's equation (3.2.16).

In any intermediate step, the dynamic condition is not satisfied, that is the pressure p* is different than the sum of the ambient p_S (=0) plus the hydrostatic pressure ρgz. This difference is introduced as a source term to calculate the correct vertical velocity u_z^* on the free surface by solving the corresponding inviscid transport equation:

$$\rho\left[\frac{\partial u_x u_z^*}{\partial x} + \frac{\partial u_y u_z^*}{\partial y} + \frac{\partial u_z u_z^*}{\partial z}\right] = -\frac{\partial p^*}{\partial z} \quad (3.2.28a)$$

$$\rho \, \text{div}(u_z^* \mathbf{U}) = -\frac{\partial p^*}{\partial z} \quad (3.2.28b)$$

Equation (3.2.28) is solved numerically by applying the finite volume method. The finite volumes are defined by the panel surface (1234) and a suitably selected height δz^* (figure 3.2.4). Equation (3.2.28) is then integrated in the finite volume, after applying Gauss' divergence theorem.
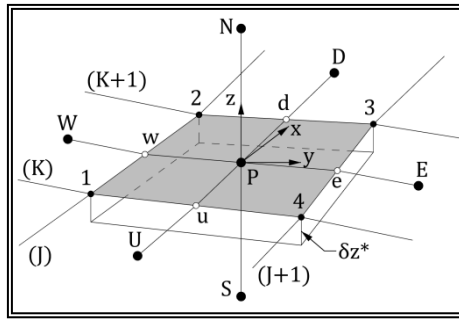
Figure 3.2.4 Finite volume for the calculation of the free surface.

$$\int_{CV} \text{div}(a)dV = \int_A \mathbf{n} \cdot a \, dA \quad (3.2.29)$$

$$\int_{CV} \rho \, \text{div}(u_z^* \mathbf{U})dV = -\int_{CV} \frac{\partial p^*}{\partial z} dV \Rightarrow$$

$$\rho \int_A \mathbf{n} \cdot (u_z^* \mathbf{U})dA = -\int_{CV} \frac{\partial p^*}{\partial z} dV \Rightarrow I = II \quad (3.2.40)$$

where A is the surface of the finite volume CV and $\mathbf{n}$ is the unit outward normal vector at a point of A.

$$I = \rho \int_A \mathbf{n} \cdot (u_z^* \mathbf{U})dA =$$

$$= \rho \int_{(e)} \mathbf{n} \cdot (u_z^* \mathbf{U})dA + \rho \int_{(w)} \mathbf{n} \cdot (u_z^* \mathbf{U})dA + \rho \int_{(n)} \mathbf{n} \cdot (u_z^* \mathbf{U})dA +$$

$$+\rho \int_{(s)} \mathbf{n} \cdot (u_z^* \mathbf{U})dA + \rho \int_{(u)} \mathbf{n} \cdot (u_z^* \mathbf{U})dA + \rho \int_{(d)} \mathbf{n} \cdot (u_z^* \mathbf{U})dA \Rightarrow$$

$$I = I_e + I_w + I_n + I_s + I_u + I_d \quad (3.2.41)$$

where e, w, n, s, u, d are the east, west, north, south, upstream and downstream faces of A respectively.

By considering $\mathbf{U}, \mathbf{n}$ and u_z* constant over each face, eq. (3.2.41) is approximated:

$$\left.\begin{aligned}
I_d &= \rho \int_{(d)} u_{x,d} \cdot u_{z,d}^* dA = (23)_{pr} \cdot \delta z^* \cdot \rho \cdot u_{x,d} \cdot u_{z,d}^* \\
I_u &= \rho \int_{(u)} -u_{x,u} \cdot u_{z,u}^* dA = -(14)_{pr} \cdot \delta z^* \cdot \rho \cdot u_{x,u} \cdot u_{z,u}^* \\
I_e &= \rho \int_{(e)} u_{y,e} \cdot u_{z,e}^* dA = (34)_{pr} \cdot \delta z^* \cdot \rho \cdot u_{y,e} \cdot u_{z,e}^* \\
I_w &= \rho \int_{(w)} -u_{y,w} \cdot u_{z,w}^* dA = -(12)_{pr} \cdot \delta z^* \cdot \rho \cdot u_{y,w} \cdot u_{z,w}^* \\
I_n &= \rho \int_{(n)} u_{z,P} \cdot u_{z,P}^* dA = (E_{1234}) \cdot \rho \cdot u_{z,P} \cdot u_{z,P}^* \\
I_s &= \rho \int_{(s)} u_{z,P} \cdot u_{z,P}^* dA = -(E_{1234}) \cdot \rho \cdot u_{z,P} \cdot u_{z,P}^* = -I_n
\end{aligned}\right\} \quad (3.2.42)$$

Furthermore II is approximated:

$$II = -\int_{CV} \frac{\partial p^*}{\partial z} dV = -(E_{1234}) \cdot (p_P^* - \rho g z_P) \quad (3.2.43)$$

In equations (3.2.42) and (3.2.43) the subscript P denotes values at the control point of the panel, while subscripts e, w, n, s, u, d denote values at the middle of the corresponding face of the panel. Furthermore (E_{1234}) is the area of the projection $(1234)_{pr}$ of the panel (1234) on the xy-plane (horizontal). Finally $(12)_{pr}$, $(34)_{pr}$, $(23)_{pr}$, $(14)_{pr}$, are the lengths of the projections of the corresponding faces of $(1234)_{pr}$ on x and y-axis respectively.

In equation (3.2.42) $u_{x,d}$, $u_{x,u}$, $u_{y,e}$, $u_{y,w}$, are the exact velocity components at the middle of the corresponding face of the panel, as calculated by the potential theory and $u_{z,P}$, is the exact vertical velocity component at the control point of the panel, as calculated by the potential theory. Finally, $u_{z,d}^*$, $u_{z,u}^*$, $u_{z,e}^*$, $u_{z,w}^*$ are the unknown values of u_z^* at the middle of the corresponding face of the panel and are approximated by the first order upstream difference scheme:

$$\left.\begin{aligned}
u_{z,d}^* &= u_{z,P}^* \\
u_{z,u}^* &= u_{z,U}^* \\
u_{y,e} > 0, \quad u_{z,e}^* &= u_{z,P}^* \\
u_{y,e} < 0, \quad u_{z,e}^* &= u_{z,E}^* \\
u_{y,w} > 0, \quad u_{z,w}^* &= u_{z,W}^* \\
u_{y,w} < 0, \quad u_{z,w}^* &= u_{z,P}^*
\end{aligned}\right\} \quad (3.2.44)$$

where the subscripts E, W, U, D denote values at the neighboring control points.

Due to the nature of the problem, $u_{x,d}$, $u_{x,u}$, are always positive, hence there is no need to check the values of $u_{x,d}$, $u_{x,u}$. Equations (3.2.42) and (3.26) after applying (3.2.44) are cast in the common form:

$$A_P u_{z,P}^* = A_E u_{z,E}^* + A_W u_{z,W}^* + A_U u_{z,U}^* + A_D u_{z,D}^* + (E_{1234})(p_P^* - \rho g z_P) \quad (3.2.45)$$

As was mentioned before, δz^* is the height of the finite volume and acts as an arbitrary parameter that controls the convergence of the procedure. It is involved in the convective terms A_i of (3.2.45), but essentially determines the influence of the pressure gradient.

Since the convective coefficients are approximated by the first order upstream difference scheme, only one sweep of the computational domain is needed to solve for the vertical velocity component. Although the corresponding solution is related only to the free-surface renewal, the disadvantage of the first order approximation is that necessitates fine discretization to obtain satisfactory results.

The calculated vertical velocity components are then used to calculate a new surface by introducing two corrective steps similar to those of paragraph 3.1 (Tzabiras, 2004). First, the free surface is updated following the local flow lines, in the Lagrangian sense. This is done in two alternative ways. The first way is to transfer a fluid particle α on the transverse plane K, to a new location b on plane K+1 (figure 3.2.5). Point b is calculated as follows. First the line that passes through points α and P′ and is parallel to the local velocity vector passing through P, is defined. Point P is the center of a surface panel, located on plane K+1/2 and P′ is a point on the same vertical line as P. Point b is defined as the intersection of the α-P′ line with the K+1 plane. Points b form a new transverse cut of the free surface on plane K+1. Then, the new nodes on K+1, corresponding to the constant coordinate x_3-lines, are found by means of interpolation among points b.
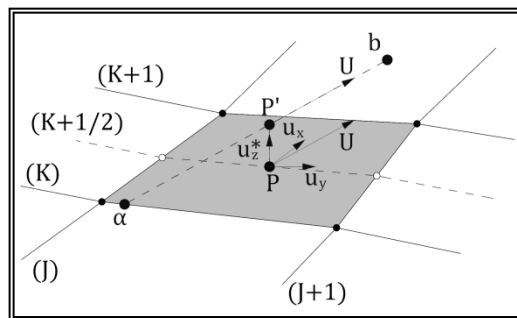
Figure 3.2.5 First correction of free surface.
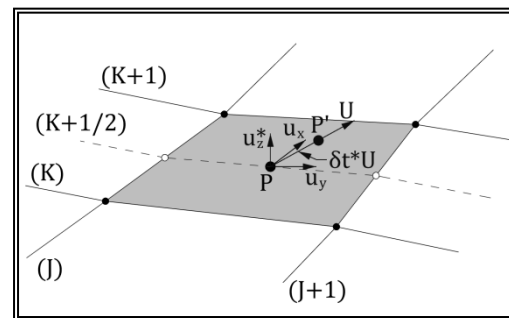
Figure 3.2.6 First correction of free surface using a time step δt.

Alternatively, the free surface is updated as follows. Following the local flow lines, a fluid particle P on the center of a panel, on the transverse plane K+1/2, is transferred to P′ in the Lagrangian sense, with the translation being equal to the product of the local velocity vector U and a time step δt (figure 3.2.6). The location of points P′ does not coincide with the transverse cuts of the original surface. Consequently the new nodes are the calculated by interpolations amongst points P′.

Next, the new cut is corrected by δz in order to satisfy locally the kinematic condition. In an integrated form, this condition is satisfied when the flux through the examined panel becomes equal to zero. Approximately, this can be achieved moving the corner point C of panel (ABCD) vertically by δz (C to C′), (figure 3.2.7). The location of the B′ point is considered the result of a similar translation for the neighboring panel to the right of (ABCD).

To accelerate convergence, the method may be applied over a number on surface panels in the longitudinal direction (Tzabiras, 1997). Anyhow, to avoid convergence problems the surface renewal is restricted by an external parameter which stabilizes the whole procedure but decelerates convergence.
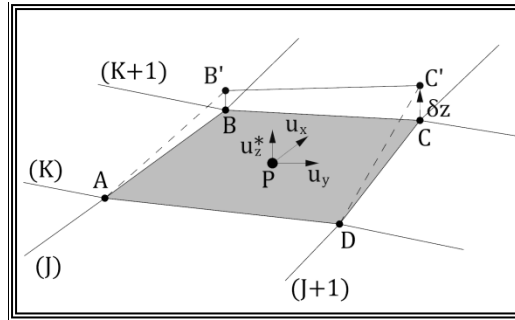
Figure 3.2.7 Second correction of free surface (Kinematic condition).

After the water surface is updated, the potential problem is solved and the whole procedure is repeated until the dynamic boundary condition converges. The satisfaction of the dynamic boundary condition is tested through $\overline{|\delta z|}$ which is the mean value of the absolute difference between the calculated and the ideal hydrostatic pressure at the control points of all surface panels, transformed in [m]. Owing to the free-surface approximation with quadrilateral panels, this value decreases as the problem converges but exhibits a limiting behavior. Therefore, convergence with respect to $\overline{|\delta z|}$ is satisfied, when it becomes lower than a suitable value depending on both the Froude number and the scale. By definition, the smaller the limiting value of $\overline{|\delta z|}$, the more accurate the solution. An example of the convergence history is presented in figure 3.2.8.

Since the free-surface is updated on every step, the wave resistance and the value of the respective coefficient C_W also change. An example of the convergence history of C_W, is presented in figure 3.2.9.
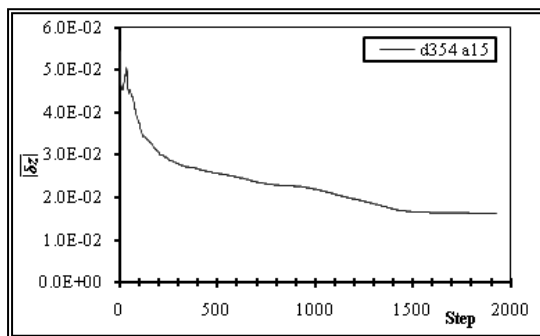
Figure 3.2.8 Convergence of the dynamic boundary condition.
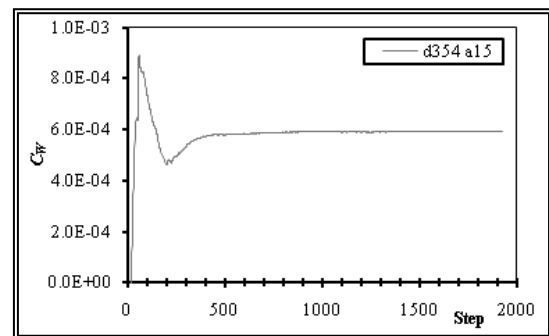
Figure 3.2.9 Convergence of the wave resistance coefficient.

The method can also be applied to ships with both "dry" and "wet" transom sterns. In the above cases a further domain of panels is introduced on the water surface, astern the transom (figures 3.2.10, 3.2.11). The method is applied without any special difficulty, by simply overlapping one line at the boundary of the two domains in order to compute the new free surface. The condition of the transom (wetted or dry) is prescribed by the user. When the transom is declared "dry" then the first row panels of the stern domain are bound to the transom edge. In the case were the transom is declared "wet", extra panels are added on the transom surface and the height of the first row panels of the stern domain is calculated using the method of this paragraph.
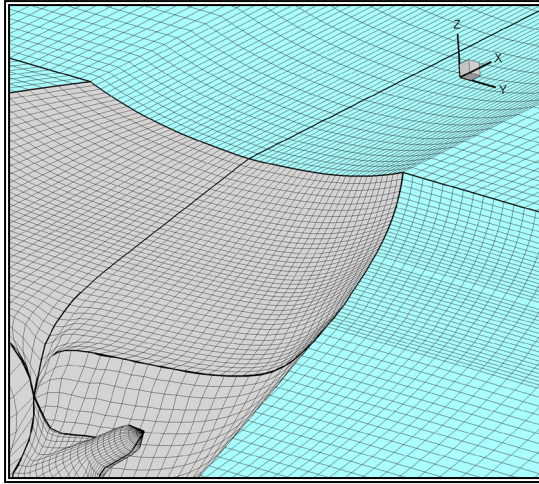
Figure 3.2.10 Panels in the case of a "dry" transom stern.
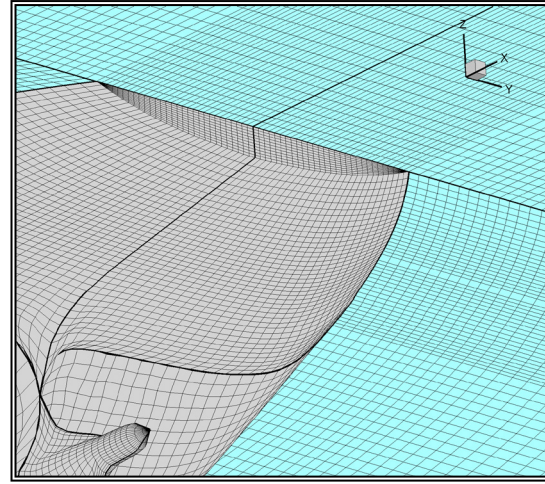
Figure 3.2.11 Panels in the case of a "wet" transom stern.

3.2.5 Wave Making Resistance, Sinkage and Trim Calculations

The wave making resistance as well as the vertical forces and moments are calculated by integrating the pressure on the hull panels. As wave making resistance R_W in this work, we define the pressure resistance, since the potential theory is unable to predict any other resistance component (viscous pressure and frictional). Hence the wave making resistance is defined as the integral on the surface of the hull of the projection of the dynamic pressure (the total pressure minus the hydrostatic pressure) on x-axis (longitudinal):

$$R_W = \iint_{WS} (p^* - \rho gh) \cdot (\mathbf{n} \cdot \mathbf{i})\, ds \quad (3.2.46)$$

where $\mathbf{n}$ is the unit vector normal to the body surface and $\mathbf{i}$ the one parallel to the x-axis. The wave resistance coefficient C_W is then defined as:

$$C_W = -\frac{R_W}{\frac{1}{2}\rho \cdot WS \cdot V_S^2} \quad (3.2.47)$$

where ρ is the water density, WS is the actual wetted surface, as calculated by the present method and V_S is the ship's speed.

The integration on the surface of the hull, of the projection of the total pressure on z-axis (vertical), gives the vertical force and moment that cause the ship to change its attitude.

$$R_Z = \iint_{WS} p^* \cdot (\mathbf{n} \cdot \mathbf{k})\, ds \quad (3.2.48)$$

where $\mathbf{k}$ is the unit vector, parallel to the z-axis.

This force is used to calculate the running sinkage (equation 3.2.49) and trim (equation 3.2.50), whenever this is required and the longitudinal position of the centre of gravity (c.g.), x_g is known. Trim is the total (hydrostatic + hydrodynamic) trim and is defined as positive by stern while sinkage is defined as the increase of draft at x=0 with respect to the ship's reference system (figure 3.2.12).

$$\text{sinkage} = \frac{\Delta - R_Z}{\rho g A_{WL}} \qquad (3.2.49)$$

$$\tan(\text{trim}) = \frac{\Delta \cdot x_g - R_Z \cdot x_p}{\rho g I_{yy}} \qquad (3.2.50)$$

where g is the gravitational acceleration, A_{WL} is the water plane area, x_p is the longitudinal position of the center of pressure, Δ is the displacement and I_{yy} is the second moment of the water plane area, about y-axis.
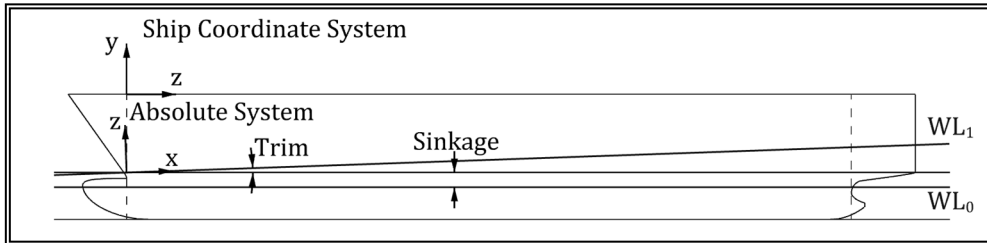
Figure 3.2.12 Definition of the ship reference and the absolute coordinates' system.

The procedure of changing the ship attitude starts after a user defined number of iterations. In between two consecutive calculations of sinkage and trim, a number of iterations, defined by the user, are performed, to allow for a degree of convergence for the free-surface. This procedure is followed until convergence for free-surface, wave making resistance, sinkage and trim is achieved.

The convergence rates for sinkage and trim, are presented in figures 3.2.13 & 3.2.14 respectively. The calculations for the sinkage and trim start after 200 steps and then are carried out every 50 steps. Ultimately it is the convergence of the dynamic boundary condition on the free surface after 1800 iterations (figure 3.2.8) that dictates the overall convergence in this case, since all other values converge after about 800 iterations.
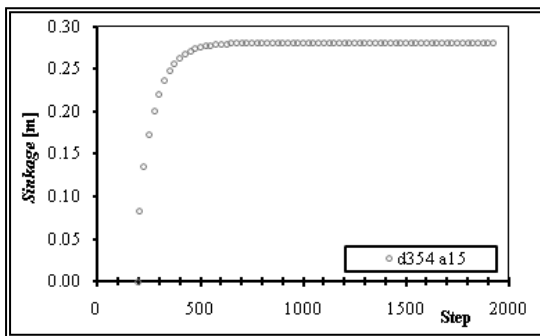
Figure 3.2.13 Convergence of running sinkage.
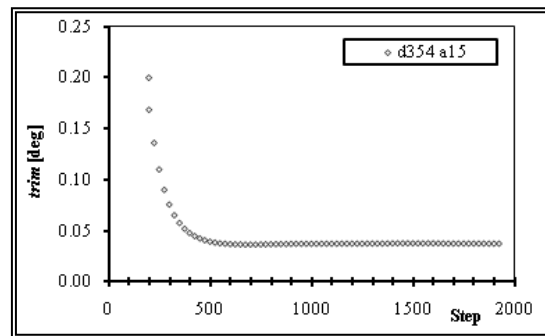
Figure 3.2.14 Convergence of trim.

3.3 A Hybrid RANS-Potential Method for Free Surface Calculations

As mentioned in the previous paragraphs, the direct calculation of the free surface, using the RANS solver, yields rather accurate results but is very expensive in terms of computational cost. On the other hand, the potential approach is significantly cheaper and the resulting wave pattern is mostly in good accordance with experimental data. There are areas of the flow through, where viscosity cannot be neglected, namely near the stern o the ship. In those areas, the potential method tends to over-predict the height of the waves.

The problem is greatly exaggerated in cases of ships with a "wet" transom stern. The flow at the transom stern of a ship is detached and depending on the ship speed, may reattach on the transom itself and a zone of circulating fluid is formed. The potential theory fails completely to model the above behavior since it is mostly affected by viscosity. In such a case, the potential method results in an extremely high stern wave, so much so that the wave making resistance may even become negative.

The above problems need to be addressed and to achieve that, a Hybrid RANS-potential method for calculating the free surface was developed at LSMH-NTUA. The starting point of the new method is the previously used method, where the free-surface is calculated by means of the potential solver and is then used as a fixed boundary for the solution of the viscous flow. The numerical grid for the RANS calculations conforms to the potential free surface (figure 3.3.1) and the transport and equations are solved by employing Dirichlet conditions on the surface, for the velocity components (Kinematic condition) and for the pressure (Dynamic condition).
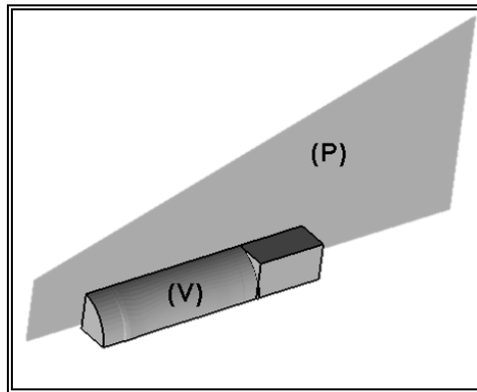
Figure 3.3.1 Computational domain for the potential method (P) and the RANS solver (V).

In the new hybrid method, the free surface is considered a fixed boundary, up to a predetermined point along the ship. Downstream that point the surface is free to deform. Special treatment of the boundary conditions is required, in order to avoid convergence problems near the area where the method of calculation of the water surface changes, In figures 3.3.2 and 3.3.3, longitudinal sections of the wave patter, at a fixed distance from the side of the ship are presented for the Nawigator model (Bugalski, 2004), at a Froude number of Fn=0.219. The lines correspond to

numerical solutions with three deferent approaches for the boundary conditions while the x-marks are data measured experimentally.

In the following figures, the solid lines correspond to a numerical solution where along the fixed part of the surface, the dynamic boundary condition is applied for the transport equations while the kinematic condition is applied during the pressure correction. The dashed lines correspond to a numerical solution where along the fixed part of the surface, the kinematic boundary condition is applied for the transport equations and the pressure also satisfies the dynamic condition. Finally the dotted lines correspond to a numerical solution where along the fixed part of the surface, the kinematic boundary condition is applied for the transport equations and the pressure is determined through the Neumann condition normal to the water surface.

In all cases a surface tracking procedure is employed along the free to deform portion of the surface, where the free surface is corrected in a number of steps, until both kinematic and dynamic boundary conditions are satisfied. The transition point is located at a distance of 45 m from the bow of the ship or at 81.8% of the waterline length. The grid size in all numerical tests was NIxNJxNK=81x141x481 where NK is the number of planar 2-D section perpendicular to the ship longitudinal axis, NI is the number of grid nodes in the circumferential direction of each planar section and NJ is the number of grid nodes in the radial direction of each planar section.
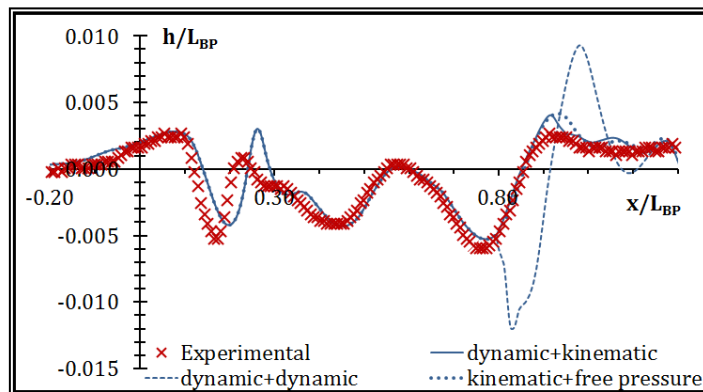
Figure 3.3.2 Wave pattern at a distance of 0.1108 m from side of the Nawigator model, Froude number Fn=0.219.
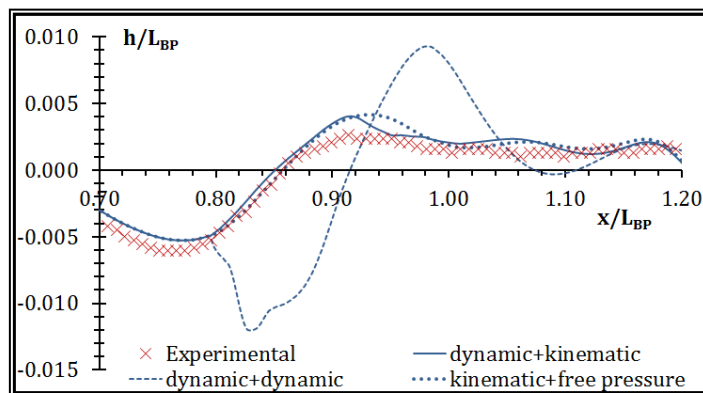
Figure 3.3.3 Detail near the stern, of the wave pattern at a distance of 0.1108 m from side of the Nawigator model, Froude number Fn=0.219.

Another application of the new hybrid method is presented in figures 3.3.4 and 3.3.5. Specifically the wave pattern on the hull of a C_B=0.60 Series-60 model is presented, at a Froude number Fn=0.316 (Tzabiras & Polyzos, 2015). The continuous line is the wave patterns as calculated directly by means of the RANS solver, the dashed line corresponds to the potential method and the x-marks are data measured experimentally.
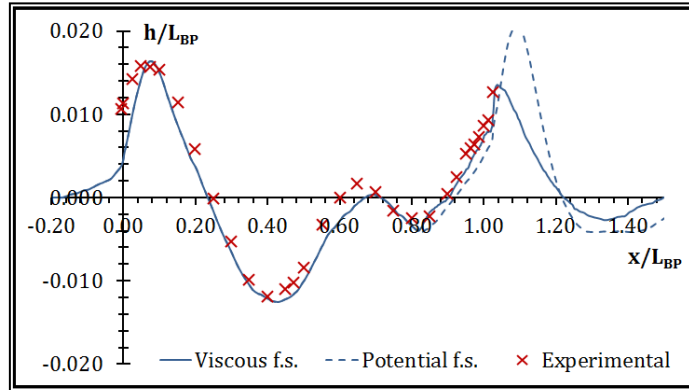
Figure 3.3.4 Wave pattern on the hull of a C_B=0.60 Series-60 model, Froude number Fn=0.316 (Tzabiras & Polyzos, 2015).
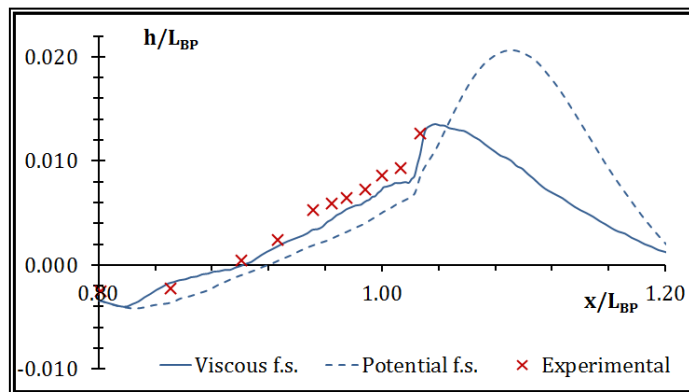
Figure 3.3.5 Detail near the stern, of the wave pattern on the hull of a C_B=0.60 Series-60 model, Froude number Fn=0.316 (Tzabiras & Polyzos, 2015).

With the new hybrid method a significant reduction in computing time is achieved. Specifically when employing directly the RANS solver, starting from a flat water surface, a total of about 1000 steps are required for the convergence of the free surface, for a conventional ship. When staring with the surface as calculated by the potential solver, around 100-200 steps are required for the correction of the free surface around the stern. Even when taking into account the time required for the convergence of the potential solver, the total time gain is in the order of 75% (Tzabiras & Polyzos, 2015).

The presented hybrid method combines the accuracy and efficiency of the potential flow solution at the bow of ships, with the accuracy of the RANS based solution at the stern of ships, where the effect of viscosity cannot be neglected. When combined with the three block setup of paragraph 2.5, the method is able to predict the wave pattern at a "wetted" transom stern.

(This page intentionally left blank)

CHAPTER 4   THE METHOD FOR GENERATING GRIDS AROUND APPENDAGES

(This page intentionally left blank)

4.1   The Overlapping Grid Block Method

The use of structured grids presents several advantages, over the use of unstructured grids, as discussed in previous paragraphs. On the other hand, when structured grids are employed, complex geometries are very difficult if not impossible to model. To circumvent this obstacle, two methods have been developed. The first uses blocks of structured grids that in pairs have common boundaries. The main drawback of this method is that generating grids with predefined boundaries is usually difficult. Furthermore in the case of a geometrical alteration, for example when altering the rudder angle of attack, at least one block, if not more, has to be modified.

A second method is to use overlapping blocks of structured grids. In this case a separate grid block is generated for each component and the transport equations are solved independently for each block. In the case of a ship with appendages, there may be one or more blocks for the hull and one or more blocks for each appendage. The transfer of information between blocks is accompliced by using part of the solution of one block as the boundary condition for those boundaries of other blocks that lie within the first one. Each block is now easier to generate since there is no need for common boundaries. The only extra effort required is in the bookkeeping of which volume lends boundary conditions to whom. In the case of boundaries moving relative to each other, the grid blocks remain unaltered and only the tables that prescribe the transfer of information have to be recalculated. The above scheme is called the Overlapping Grid Block method or Chimera and has been successfully employed in various complex problems of aerodynamics and hydrodynamics (Brezzi, 2001, Chan, 2009, Dougherty, 1985, Steger, 1987 & 1991, Tarhan, 2002, Tu, 1992) as well as for Navier-Stokes calculations about appended ships (Carrica, 2007 & 2010, Kim, 2007, Lin, 1995, Regnstrom, 2006, Simonsen, 2005).

The two key points with regard to the implementation of the Overlapping Grid Block method are:

- The accurate and efficient exchange of information between the blocks and
- The conservation of mass throughout the computational domain

In order to explore the two points, let us consider the 2-D problem of a hydrofoil at an angle of attack where the far field is modeled via a Cartesian Orthogonal grid, while the area near the hydrofoil is modeled via a C-type curvilinear grid (figure 4.1.1). In the following, the far field grid will be called the Master grid, while the near field grid, the Slave grid, since the solution on the Slave grid is dependent of the Master grid solution.

In the Overlapping Grid Block method, the flow on the Master grid is solved first, without taking into consideration the presence of the hydrofoil. Then the flow near the hydrofoil is solved. In order to do so, appropriate conditions must be imposed on the boundaries of the C-type grid. According to the nomenclature of figure 4.1.2, the four boundaries of the slave grid are: the North (N) or external boundary, the South (S) that comprises the solid boundary and the double line abaft the trailing edge and finally the West (W) and East (E) boundaries that form the outlet boundary. In this

example, the South boundary is internal and the boundary conditions are not related to the overlapping grid block method.
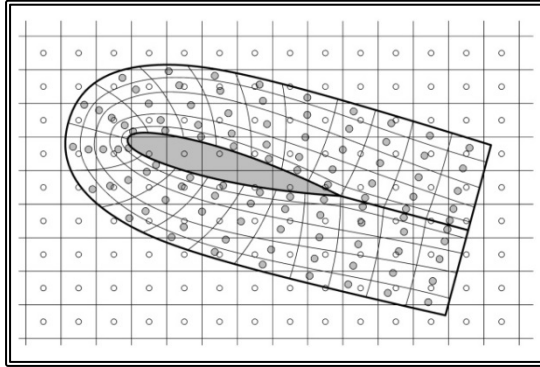
Figure 4.1.1 A 2-D orthogonal curvilinear grid block (slave) around a hydrofoil inside a 2-D Cartesian grid (master)
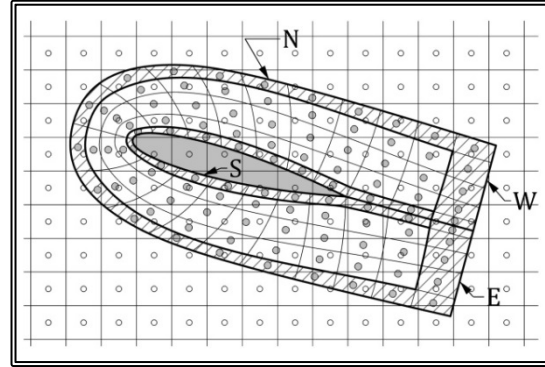
Figure 4.1.2 Definition of the boundaries of a 2-D slave grid block

The boundary conditions on the North boundary are as follows:

$$u_{1,N} = u_{1,Master}$$

$$u_{2,N} = u_{2,Master}$$

$$k_N = k_{Master}$$

$$\varepsilon_N = \varepsilon_{Master}$$

$$\partial p / \partial n = 0 \qquad (4.1.1)$$

That is, for all flow variables bar pressure, the conditions derive from the solution of the Master grid, while for the pressure, Neumann conditions are applied.

For the outlet boundaries E, W, we apply the Open Boundary conditions for the velocity components, i.e. we solve up to the last finite volume, while for the pressure and turbulence variables the conditions derive from the solution of the Master grid:

$$k_{E,W} = k_{Master}$$

$$\varepsilon_{E,W} = \varepsilon_{Master}$$

$$p_{E,W} = p_{Master} \qquad (4.1.2)$$

The above method is adopted so that by employing the pressure correction algorithm for the slave block, the continuity of mass is ensured.

In order to calculate the value of a flow variable at the center of a slave finite volume, first we have to determine the master grid finite volume inside whom lies the center of said slave volume. Then the required flow variable at the center of the slave volume, is considered equal to that at the center of the master volume. This procedure is followed for every finite volume on the external boundaries of the slave grid (figure 4.1.3).
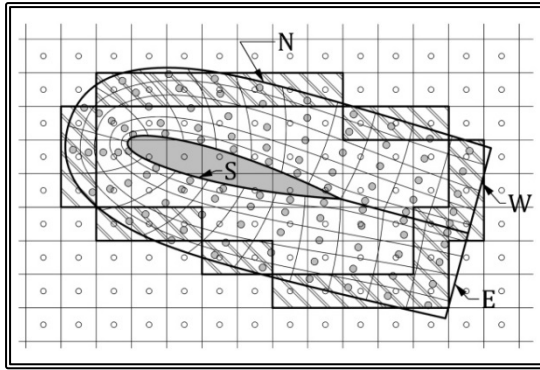
Figure 4.1.3 Donor finite volumes for the boundary conditions of the slave block
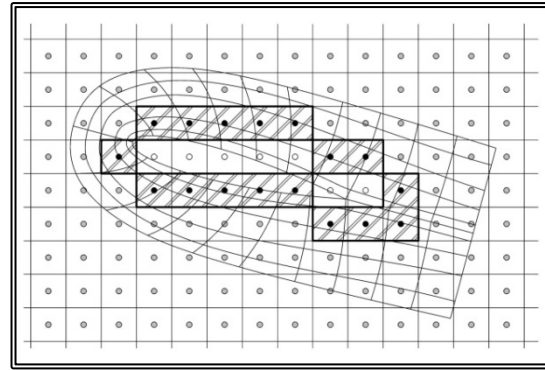
Figure 4.1.4 Donor finite volumes for the boundary conditions of the Master block

Depending on the problem, the procedure could be terminated after the above first step. In general this is not the case though. For most of the problems an iterative procedure is necessary, where after the first solution of the slave grid block, it assumes the role of the donor for the Master block. This time the conditions are not imposed on the boundaries of the Master block but on internal finite volumes. The procedure starts with a set of slave finite volumes that are internal and at a set distance from the external boundaries.

As an example, let us consider that the North boundary on figure 4.1.2 is characterized by a value of the J-index, J=NJ, the West boundary is I=1 and the East boundary I=NI, where NIxNJ the number of slave grid nodes. We find the master finite volumes that contain the slave volumes characterized by J=NJ-3, I=3 and I=NI-3 (figure 4.1.4). These volumes form a closed loop. After ensuring that the set of master volumes that we selected above, are not amongst the original donor master volumes, we consider the values for the flow variables on those nodes, equal to those of the slave block.

Then the master grid block is solved, by enforcing the slave derived conditions on the closed loop and by leaving the volumes that are inside of the loop, blank, i.e. we only solve on the outside of the loop. In figure 4.1.4, the centers of the volumes on which we impose the conditions are denoted by the blacked-out circles, the centers of the blank volumes by circles and centers of the rest of the finite volumes by gray circles. The new solution contains information derived from the slave block but is still not the "correct" solution since the slave solution was based on the original master solution, thus creating the need for an iterative procedure. This iterative procedure though requires only a few steps to converge, in the order of ten. A final note on the method of the overlapping grid blocks, is that the accuracy of the method is affected by differences in the finite volume size of the two grid blocks.

4.2   The Geometrical Problem, the Appendages of a Ship

Since fuel efficiency and the corresponding reduction in the powering demand of as ship is one of the primary objectives of the design process, the surface of a ship hull tends to be streamlined with smooth transitions and hardly any step or other geometrical discontinuity. Consequently generating a structured numerical grid around a hull can be achieved using a single grid block, usually comprising a number of successive 2-D grids that when combined in the third direction, form a 3-D grid block. The generation of such grids is described in the literature (Tzabiras, 2009) and their use has proven to be quite successful in calculating the resistance and propulsion characteristics of ships (Tzabiras, 2004).

The above methodology is applied in the case of a ship without appendages or else in the case of a "bare" hull. The bare hull is what provides the ship with buoyancy but in order for the ship to function several other object are needed. In order to propel the ship, a propeller is usually needed. A shaft is required to transmit the torque from the engine and drive the propeller. In many ships, especially in ships with more than one propeller, the propeller shaft needs to be quite long requiring some form of support such as one or more struts in the form of single struts (I-type bracket) or pairs of struts (V-type bracket). Then, for a propeller driven ship to steer, one or more rudders are required. Furthermore in order to increase directional stability, a skeg is used and in order to reduce the ship's motions in waves, a number of stabilizing fins are employed.
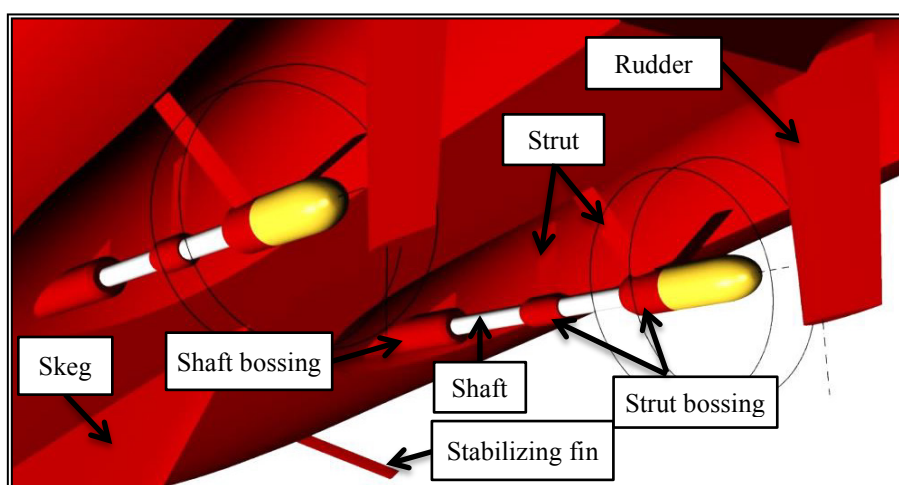
Figure 4.2.1 Appendages on a twin propeller ship
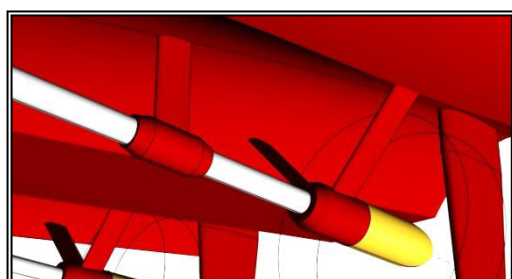
Figure 4.2.2 I-type bracket and V-type bracket on the shaft of a twin propeller ship
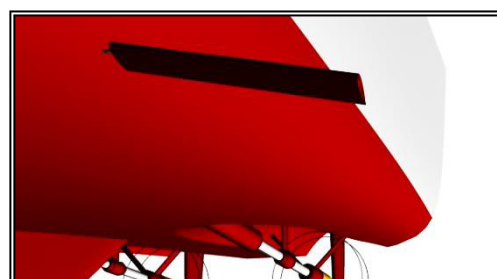
Figure 4.2.3 Stabilizing fin on ship

Every object that extrudes from the bare hull will in the present be referred to as an appendage. Such objects are the skeg, the rudder, the propeller shaft, the propeller shaft bossing, the propeller shaft struts and their bossing, the stabilizer fins etc. Modeling of the skeg can usually be incorporated into the bare hull grid. For the rest of the appendages it is almost always impossible to incorporate them into a single structured grid block, and as a result a separate grid block has to be devised for each object or even in some cases each component part of an object has to be modeled separately.

The first step in modeling the appendages of a ship is to identify the separate objects, i.e. the objects that can be modeled by a single grid block. The rudder or rudders can in most cases be modeled by a single grid block. Stabilizing fins can be considered as almost horizontal rudders with a high length to chord ratio. Consequently the stabilizing fin may not be considered independently but where applicable, the rudder grid block generator may be employed.

Regarding the propeller shaft with its components the following subdivision has been adopted. The shaft bossing, i.e. the section of the shaft just as it exits the hull will be modeled as one grid block. Each strut will be modeled as a separate grid block. That is for a V-type bracket two blocks will be generated. Each strut bossing will be modeled as one grid block. In the V-type bracket case since both struts are connected to one bossing, there will be one grid block for both.

The propeller shaft will be modeled by a number of blocks. Specifically each part of the shaft in-between two objects will be modeled as a cylindrical block. If we consider the case of a twin propeller ship with a shaft supported by a single V-type bracket, then there will be one grid block for the shaft bossing, another for the portion of the shaft between the shaft bossing and the V-type bracket bossing, two blocks for the two struts, one block for the struts bossing and finally a further cylindrical block for the portion of the shaft, abaft the struts bossing. In the case of a ship with one I-type bracket and a further V-type bracket, the grid blocks would be those of the previous example, plus one block for the strut of the I-type bracket, one block for the I-type bracket bossing and a third cylindrical block for the portion of the shaft in-between the two brackets.
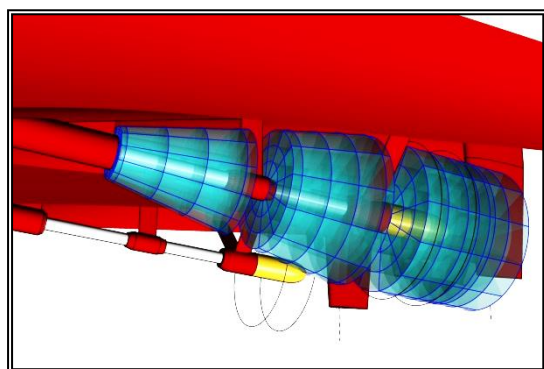
Figure 4.2.4 The proposed propeller shaft grid block arrangement
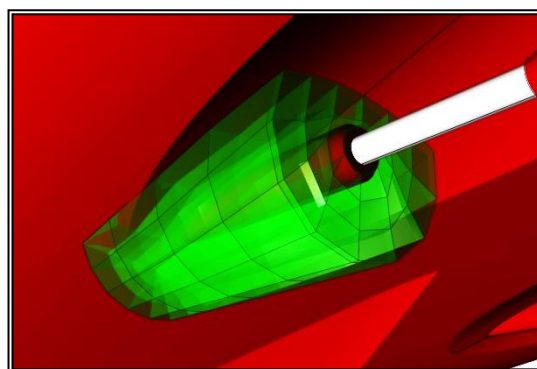
Figure 4.2.5 The proposed propeller shaft bossing grid block arrangement
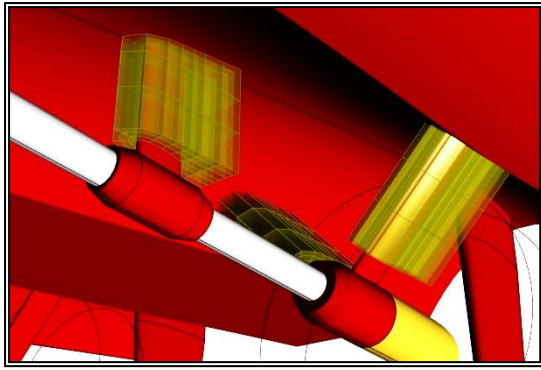
Figure 4.2.6 The proposed propeller shaft struts' grid block arrangement
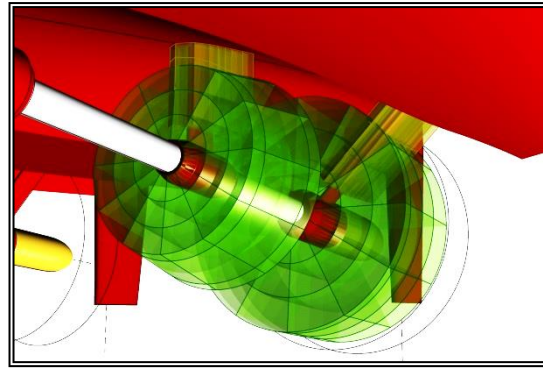
Figure 4.2.7 The proposed strut bossings' grid block arrangement
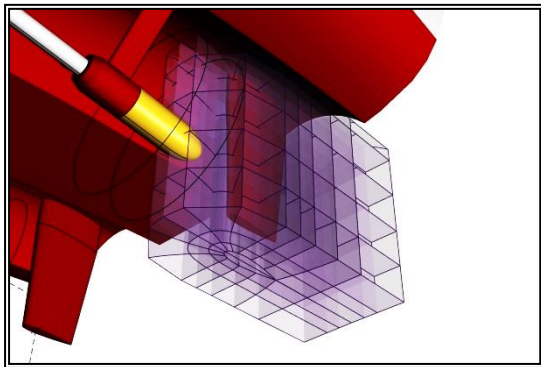
Figure 4.2.8 The proposed rudder grid block arrangement
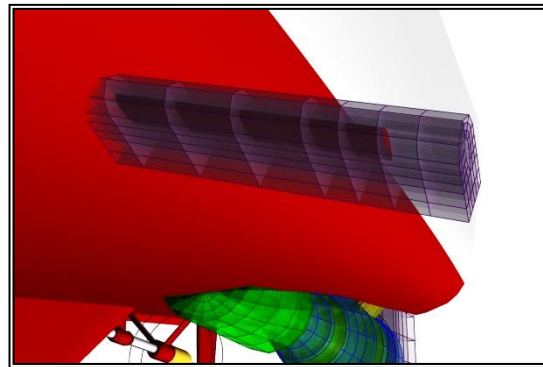
Figure 4.2.9 The proposed stabilizing fin grid block arrangement

By adopting the above subdivision most cases of the complex appendages found on ships can be modeled using a small number of types of grid blocks. Each block can be parameterized in order to cover most foreseeable designs. The overall method despite using only five component types, rudder, shaft, shaft bossing, strut and strut bossing, can be employed for most cases of ships with one or more propellers, one or more rudders and combinations of struts in the form of I-type brackets or V-type brackets.
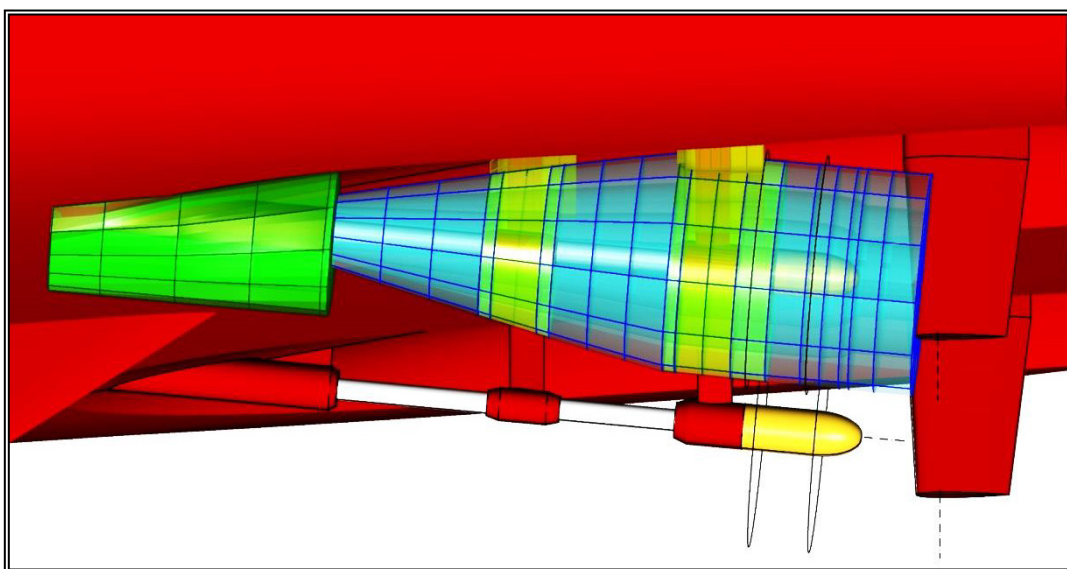
Figure 4.2.10 View of the proposed shaft (blue), the shaft bossing (green), the struts (yellow) and the strut bossings' (green) grid blocks
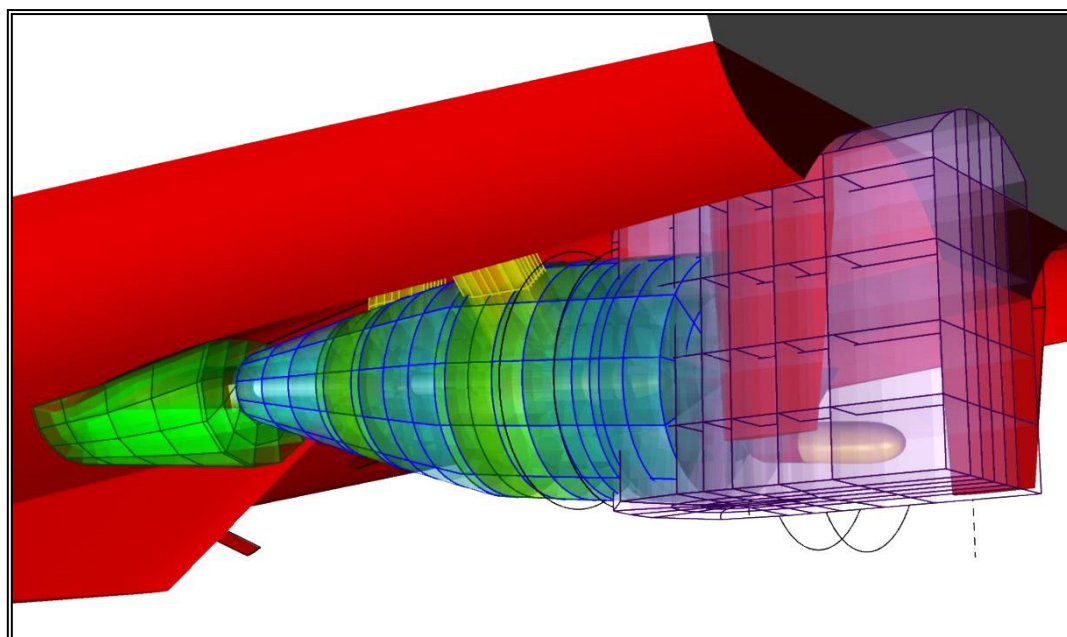
Figure 4.2.10 View of the proposed shaft (blue), the shaft bossing (green), the struts (yellow), the strut bossings' (green) and the rudder (purple) grid blocks

4.3   Geometrical Representation of the Appendages

In the present work, the geometry of the appendages is described in a semi-parametric way. That is, a number of hydrofoil sections are used to define the thickness distribution on the rudder and the shaft struts, while a parametric approach is adopted for all other geometrical characteristics. The location of the propeller shaft is defined by the vector of the shaft datum point with respect to the ship coordinate system, where the shaft end is considered as the datum. The shaft orientation is defined through the angle between the shaft axis and a longitudinal vertical plane and the angle between the shaft axis and a horizontal plane (figure 4.3.1). At the location where the shaft penetrates the hull surface, the shaft bossing is located. Also the shaft may be supported by up to two brackets, each equipped with a bossing. Finally at the end of the shaft, there may be a propeller hub. The geometry of the above objects is parametrically defined through a set of form parameters and dimensions (figure 4.3.2)
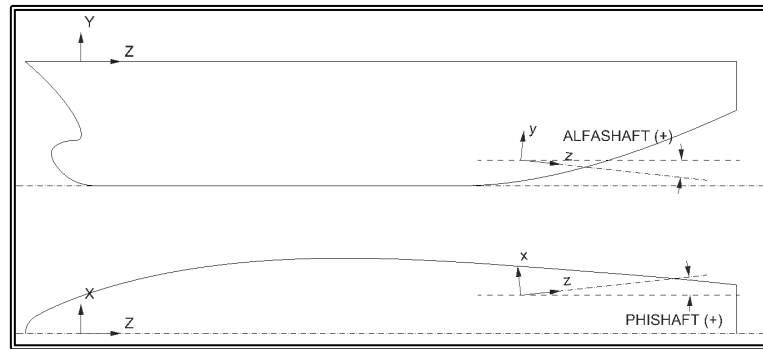
Figure 4.3.1. Definition of the shaft and the shaft bossing strut orientation.
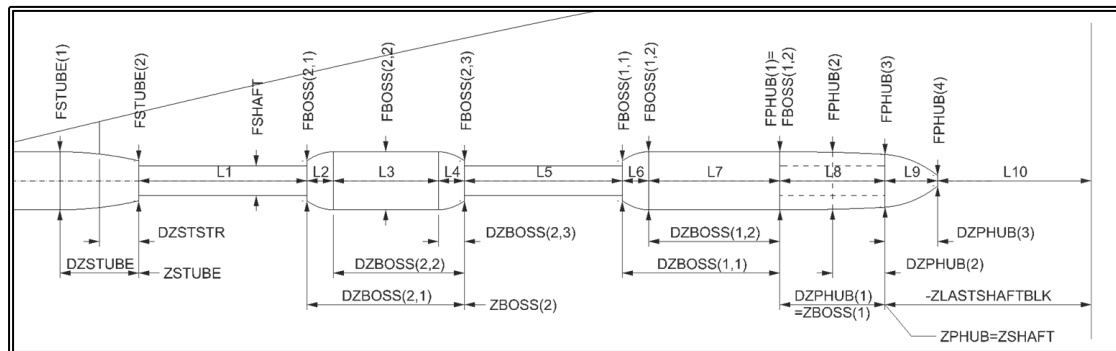
Figure 4.3.2. Definition of the shaft. shaft bossing and strut bossings' dimensions.

The shaft bossing may be of three types (figure 4.3.3a-c). Type-A (ISTUBE=1) is a shaft bossing of constant radius, greater that the shaft radius consequently at the aft end of a type-A shaft bossing there is a discontinuity (step) in the radius. Type-B (ISTUBE=2) is a shaft bossing of constant radius with a tapered end. Type-C (ISTUBE=3) is a shaft bossing of constant radius with a smoothly varying radius at its end. The radius at the end section is described by a second degree curve defined by the start and the end radius, with a horizontal tangent at the start. The end radius of a type-B or type –C shaft bossing may or may not be equal to the shaft radius and as a result there may or may not exist a discontinuity in the radius.
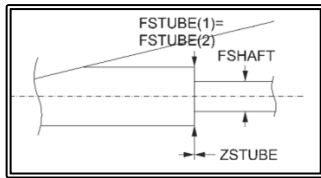
Figure 4.3.3a. Type-A shaft bossing of constant diameter.
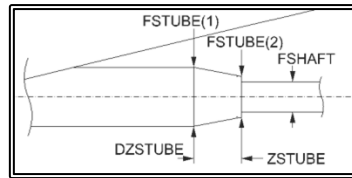
Figure 4.3.3b. Type-B shaft bossing with tapered end.
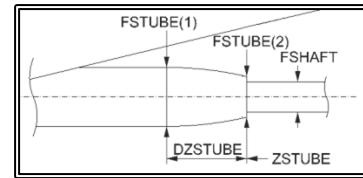
Figure 4.3.3c. Type-C shaft bossing with varying diameter end.

The shaft bossing may also feature a reinforcing strut. The end of the strut is at some distance from the bossing end while the thickness of the strut is constant (figure 4.3.4). The reinforcing strut may also be at an angle with respect to the vertical (figure 4.3.5).
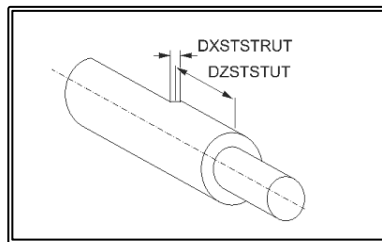
Figure 4.3.4. Definition of the shaft bossing, strut geometry.
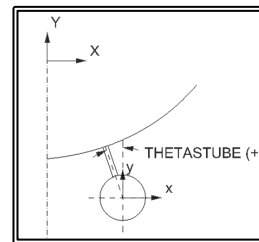
Figure 4.3.5. Definition of the shaft bossing strut orientation.

The propeller hub may also be modeled as one of three types (figure 4.3.6a, b). Type-0 (IPHUB=0) corresponds to no propeller hub and the shaft ends abruptly. Type-A (IPHUB=1) is a propeller hub with its profile defined by a 3rd degree curve that fits through three points and has zero tangency at its fore end. Type-B (IPHUB=2) corresponds to a propeller hub with end cup. The diameter of the hub is defined as before, by a 3rd degree curve that fits through three points and has zero tangency at its fore end, while the diameter of the hub cup is defined by a 2nd degree curve that fits through two points and has the same tangency at its fore end as the propeller hub.

At the fore end of the propeller hub, the diameter may equal to that of the aftmost strut bossing. In the case where there is no strut bossing or the diameter of the bossing is different to that of the hub, there is a discontinuity (step) in the radius. The hub cup may end at a point or at a vertical cylindrical surface of some diameter. In the latter case, as well as in the case without a hub cup, there is a discontinuity in the radius.
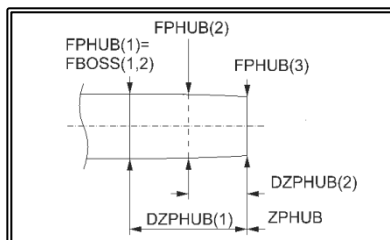
Figure 4.3.6a. Type-A propeller hub.
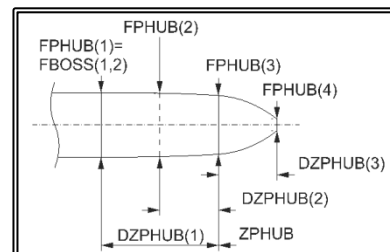
Figure 4.3.6b. Type-B propeller hub with end cup.

The shaft may be supported by up to two brackets, through their respective bossings. Each bossing may be of one of six types (figures 4.3.7a-f). Type-A (IBOSS(KB)=1), is a bossing with constant diameter. Type-B (IBOSS(KB)=2), is a bossing of constant

diameter with a tapered fore end. Type-C (IBOSS(KB)=3), is a bossing of constant diameter with a tapered fore end and a tapered aft end. Type-D (IBOSS(KB)=4), is a bossing of constant diameter with a fore end with varying radius described by a second degree curve having zero tangency at its aft end. Type-E (IBOSS(KB)=5), is a bossing of constant diameter with a varying diameter fore end described by a second degree curve having zero tangency at its aft end and a varying diameter aft end described by a second degree curve having zero tangency at its fore end. Finally type-F (IBOSS(KB)=6), is a bossing of varying radius described by a second degree curve that fits through three points. Types C, E and F apply only to a fore strut bossing, i.e. a bossing not abutting the propeller hub. The radius ate either end of a bossing may or may not be equal to the shaft radius and as a result there may or may not exist a discontinuity.
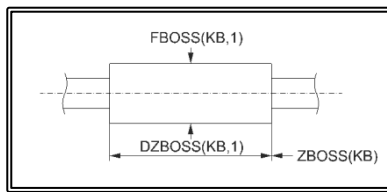
Figure 4.3.7a. Type-A strut bossing of constant radius.
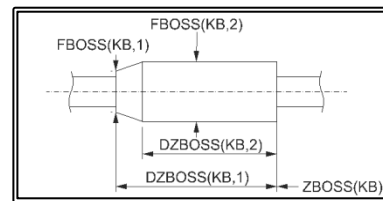
Figure 4.3.7b. Type-B strut bossing with tapered fore end.
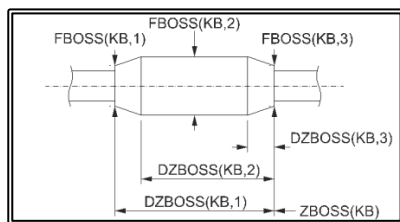
Figure 4.3.7c. Type-C strut bossing with both ends tapered.
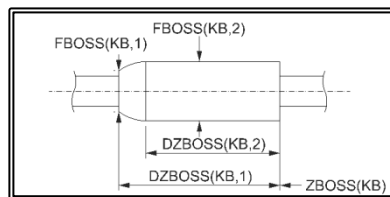
Figure 4.3.7d. Type-D strut bossing with varying fore end radius
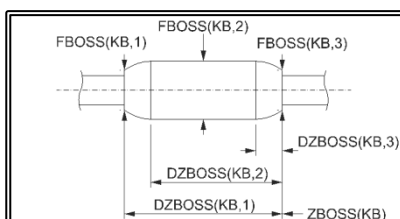
Figure 4.3.7e. Type-E strut bossing with varying radius at both ends.
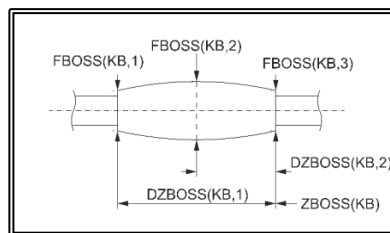
Figure 4.3.7f. Type-F strut bossing of varying radius.

Each bracket may be of I-type or V-type. In the former the bracket comprises one strut while in the later the bracket comprises two struts. Each strut is parametrically defined (figure 4.3.8). Initially the location and orientation of a reference line is defined for each strut (figure 4.3.9). Then the chord and twist for two sections are provided by the user. The overall strut twist is defined as the sum of two angles. The first angle is calculated as the linear interpolation of the angles of the two input sections. The second angle follows a sinusoidal distribution where the number of half-periods and the amplitude are input. This second angle is always zero at the intersection of the strut axis with the hull and the strut's bossing. The hydrofoil profile on each of the two input sections is defined by means of a number of points. In order

to calculate the offset at a desired location, a spline interpolation is employed while enforcing a tangent at the leading edge, normal to the chord line.
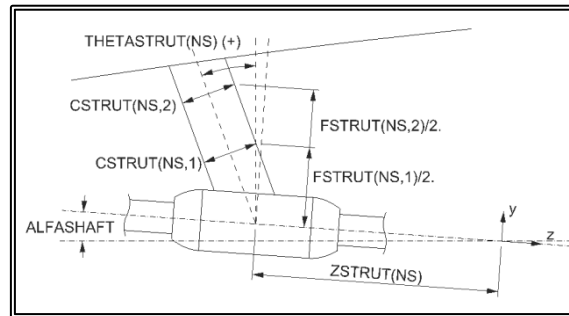
Figure 4.3.8. Definition of the struts dimensions
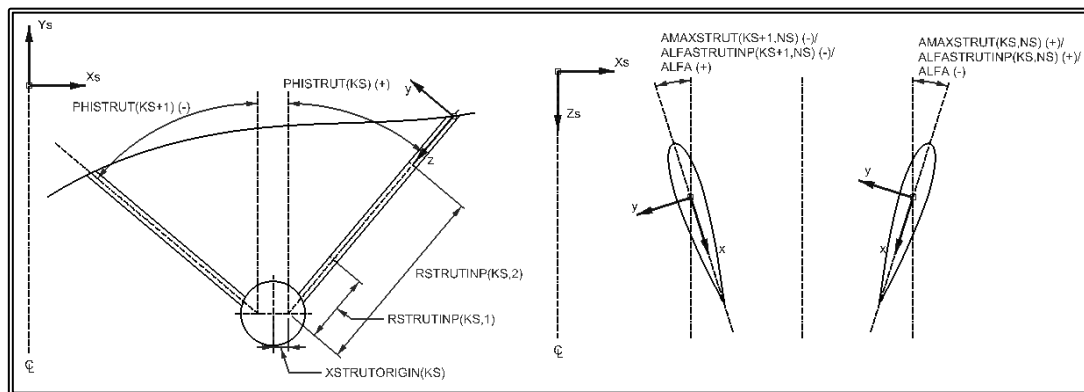
Figure 4.3.9. Definition of the struts orientation

The rudder may be of two types (figures 4.3.10a, b). Type-A (IRUDDER =1) is a hanging rudder with exposed shaft, while type-B (IRUDDER =2) is also a hanging rudder but with a hydrodynamic fairing around the shaft. In the latter, the fairing has to be of constant section along its height.

Initially the location and orientation of a reference line is defined for the rudder (figure 4.3.11). The profile of the rudder is considered a trapezoid with either straight or curved legs. In the first case, the shape of the ruder is defined by means of two sections, one at the tip and one at the base. In the second case, a third section must also be defined and the shape of the two legs is that of a second degree curve that interpolates the leading and trailing edges of the three sections. For each section, the location, chord length and angle of attack are defined. The hydrofoil profile on each section is defined by mean of a number points and a spline is fitted for interpolation purposes, where the tangent at the leading edge is always normal to the chord line. The user also provides the overall angle of incidence ALPHARUDDER, while the angle of attack on an arbitrary section of the rudder is calculated as the sum of the angle of incidence, a linear interpolation of the angles of the tip and base sections and a sinusoidal distribution prescribed through the number of half-periods IARUDDER and the amplitude AMAXRUDDER.

4.3. GEOMETRICAL REPRESENTATION OF THE HULL AND THE APPENDAGES
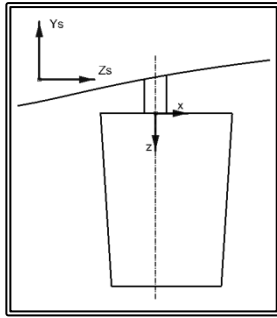
Figure 4.3.10a. Type-A rudder.
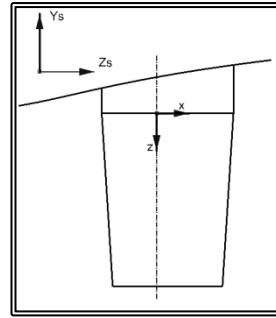
Figure 4.3.10b. Type-B rudder.
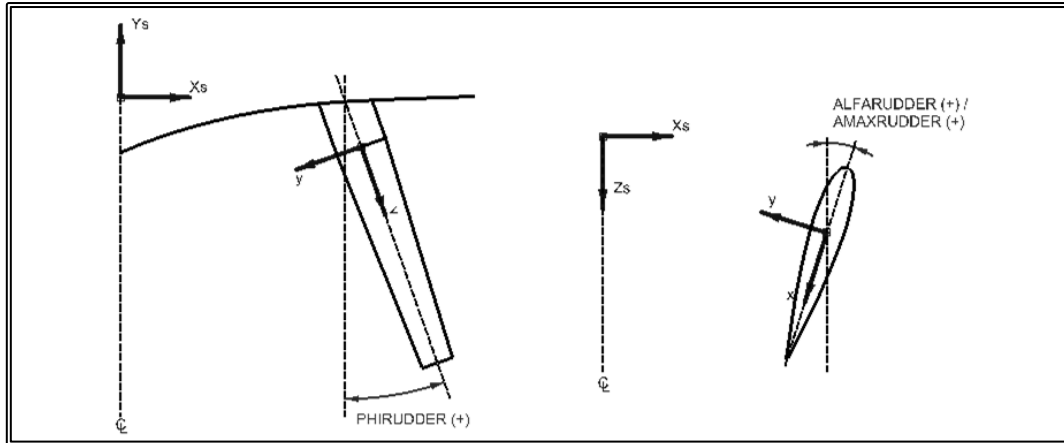
Figure 4.3.11. Definition of the rudder orientation
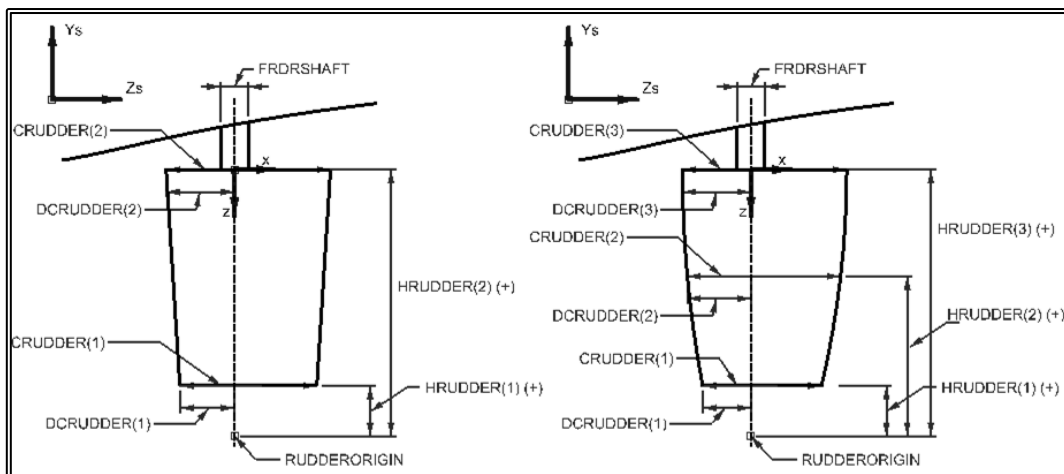
Figure 4.3.12. Definition of the rudder dimensions

4.4   Generation of a General 2-D Orthogonal Curvilinear Grid

As the explained in paragraph 2.1.2, the use of a local orthogonal curvilinear system in conjunction with a curvilinear orthogonal grid, is beneficial both in terms of accuracy and convergence, when numerically solving the strongly coupled momentum and continuity equations for a flow around bodies with arbitrary geometries. The generation of an orthogonal curvilinear grid in not a trivial task though especially in the 3-D case. An efficient way of generating a 3-D grid with most of the advantages of a fully orthogonal curvilinear 3-D grid is the generation of a partially orthogonal 3-D grid consisting of successive 2-D orthogonal curvilinear grids. The resulting grid is orthogonal curvilinear on each of the successive sections, while in the third direction it is non-orthogonal. The successive 2-D grids are actually not required to be planar; they can lay on an arbitrary surface thus enabling the grid to conform to specified geometries such as the hull of a ship. In the present work it was decided that all grid blocks should be partially orthogonal curvilinear.

A method for generating 2-D orthogonal curvilinear grids, based on the conformal mapping of an arbitrary shape to a unit circle, was presented in paragraph 2.5.2. This method is employed for the generation of the 2-D sections for the rudder grid block. A disadvantage of the conformal mapping method is that only the shape of the solid boundary (South edge-S) (figure 2.5.2) can be prescribed. The West (W) and East (E) boundaries are always straight line segments, normal to the South boundary. Finally the shape of the North (N) boundary cannot be defined by the user, rather the distance from the South edge can only by prescribed. In the overlapping grid method being able to pre-determine the shape of the boundaries is rather useful.

In light of the above, it was decided that for the generation of the 2-D orthogonal curvilinear grids, the method presented by Tzabiras et al. (1986) would be adopted for the shaft bossing, the strut and the strut bossing blocks. The method can also be employed for the rudder 2-D sections. The method uses singularity distributions on the boundaries to solve the potential flow problem. Then the grid nodes are calculated as the intersection points of stream and equi-potential lines. The method is based on the classical Hess & Smith (1968) method for solving the 2-D incompressible potential flow problem with two solid boundaries. In figure 4.4.1 the definition of the computational domain is presented, where N, S are the two solid boundaries, treated as stream lines. The E, W boundaries are treated as equi-potential lines and U_∞ is the velocity vector of the onset flow.
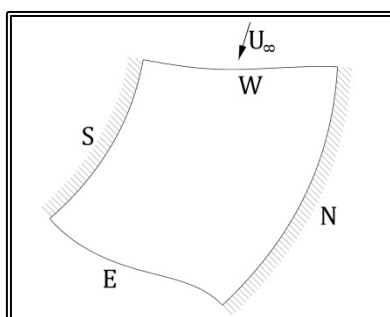
Figure 4.4.1 Definition of the calculation domain boundaries

For the solution of the above potential flow problem, a singularity distribution is considered on each of the four boundaries. Then the velocity vector $\mathbf{U}$ at any point of the flow field is:

$$\mathbf{U} = \mathbf{U}_\infty + \mathbf{u} \quad (4.4.1)$$

where $\mathbf{u}$ is the velocity induced by the singularities. If we consider the static problem and the flow field inviscid ($\mu = \nu = 0$) and incompressible ($\rho=$constant), the Navier-Stokes equations reduce to the Eulerian equation of motion (in 2-D):

$$\left.\begin{aligned} \operatorname{div}(u_x\mathbf{U}) &= -\frac{1}{\rho}\frac{\partial p}{\partial x} \\ \operatorname{div}(u_y\mathbf{U}) &= -\frac{1}{\rho}\frac{\partial p}{\partial y} \end{aligned}\right\} \quad (4.4.2)$$

The equation of continuity also is simplified:

$$\operatorname{div}(\mathbf{U}) = 0 \quad (4.4.3)$$

The above equations define an incompressible and inviscid flow, but not a potential flow. In a potential flow, the velocity vector is equal to the negative gradient of a scalar potential function, the velocity potential Φ:

$$\mathbf{U} = -\nabla\Phi \quad (4.4.4)$$

From vector calculus it is known that the curl of a gradient is equal to zero:

$$\nabla \times \nabla\Phi = 0 \quad (4.4.5)$$

Subsequently the vorticity of a potential flow field is zero:

$$\nabla \times \mathbf{U} = 0 \quad (4.4.6)$$

This implies that a potential flow is also an irrotational flow. Since the velocity vector satisfies the continuity equation (4.4.3), by replacing (4.4.4) into (4.4.3) we arrive at the conclusion that the potential Φ satisfies Laplace equation:

$$\nabla^2\Phi = 0 \quad (4.4.7)$$

Since N, S are stream lines and E, W equi-potential lines, the boundary conditions are:

$$\left.\frac{\partial \Phi}{\partial n}\right|_{N,S} = 0 \quad (4.4.8a)$$

$$\left.\frac{\partial \Phi}{\partial s}\right|_{E,W} = 0 \quad (4.4.8b)$$

where n is the direction normal to the boundary and s the tangential direction. Equations (4.4.7) and (4.4.8) comprise a well-set problem for the potential Φ. In order to solve this problem, a source or sink distribution is assumed on N, S boundaries, whereas an eddy distribution is assumed on E and W boundaries. Then each boundary is covered by a number of rectilinear elements (panels) and on each element, the distribution of source or eddy is assumed constant. By applying the boundary condition on each element, we arrive at the following system of linear equations:

$$\sum_{j=1}^{N} A_{ij} \cdot \sigma_j + F_i = 0, i = 1, \dots, N \quad (4.4.9)$$

where N is the total number of elements, σ_j is the singularity density on the j-element, A_{ij} is the induced normal or tangential (according to the nature of the singularity) velocity on the i-element from the j-element and F_i is the induced velocity on the i-element from the external singular points.

The system of linear equations (4.4.9) is solved iteratively by employing a Gauss-Seidel algorithm thus determining the unknown singularity densities σ_j. Then the singularities are used to calculate the velocities, the potential and the stream function on every point of the computational domain. Let us consider one of the rectilinear elements with a constant source distribution 4π. The velocity components (U_S, V_S) at a point with (x_0, y_0) coordinates with respect to the local element coordinate system (x, y) (figure 4.4.2) are:

$$U_s = \ln\left[\frac{(x_0+a)^2+y_0{}^2}{(x_0-a)^2+y_0{}^2}\right] \quad (4.4.10a) \qquad V_s = 2\cdot\tan^{-1}\left[\frac{2\cdot y_0\cdot a}{x_0{}^2+y_0{}^2-a^2}\right] \quad (4.4.10b)$$

The Potential is:

$$\Phi = -\left[-x_0\cdot U - y_0\cdot V - a\cdot\ln[\{(x_0+a)^2+y_0{}^2\}\{(x_0-a)^2+y_0{}^2\}]\right] \quad (4.4.11)$$

While the Stream Function depends on the relative location of the point with respect to the element:

$$I = a\left[\tan^{-1}\left(\frac{y_0}{a-x_0}\right) + \tan^{-1}\left(\frac{y_0}{-a-x_0}\right)\right]$$

$$+x_0\left[\tan^{-1}\left(\frac{y_0}{-a-x_0}\right) + \tan^{-1}\left(\frac{y_0}{a-x_0}\right)\right] + \frac{y_0}{2}\ln\left[\frac{(a-x_0)^2+y_0{}^2}{(-a-x_0)^2+y_0{}^2}\right]$$

$$\begin{cases} x_0 > a, & y_0 > 0, & \Psi = I \\ -a < x_0, & y_0 > 0, & \Psi = I - 2\pi(a-x_0) \\ x_0 < -a, & y_0 > 0, & \Psi = I - 4a\pi \\ x_0 < -a, & y_0 < 0, & \Psi = I + 4a\pi \\ -a < x_0, & y_0 < 0, & \Psi = I - 2\pi(a-x_0) + 4a\pi \\ x_0 > a, & y_0 < 0, & \Psi = I \end{cases} \qquad (4.4.12)$$

In the above formulation, special care is required in the calculation of the arctangents, when the relative angle becomes 180 degrees.

The corresponding expressions for an eddy distribution are:

$$U_e = V_s, V_e = -U_s \quad (4.4.13a)$$

$$\Phi_e = -\Psi_s, \Psi_e = \Phi_s \quad (4.4.13b)$$

where the s indicator stands for a source and e for an eddy distribution.
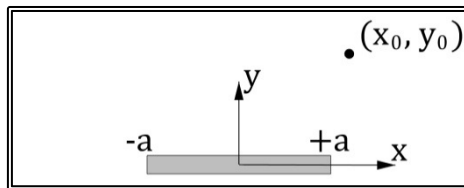
Figure 4.4.2 Definition of the reference coordinate system

The software that implements the above methodology requires as input the geometry of the four boundaries, each boundary described by the coordinates if a number of points, NI for S, N and NJ for E, W. As an example in figure 4.4.3, the input points for a C-type grid around a symmetrical hydrofoil are presented. Since the hydrofoil is symmetric, only one-half of the grid needs to be generated. The software then covers the four boundaries with a user-determined number of rectilinear elements and solves the potential flow problem for a given onset velocity and / or for a given number of external singularity points. In the example of figure 4.4.3, a single eddy is placed on point A.
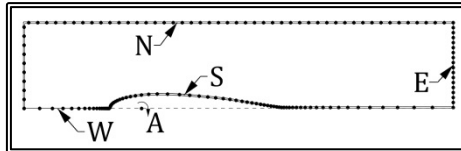
Figure 4.4.3 Input nodes for the calculation of a 2-D orthogonal curvilinear grid around a hydrofoil

Using as starting point the nodes on the S and W-edges, where the S-edge is considered the J=1 grid line and the W-edge the I=1 grid line, the software generates the grid as follows. First, given three grid nodes P(I,J), P(I+1,J) and P(I,J+1), the center point P′ of the P(I+1,J)-P(I,J+1) line segment is calculated (figure 4.4.4). The length of the P(I,J)-P′ line segment is doubled and P_0'' is calculated as the end point of the new line. The velocity vectors are then calculated at the mid points of the P(I+1,J)- P_0'' and P(I,J+1)- P_0'' lines.
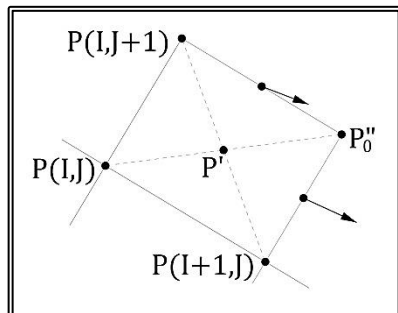
Figure 4.4.4 The procedure for calculating the grid nodes, first step
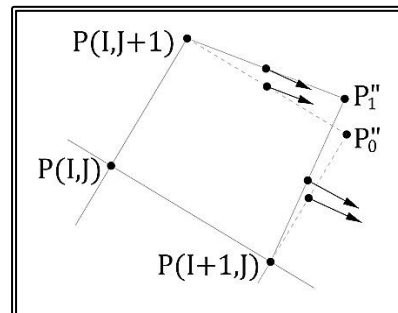
Figure 4.4.5 The procedure for calculating the grid nodes, second step
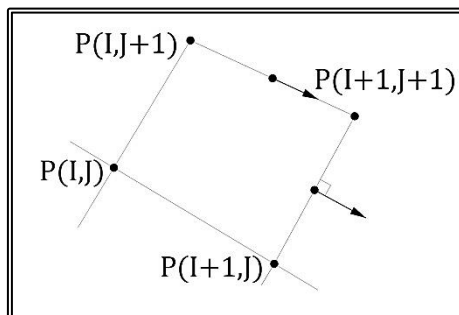
Figure 4.4.6 The procedure for calculating the grid nodes, final step

Then the line segments passing through P(I,J+1) and P(I+1,J), being parallel and normal to the respective velocity vectors are generated and the location of P_1'' is found as the intersection of the above lines (figure 4.4.5). The velocity vectors are then calculated at the mid points of the P(I+1,J)- P_1'' and P(I,J+1)- P_1'' lines.

The above procedure is repeated until the P(I+1,J)-P_n'' line is normal to the velocity vector at its midpoint and the P(I,J+1)-P_n'' line is parallel to the corresponding velocity vector. Then the location of the P(I+1,J+1) grid node is considered that of P_n''. Once the P(I+1,J+1) grid node is calculated, the procedure is repeated for the P(I+2,J+1) grid node and once all (J+1) nodes are calculated, the procedure is repeated for the J+2 nodes.

Following the above algorithm, the iso-I grid lines are always normal to the local velocity vectors while the iso-J grid lines are always parallel to the local velocity vectors, thus the resulting grid is orthogonal.

In figure 4.4.7, the 2-D C-type orthogonal curvilinear grid for a symmetrical hydrofoil is presented, where the input nodes where those of figure 4.4.4. Since the hydrofoil is symmetrical, half of the grid was generated by means of the above methodology and the final grid is generated by mirroring the top half.
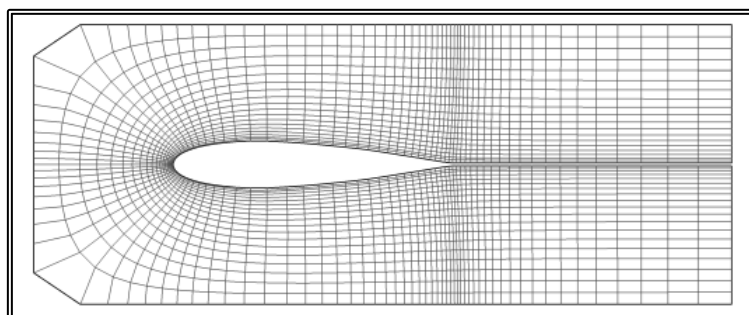
Figure 4.4.7 A 2-D orthogonal curvilinear grid around a hydrofoil

Since the input nodes on two of the boundaries are used as the respective grid nodes, the user can arrange the input nodes so that the grid becomes finer in areas of significant variations of flow. In the presented example the grid is finer along the I-direction, near the leading and trailing edges and also near the hydrofoil surface, along the J-direction. A detail of the grid, near the leading edge is presented in figure 4.4.8
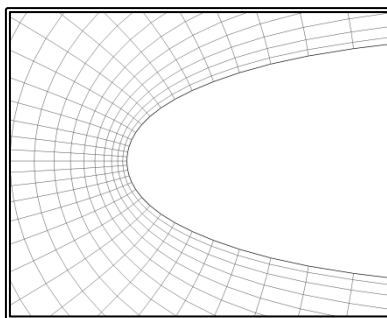
Figure 4.4.8 Detail of a 2-D orthogonal curvilinear grid around a hydrofoil, near the leading edge

4.5   Propeller Shaft Grid Block Generation

In the selected grid block arrangement, the propeller shaft is modeled by up to three cylindrical blocks. Specifically the first block covers the area from the shaft bossing and up to the foremost strut bossing, the second block covers the section abaft the foremost strut bossing and up to the second strut bossing and the third block covers the section abaft the second bossing, the propeller hub where applicable and the wake of the shaft. If only one strut bossing exists, then the second block is absent. In the case of an unsupported shaft, only one block is used.

Each shaft grid block comprises successive 2-D cylindrical planar grids (xy-planes, I, J-indexes), normal to the shaft axis (z-direction). The planar grids vary along the longitudinal direction (K-index) hence the 3-D grid is only partially orthogonal. The grid is actually constructed by first generating a Cartesian non-orthogonal planar K,J-grid on the vertical plane (I=1, zy-plane). Then the 3-D grid is generated by rotating the above parent grid by NI-1 angles, ranging for 0 to 360°, and by joining the nodes in the peripheral direction (x-direction, I-index) with circle arcs.

All shaft block share the same coordinate system where the z-axis is parallel to the shaft axis, x-axis is horizontal, i.e. parallel to the ship's base plane and y-axis completes the right-hand orthogonal system. The datum of the system coincides with the aft end of the shaft bossing.

In order to achieve the transfer of information with the neighboring grid block, the shaft block extends uprstream (K=1) and downstream (K=NK) onto the neighboring objects. The last block extends downstream into the shaft wake by some distance. The North boundary (J=NJ) is the external boundary while the South boundary (J=1) covers the shaft surface. The East boundary (I=NI) is vertical, while the West boundary (I=1) coincides with the I=NI-1 planar grid in order to apply the cylindrical conditions (paragraph 2.3.4). The radial extend of the block is defined by the user, as is also the upstream and downstream extend.

The method also takes into account discontinuities in the solid boundary, i.e. steps in the shaft and or bossing radius, by introducing additional grid lines that form a sub-block. Grid resolution is variable, both in the longitudinal and the radial direction to enhance accuracy. In the longitudinal direction, grid resolution is finer near discontinuities of diameter while in the radial direction grid is finer near the solid boundaries.

The generation of the parent grid begins by calculating the distribution of grid nodes along the shaft axis. The distribution is not uniform and near discontinuities of the diameter, the grid becomes finer. Then, four characteristic radii are calculated for each node. R0 follows the shape of the shaft, the shaft bossing and the strut bossing, R1 is the shaft diameter, R2 is the line formed by the struts' bossing and RN is the maximum radius. The maximum radius is user defined but may be smaller than that so that the block does not penetrate the hull surface (figure 4.5.1).
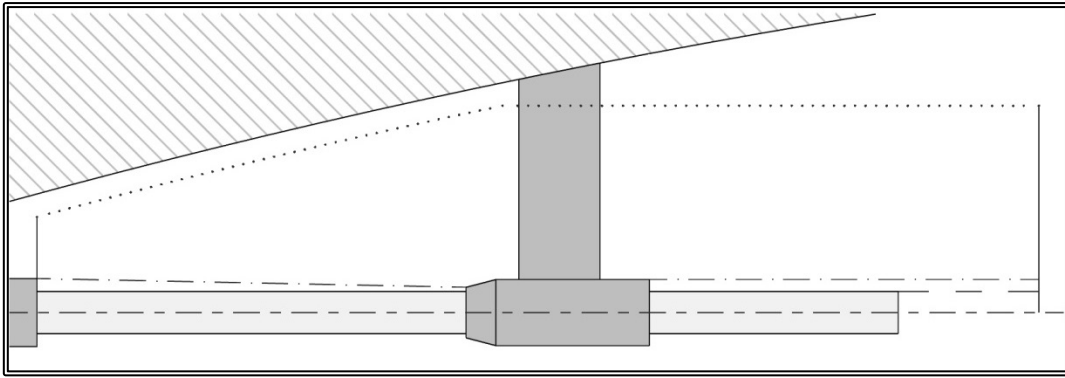
Figure 4.5.1. Characteristic radii, R0: continuous line, R1: dashed line, R2: dash-dot line, RN: dotted line.

The radial distribution is then calculated so that the grid is finer near solid boundaries. In the case were there are discontinuities in the diameter, extra grid points are added in the radial direction, between R0 and R3, to form a sub-grid. This sub grid runs the length of the main grid, has common indexing as the main grid and some of its cells remain inactive during the solution of the problem (figures 4.5.2, 4.5.3). In the peripheral direction, the distribution of nodes is uniform (figure 4.5.4).
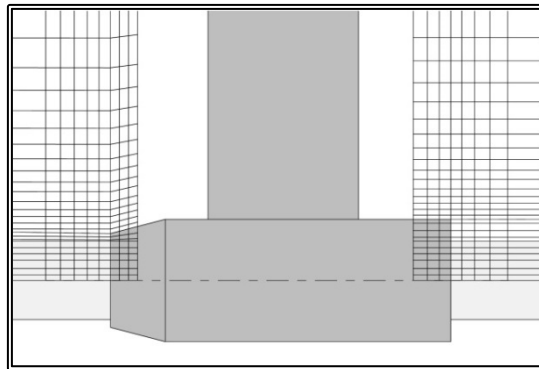
Figure 4.5.2. Detail of a 2-D grid featuring a sub-grid due to the discontinuities of the diameter.
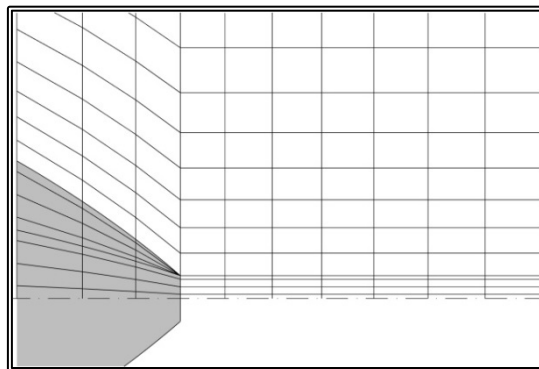
Figure 4.5.4. Detail of a 2-D grid near the end of a propeller hub with end cap, featuring a sub-grid due to the discontinuity of the diameter at the tip of the propeller hub end cap.
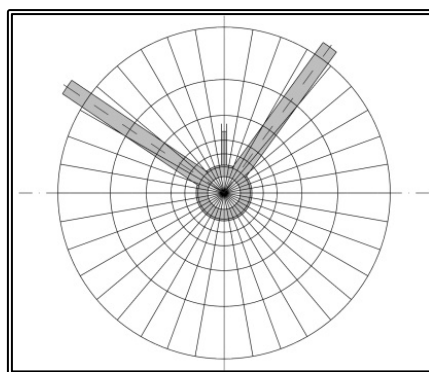
Figure 4.5.4. Distribution of the rotation angles, looking fwd.

The computational steps for the generation of a shaft grid block, are as follows:

1. Find block origin and orientation; calculate the translation vector and the rotation matrix with respect to the global (ship) coordinate system.
2. Transfer shaft geometry to the block coordinate system.
3. Read the number of grid K-nodes on the shaft section, fore of the shaft and aft of the shaft section.
4. If the grid block is the third block, read the number of K-nodes abaft the shaft, in the wake.
5. Read the number of J-nodes as well as the number of J-nodes for the sub-grid, were applicable.
6. Read the number of I-nodes.
7. Calculate the longitudinal distribution on the fore and aft section, i.e. on the bossing. The nodes fore and aft of the shaft section are distributed in such a way that the planes of the 2-D I,J-grids coincide with the planes of the respective grid block. For example, the distribution on the shaft bossing, fore section of shaft block 1, is the same as the distribution of the shaft bossing grid block. This is done to facilitate the transfer of information amongst the grid blocks.
8. Calculate the longitudinal distribution on the shaft section. The distribution is finer near the two ends of the section and in between the node spacing varies exponentially. The number of nodes and the node spacing at both ends of the grid is defined by the user.
9. If the grid block is the third block, calculate the longitudinal distribution on the wake. The number of nodes, as well as the spacing of the first two nodes are defined by the user. The software then calculates the node distribution so that the nod spacing varies exponentially.
10. Calculate at the location of each K-node the minimum radius$R0$ that conforms to the shaft and the fore and aft sections.
11. In the case of discontinuities in $R0$, calculate the intermediate radii $R1$, $R2$.
12. Calculate RN. The maximum radius is defined by the user but is reduced automatically, to avoid penetration of the hull by the block. A minimum distance is defined by the user and the software adjusts RN so that the minimum distance between the shaft block and the hull is always maintained.
13. Calculate the radial distribution of nodes. On each one of the $R0$-$R1$, $R1$-$R2$ and $R2$-RN sections, the radial distribution is variable. The user defines the number of nodes and the grid spacing in the solid boundary and the software adjusts the radial distribution so that node spacing varies exponentially.
14. Generate the 2-D J,K-parent grid.

15. Calculate the peripheral distribution. In the I-direction the nodes are uniformly distributed.
16. Generate the 3-D grid.

In figures 4.5.5-4.5.15, examples of 2-D J-K-grids are presented for various shaft arrangements. In figure 4.5.16 an example of a 3-D grid block around the fore part of the shaft is presented, while in figure 4.5.17 an example of a 3-D grid block around the aft part of the shaft and the shaft wake is presented
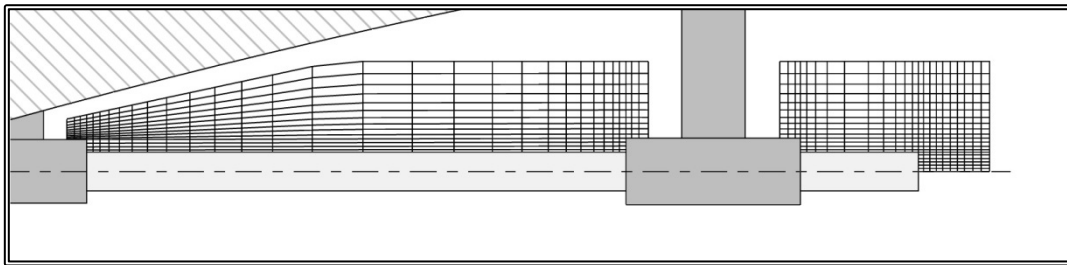
Figure 4.5.5. 2-D grid about a shaft with Type-A shaft bossing, one Type-A strut bossing, no propeller hub.
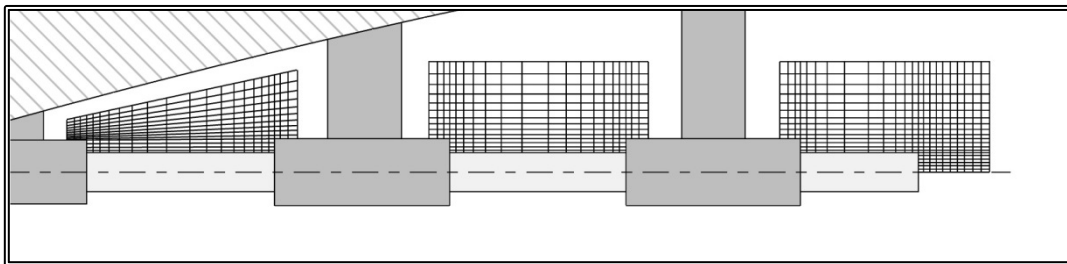
Figure 4.5.6. 2-D grid about a shaft with Type-A shaft bossing, two Type-A strut bossings, no propeller hub.
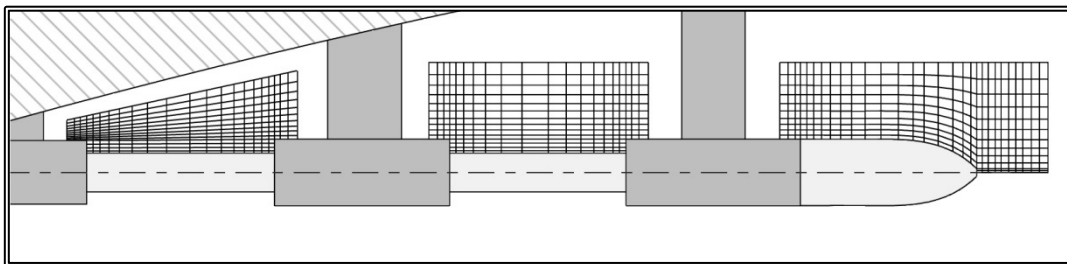
Figure 4.5.7. 2-D grid about a shaft with Type-A shaft bossing, two Type-A strut bossings and a propeller hub and hub cap.
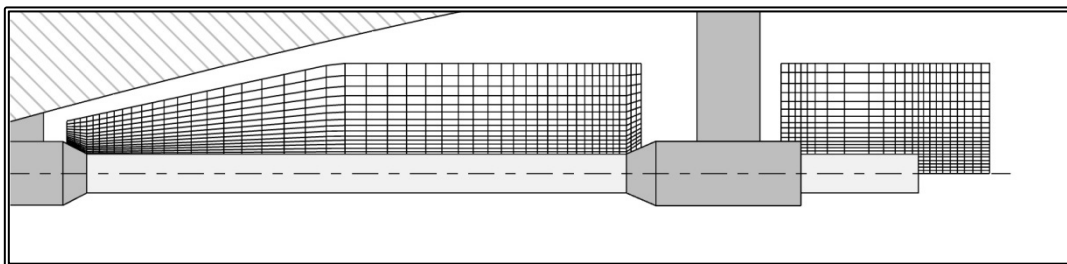
Figure 4.5.8. 2-D grid about a shaft with Type-B shaft bossing, one Type-B strut bossing, no propeller hub.
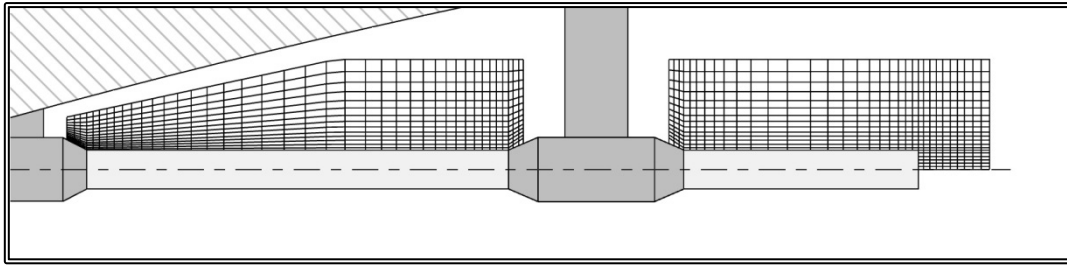
Figure 4.5.9. 2-D grid about a shaft with Type-B shaft bossing, one Type-C strut bossing, no propeller hub.
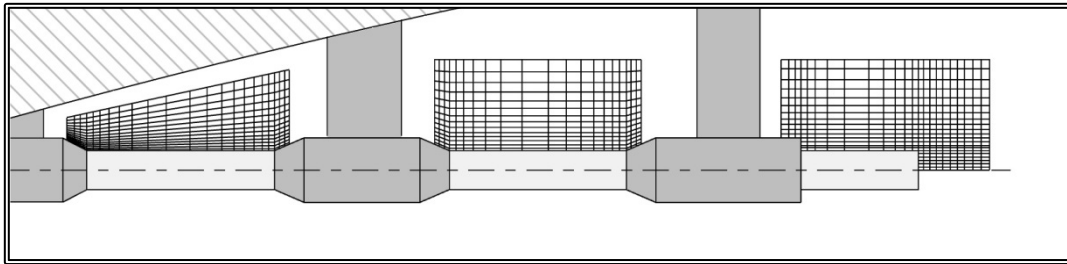
Figure 4.5.10. 2-D grid about a shaft with Type-B shaft bossing, two strut bossings (Type-B and Type-C), no propeller hub.
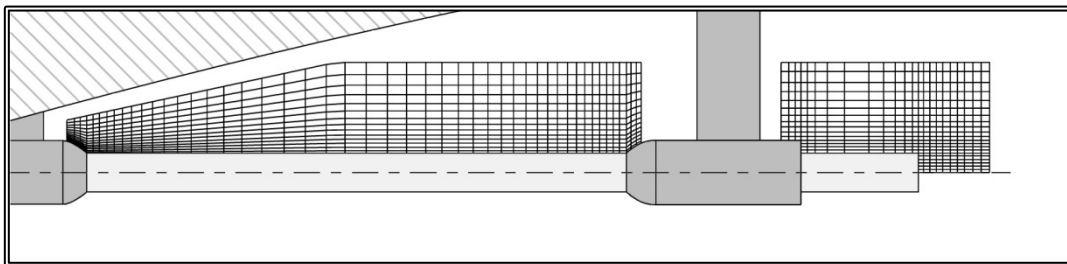
Figure 4.5.11. 2-D grid about a shaft with Type-C shaft bossing, one Type-C strut bossing, no propeller hub.
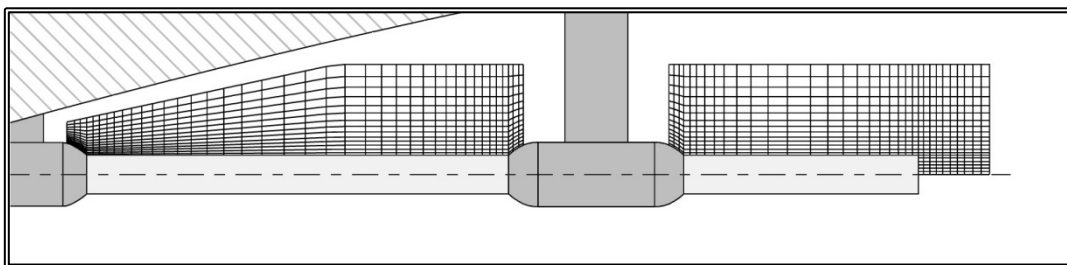
Figure 4.5.12. 2-D grid about a shaft with Type-C shaft bossing, one Type-D strut bossing, no propeller hub.
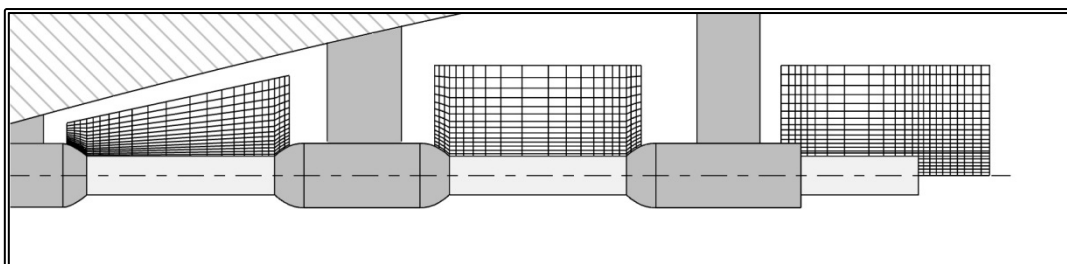
Figure 4.5.14. 2-D grid about a shaft with Type-C shaft bossing, two strut bossings (Type-C and Type-D), no propeller hub.
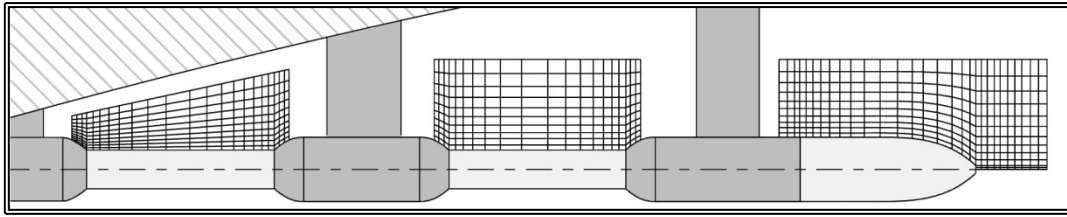
Figure 4.5.14. 2-D grid about a shaft with Type-C shaft bossing, two strut bossings (Type-C and Type-D) and a propeller hub and hub cap.
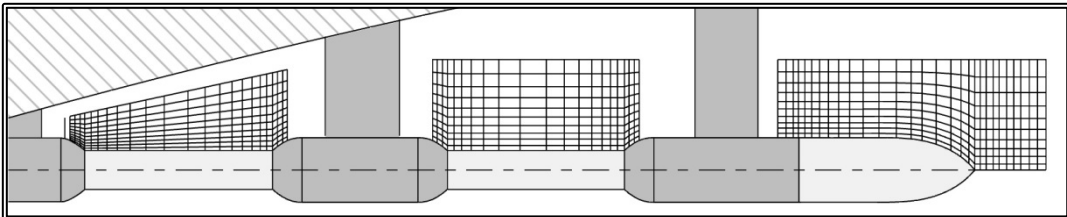
Figure 4.5.15. 2-D grid about a shaft with Type-C shaft bossing, two strut bossings (Type-C and Type-D) and a propeller hub and hub cap ending at a point.
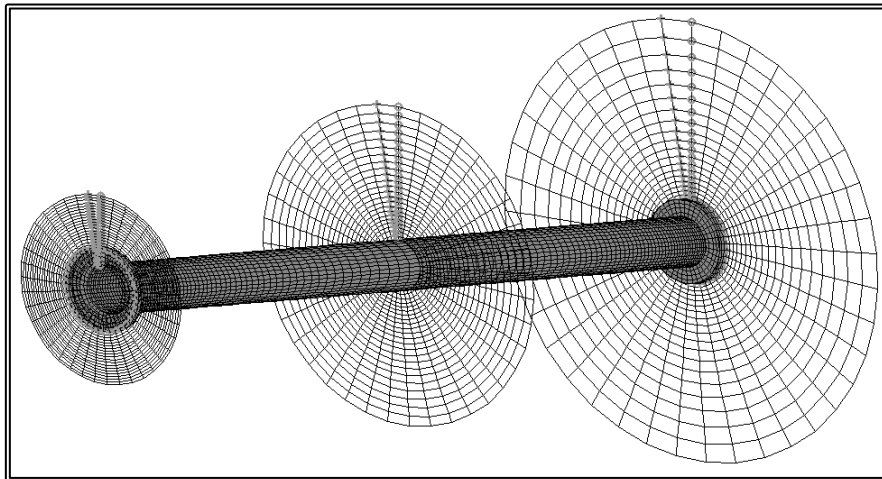
Figure 4.5.16. 3-D grid (NIxNJxNK=41x24x120) about the fore part of a shaft, for clarity only the grid nodes on the solid surface, plus three 2-D cylindrical grids at the upstream end, the downstream end and at the middle.
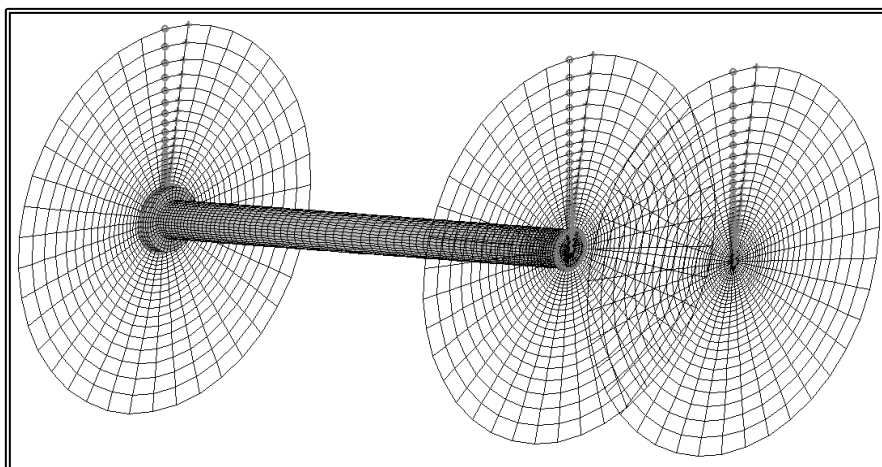
Figure 4.5.17. 3-D grid (NIxNJxNK=41x28x120) about the aft part of a shaft, for clarity only the grid nodes on the solid surface, plus three 2-D cylindrical grids at the upstream end, the downstream end and at the end of the shaft.

4.6   Propeller Shaft Bossing Grid Block Generation

The propeller shaft bossing is model by a single grid block comprising 2-D curvilinear orthogonal C-type grids, normal to the shaft axis. Each orthogonal curvilinear grid is generated by employing the singularity distribution method presented in paragraph 4.4. Since both the hull and the bossing geometry vary along the shaft axis, the 2-D grids differ and the resulting 3-D grid is partially orthogonal.

The system of coordinates for the shaft bossing grid block is the same as for the shaft grid block, i.e. the z-axis is parallel to the shaft axis, x-axis is horizontal, i.e. parallel to the ship's base plane while y-axis completes the right-hand orthogonal system. The datum of the system coincides with the aft end of the shaft bossing.

The grid block extends upstream (K=1) the point where the shaft bossing emerges from the hull in order for the conditions from the ship block to be applied as boundary conditions. The location of the downstream end of the grid (K=NK) is at the end of the shaft bossing. In order to exchange the conditions with the shaft block, the latter extends upstream onto the shaft bossing. The West (I=1) and East (I=NI) boundaries lay on the hull and as a result they are treated as solid boundaries. The North boundary (J=NJ) is the external boundary while the South boundary (J=1) covers the bossing surface and the symmetry plane. The radial extend of the block is defined by the user, as is also the upstream extend.

In order to generate the shaft bossing grid, the distribution of 2-D planar grids along the shaft axis is calculated. The distribution is not uniform and near discontinuities such as the bossing end and the strut end, the grid becomes finer (figure 4.6.1a).

Due to the complex geometry of the computational domain, the grid is considered to comprise of 3 parts Part-A extends from the upstream boundary, up to the point where the shaft bossing emerges from the hull. Part-B continues until the point where the strut has emerged fully. The last part, part-C, covers the remaining portion of the bossing (figure 4.6.1a).
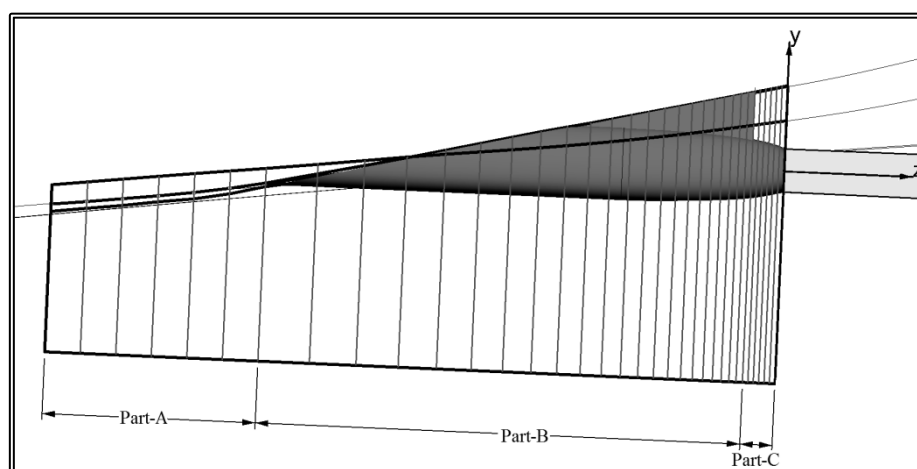
Figure 4.6.1a. Distribution of 2-D planar grids along the length of the shaft bossing, grid block
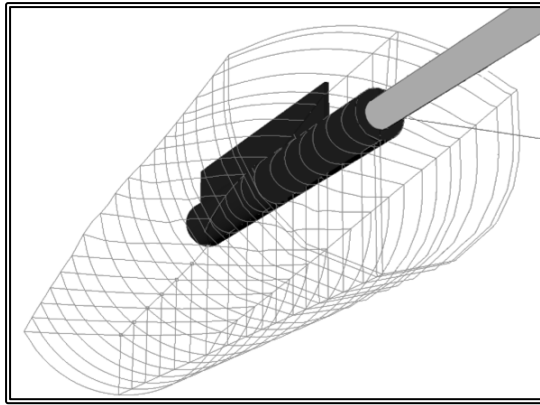
Figure 4.6.1b. Distribution of 2-D planar grids along the length of the shaft bossing
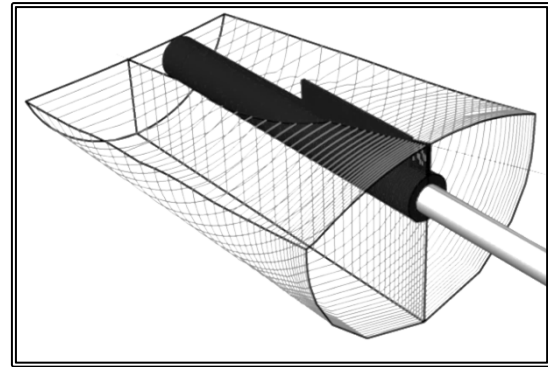
Figure 4.6.1c. Distribution of 2-D planar grids along the length of the shaft bossing

On part-A the South boundary (J=1) is a single point while the North boundary (J=NJ) is a circular arc (figure 4.6.2). On part-B, the South boundary lays on the portion of the bossing that has emerged from the hull and where applicable, the reinforcing strut. The North boundary, depending on the shape of the hull, is a circular arc or a semi-circle plus two vertical line segments (figures 4.6.3 and 4.6.4). On part-C, the South boundary lays on the bossing surface and on the symmetry plane. The North boundary comprises a semi-circle and two line segments (figure 4.6.5). On all parts, the East (I=NI) and West (I=1) boundaries conform to the hull surface.
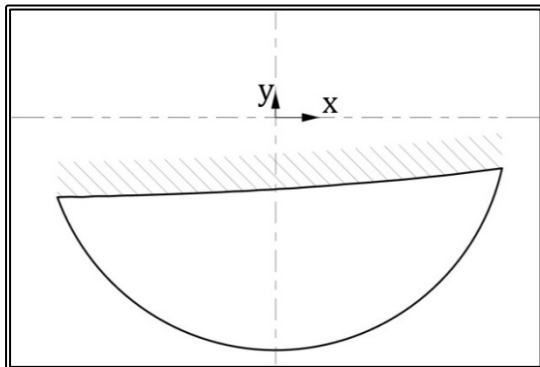
Figure 4.6.2. The boundaries of a2-D grid on part-A.
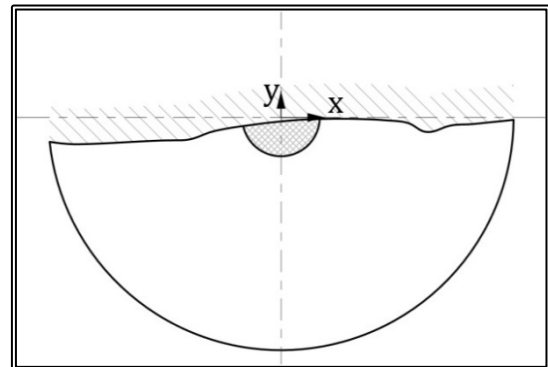
Figure 4.6.4. The boundaries of a 2-D grid on part-B, where the bossing has partially emerged from the hull.
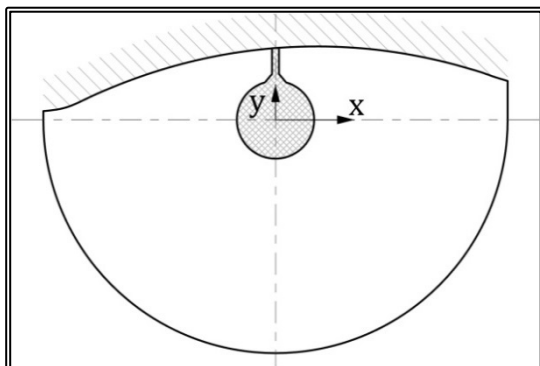
Figure 4.6.4. The boundaries of a 2-D grid on part-B, where the bossing has emerged fully from the hull and there is a reinforcing strut of non-zero thickness.
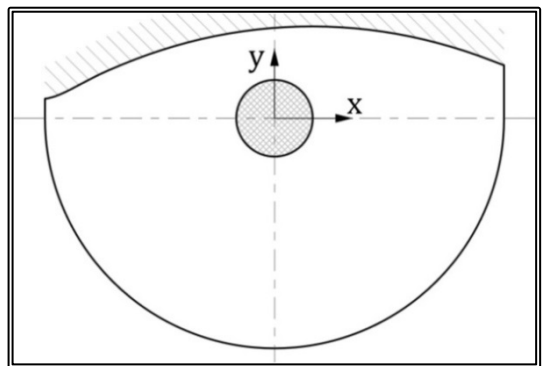
Figure 4.6.5. The boundaries of a 2-D grid on part-C.

Then a 2-D orthogonal curvilinear grid is generated on each plane (xy-plane, I, J-indexes), about the shaft bossing. This orthogonal curvilinear grid is generated by employing the singularity method for the given boundaries (Tzabiras, 1986), where one set of grid lines, the equi-I lines, is calculated as streamlines while the other set, equi-J lines, consists of equi-potential lines (figures 4.6.6-4.6.9). The generation of the 2-D grids will be discussed in further detail, in paragraph 4.6.1.
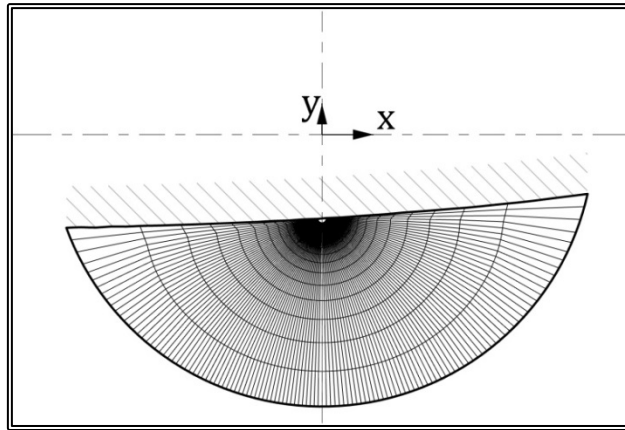
Figure 4.6.6. 2-D grid (NIxNJ=121x20) about a shaft bossing, part-A.
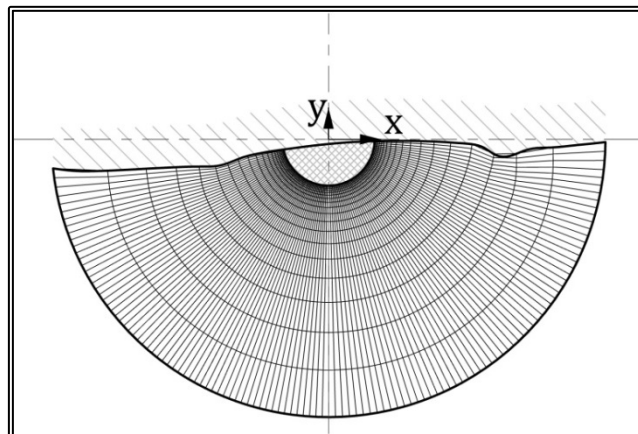
Figure 4.6.7. 2-D grid (NIxNJ=121x20) about a shaft bossing, part- B, where the bossing has partially emerged from the hull.
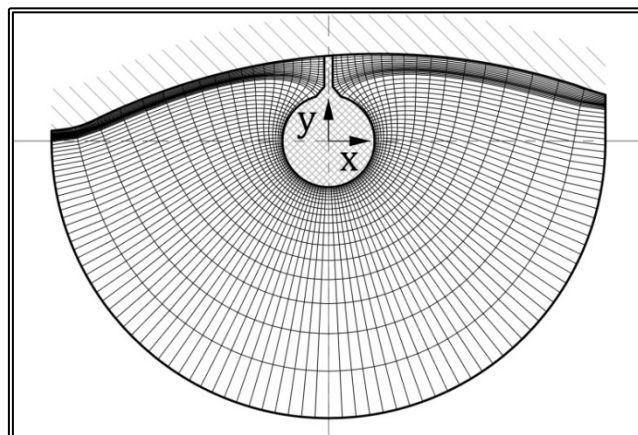
Figure 4.6.8. 2-D grid (NIxNJ=121x20) about a shaft bossing, part- B, where the bossing has emerged fully from the hull and there is a reinforcing strut of non-zero thickness.
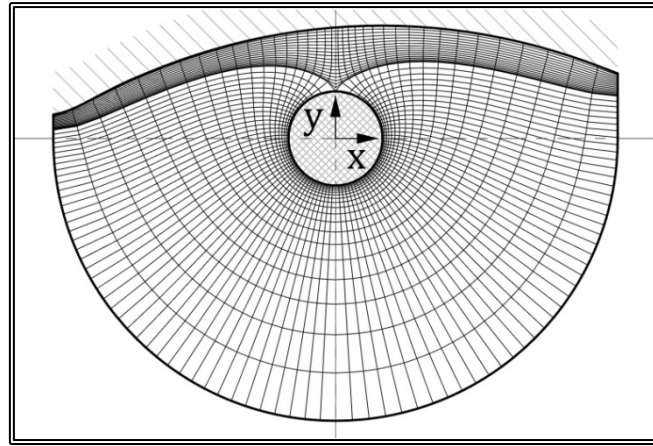
Figure 4.6.9. 2-D grid (NIxNJ=121x20) about a shaft bossing, part-C.

In the case of a shaft bossing supported by a strut whose end is not faired, rather ends with a non-zero thickness, this geometrical discontinuity needs to be addressed. In order for this discontinuity to be modeled, extra grid nodes (extra equi-J lines) are added to form a sub-grid (figure 4.6.10). This sub grid runs the length of the block, has common indexing as the main grid and some of its sells remain inactive during the solution of the problem.
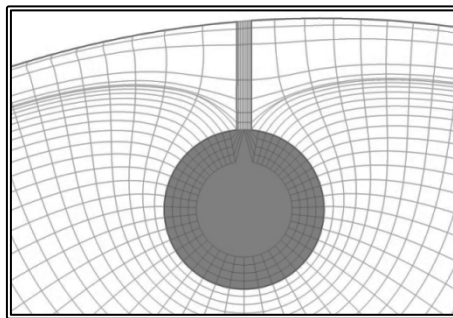
Figure 4.6.10. 2-D inner grid for strut thickness discontinuity. The shaded portion

In the longitudinal direction (z-direction, K-index), the nodes of subsequent 2-D grids are joined to form the partially orthogonal 3-D grid (figure 4.6.11).
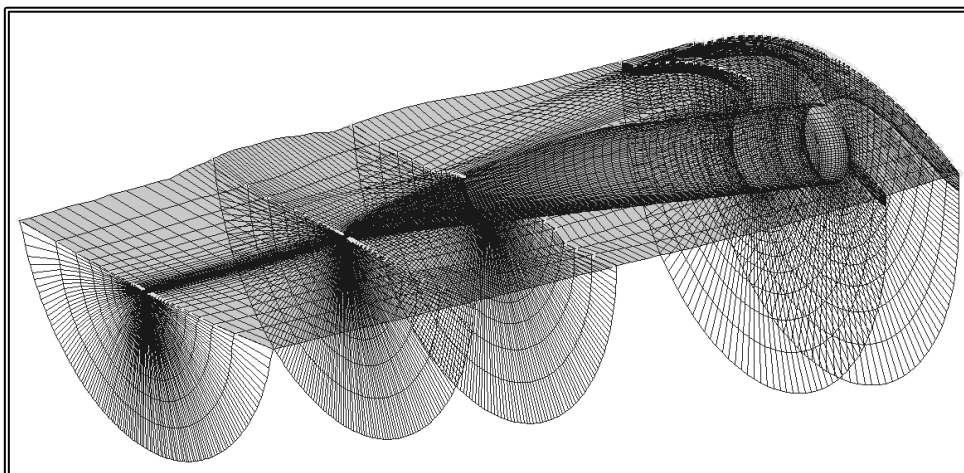
Figure 4.6.11. 3-D grid (NIxNJxNK=121x20x120) about a shaft bossing, for clarity only the grid nodes on the solid boundaries (South, East, West) plus the 2-D grids on the end of each part are presented and a further 2-D grids inside part-B.

The computational steps for the generation of a shaft bossing grid block, are as follows:

1. Find block origin and orientation; calculate the translation vector and the rotation matrix with respect to the global (ship) coordinate system.
2. Read the number of grid K-nodes on the bossing and the upstream part-A.
3. Read the number of J-nodes as well as the number of J-nodes for the sub-grid, were applicable.
4. Read the number of I-nodes.
5. Read the block radius.
6. Calculate the longitudinal distribution on the upstream part-A.
7. Calculate the longitudinal distribution on the bossing, parts B and C. The distribution is finer near the ends of the parts and in between the node spacing varies exponentially. The number of nodes and the node spacing at the ends of both parts is defined by the user.
8. Generate the 2-D I,J outer grids.
9. Generate the 2-D I,J inner grids, where applicable.
10. Generate the 3-D grid.

4.6.1   2-D Propeller Shaft Bossing Grid Generation

The shaft bossing grid comprises 2-D curvilinear orthogonal C-type grids, normal to the shaft axis. The 2-D grids are generated by employing the method presented in paragraph 4.4. This method uses singularity distributions on the boundaries to solve the potential flow problem. Then the grid nodes are calculated as the intersection points of stream and equi-potential lines. The method requires the node distribution on four edges that form the calculations domain. The nodes on the South and East edges are also the J=1 and I=NI nodes of the grid.

Two important characteristics of the method are that the edges must be arranged in a count-clockwise direction and that the edges cannot fold. Those two characteristic necessitate the subdivision of each 2-D grid into two sub-grids, the right-hand and the left-hand, where the mirror image of the left hand-side sub-grid has to be calculated (figure 4.6.12).
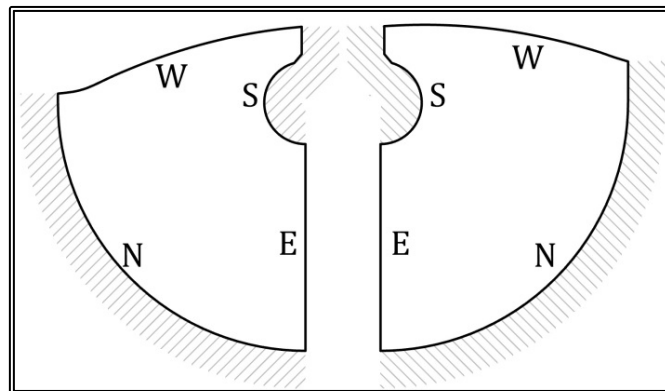
Figure 4.6.12. Definition of the right-hand and the left-hand domains. The North and South edges are treated as solid boundaries, while the East and West edges are treated as equi-potential lines.

In order to define the four edges for each sub grid, the locations of 12 characteristic points are calculated (figure 4.6.13). Then, the distribution on the South and East edges is calculated. The distribution is finer near the solid boundaries and the geometrical discontinuities. The distribution on the East edge of both sub-domains is obviously the same, so that the resulting grids have that particular line common. The distribution on the other two edges is uniform (figure 4.6.14)
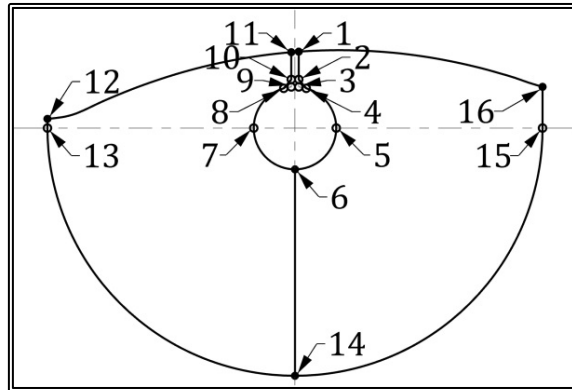
Figure 4.6.14. Definition of the characteristic points.
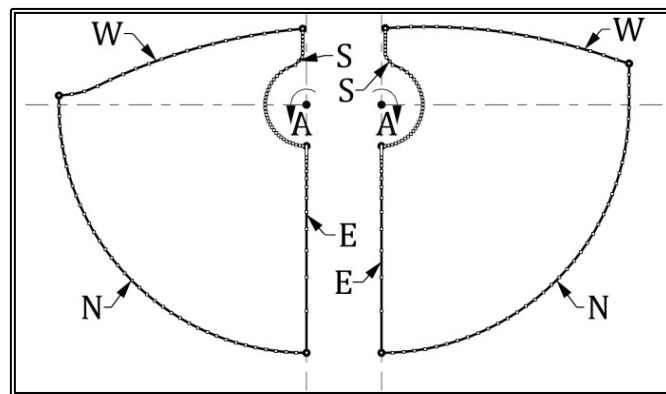
Figure 4.6.14. Distribution of nodes on the four edges.

Then, by introducing an eddy at x=0, y=0, the potential flow problem is solved cording to paragraph 4.4 and the two sub-grids are generated (figure 4.6.15). Then the left-hand grid is mirrored and the final grid is generated by merging the two sub-grids.
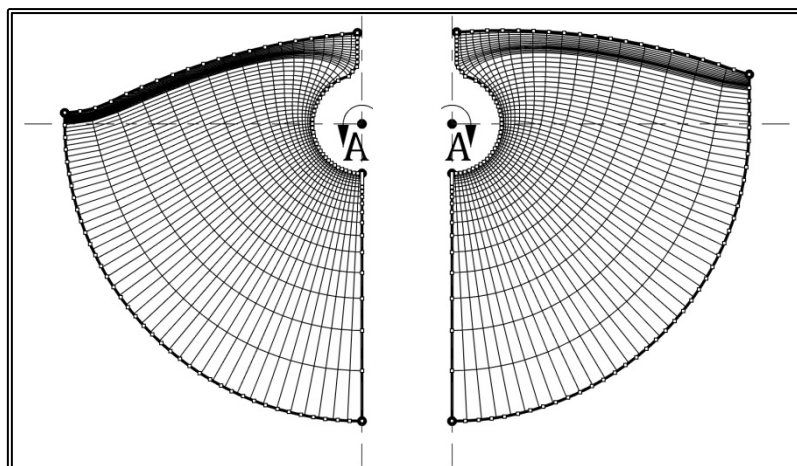
Figure 4.6.15. The two halves of the 2-D grid.

The computational steps for the generation of a 2-D bossing outer grid are as follows:

1. Calculate the bossing radius at the location of the section.
2. Calculate the strut thickness
3. Calculate the initial locations of the characteristic points.
4. Correct the location of the characteristic points, taking into account the hull geometry.
5. Split the domain into the left-hand and right-hand sub-domains
6. Calculate the number if I-nodes on the strut.
7. Calculate the distribution of nodes on the four edges of the right-hand sub-domain.
8. Generate the right-hand sub-grid
9. Mirror the left-hand sub-domain.
10. Calculate the distribution of nodes on the four edges of the mirrored left-hand sub-domain.
11. Generate the mirrored left-hand sub-grid
12. Mirror the generated grid into the left-hand sub-grid.
13. Merge grids
14. Generate the inner grid.

4.7   Strut Bossing Grid Block Generation

The bossing of each shaft bracket is modeled by an O-type grid block, comprising 2-D curvilinear orthogonal O-type grids. Each orthogonal curvilinear grid is generated by employing the singularity distribution method presented in paragraph 4.4. Since the bossing profile and the strut thickness vary along the shaft axis, the 2-D grids differ and the resulting 3-D grid is partially orthogonal. The grid also has to conform to the strut geometry and as a result, the sections are not planar. Nevertheless when projected on a plane normal to the shaft axis, each grid becomes orthogonal curvilinear.

The bossing grid block is divided into three parts along its length. The first part, part-A, extends from foremost end of the bossing up to the strut leading edge. Part-B covers the chord of the strut, while part–C extends from the strut trailing edge up to the aft end of the bossing.

The block has its own coordinate system with the z-axis coinciding with the shaft axis and with a aft direction, y-axis is normal to the shaft axis pointing upwards and finally the x-axis is horizontal and completes the right-hand orthogonal system. The datum of the system is located at the intersection of strut reference lines with the shaft axis. The bossing block coordinate system is presented in figure 4.7.1.

The upstream (K=1) boundary of the block is normal to the shaft axis, is located at the foremost end of the bossing and is treated as an inflow boundary. The downstream (K=NK) boundary is normal to the shaft axis, is located at the aftmost end of the bossing and is treated as an outflow boundary. The South boundary (J=1) lays on the bossing surface and is treated as a solid boundary. The North boundary (J=NJ) is the external boundary with its location defined by the user. Finally the East boundary (I=NI) lays on the vertical plane facing downwards, while the West boundary (I=1) coincides with the I=NI-1 grid section in order to apply the cylindrical conditions (paragraph 2.3.4).
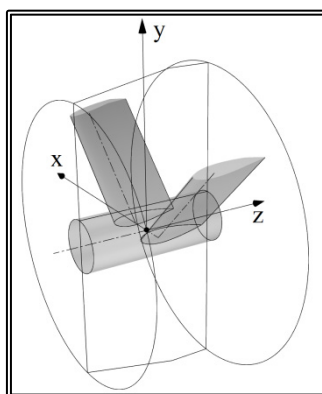
Figure 4.7.1. Definition of the strut bossing grid block coordinate system.

The distribution of 2-D sections along the z-axis (K-index) is not uniform; the grid is finer near the strut leading and trailing edges. The distribution of nodes on each section is also variable. In the radial direction (J-index), grid resolution is finer near the bossing surface (J=1), while in the peripheral direction (I-index), grid resolution,

with respect to the arc length of the section, is finer near the strut surfaces. In all directions, the number of grid nodes and the grid resolution for the first two nodes is defined by the user. Then the software arranges the nodes so that the node spacing follows an exponential distribution. In the K-direction, the grid resolution is defined by the user at both the leading and trailing edges.

The generation of a 3-D grid around a strut bossing, that can account for various struts and bossing geometries is a complex task. If the 3-D grid has to be, at least partially, orthogonal curvilinear, then the task becomes even more complex. In the presented method, the 3-D grid comprises non-planar 2-D orthogonal curvilinear grids. Each 2-D grid comprises at least two and up to six 2-D sub-grids, the domains for each sub-grid are presented in figures 4.7.2-4.7.5. Sub-grids A1, A6 are always present. Sub-grids A3, A4 are present in the case of a V-type bracket, i.e. a bracket with two struts. Sub-grid A2 is present in the case of a single strut with a non-zero trailing edge thickness, while sub-grids A2 and A5 are present in the case of two struts with a non-zero trailing edge thickness. Upstream the strut leading edge, Sub-grids A2 and A5 are reduced in a single J-line each.
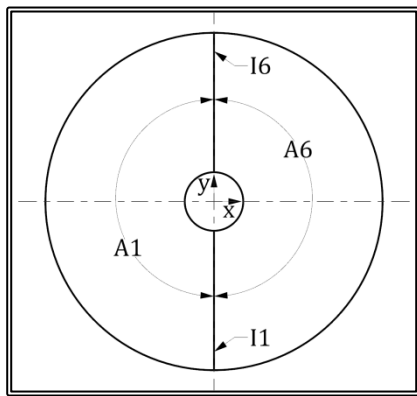
Figure 4.7.2. Sections A1, A6, in the case if and I- type bracket with zero trailing edge thickness.
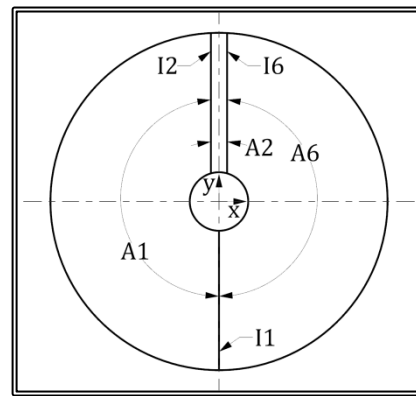
Figure 4.7.4. Sections A1, A2, A6, in the case if and I- type bracket with non-zero trailing edge thickness.
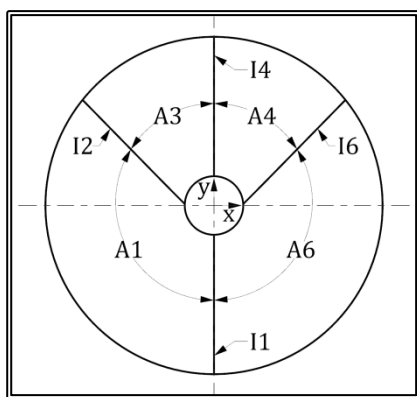
Figure 4.7.4. Sections A1, A3, A4, A6, in the case if and V- type bracket with zero trailing edge thickness.
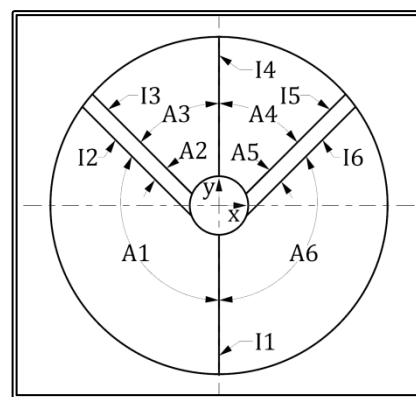
Figure 4.7.5. Sections A1, A2, A3, A4, A5, A6, in the case if and V- type bracket with non-zero trailing edge thickness.

Each of the A1, A3, A4, A6 sub-grids is generated by employing the singularity distribution method presented in paragraph 4.4 requiring the definition of four edges. Of the four edges of each sub-grid, one lays on the bossing and another lays on the

grid block North boundary. Of the other two edges, one lays on the strut surface and the other is vertical. Consequently, in order to calculate the sub-grids of each 2-D section, six J,K-grids plus two I,K-grids are required.

In order to calculate the J,K-grids, the radial distribution of nodes is first calculated. Then, the equi-J lines are drawn on the planes of the six sections. The distribution of nodes along the chord of the struts, as well as upstream the leading edges and downstream the trailing edge, are calculated and the equi-K lines are drawn (figure 4.7.6). Having the nodes of the J=1 and J=NJ lines for each of the six J,K-grids, the nodes of the J=1 (south) and J=NJ (north) I,K-grids can be calculated by means of linear interpolation in cylindrical coordinates (figures 4.7.7 and 4.7.8). Finally the 2-D orthogonal curvilinear grid is generated on each I, J-section by employing the singularity method for the given boundaries (Tzabiras, 1986) (figures 4.7.9 to 4.7.11). The A2 and A5 sub-grids are non-orthogonal, generated by means of linear interpolations in cylindrical coordinates. The generation of the 2-D grids will be discussed in further detail, in paragraph 4.7.1.
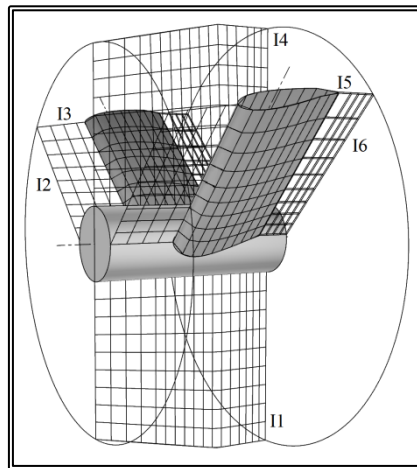
Figure 4.7.6. I=I1, I=I2, I=I3, I=I4, I=I5 and I=I6, J,K-grids (NJxNK=10x18) for a V-type bracket with zero trailing edge thickness.
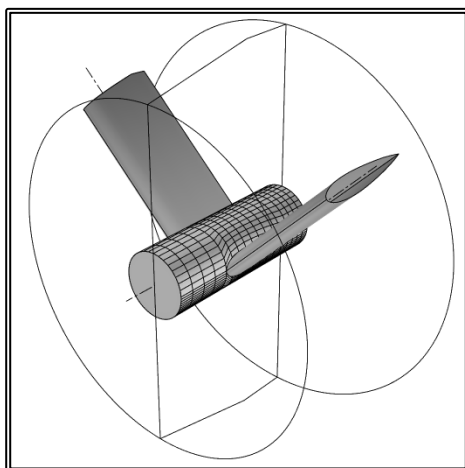
Figure 4.7.7. J=1, I,K-grid (NIxNK=62x18) for a V-type bracket with zero trailing edge thickness.
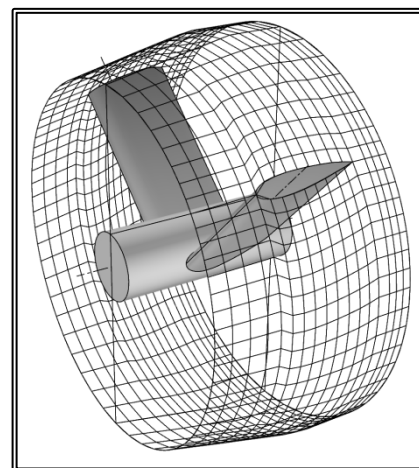
Figure 4.7.8. J=NJ, I,K-grid (NIxNK=62x18) for a V- type bracket with zero trailing edge thickness.
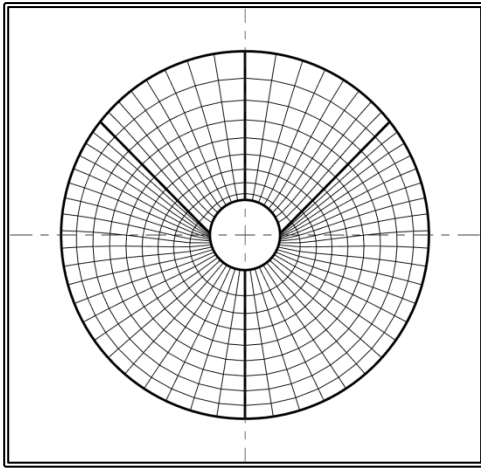
Figure 4.7.9. 2-D grid (NIxNJ=62x10) about a V- type bracket bossing, upstream the strut leading edge.
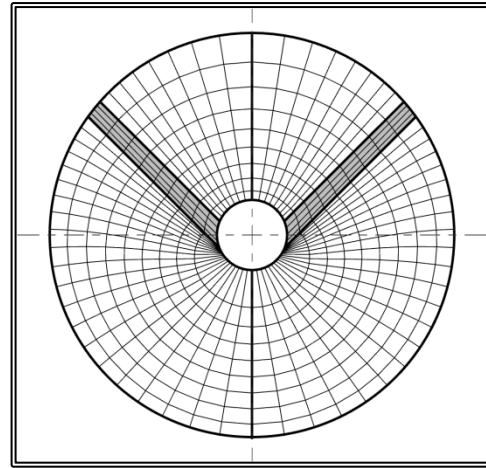
Figure 4.7.10. 2-D grid (NIxNJ=62x10) about a V- type bracket bossing, at the location of the strut maximum thickness, the shaded portion of the grid remains inactive along the chord of the strut.
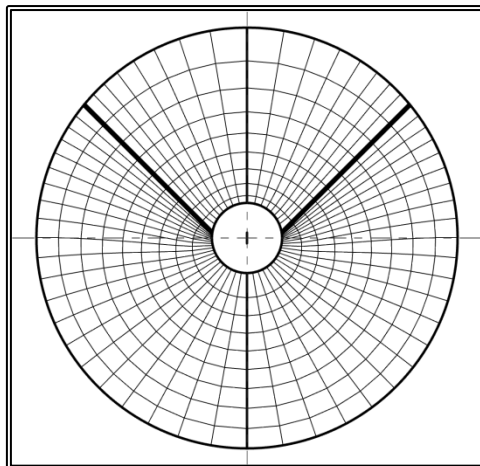
Figure 4.7.11. 2-D grid (NIxNJ=62x10) about a V- type bracket bossing, downstream the strut trailing edge.

In the longitudinal direction (z-direction, K-index), the homologue grid nodes of subsequent planes are joined to form the partially orthogonal 3-D grid (figure 4.7.12).

The computational steps for the generation of a strut bossing grid block, are as follows:

1. Find block orientation.
2. Find block origin; calculate the translation vector and the rotation matrix with respect to the global (ship) coordinate system.
3. Calculate the strut(s) angles of reference
4. Read the block dimensions.
5. Read the number of grid K-nodes, calculate the section distribution.
6. Read the number of J-nodes.
7. Read the number of I-nodes as well as the number of I-nodes for the sub-grids, were applicable.

8. Generate the 2-D J,K grids on the strut(s) planes, the vertical plane ($\varphi=0^o$) and the inverted plane ($\varphi=180^o$).
9. Generate the 2-D I,K South (J=1) and North (J=NJ) grids.
10. Generate the 2-D planar I,J grids.
11. Project the 2-D planar I,J grids.
12. Generate the 3-D grid.
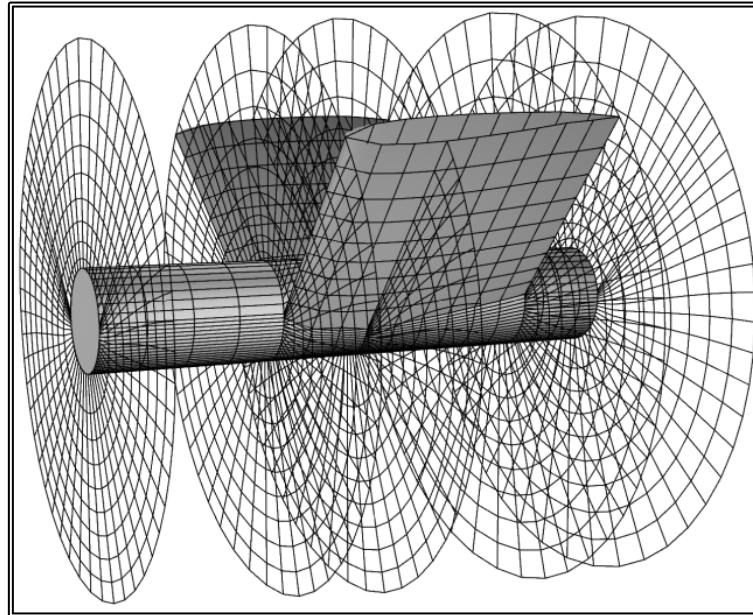
Figure 4.7.12. 3-D grid (NIxNJxNK=62x10x18) about a V- type bracket bossing, for clarity the grid nodes on the solid boundaries are presented along with the 2-D grids at the block upstream boundary, the strut leading edge, the strut trailing edge, the block downstream boundary and near the maximum strut thickness. Also for clarity, the grid is scaled along z-axis by a factor of two.

4.7.1   2-D Strut Bossing Grid Generation

The strut bossing grid comprises 2-D O-type grids. Each 2-D grid comprises up to six sub-grid, of which four are curvilinear orthogonal, generated by means of the method presented in paragraph 4.4. This method uses singularity distributions on the boundaries to solve the potential flow problem. Then the grid nodes are calculated as the intersection points of stream and equi-potential lines. The method requires the node distribution on four edges that form the calculations domain. The nodes on the South and West edges are also the J=1 and I=1 nodes of the grid. Since the rudder is symmetrical, only one-half of the grid has to be calculated.

The distribution on the South and West edges is calculated. The distribution is finer near the bossing and the strut surface. The distribution on the other two edges is uniform (figure 4.7.14).
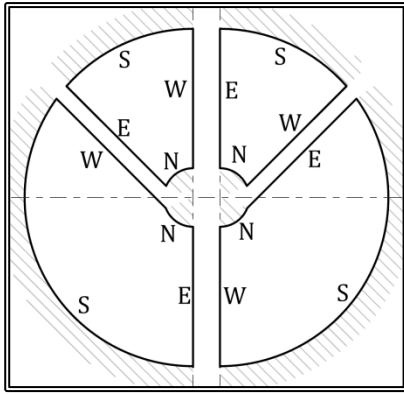
Figure 4.7.14. Definition of the computational domains. The North and South edges are treated as solid boundaries, while the East and West edges are treated as equi-potential lines.
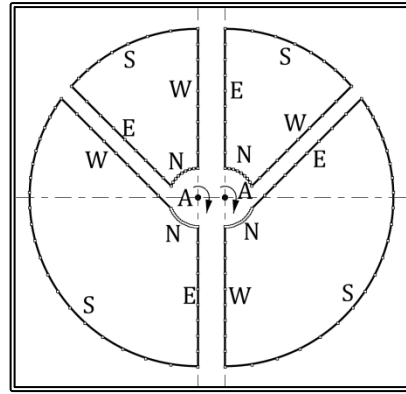
Figure 4.7.14. Distribution of nodes on the four edges of each sub-grid.

Then, by introducing an eddy at x=0, y=0, the potential flow problem is solved according to the method of paragraph 4.4 and the sub-grids are generated (figure 4.7.15). Then the sub grids are merged, to form the 2-D grid.
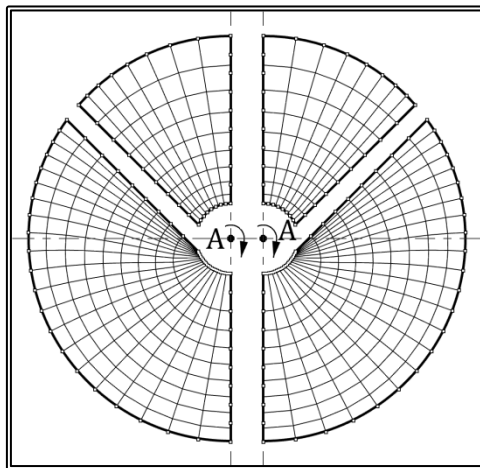
Figure 4.7.15. The 2-D sub-grids.

The computational steps for the generation of a 2-D rudder outer grid are as follows:

1. Calculate distribution on the edges.
2. Generate the 2-D sub-grids.
3. Interpolate the grid nodes on lines I=I2 and I=I5.
4. Project the sub-grids
5. Merge the sub-grids into the final 2-D grid.

4.8   Strut Grid Block Generation

Each shaft bracket is modeled by up to two grid blocks, depending on its type. An I-type bracket, i.e. a bracket with a single strut is modeled through one block while a V-type bracket, i.e. a bracket with a pair of struts, is modeled using two blocks, one for each strut. The strut blocks comprise 2-D curvilinear orthogonal C-type grids, normal to the strut reference line. Each orthogonal curvilinear grid is generated by employing the singularity distribution method presented in paragraph 4.4. Since the hydrofoil section, the chord and the twist may vary along the reference line, the 2-D grids differ and the resulting 3-D grid is partially orthogonal. Also near the hull, the grid conforms to the hull surface and as a result, the sections are not planar.

The coordinate system is different for each block: the z-axis lays on the same plane as the strut reference line and is perpendicular to the ship's longitudinal axis. The z-axis direction is downwards. The x-axis is parallel to a characteristic chord towards the trailing edge. Finally the y-axis completes the right-hand orthogonal system. The datum of the system is at the intersection of the strut reference line with the hull surface. The strut block coordinate system is presented in figure 4.8.1.
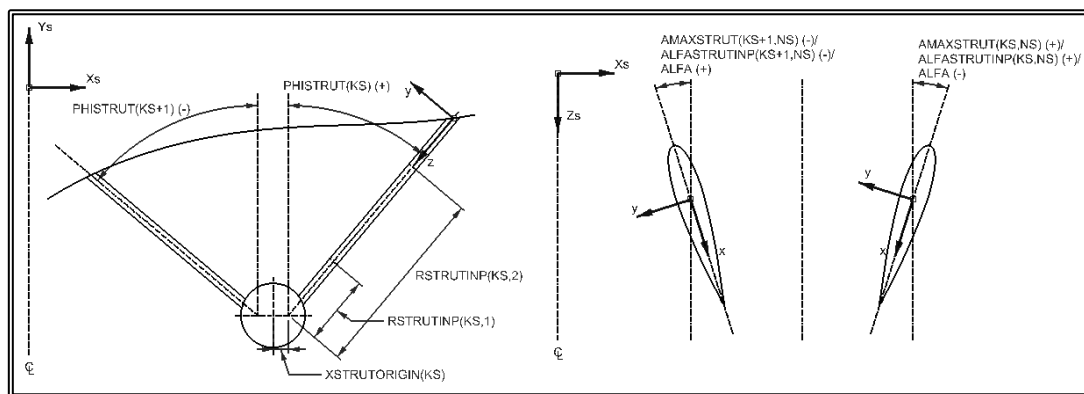
Figure 4.8.1. Definition of the strut grid block coordinate system.

The upstream (K=1) boundary of the block lays on the hull surface and is treated as a solid boundary. The location of the downstream (K=NK) boundary is defined by the user. The West (I=1) and East (I=NI) boundaries are the outflow boundaries and their distance from the strut trailing edge is user defined. The South boundary (J=1) covers the strut surface and the symmetry plane abaft the trailing edge. Finally the North boundary (J=NJ) is the external boundary. The extend of the block ahead of the strut leading edge and to the side, is defined by the user. The block longitudinal extent may be automatically reduced by the software, to avoid intersection of the block with the strut's bossing, while the transverse extent may also be reduced, to avoid intersection of the two blocks around a V-type bracket.

The strut grid block is divided into two parts along its length. The first part, part-A, extends from the hull up to a user defined distance, while part-B covers the rest of the block. The grid sections of part-B are always planar and normal to the z-axis. The sections of part-A are non-planar, in order to conform the hull contours. Nevertheless when projected on a plane normal to the z-axis, each grid becomes orthogonal curvilinear.

The distribution of 2-D sections along the z-axis (K-index) is not uniform; the grid is finer near the hull. The distribution of nodes on each section is also variable. In the radial direction (J-index), grid resolution is finer near the solid boundary (J=1), while in the peripheral direction (I-index), grid resolution, with respect to the arc length of the section, is finer near the leading and trailing edges. In all directions, the number of grid nodes and the grid resolution for the first two nodes is defined by the user. Then the software arranges the nodes so that the node spacing follows an exponential distribution. In the peripheral direction, the grid resolution is defined by the user at the leading and trailing edges.

In order to generate the grid block, the software initially calculates the distribution of sections. The intersection of the strut with the hull surface is calculated, forming the strut profile for the upstream section (K=1). Then the strut profile for each section of part-A is calculated, taking into account the strut geometry and the fact that section K=1 is not planar. The profile for each section of part-B is also calculated. The sections of part-B are planar but still, the strut geometry must be taken into account.

Then the strut profile on each section is projected on a plane normal to the z-axis and the 2-D orthogonal curvilinear grid is generated (xy-plane, I, J-indexes) by employing the singularity method for the given boundaries (Tzabiras, 1986) (figure 4.8.2). The initially planar sections of part-A of the grid block are then projected in such a way as to conform the hull contours. The generation of the 2-D grids will be discussed in further detail, in paragraph 4.8.1.
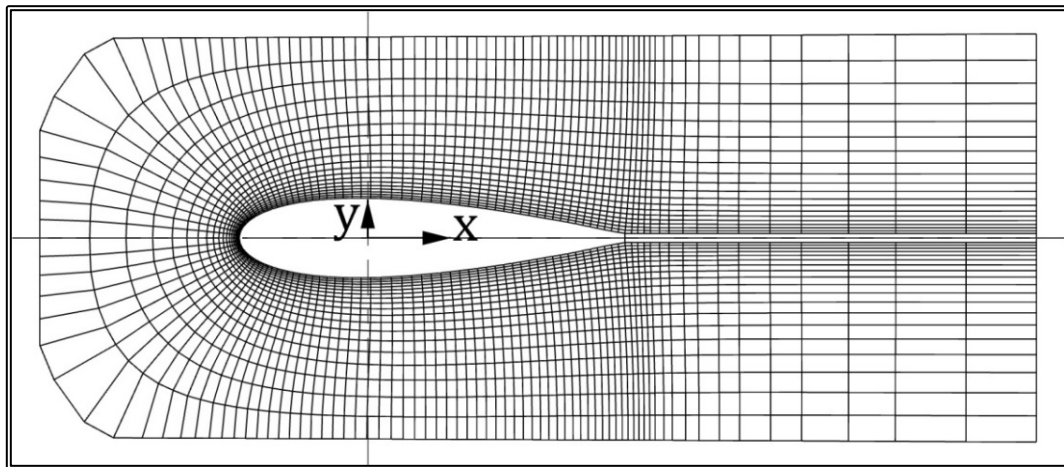
Figure 4.8.2. 2-D grid (NIxNJ=147x20) about a strut section.
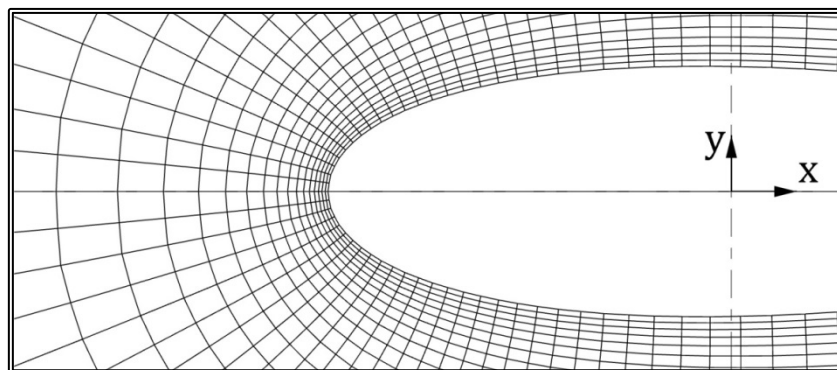
Figure 4.8.4. Detail of a 2-D grid (NIxNJ=147x20) near the leading edge of a strut section.

In the case of the struts' grid blocks there may be one type of geometrical discontinuity that needs to be addressed, that of a trailing edge of a non-zero thickness. In order for this discontinuity to be modeled, extra grid nodes (extra equi-J lines) are added to form a sub-grid. This sub grid runs the length of the main grid, has common indexing as the main grid and the finite volumes that are inside the strut, remain inactive during the solution of the problem (figure 4.8.4a). Abaft the trailing edge, the grid is a simple orthogonal grid (figure 4.8.4b) while inside the strut the grid is generated by linear interpolation forming a non-orthogonal grid.
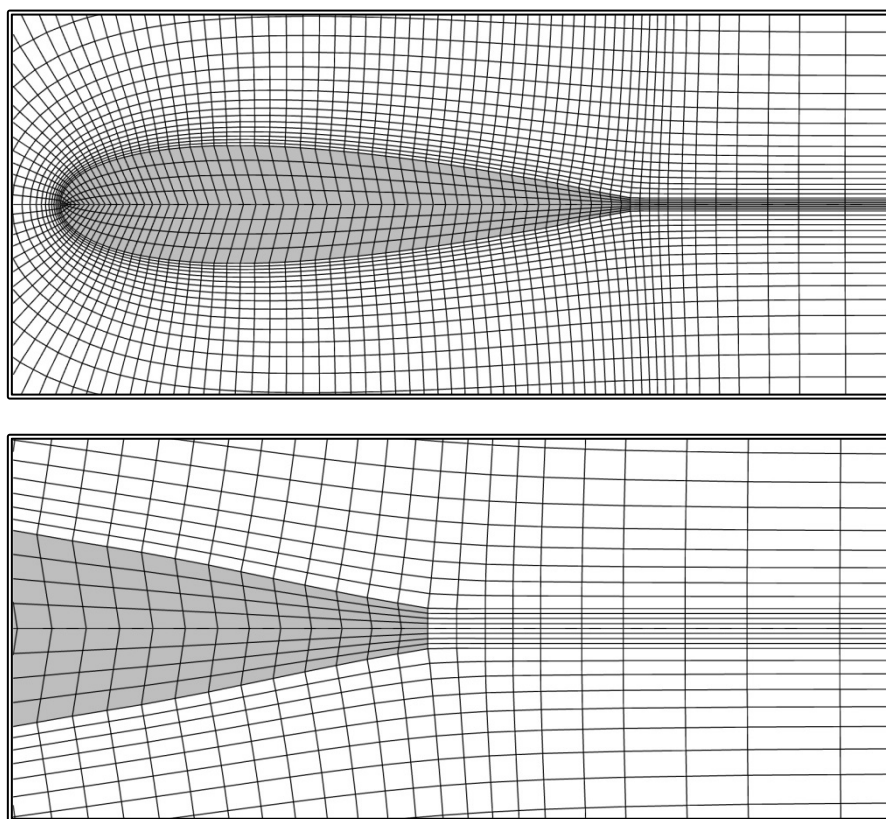
Figure 4.8.4a, b. 2-D inner grid for non-zero strut trailing edge thickness. The shaded portion of the grid remains inactive.

In the longitudinal direction (z-direction, K-index), the homologue grid nodes of subsequent planes are joined to form the partially orthogonal 3-D grid (figures 4.8.5, 4.8.6).

The computational steps for the generation of a shaft bossing grid block, are as follows:

1. Find block origin and orientation; calculate the translation vector and the rotation matrix with respect to the global (ship) coordinate system.
2. Calculate the offsets on two reference sections. These sections are normal to the strut z-axis, one at the root of the strut (upstream edge) and one at the downstream edge of the grid. The offsets are generated by the offsets of the two input sections.
3. Read the block dimensions and if necessary correct to avoid intersections with the bossing or the other strut block.
4. Read the number of grid K-nodes, calculate the section distribution.

5. Read the number of J-nodes as well as the number of J-nodes for the sub-grid, were applicable.
6. Read the number of I-nodes.
7. Calculate the node distribution on the strut, for the two reference sections.
8. Calculate the z-coordinate of all the nodes laying on the strut, for the upstream section.
9. Calculate the coordinates of all nodes laying on the strut, for all sections.
10. Generate the 2-D planar I,J outer grids.
11. Generate the 2-D planar I,J inner grids, where applicable.
12. Project the 2-D planar I,J grids of part-A sections so as to conform to the hull.
13. Generate the 3-D grid.
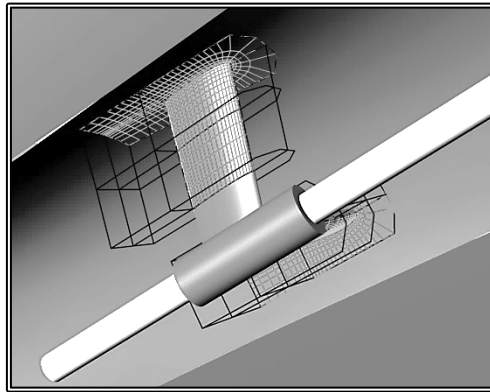
Figure 4.8.5. Grid nodes on the solid boundaries about the struts of V-type bracket. NIxNJxNK=57x7x14
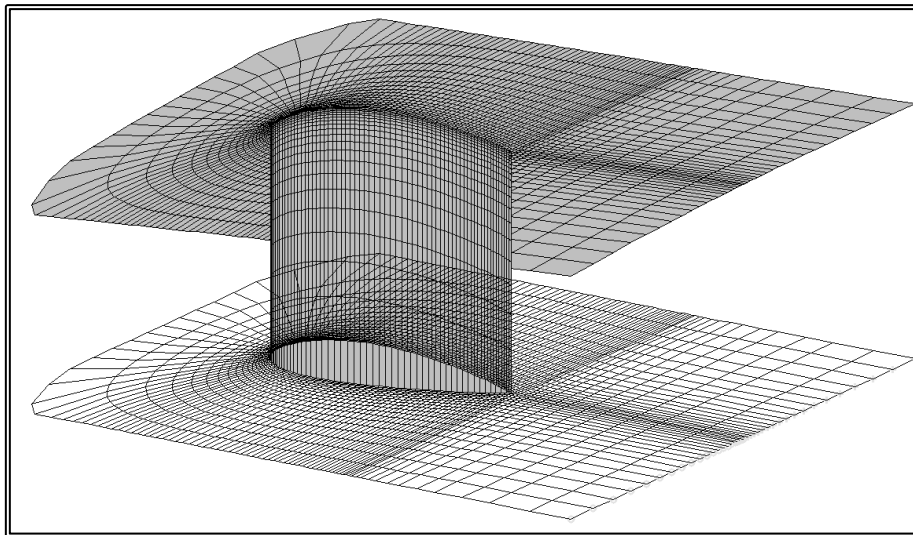
Figure 4.8.6. 3-D grid (NIxNJxNK=147x20x20) about a strut, for clarity only the grid nodes on the solid boundaries (Upstream and South) plus two 2-D grids are presented.

4.8.1   2-D Strut Grid Generation

The strut grid comprises 2-D curvilinear orthogonal C-type grids, normal to the z-axis. The 2-D grids are generated by employing the method presented in paragraph 4.4. This method uses singularity distributions on the boundaries to solve the potential flow problem. Then the grid nodes are calculated as the intersection points of stream

and equi-potential lines. The method requires the node distribution on four edges that form the calculations domain. The nodes on the South and West edges are also the J=1 and I=1 nodes of the grid.

Two important characteristics of the method are that the edges must be arranged in a count-clockwise direction and that the edges cannot fold. Those two characteristic necessitate the subdivision of each 2-D grid into two sub-grids, the top and the bottom-one, where the mirror image of the bottom side sub-grid has to be calculated (figure 4.8.7).
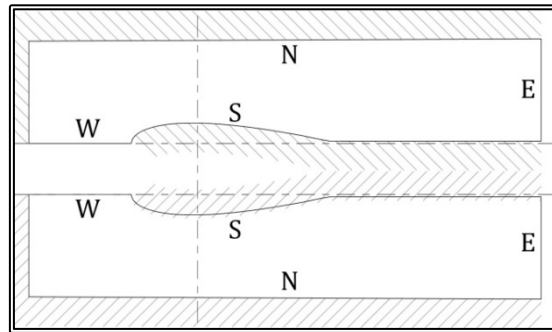
Figure 4.8.7. Definition of the top and the bottom domains. The North and South edges are treated as solid boundaries, while the East and West edges are treated as equi-potential lines.

In order to define the four edges, the locations of 6 characteristic points are calculated for each sub grid (figure 4.8.8). Then, the distribution on the South and West edges is calculated. The distribution is finer near the solid boundary, the leading edge and the trailing edge. The distribution on the West edge of both sub-domains is obviously the same, so that the resulting grids have that particular line common. The distribution on the other two edges is uniform (figure 4.8.9).
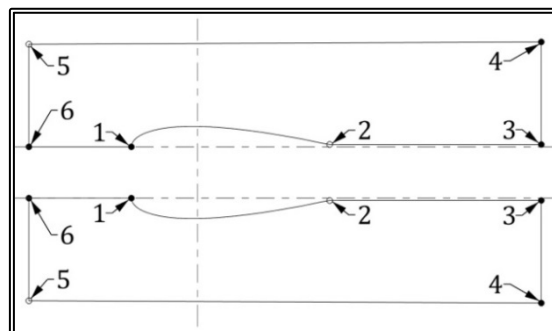
Figure 4.8.8. Definition of the characteristic points.
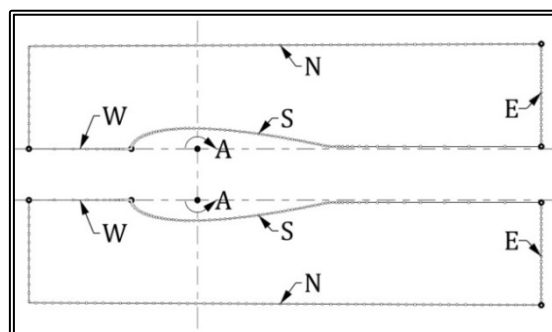
Figure 4.8.9. Distribution of nodes on the four edges.

Then, by introducing an eddy at x=0, y=0, the potential flow problem is solved according to the method of paragraph 4.4 and the two sub-grids are generated (figure 4.8.10). Then the left-hand grid is mirrored and the final grid is generated by merging the two sub-grids.
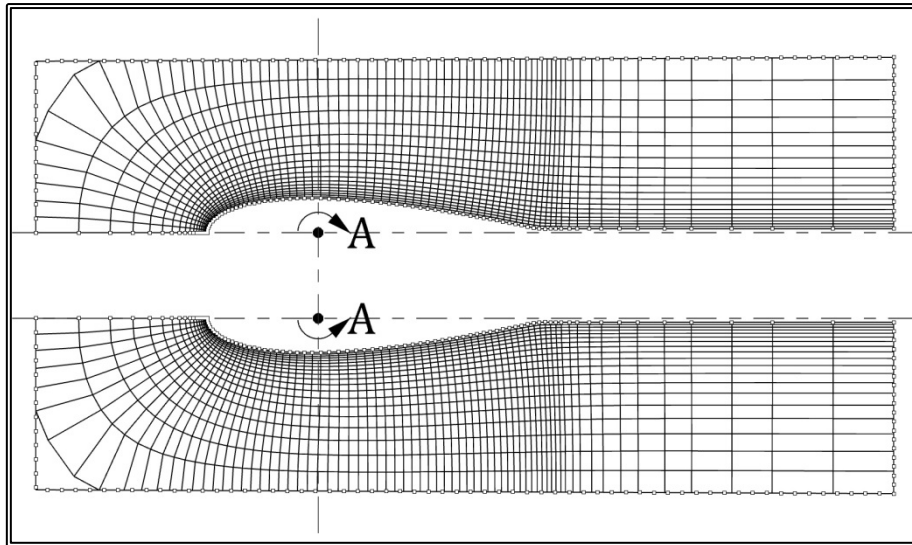
Figure 4.8.10. The two halves of the 2-D grid.

The computational steps for the generation of a 2-D bossing outer grid are as follows:

1. Calculate the nodes that lay on the strut section, taking into account the fact that the sections of part-A are not planar.
2. Split the domain into the left-hand and right-hand sub-domains
3. Calculate the locations of the characteristic points for each sub-domain.
4. Calculate the number if I-nodes on the strut.
5. Calculate the distribution of nodes on the four edges of the top sub-domain.
6. Generate the top sub-grid
7. Mirror the bottom sub-domain.
8. Calculate the distribution of nodes on the four edges of the mirrored bottom sub-domain.
9. Generate the mirrored bottom sub-grid
10. Mirror the generated grid into the bottom sub-grid.
11. Merge grids
12. Generate the inner grid.

4.9 Rudder Grid Block Generation

The rudder is modeled by a single grid block, comprising 2-D curvilinear orthogonal C-type grids, normal to the rudder axis. Each orthogonal curvilinear grid is generated by employing either the singularity distribution method presented in paragraph 4.4 or the conformal mapping method of paragraph 2.4.2. Since the hydrofoil section, the chord and the twist may vary along the rudder axis, the 2-D grids differ and the resulting 3-D grid is partially orthogonal. Also near the hull, the grid conforms to the hull surface and as a result, the sections are not planar (figure 4.9.1).
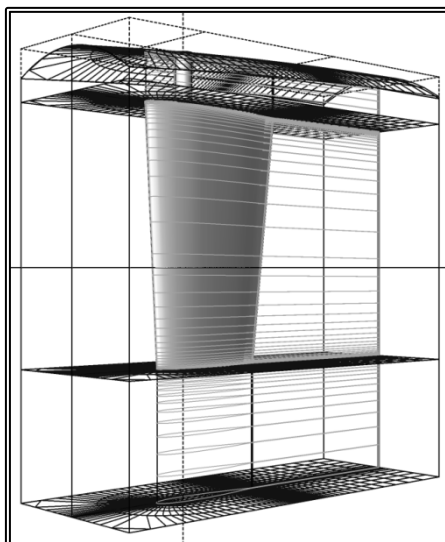
Figure 4.9.1. 2-D grid sections along the rudder axis.

The rudder grid block is divided into three parts along its length. The first part, part-A, extends from the hull up to the root of the rudder (H1 in figure 4.9.2). Part-B covers the length of the rudder, while part–C extends underneath the rudder tip up to a user defined distance (H2 and H3 in figure 4.9.2).

The grid sections of part-B and part-C are always planar and normal to the rudder axis. The sections of part-A are non-planar, in order to conform the hull contours. Nevertheless when projected on a plane normal to the z-axis, each grid becomes orthogonal curvilinear.

The block has its own coordinate system with the z-axis coinciding with the rudder axis and with a downwards direction, x-axis parallel the root chord towards the trailing edge and finally the y-axis completing the right-hand orthogonal system. The datum of the system is located on the root of the rudder. The rudder block coordinate system is presented in figure 4.9.2.

The upstream (K=1) boundary of the block lays on the hull surface and is treated as a solid boundary. The location of the downstream (K=NK) boundary is defined by the user. The West (I=1) and East (I=NI) boundaries are the outflow boundaries and their distance from the strut trailing edge is also user defined. The South boundary (J=1) covers the rudder surface and the symmetry plane abaft the trailing edge. Finally the North boundary (J=NJ) is the external boundary. The extend of the block ahead of the strut leading edge and to the side, is defined by the user.
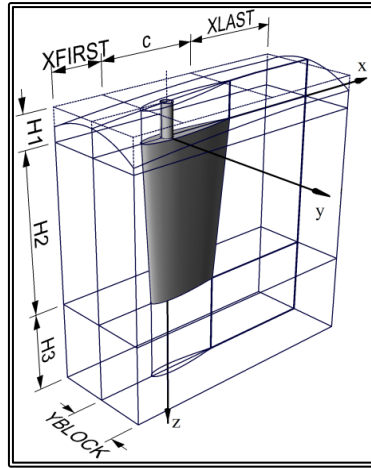
Figure 4.9.2. Definition of the rudder grid block coordinate system and dimensions.

The distribution of 2-D sections along the z-axis (K-index) is not uniform; the grid is finer near the hull, the rudder root and tip. The distribution of nodes on each section is also variable. In the radial direction (J-index), grid resolution is finer near the rudder surface (J=1), while in the peripheral direction (I-index), grid resolution, with respect to the arc length of the section, is finer near the leading and trailing edges. In all directions, the number of grid nodes and the grid resolution for the first two nodes is defined by the user. Then the software arranges the nodes so that the node spacing follows an exponential distribution. In the peripheral direction, the grid resolution is defined by the user at both the leading and trailing edges.

In order to generate the grid block, the software initially calculates the distribution of sections along the z-axis. Then the profile of each section of part-B is calculated, taking into account the rudder geometry and possibly the twist. Then a 2-D orthogonal curvilinear grid is generated on each section (xy-plane, I, J-indexes) (figure 4.9.3).
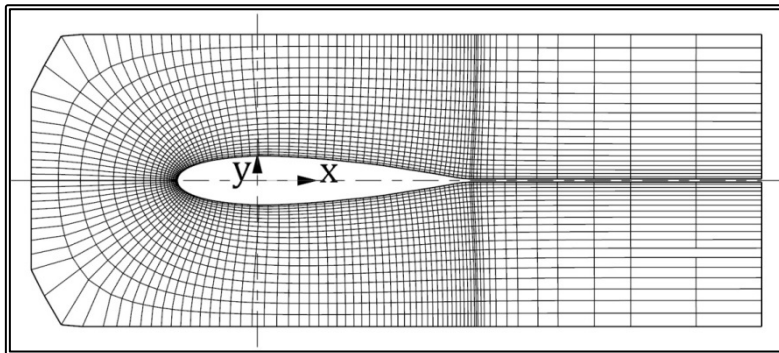
Figure 4.9.4. 2-D grid (NIxNJ=147x20) about a rudder section.
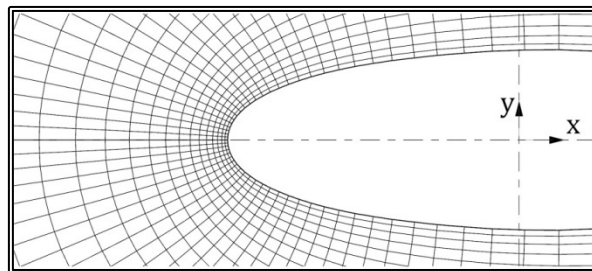
Figure 4.9.4. Detail of a 2-D grid (NIxNJ=147x20) near the leading edge of a rudder section.

All sections of part-C are considered the same as the section at the tip of the rudder, consequently al 2-D grids of part-C are the same as the 2-D grid on the rudder tip. Part-A of the rudder is also considered prismatic and as a result the 2-D grids of part-A are the same as the 2-D grid on the root of the rudder. In order for the grid to conform to the hull contours, the upstream section (K=1) is projected on the hull. The rest of the 2-D grids of part-A are also deformed by an amount varying linearly between zero at the rudder root and one at section K=1. The generation of the 2-D grids will be discussed in further detail, in paragraph 4.9.1.

In the case of the rudder grid block there may be three types of geometrical discontinuity that need to be addressed. In the case of a rudder with an exposed shaft, there is a step at the rudder root. Also the rudder tip may not be faired but end at a step. Finally the rudder thickness at the trailing edge may be non-zero. In order to model all three discontinuities, extra grid nodes (extra equi-J lines) are added to form a sub-grid. This sub grid runs the length of the main grid, has common indexing as the main grid and the finite volumes that are inside the rudder, remain inactive during the solution of the problem.

The shape of the inner grid depends on the discontinuity. In the case of the exposed shaft, the inner grid is itself a 2-D orthogonal curvilinear grid in-between the rudder surface and the shaft (figure 4.9.5). Beneath the rudder tip, the inner grid is also itself a 2-D orthogonal curvilinear grid in-between the rudder surface and the center line (figure 4.9.6). In both of the above cases, the 2-D grids are generated by employing the singularity distribution method presented in paragraph 4.4. Abaft the trailing edge, the grid is a simple orthogonal grid (figure 4.9.7). The generation of the 2-D inner grids will be discussed in further detail, in paragraph 4.9.2.

In the vertical direction (z-direction, K-index), the homologue grid nodes of subsequent planes are joined to form the partially orthogonal 3-D grid (figures 4.9.8-4.9.13).

The computational steps for the generation of a rudder grid block, are as follows:

1. Find block origin and orientation; calculate the translation vector and the rotation matrix with respect to the global (ship) coordinate system.
2. Read the block dimensions.
3. Read the number of grid K-nodes, calculate the section distribution.
4. Read the number of J-nodes as well as the number of J-nodes for the sub-grid, were applicable.
5. Read the number of I-nodes.
6. Calculate the node distribution on the input sections of the rudder.
7. Calculate the node distribution on all part-B sections of the rudder.
8. Generate the 2-D planar I,J outer grids for part-B sections.
9. Generate the 2-D planar I,J inner grids for part-B sections, where applicable.
10. All part-A, 2-D planar I,J outer and inner grids are the same as the corresponding grids on the rudder root.
11. All part-C, 2-D planar I,J outer and inner grids are the same as the corresponding grids on the rudder tip.
12. Project the 2-D planar I,J grids of part-A sections so as to conform to the hull.
13. Generate the 3-D grid.
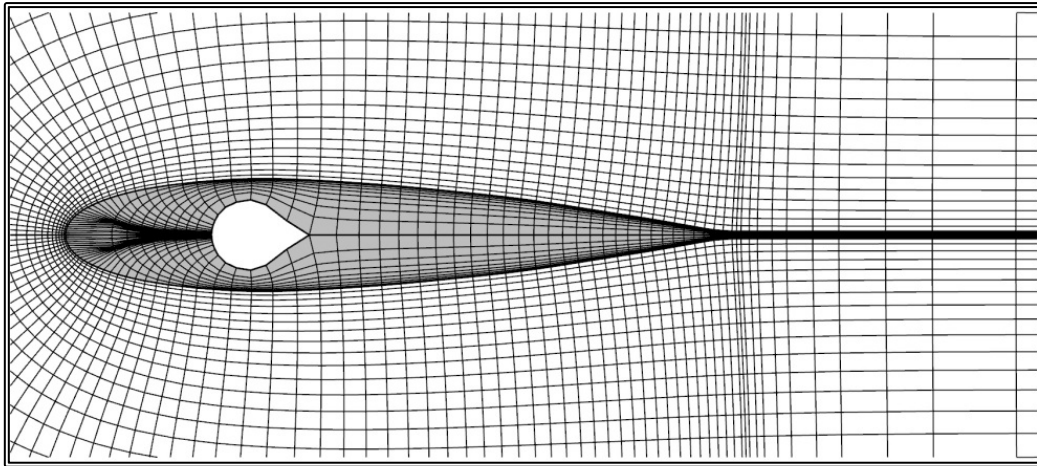
Figure 4.9.5. 2-D inner grid (NIxNJ=147x10) in the case of an exposed rudder shaft (Type-A).
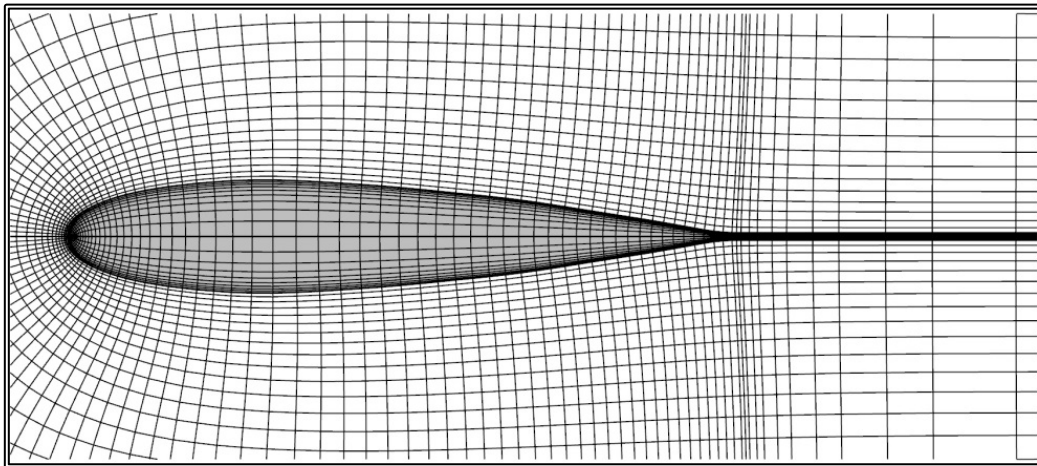
Figure 4.9.6. 2-D inner grid (NIxNJ=147x10) in the case of a hydrodynamic fairing covering the rudder shaft (Type-B). The shaded portion of the grid remains inactive along the length of the rudder.
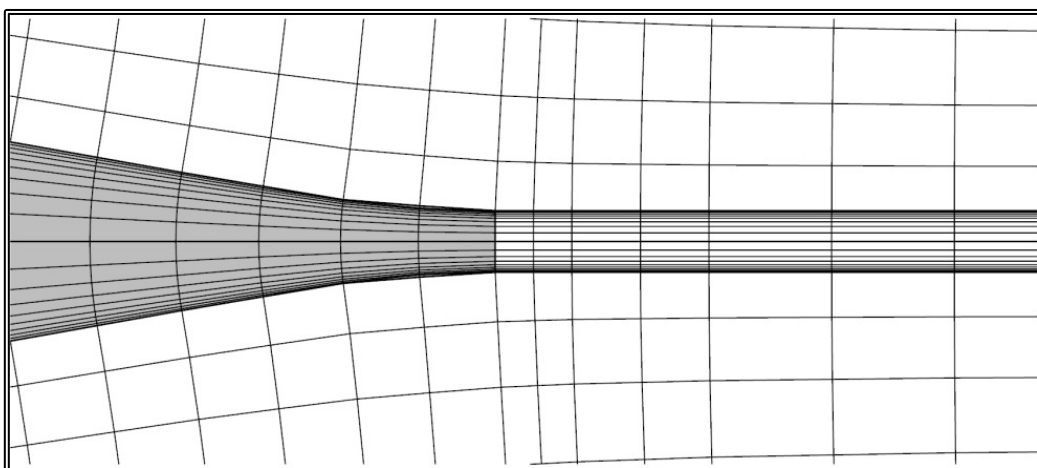
Figure 4.9.7. Detail of 2-D inner grid (NIxNJ=147x10) for non-zero strut trailing edge thickness.
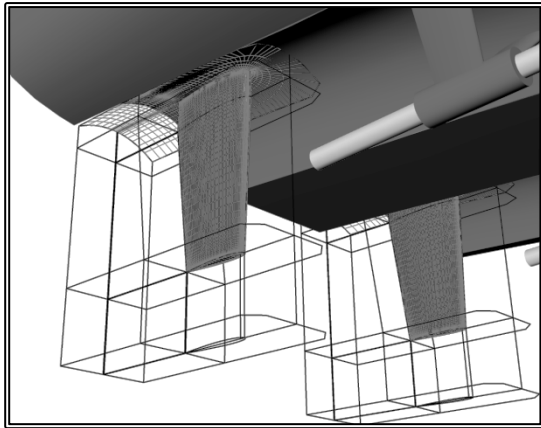
Figure 4.9.8. Grid nodes on the solid boundaries of a Type-B rudder grid block (NIxNJxNK =117x14x81).
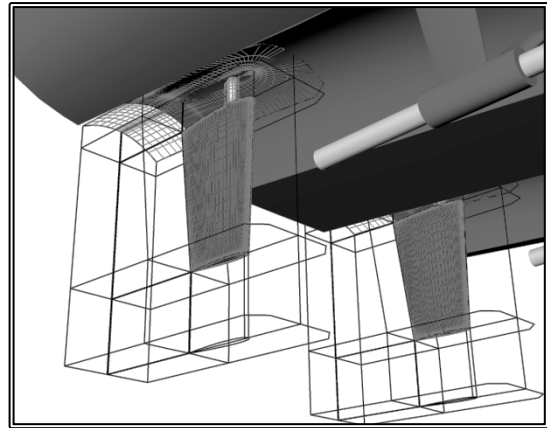
Figure 4.9.9 Grid nodes on the solid boundaries of a Type-A rudder grid block (NIxNJxNK =117x14x79).
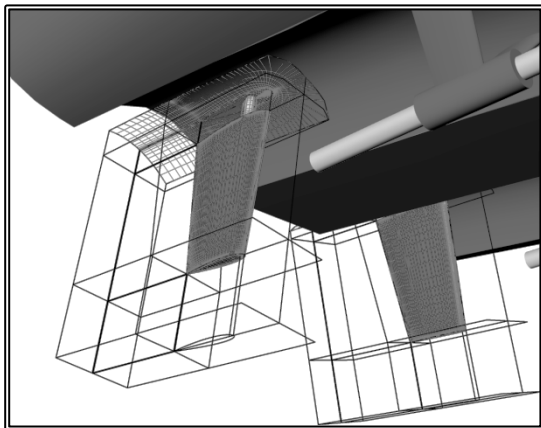
Figure 4.9.10. Grid nodes on the solid boundaries of a Type-A rudder grid block. The rudders are canted inwards by 10 degrees (NIxNJxNK =117x14x79).
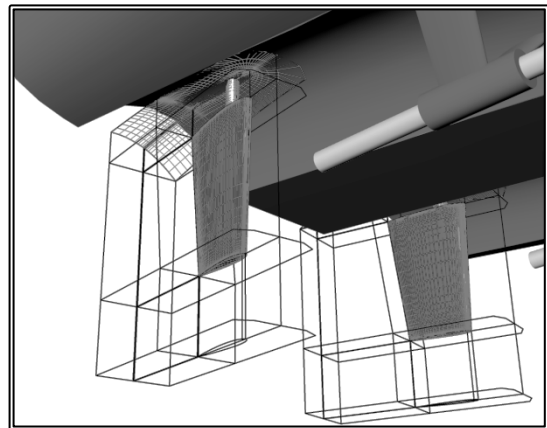
Figure 4.9.11. Grid nodes on the solid boundaries of a Type-A rudder grid block. The rudders present an angle of attack of 10 degrees (NIxNJxNK =117x14x81).
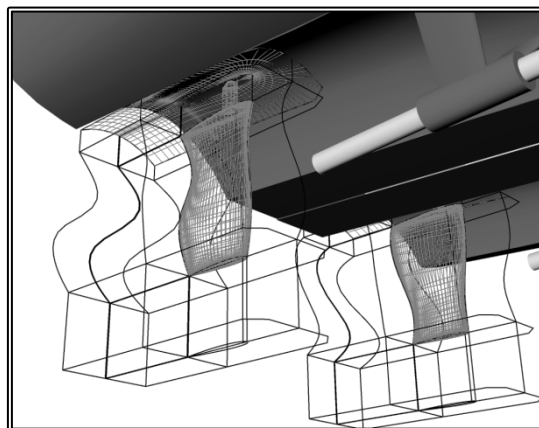
Figure 4.9.12. Grid nodes on the solid boundaries of a r Type-A rudder grid block. The rudders feature a periodic twist of maximum angle of 10 degrees (NIxNJxNK =117x14x81).
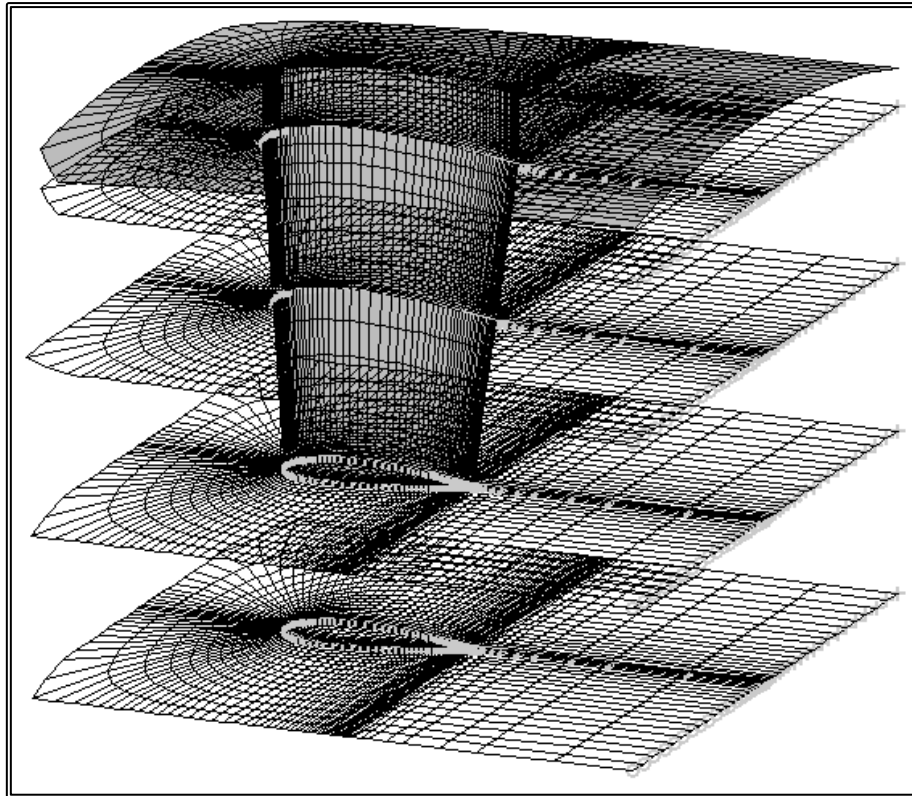
Figure 4.9.14. 3-D grid (NIxNJxNK=147x29x33) about a Type-B rudder, for clarity the grid nodes on the solid boundaries are presented along with four 2-D grids, one at the end of part-A, one at the tip of the rudder, one at the downstream boundary of the block and a further one at the mid of part-B .

4.9.1   2-D Outer Rudder Grid Generation

The outer rudder grid comprises 2-D curvilinear orthogonal C-type grids, normal to the z-axis. The 2-D grids are generated by employing either the conformal mapping method (paragraph 2.4.2) or the method of paragraph 4.4. The later uses singularity distributions on the boundaries to solve the potential flow problem. Then the grid nodes are calculated as the intersection points of stream and equi-potential lines. The method requires the node distribution on four edges that form the calculations domain. The nodes on the South and West edges are also the J=1 and I=1 nodes of the grid. Since the rudder is symmetrical, only one-half of the grid has to be calculated.
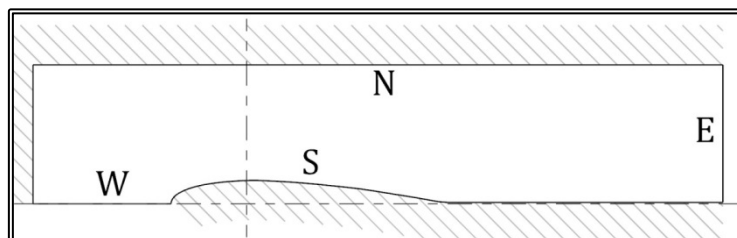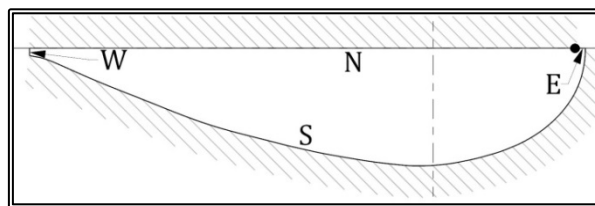

Figure 4.9.14. Definition of the computational domain, for the outer grid. The North and South edges are treated as solid boundaries, while the East and West edges are treated as equi-potential lines.

In order to define the four edges, the locations of 6 characteristic points are calculated (figure 4.9.15). Then, the distribution on the South and West edges is calculated. The distribution is finer near the solid boundary, the leading edge and the trailing edge. The distribution on the other two edges is uniform (figure 4.9.16).
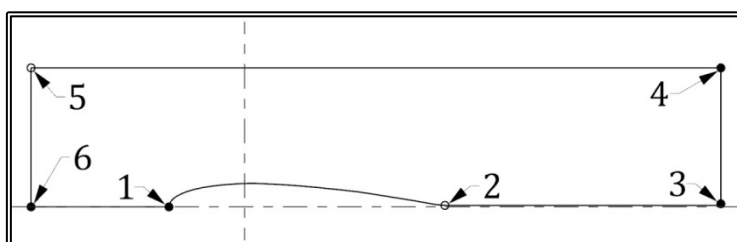
Figure 4.9.15. Definition of the characteristic points of the outer grid.
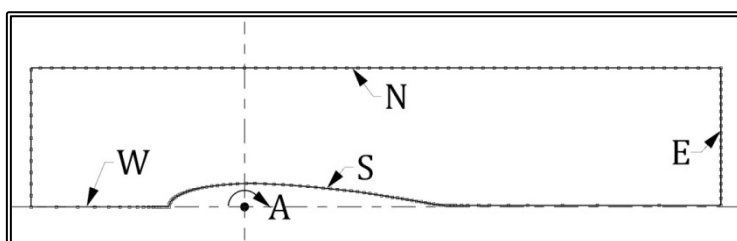
Figure 4.9.16. Distribution of nodes on the four edges of the outer grid.

Then, by introducing an eddy at x=0, y=0, the potential flow problem is solved according to the method of paragraph 4.4 and one-half of the grid are generated (figure 4.9.17). Then the grid is mirrored and the two grids are merged, to form the outer 2-D grid.
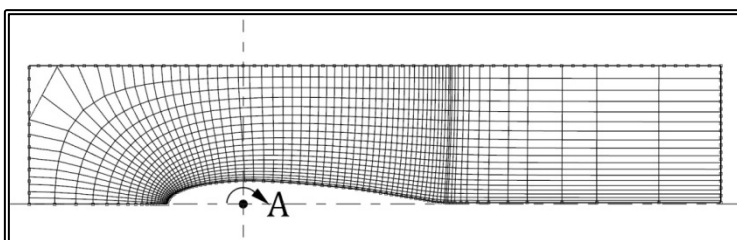
Figure 4.9.17. One halve of the 2-D outer grid.

The computational steps for the generation of a 2-D rudder outer grid are as follows:

1. Calculate the locations of the characteristic points.
2. Calculate the number if I-nodes on the rudder.
3. Calculate the distribution of nodes on the four edges of the domain.
4. Generate the grid
5. Mirror the generated grid.
6. Merge the two grids.

4.9.2   2-D Inner Rudder Grid Generation

The inner rudder grid comprises 2-D curvilinear orthogonal C-type grids, normal to the z-axis. The 2-D grids are generated by employing the same method as that for the outer grid. The inner and outer grids must share the grid nodes on the rudder surface. Also according to the method, the nodes on the South and East edges are also the J=1

and I=NI nodes of the grid and the four edges must be arranges in a counter-clockwise direction. As a result the hydrofoil section has to be rotated by 180 degrees (figures 4.9.18 and 4.9.19).
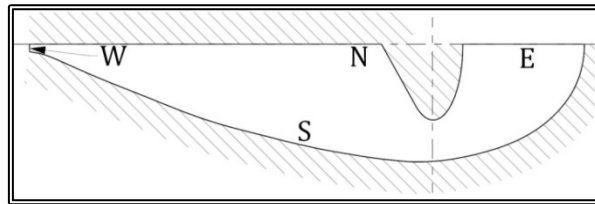
Figure 4.9.18. Definition of the computational domain, for an inner grid, with a rudder shaft. The North and South edges are treated as solid boundaries, while the East and West edges are treated as equi-potential lines. For clarity, the figure is scaled in the y-direction by a factor of 2.5.

Figure 4.9.19. Definition of the computational domain, for an inner grid, without a rudder shaft. The North and South edges are treated as solid boundaries, while the East and West edges are treated as equi-potential lines. For clarity, the figure is scaled in the y-direction by a factor of 2.5.

In the case of the inner grid without a rudder shaft, the datum is relocated nearer to the leading edge and the East edge is the line segment between the datum and the leading edge (figure 4.9.19)

Then the locations of the characteristic points are calculated (figures 4.9.20 and 4.9.21). The distribution on the West edge is calculated, while the distribution on the south edge is the same as on the south edge of the outer grid. The distribution on the other two edges is uniform. (figures 4.9.22 and 4.9.23).
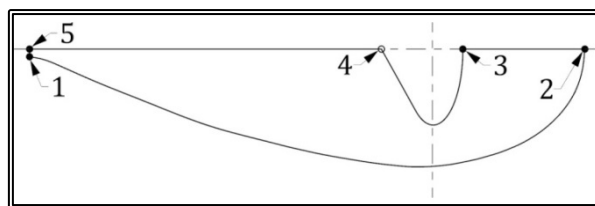
Figure 4.9.20. Definition of the characteristic points of an inner grid, with a rudder shaft. For clarity, the figure is scaled in the y-direction by a factor of 2.5.
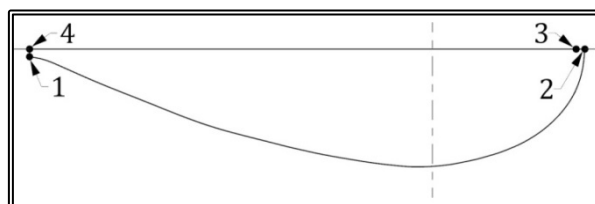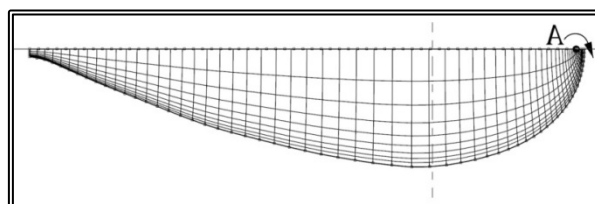

Figure 4.9.21. Definition of the characteristic points of an inner grid, without a rudder shaft. For clarity, the figure is scaled in the y-direction by a factor of 2.5.
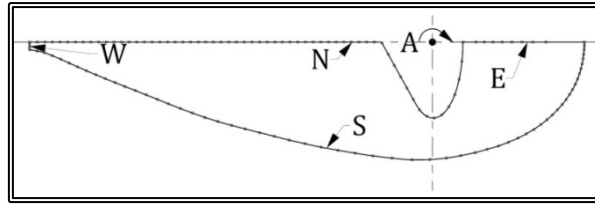
Figure 4.9.22. Distribution of nodes on the four edges of an inner grid, with a rudder shaft. For clarity, the figure is scaled in the y-direction by a factor of 2.5.
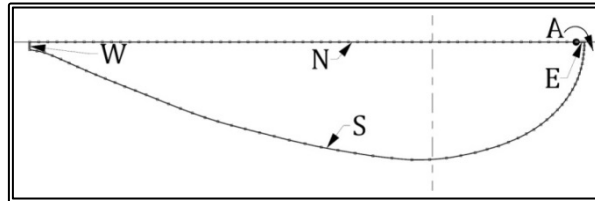
Figure 4.9.24. Distribution of nodes on the four edges of an inner grid, without a rudder shaft. For clarity, the figure is scaled in the y-direction by a factor of 2.5.

Then, by introducing an eddy at x=0, y=0, the potential flow problem is solved according to the method of paragraph 4.4 and one-half of the grid are generated (figures 4.9.24 and 4.9.25). Then the grid is rotated by 180 degrees, then mirrored and the two grids are merged, to form the inner 2-D grid.

The computational steps for the generation of a rudder 2-D inner grid are as follows:

1. Calculate the locations of the characteristic points.
2. Translate the datum, where necessary
3. Calculate the distribution of nodes on the four edges of the domain.
4. Rotate the edge nodes by 180 degrees.
5. Generate the grid
6. Rotate the grid by 180 degrees.
7. Mirror the generated grid.
8. Translate the datum to its original position, where necessary
9. Merge the two grids.
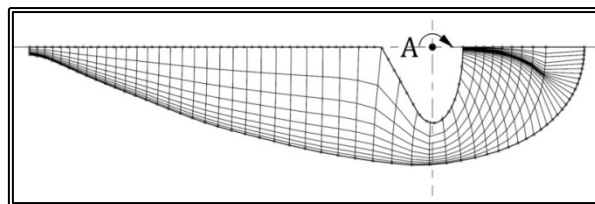
Figure 4.9.24. One halve of the 2-D inner grid, with a rudder shaft. For clarity, the figure is scaled in the y-direction by a factor of 2.5.

Figure 4.9.25. One halve of the 2-D inner grid, without a rudder shaft. For clarity, the figure is scaled in the y-direction by a factor of 2.5.

4.10   Exchange of Flow Variables between Grid Blocks

One of the key components of the Overlapping Grid Block method, as presented in paragraph 4.1, is the accurate and efficient exchange of information between the grid blocks. At any given step of the method, flow variables (velocity components, pressure, turbulent kinetic energy, turbulent kinetic energy dissipation rate and turbulent viscosity) as calculated on one grid block, the Master or donor grid block, need to be passed on to another grid block, the Slave block, in order for the flow to be solved on the later. When the slave block is one of the appendage blocks, the flow variables are transferred as conditions on its boundaries, where the master block is either the ship block or another appendage block. When the ship block is the slave, the flow variables are transferred as fixed values on a closed loop of internal finite volumes. In the following, the methodology for the first case, i.e. where one of the appendage blocks is the slave block, will be presented in detail. The method for handling the second case is very similar and will be briefly discussed at the end of this paragraph.

The method begins by obtaining the required data for the master block:

- dimensions: NIM, NJM, NKM
- coordinates of the grid nodes, XM(NIM,NJM,NKM), YM(NIM,NJM,NKM), ZM(NIM,NJM,NKM)
- translation vector SM and rotation matrix RM, that relates the coordinate system of the master grid block to the global (ship) coordinate system
- distribution of flow variables, u_1-velocity component UM(NIM,NJM,NKM), u_2-velocity component VM(NIM,NJM,NKM), u_3-velocity component WM(NIM,NJM,NKM), pressure PM(NIM,NJM,NKM), turbulent kinetic energy TEM(NIM,NJM,NKM), turbulent kinetic energy dissipation rate EDM(NIM,NJM,NKM) and turbulent viscosity VISM(NIM,NJM,NKM)

Then, the required data for the slave block are gathered:

- dimensions: NIS, NJS, NKS
- coordinates of the grid nodes, XS(NIS,NJS,NKS), YS(NIS,NJS,NKS), ZS(NIS,NJS,NKS)
- translation vector SS and rotation matrix RS, that relates the coordinate system of the master grid block to the global coordinate system

In the above, the coordinates of the grid nodes are expressed at respective coordinate system of each block, while the u_1, u_2-velocity components are expressed at the local curvilinear coordinate system. The I=1 and J=1 grid lines are duplicated, as explained in paragraph 2.3.4.

For each of the external boundaries of the slave block, the following procedure if applied on all external finite volumes:

1. The center XCSL of the slave volume is calculated, in the slave coordinate system.

2. The coordinates of the center of the slave volume are calculated in the global coordinate system, XCSP.
3. The coordinates of the center of the slave volume are calculated in the master block coordinate system, XCMR.
4. The finite volume of the master block that contains the center of the slave volume is located.
5. The flow variables at the center of the slave boundary volume, UMC, VMC, WMC, PMC, TEMC, EDMC and VISMC are calculated through zero-order or linear interpolations.
6. The velocity components are projected to the global coordinate system, USP, VSP, WSP.
7. The velocity components are projected to the slave coordinate system, USC, VSC, WSC.
8. The u_1, u_2-velocity components are projected to the local curvilinear coordinate system.
9. Finally, where required, the flow variables are calculated at the faces of the boundary volume, through linear interpolation amongst the corresponding values at the centers of the neighboring boundary volumes.

Steps 4, 5 and 8 will be discussed in detail, in the following paragraphs. Step 9 is performed when a staggered grid arrangement is employed. Depending on the boundary, the variables the require relocation are:

* for the East and West boundaries (I=NI and I=1, respectively) the u_2-velocity component has to be relocated
* for the North and South boundaries (J=NJ and J=1, respectively) the u_1-velocity component has to be relocated and
* for the Upstream and Downstream boundaries (K=1 and K=NK, respectively) both u_1 and u_2-velocity component have to be relocated

When the ship block is the slave block, the flow variables are transferred as fixed values on a closed loop of internal finite volumes. The values derive from a closed loop of master finite volumes. This loop has to be at a certain distance from the outer boundaries of the master block. That is important since the conditions on the master boundary came from the ship block itself. The methodology in this case is similar to the one described above with the only difference being that the main sweep is not for the slave grid nodes on the boundary but for the master grid nodes on the closed loop mentioned above.

4.10.1 Inclusion Test

The method for locating amongst a grid of finite volumes the one that contains a specified point in space is called Inclusion Test. Many algorithms performing the test, have been proposed in the literature. The algorithm adopted in the present work is perhaps the simplest and as a result quite inexpensive in terms of computational cost. On the other hand the presented method fails for complex volume geometries, a problem of no importance in our case since the numerical grids comprise simple hexahedral volumes.

In order to explain the method, let us consider the case of a cylindrical slave block overlapped by an orthogonal Cartesian grid (master). Let us also consider that both master and slave blocks comprise planar cylindrical and orthogonal 2-D grids respectively, with all planar grids being perpendicular to a common axis, say the x_3-axis. Finally the planes of the slave 2-D grids do not in general coincide with the planes of the master 2-D grids, i.e. the plane of a 2-D slave grid is in-between the planes of two successive master 2-D grids. In figure 4.10.1 such a 2-D cylindrical grid overlapped by an orthogonal Cartesian grid is presented.
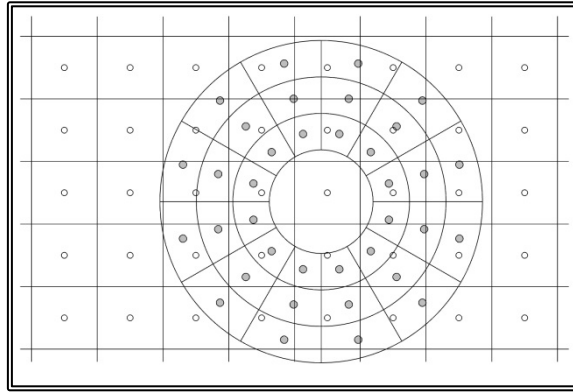
Figure 4.10.1 A 2-D cylindrical grid (Slave) overlapped by an orthogonal Cartesian grid (Master)

In the present method, a face A(I,J,K) is defined by four grid nodes, (I,J,K), (I+1,J,K), (I,J+1,K), (I+1,J+1,K). Respectively a volume V(I,J,K) is defined by eight grid nodes, four on each one of two successive planes, (I,J,K), (I+1,J,K), (I,J+1,K), (I+1,J+1,K) and (I,J,K+1), (I+1,J,K+1), (I,J+1,K+1), (I+1,J+1,K+1).

The coordinates of the center of a face is considered equal to the mean values of the corresponding coordinates of the four nodes that define that face:

$$\mathbf{xca}(I, J, K) = \mathbf{x}(I, J, K) + \mathbf{x}(I + 1, J, K) + \mathbf{x}(I, J + 1, K) + \mathbf{x}(I + 1, J + 1, K) \quad (4.10.1)$$

Also the coordinates of the center of a volume is considered equal to the mean values of the corresponding coordinates of the eight nodes that define that volume:

$$\mathbf{xcv}(I, J, K) = \mathbf{x}(I, J, K) + \mathbf{x}(I + 1, J, K) + \mathbf{x}(I, J + 1, K) + \mathbf{x}(I + 1, J + 1, K)$$

$$+\mathbf{x}(I, J, K + 1) + \mathbf{x}(I + 1, J, K + 1) + \mathbf{x}(I, J + 1, K + 1) + \mathbf{x}(I + 1, J + 1, K + 1)$$
$$(4.10.2)$$

Given the coordinates of a point p, say the center of a slave grid volume, a triple sweep along the K,I,J directions of the master grid is performed. On a (I,J,K) step of the sweep, the A=A(I,J,K) and B=A(I,J,K+1) faces are defined along with the V(I,J,K) volume (figure 4.10.2). The centers of the faces are also defined, a= **xca**(I,J,K) and b=**xca**(I,J,K+1). Then the line segment [ab] that joins the two face centers is defined and its length SAB is calculated. Then the intersection point c, of the [ab] line segment and the line that is normal to [ab] and passes through p is located. Finally the line segment lengths SAC and SCP are calculated. Once the sweep is completed, point p is considered to be included in the V(I,J,K) master volume from whom SCP is minimum. During the sweep the K-direction weight factor is also calculated:

$$WFK = SAC/SAB \qquad (4.10.3)$$
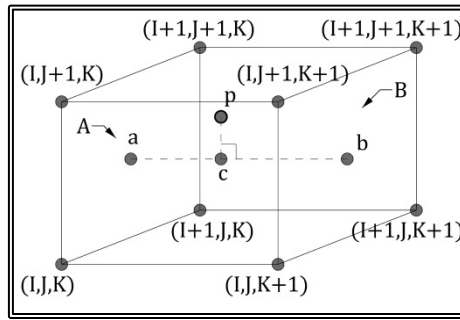
Figure 4.10.2 Definition of the Inclusion test parameters

In figure 4.10.3, an application of the above method is presented, for the North boundary of the slave grid of figure 4.10.1. The North boundary finite volumes are denoted by a +45 degree line hatch, while the donor master volumes are denoted by a crosses hatch.
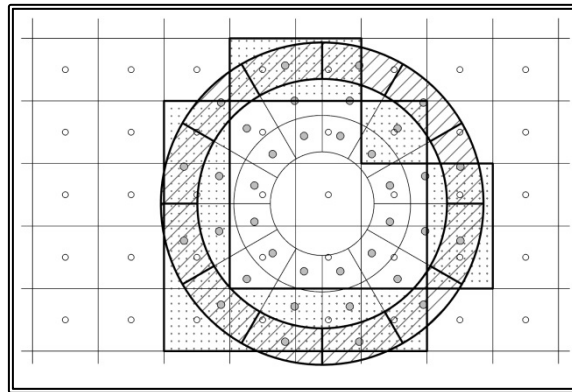
Figure 4.10.3 Application of the inclusion test for the North-boundary of a 2-D cylindrical grid (Slave) overlapped by an orthogonal Cartesian grid (Master)

4.10.2 Interpolation of Flow Variables

On step 4 of the algorithm for the calculation of boundary conditions for the slave block, the finite volume of the master block that contains the center of the slave boundary volume is located by means of the inclusion method presented in the previous paragraph. On the next step, the flow variables at the center of the slave boundary volume need to be calculated from the respective values for the master grid.

The simplest and computationally cheapest way is to consider that a flow variable at the center of a slave volume P_S, has the same value as that at the center P_M of the master volume that contains the center of the former volume.

$$\Phi_S = \Phi_M \qquad (4.10.4)$$

In equation (4.10.4) Φ stands for each of the three velocity components, the pressure, the turbulent kinetic energy, the turbulent kinetic energy dissipation rate and the turbulent viscosity. Also by the subscript S, the slave block is denoted, while the master block is denoted by the subscript M.

Since all variables are stored on the successive K-planes and in the general case the plane of the slave grid does not coincide with a plane of the master grid, we apply a linear interpolation in the K-direction. Let's say that P_S is located between two sections of the master grid, sections K and K+1. From the inclusion test of the previous paragraph we obtained the K-direction weight factor WFK. The value of a flow variable at the center of the slave volume can be calculated from the respective values at the centers of the K-faces of the master volume:

$$\Phi_S = (1 - WFK) \cdot \Phi_{M,K} + WFK \cdot \Phi_{M,K+1} \quad (4.10.5)$$

where $\Phi_{M,K}$ is the value of the variable at the K-face of the volume and $\Phi_{M,K+1}$ the value at the K+1-face of the volume. This approach, presented in figure 4.10.4, is zero-order in terms of accuracy and should only be applied when very fine messes are used.
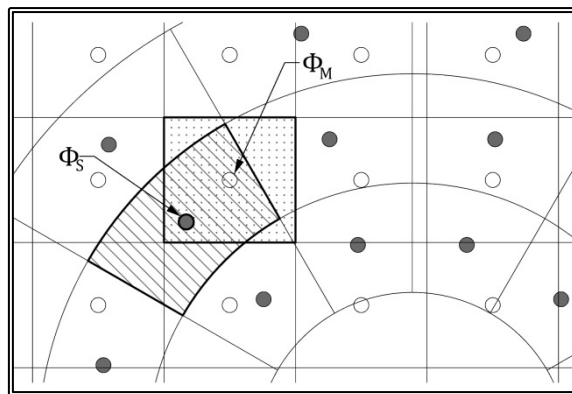
Figure 4.10.4 Zero-order interpolation of the flow variables

A more accurate method is that of bi-linear interpolation amongst four values. The bi-linear method begins by locating the master volume that contains the center of the slave volume P_S. The master volume is surrounded by eight volumes:

- East, VE=V(I+1,J,K)
- West, VW=V(I-1,J,K)
- North, VE=V(I,J+1,K)
- South, VE=V(I,J+1,K)
- North-East, VE=V(I+1,J+1,K)
- South-East, VE=V(I+1,J-1,K)
- North-West, VE=V(I-1,J+1,K)
- South-West, VE=V(I-1,J-1,K)

The centers of the K, K+1 faces of four neighboring volumes, form a new volume, in total four new volumes (figure 4.10.5). By applying the inclusion test on the new volumes we can determine the one volume that contains the center point of the slave volume P_S as well as the K-direction weight factor WFK.
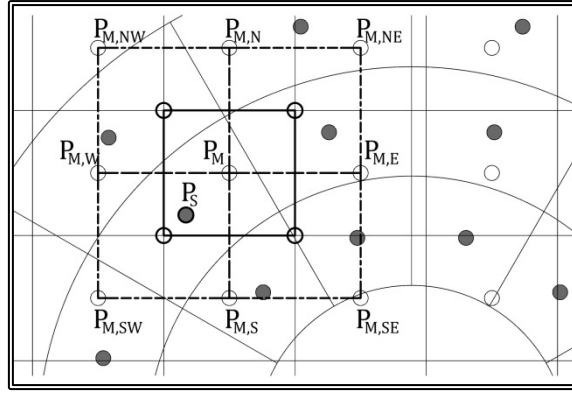
Figure 4.10.5 Bi-Linear interpolation of the flow variables

Then on each of the K, K+1 faces of the new volume we can calculate the weight factors for the bi-linear interpolation:

$$WFI_K = |PE_{4,K}|/[|PE_{4,K}| + |PE_{2,K}|]$$

$$WFJ_K = |PE_{1,K}|/[|PE_{1,K}| + |PE_{3,K}|]$$

$$WFA_K = (1 - WFI_K) \cdot (1 - WFJ_K)$$

$$WFB_K = WFI_K \cdot (1 - WFJ_K)$$

$$WFC_K = WFI_K \cdot WFJ_K$$

$$WFD_K = (1 - WFI_K) \cdot WFJ_K \quad (4.10.6)$$

where all dimensions are defined in figure 4.10.6.
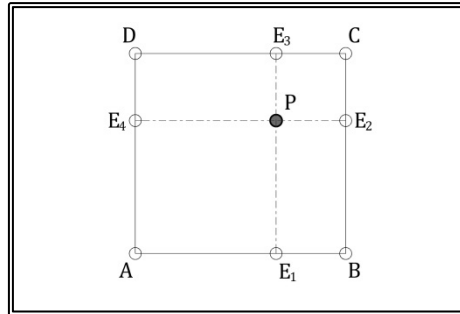
Figure 4.10.6 Definition of the dimensions for the calculation of the bi-linear interpolation weight factors

Then on each of the K, K+1 section and for each of the variables, we calculate corresponding value at the projection on the K-section $P_{S,K}$, of the slave volume center point P_S,:

$$\Phi_{S,K} = WFA_K \cdot \Phi_{A,K} + WFB_K \cdot \Phi_{B,K} + WFC_K \cdot \Phi_{C,K} + WFD_K \cdot \Phi_{D,K} \quad (4.10.7)$$

The value for each variable is finally calculated by means of linear interpolation along the K-direction:

$$\Phi_S = (1 - WFK) \cdot \Phi_{S,K} + WFK \cdot \Phi_{S,K+1} \quad (4.10.8)$$

4.10.3 Rotation of U, V Velocity Components

When the flow problem is expressed in a curvilinear coordinate system (paragraph 2.1.2) the velocity components at every point of the computational domain, refer to a local coordinate system with axis parallel to the grid lines. In the case of a partially orthogonal curvilinear grid, curvilinear orthogonal in the I,J-directions and non-orthogonal along the K-direction, the above statement is true for the u_1, u_2-velocity components while the u_3-componenets are always parallel (figure 4.10.7). It is important thus to be able to express the u_1, u_2-velocity components in a global Cartesian coordinate system. With reference to figure 4.10.8 the rotation of the two velocity components from the local to the global system is:

$$u = u_1 \cdot \cos(\varphi) + u_2 \cdot \sin(\varphi)\,, v = -u_1 \cdot \sin(\varphi) + u_2 \cdot \cos(\varphi) \quad (4.10.9)$$

where u_1, u_2 the velocity components in the local system, u, v the velocity components in the Cartesian system and:

$$x_w = 0.5 \cdot [X(I,J) + X(I,J+1)], y_w = 0.5 \cdot [Y(I,J) + Y(I,J+1)]$$
$$x_e = 0.5 \cdot [X(I+1,J) + X(I+1,J+1)], y_e = 0.5 \cdot [Y(I+1,J) + Y(I+1,J+1)]$$
$$\tan(\varphi) \approx (y_e - y_w)/(x_e - x_w) \quad (4.10.10)$$

The above formulations refer to an internal finite volume. For finite volumes of the boundaries, the formulations may need alterations to avoid divisions with zero.
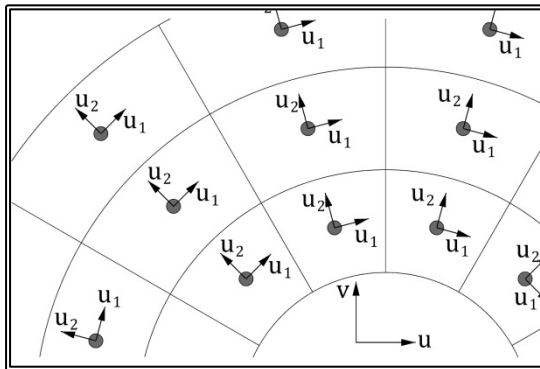
Figure 4.10.7 Definition of the local curvilinear and the global Cartesian coordinate system
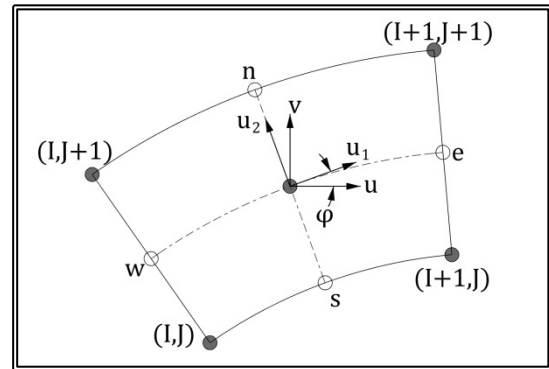
Figure 4.10.8 Rotation of the velocity components to the Cartesian coordinate system

4.11   The Proposed Solution Procedure

In the overlapping grid block method, a separate grid block is generated for each component and the transport equations are solved independently. The transfer of information between blocks is accompliced by using part of the solution of one block, the Master block, as boundary conditions for those boundaries of other blocks, Slave blocks, that lie within the Master block. In the presented method, the propeller shaft is modeled by up to three cylindrical blocks. The shaft bossing, the struts, the struts' bossings and the rudder are modeled by one block each. As an example let us consider the case of a ship with two propellers, where each propeller shaft is supported by a single I-type bracket, that is there is only one strut. The grid blocks for the above appendage arrangement are presented in figure 4.11.1.
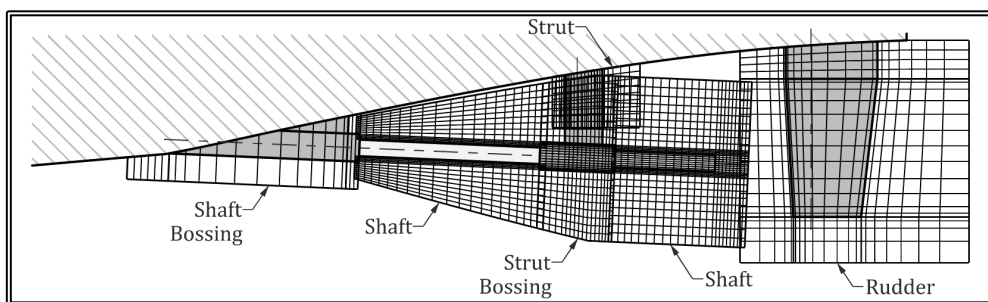
Figure 4.11.1. The arrangement of the overlapping blocks for a ship with single shaft bracket and bossing.

The solution procedure begins by solving the resistance problem for the "bare" hull, i.e. the hull without the appendages. The flow around the shaft bossing is solved next. In order to do so, the conditions on the inflow (K=1, Upstream), external (J=NJ, North) and outflow (K=NK, Downstream) boundaries of the bossing block (figure 4.11.1) derive from the solution of the ship block. More specifically on the inflow and external boundaries, Dirichlet conditions are applied to all flow variables except for pressure (u_1, u_2, u_3, k, ε) for which a Newmann condition is applied. On the outflow boundary, Dirichlet conditions are applied to the pressure and the turbulence model variables, while for the velocity components, the Open Boundary conditions are applied, i.e. the problem is solved up to the last finite volume. The West (I=1) and East (I=NI) boundaries of the shaft bossing block, lay on the hull surface and are treated as solid boundaries. The South (J=1) boundary covers the bossing surface and is also treated as a solid boundary.
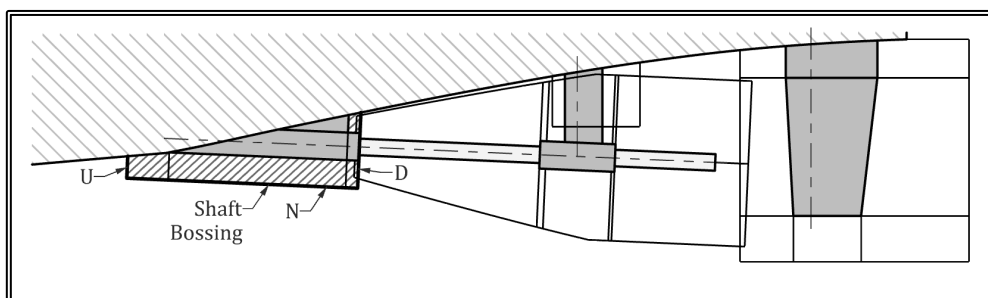
Figure 4.11.2. Definition of the external boundaries of the shaft bossing grid block.

Next, the fore shaft block is solved (Figure 4.11.3), where the boundary conditions for the inflow (K=1, upstream) boundary derive from the solution of the shaft bossing block. The outflow (K=NK, Downstream) boundary is treated as an open boundary. The North boundary (J=NJ), is treated as an external boundary and the conditions are taken from the ship block while the South boundary (J=1) covers the shaft surface and is treated as a solid boundary. Finally on the West (I=1) and East (I=NI) boundaries, the conditions for O-type grids are employed.
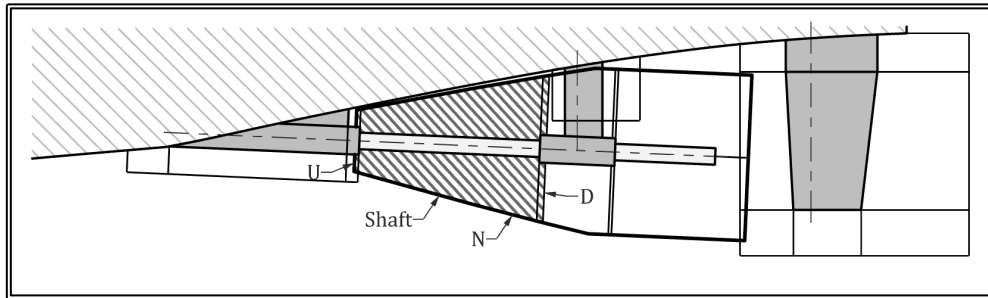
Figure 4.11.3 Definition of the external boundaries of the fore shaft grid block.

The strut bossing block is then solved (Figure 4.11.4). The boundary conditions for the inflow (K=1, upstream) boundary derive from the solution of the fore shaft block and the outflow (K=NK, Downstream) boundary is treated as an open boundary. The North boundary (J=NJ), is treated as an external boundary and the conditions are taken from the ship block while the South boundary (J=1) covers the bossing surface and is treated as a solid boundary. Finally on the West (I=1) and East (I=NI) boundaries, the conditions for O-type grids are employed.
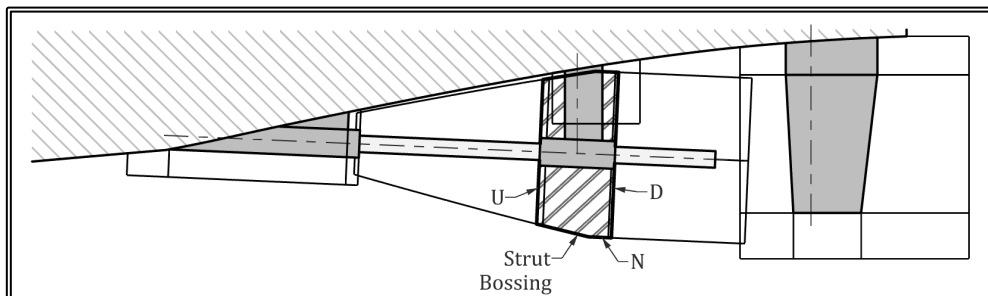
Figure 4.11.4. Definition of the external boundaries of the strut bossing grid block.

The boundary conditions for the aft shaft block are similar to the respective conditions for the fore shaft block, except for the inflow (K=1, upstream) boundary where the conditions are taken from the from the solution of the strut bossing block (Figure 4.11.5).
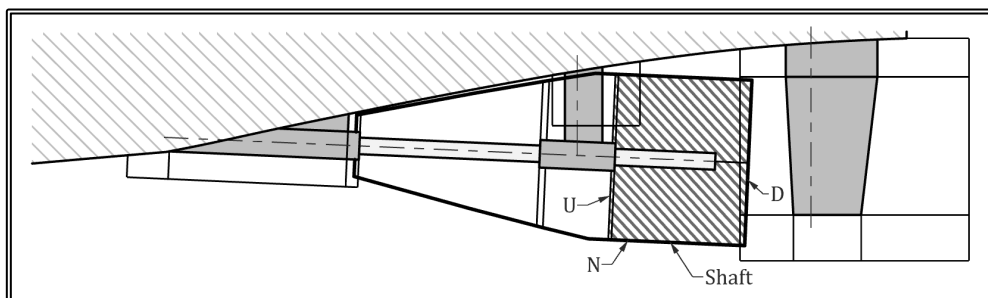
Figure 4.11.5. Definition of the external boundaries of the aft shaft grid block.

For the strut grid block, the upstream boundary (K=1) lays on the hull surface and is treated as a solid boundary. The Downstream boundary (K=NK) is treated as an external boundary with conditions been taken form the solution of the strut bossing block and possibly the shaft block that follows. The North boundary (J=NJ) is also treated as an external boundary with conditions taken form the ship block, as well as the strut bossing block and the shaft block. The South boundary (J=1) covers the strut surface as well as the symmetry plane downstream the trailing edge. Finally the West (I=1) and East (I=NI) boundaries are treated as outflow boundaries.
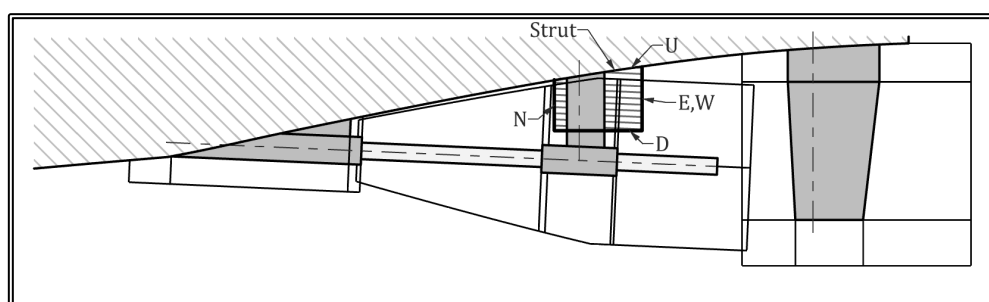
Figure 4.11.6. Definition of the external boundaries of the strut grid block.

The shaft bossing, shaft, strut and strut bossing blocks form a continuous volume of fluid and can be solved consecutively. In order then to transfer the obtained information to the ship block, the following procedure is adopted. A closed surface is defined, inside the volume covered by the combination of blocks. This surface passes through the centers of the finite volumes that are at a set distance from the external boundary of the volume (figure 2.3.7). Then the flow variables on that surface are calculated and passed on, as fixed values for the solution of the ship block. Finally the ship block is solved taking into account the information of the appendage blocks and the whole procedure can be repeated.
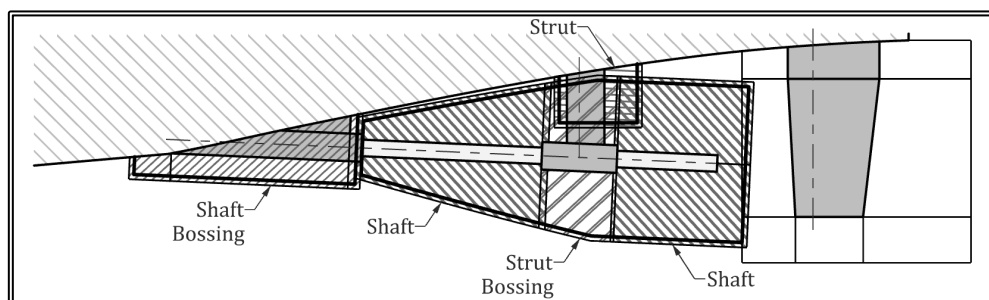
Figure 4.11.7. Definition of boundary surface for the transfer of the flow variables from the appendages blocks to the ship block.

The rudder grid block is solved independently (figure 2.3.8). The upstream boundary (K=1) lays on the hull surface and is treated as a solid boundary. The Downstream (K=NK) and North (J=NJ) boundaries are treated as an external boundaries with conditions been taken form the solution of the ship block. The South boundary (J=1) covers the rudder surface as well as the symmetry plane downstream the trailing edge. Finally the West (I=1) and East (I=NI) boundaries are treated as outflow boundaries.
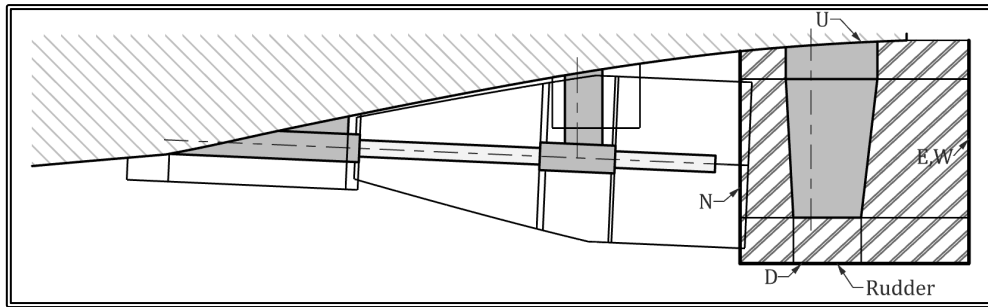
Figure 4.11.8. Definition of the external boundaries of the rudder grid block.

The computational steps for the solution of flow around the appendages are as follows:

1. Solve the flow problem around the "bare" hull.
2. Solve the shaft bossing flow, taking boundary conditions from the ship block.
3. Solve the shaft flow, taking boundary conditions from the ship and shaft bossing blocks.
4. Solve the strut bossing flow, taking boundary conditions from the ship and shaft blocks.
5. Solve the shaft flow, taking boundary conditions from the ship and strut bossing blocks.
6. Repeat steps 4 and five, in the case of more than one strut bossings.
7. Solve the strut flow, taking boundary conditions from the ship, the strut bossing and the shaft blocks.
8. Repeat step 7 for all struts.
9. Solve the flow around the ship, taking into account the information derived from the appendages blocks.
10. Solve the flow problem around the rudder, taking boundary conditions from the ship block.

CHAPTER 5   FLOW CALCULATIONS ABOUT A SINGLE APPENDAGE

(This page intentionally left blank)

5.1   Introduction, the 200/08 LSMH model

In order demonstrate the ability of the new software, to solve the viscous flow problem around the appendages of a ship; a number of numerical tests were conducted. In these tests each grid block was solved independently, using uniform flow external boundary conditions. Consequently the derived results do not correspond to the actual flow around the appendages.

Table 5.1.1 Main Particulars of Model 200/08.

	Ship	Model
Scale Factor, λ		1/8.75
Waterline Length, L_{WL} [m]	26.900	3.074
Waterline Beam, B_{WL} [m]	6.740	0.770
Mead Draft, T_M [m]	1.890	0.216
Displacement, Δ [mt]	130.00	0.1893
Longitudinal Position of Center of Buoyancy (from AFT end), LCB [m]	12.619	1.442
Wetted Surface, WS [m²]	182.910	2.389
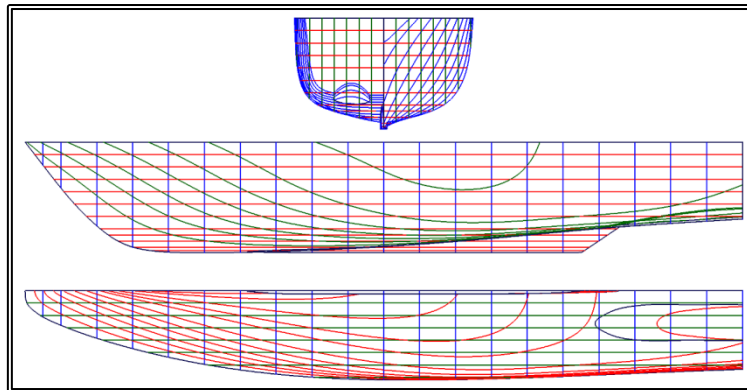
Figure 5.1.1 Lines plan of LSMH model 200/08.

For these tests the LSMH model 200/08 was selected. The main particulars of the model and the corresponding ship are presented in table 5.1.1 (Triperinas et al., 2008) while in figure 5.1.1, the lines plan of this model is presented. The model features a twin-screw configuration with each shaft suspended from the hull by a single 90 degree V-bracket. The shaft bossing and the strut bossing are cylindrical. The shaft arrangement and the corresponding dimensions in full scale are presented in figures 5.1.2 and 5.1.3. The hydrofoil section of the struts has a thickness to chord ratio of 20% (figure 5.1.4). The ship also features two trapezoidal rudders the dimensions of whom are presented in figure 5.1.5. The hydrofoil section of the rudder has a 17% thickness to chord ratio (figures 5.1.5 and 5.1.6).

The overlapping block setup employed in the test, follows the method of paragraph 4.2, that is there are two cylindrical blocks for the two parts of the shaft, one cylindrical block for the strut bossing and C-H-type blocks for the shaft bossing, each of the struts and the rudder. The numerical grids as well as the results from the calculations are presented in the following paragraphs.
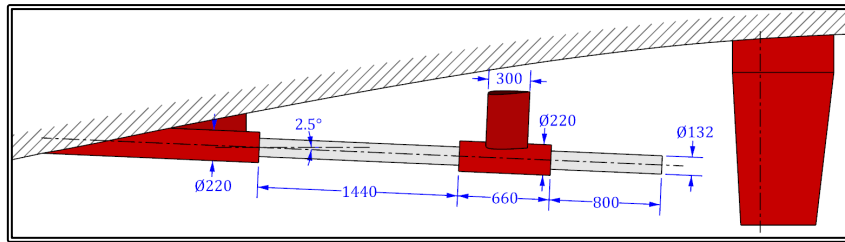
Figure 5.1.2 Shaft, shaft bossing and strut bossing arrangement.
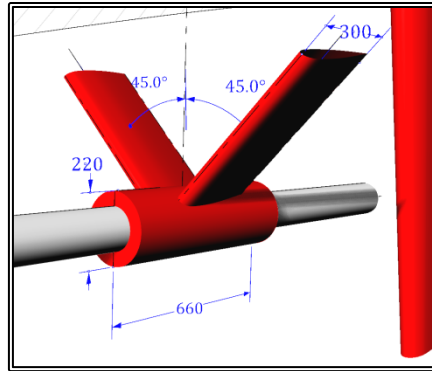
Figure 5.1.3 Strut layout.
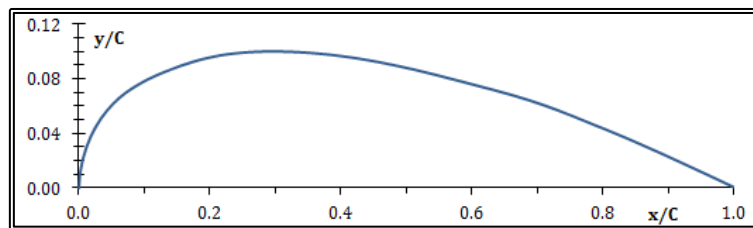
Figure 5.1.4 Strut hydrofoil section.
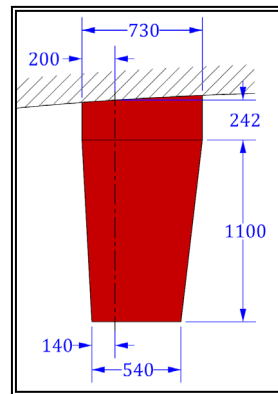
Figure 5.1.5 Rudder profile.
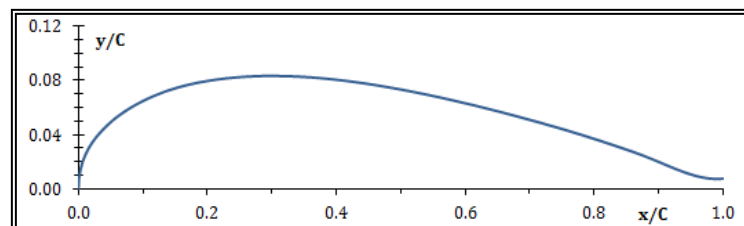
Figure 5.1.6 Rudder hydrofoil section.

5.2 Flow Calculations about the Propeller Shaft

In order to solve the viscous flow around the propeller shaft of the LSMH 200/08 model, two cylindrical O-H-type blocks were generated by employing the method described in paragraph 4.5. The first block, the one nearest to the shaft bossing, extended upwind onto the shaft bossing and downwind onto the strut bossing. The second block extended upwind onto the strut bossing and downwind up to a predetermined distance from the shaft end. In these tests, the external flow is considered undisturbed and at the inlet and external boundaries of each block the velocity is set equal to the free stream velocity U_∞ which in these tests is parallel to the shaft axis. The flow variables for both tests are presented in table 5.2.1. The calculations for the two shaft blocks are presented in the two following paragraphs.

Table 5.2.1 Flow variables for the propeller shaft test, forward section

Free Stream Velocity, U_∞	1.000	m/s
Fluid Viscosity, ν	1.030E-06	m^2/s
Reynolds's Number, Re_D	1.282E+05	
Shaft diameter, D	0.132	m

5.2.1 Propeller Shaft Calculations, Forward Section

For the first shaft block, the one nearest to the shaft bossing, two numerical tests were conducted using different grid sizes. The grid variables for both tests are presented in table 5.2.2, where NI is the number of nodes in the circumferential direction, NJ is the number of nodes in the radial direction and NK is the number of sections perpendicular to the shaft axis. NJ1 is the number of nodes in the radial direction, at each of the shaft steps, NKL is the number of sections along the shaft length and NKU and NKD, the number of sections on the propeller bossing (upstream end) and the strut bossing (downstream end) respectively. The maximum radial extend of the grid is set equal to 10 times the shaft radius but is variable along the shaft axis so that the grid does not intersect the hull. In figures 5.2.1 to 5.2.3, several sections of the two blocks are presented.

Table 5.2.2 Main grid variables for the propeller shaft test, forward section

	A	B
NI	41	81
NJ	30	50
NJ1	11	11
NK	44	84
NKU	3	3
NKL	40	80
NKD	3	3
NIxNJxNK	54,120	340,200
Radial extend	10.0xR_{Shaft}	
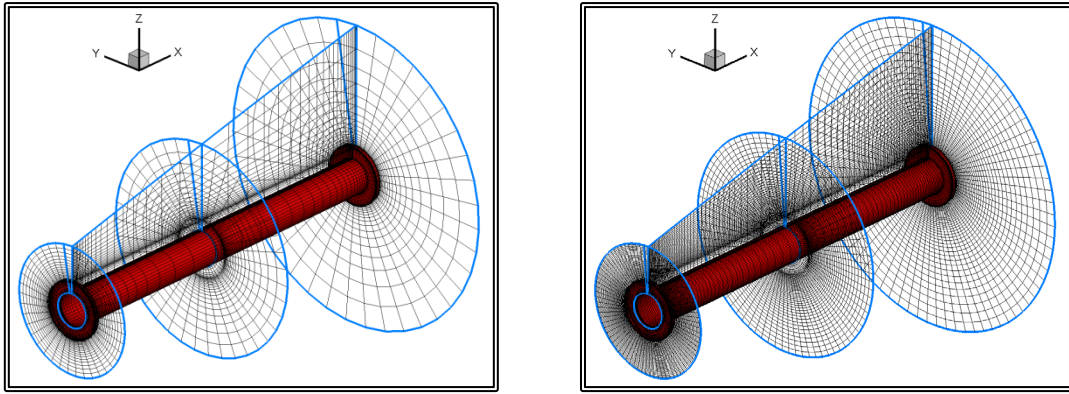
Figure 5.2.1 Perspective view of the numerical grid, test A (on the left) and B (on the right).
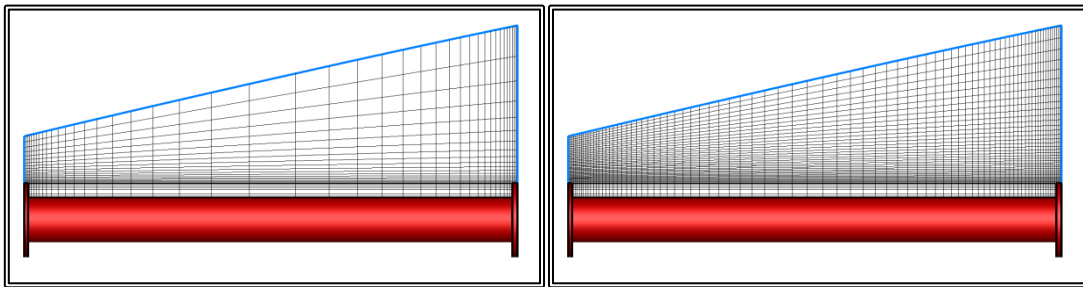
Figure 5.2.2 Side view of the numerical grid, section I=1, test A (on the left) and B (on the right).
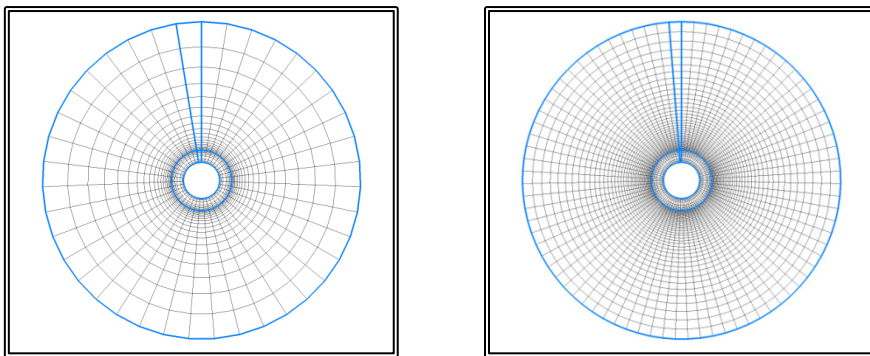
Figure 5.2.3 Section K=NK, test A (on the left) and B (on the right).

The viscous flow problem was then solved for each of the two blocks. In figure 5.2.4, the convergence history is presented. More specifically, the mass residual is depicted as a function of the pressure correction algorithm steps.

In figures 5.2.5 (a) and (b) the distribution of the pressure coefficient c_p is presented on the solid boundary. The pressure coefficient is calculated as:

$$c_P = \frac{p}{0.5 \cdot \rho \cdot U_\infty{}^2}(5.2.1)$$

Where p is the pressure and ρ is the fluid density.

In figures 5.2.6 to 5.2.8 the stream traces are presented on one longitudinal section of the flow field. In the same figures, the contours correspond to the intensity of the planar velocity, divided by the far field velocity. The peripheral velocity component is

ignored in the following figures, since the domain is symmetrical and the far field velocity is parallel to the shaft axis.
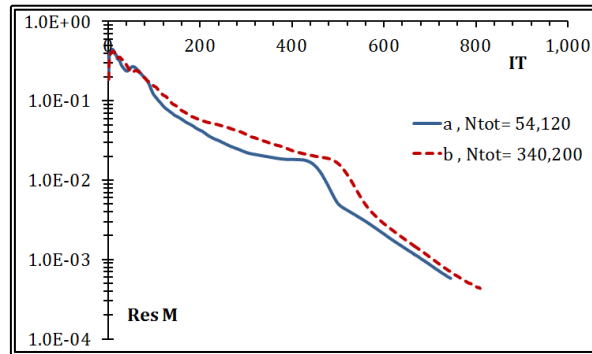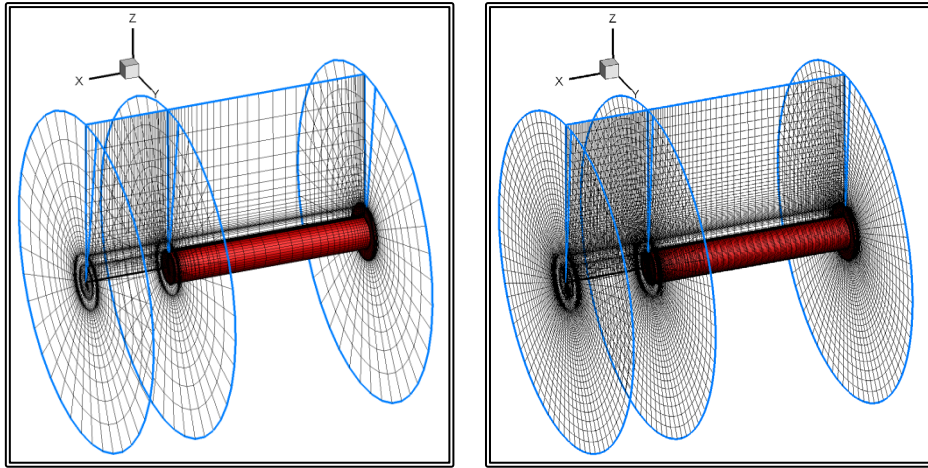

Figure 5.2.4 Mass residual convergence history, tests A and B.
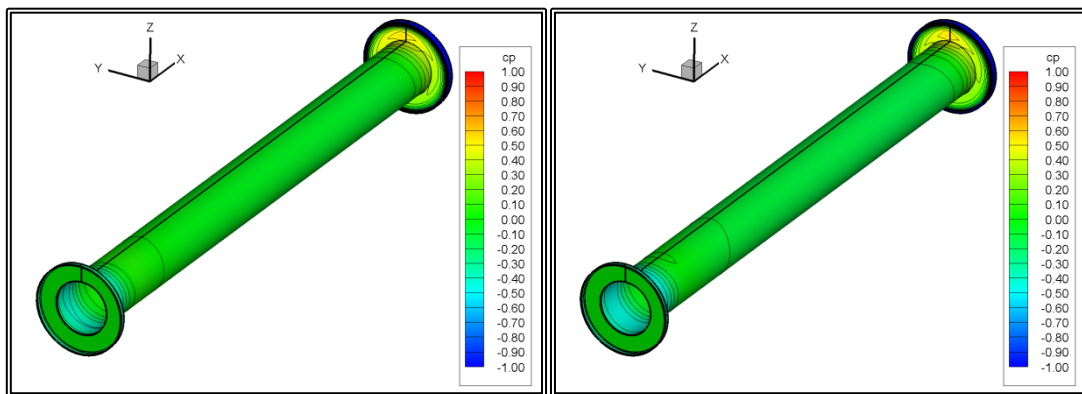
Figure 5.2.5 Pressure coefficient (c_P) contours on the shaft surface. From top right to bottom left, tests A and B.
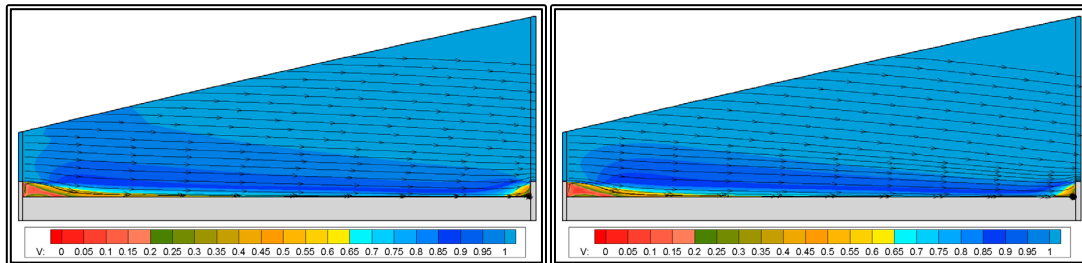
Figure 5.2.6 Cross flow envelopes and planar velocity contours. From top right to bottom left, tests A and B.
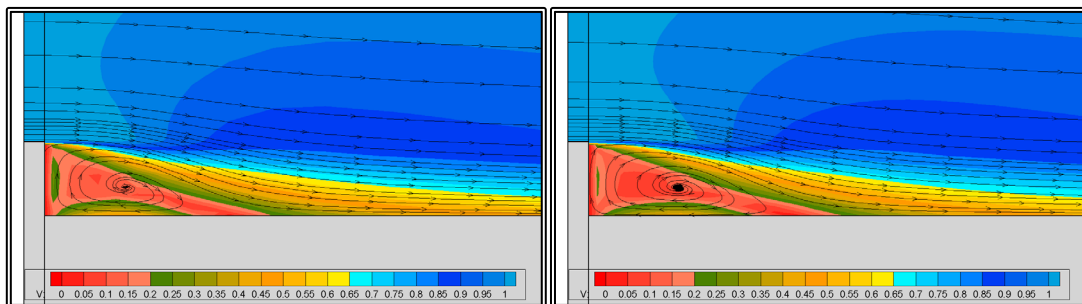
Figure 5.2.7 Detail of the cross flow envelopes and planar velocity contours, near the first step. From top right to bottom left, tests A and B.
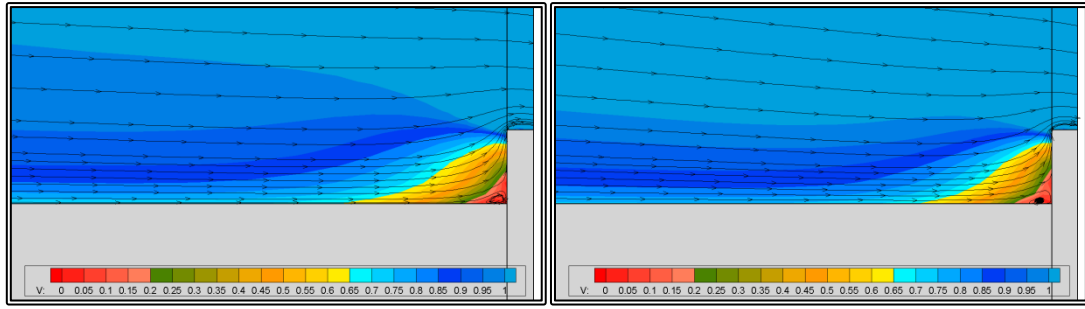
Figure 5.2.8 Detail of the cross flow envelopes and planar velocity contours, near the second step. From top right to bottom left, tests A and B.

5.2.2 Propeller Shaft Calculations, After Section

Two numerical tests were also conducted for the second shaft block The grid variables for both tests are presented in table 5.2.3, where NI is the number of nodes in the circumferential direction, NJ is the number of nodes in the radial direction and NK is the number of sections perpendicular to the shaft axis. NJ1 is the number of nodes in the radial direction at the strut bossing-shaft step, while NJ2 is the number of nodes in the radial direction at the shaft end. NKL is the number of sections along the shaft length and NKU and NKD, the number of sections on the strut bossing (upstream end) and abaft the shaft end respectively. The maximum radial extend of the grid is set equal to 10 times the shaft radius. In figures 5.2.9 to 5.2.11, several sections of the two blocks are presented.

Table 5.2.3 Main grid variables for the propeller shaft test, after section

	A	B
NI	41	81
NJ	39	59
NJ1	11	11
NJ2	10	10
NK	80	118
NKU	3	3
NKL	39	58
NKD	40	59
NIxNJxNK	127,920	563,922
Radial extend	$10.0 \times R_{Shaft}$	
Downstream extend	$5.0 \times R_{Shaft}$	

The viscous flow problem was then solved for each of the two blocks. In figure 5.2.12, the convergence history is presented. More specifically, the mass residual is depicted as a function of the pressure correction algorithm steps. In figures 5.2.13 (a) and (b) the distribution of the pressure coefficient c_p (eq. 5.2.1) is presented on the solid boundary. In figures 5.2.14 and 5.2.15 the stream traces are presented on one longitudinal section of the flow field. In the same figures, the contours correspond to the intensity of the planar velocity, divided by the far field velocity. The peripheral velocity component is ignored in the following figures, since the domain is symmetrical and the far field velocity is parallel to the shaft axis.

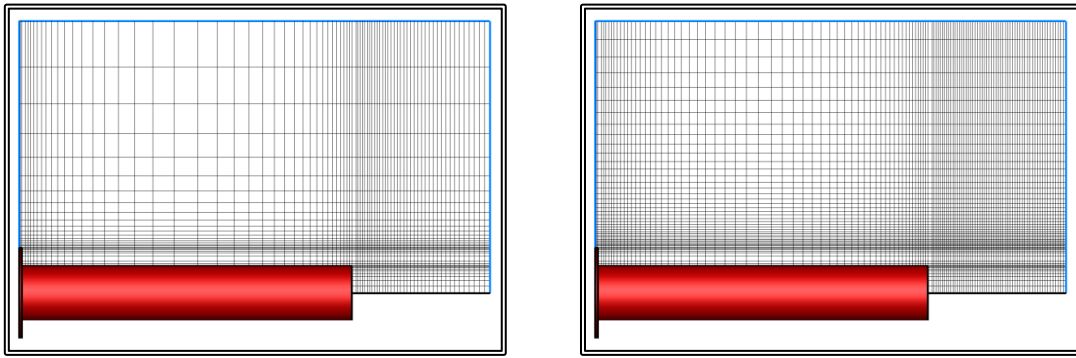**Figure 5.2.9** Perspective view of the numerical grid, test A (on the left) and B (on the right).

Figure 5.2.10 Side view of the numerical grid, section I=1, test A (on the left) and B (on the right).
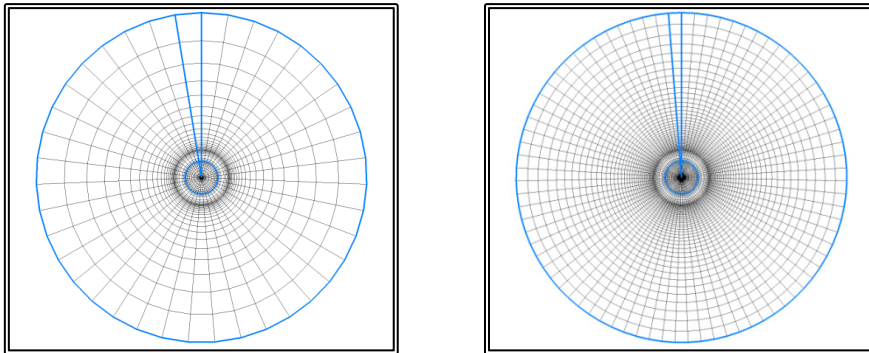

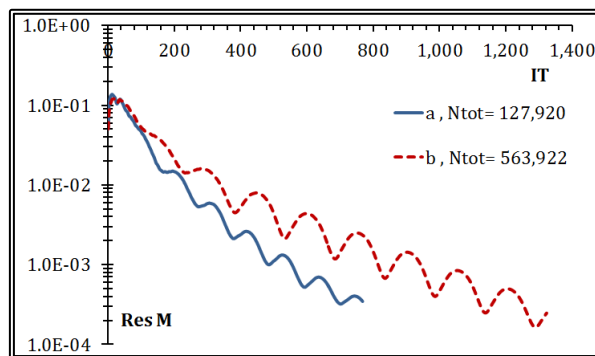**Figure 5.2.11** Section K=NK. From top right to bottom left, tests A and B.

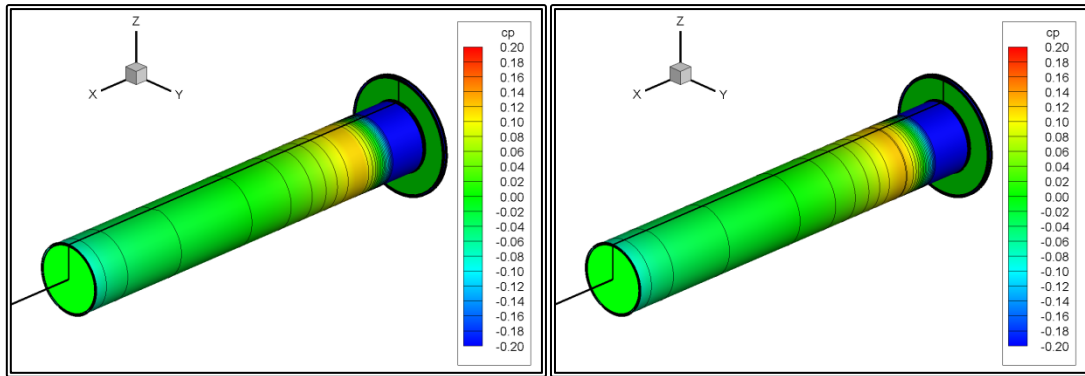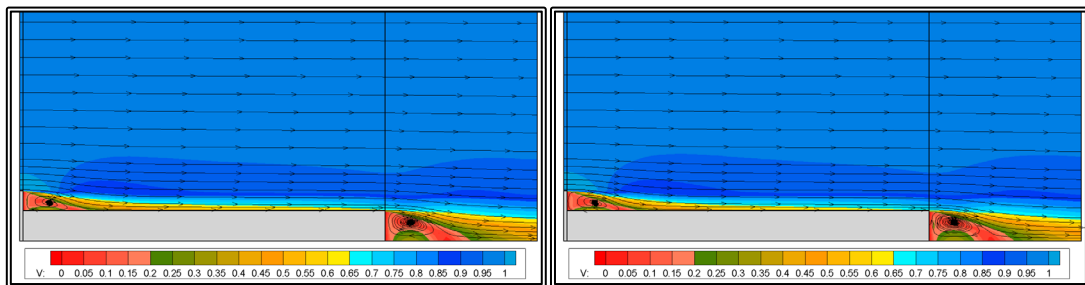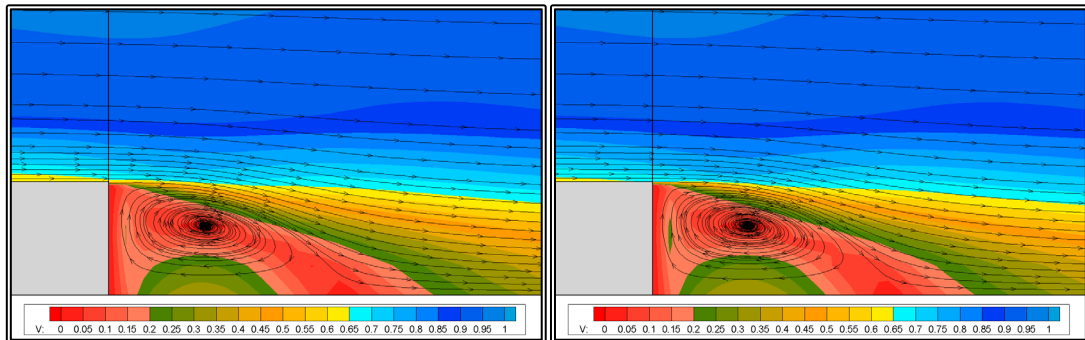**Figure 5.2.12** Mass residual convergence history, tests A and B.

Figure 5.2.13 Pressure coefficient (c_P) contours on the shaft surface. From top right to bottom left, tests A and B.

Figure 5.2.14 Cross flow envelopes and planar velocity contours. From top right to bottom left, tests A and B.

Figure 5.2.15 Detail of the cross flow envelopes and planar velocity contours, near the end of the shaft. From top right to bottom left, tests A and B.

The presented method can generate numerical grids around various configurations of a ship propeller shaft, taking into account possible steps in the shaft diameter. The modified RANS solver can now handle the o-type shaft block with the aforementioned steps. Also it is demonstrated that the solver can produce realistic results in terms of the flow characteristics and the pressure distribution on the shaft surface. Farther examination is required though, in order to determine the required grid density and to validate the produced integrated values, such as the shaft drag.

5.3   Flow Calculations about the Propeller Shaft Bossing

In order to solve the viscous flow around the shaft bossing of the LSMH 200/08 model, a C-H-type block was generated by employing the method described in paragraph 4.6. The block consists of planar orthogonal curvilinear grid sections, normal to the shaft axis. Three tests were conducted, using different grid densities. The values for the main grid variables are presented in table 5.3.1, for each of the three tests.

Table 5.3.1 Main grid variables for the shaft bossing test, forward section

	A	B	C
NI	160	200	242
NJ	40	50	61
NK	80	100	120
NIxNJxNK	512,000	1,000,000	1,771,440
Radial extend	10.0xR_{Shaft}		
Upstream extend	10.0xR_{Shaft}		

In the above table, NK is the number of planar sections normal to the shaft axis, NI is the number of nodes in the circumferential direction and NJ is the number of nodes in the radial direction. The maximum radial extend of the grid is set equal to 10 times the shaft radius. The upstream extend of the block, i.e. the distance of the first section from the point along the shaft where the bossing penetrates the hull, is also 10 times the shaft radius. In figures 5.3.1 to 5.3.12, several sections of the three blocks are presented.

One numerical test was performed with each of the grids. In all tests, the external flow is considered undisturbed and at the inlet and external boundaries of the block, the velocity is set equal to the free stream velocity U_∞ which in these tests is parallel to the shaft axis. The flow variables for all tests are presented in table 5.3.2.

Table 5.3.2 Flow variables for the shaft bossing test, forward section

Free Stream Velocity, U_∞	1.000	m/s
Fluid Viscosity, ν	1.030E-06	m²/s
Reynolds's Number, Re_D	2.136E+06	
Reference Length, L	0.220	m

The viscous flow problem was then solved. In figure 5.3.13, the convergence history is presented. More specifically, the mass residual is depicted as a function of the pressure correction algorithm steps.
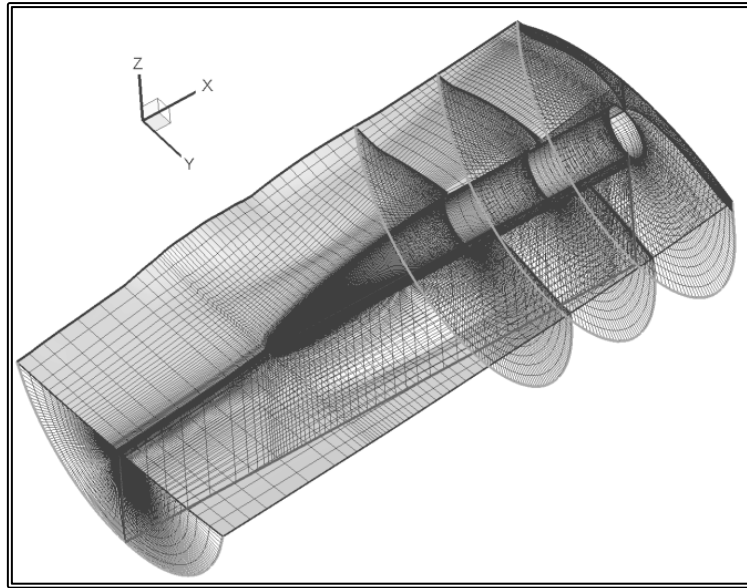
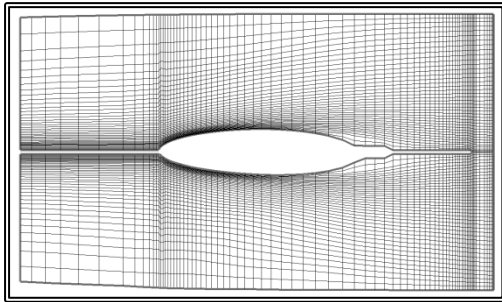**Figure 5.3.1** Perspective view of the numerical grid, test A.

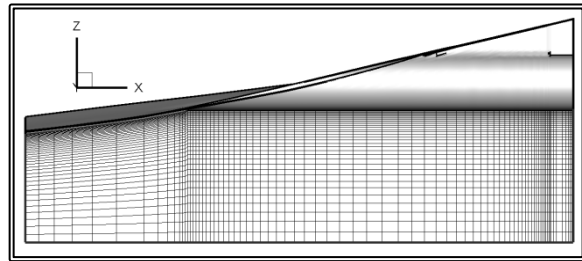**Figure 5.3.2** Numerical grid on the hull, I=1, I=NI, test A.

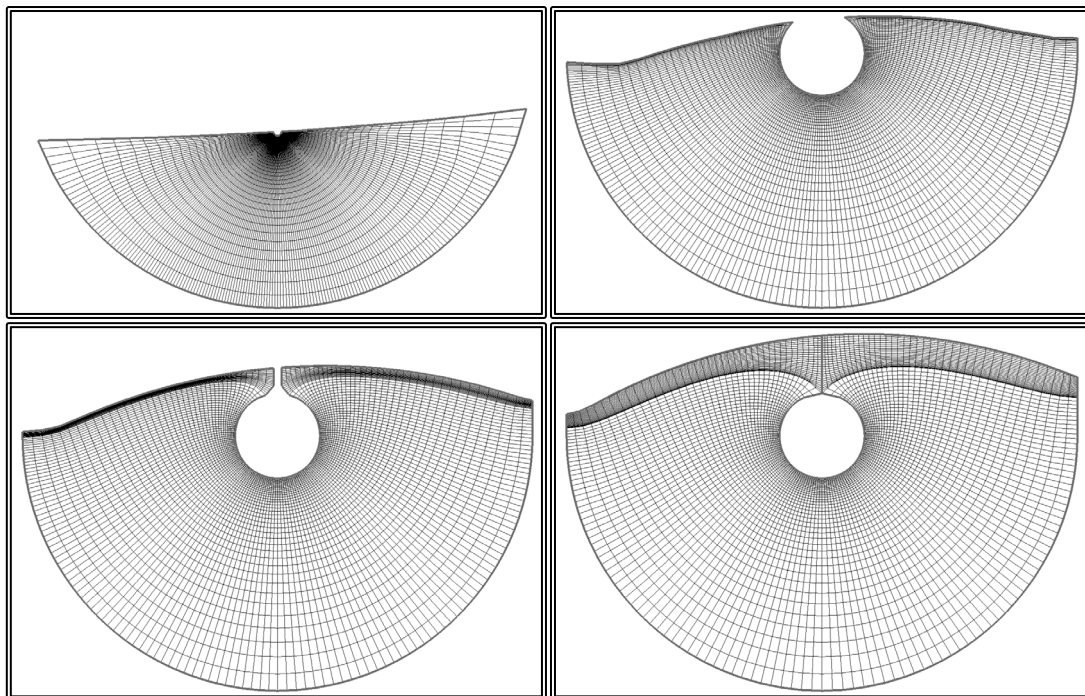**Figure 5.3.3** Numerical grid on the symmetry plane, I=NIM, test A.

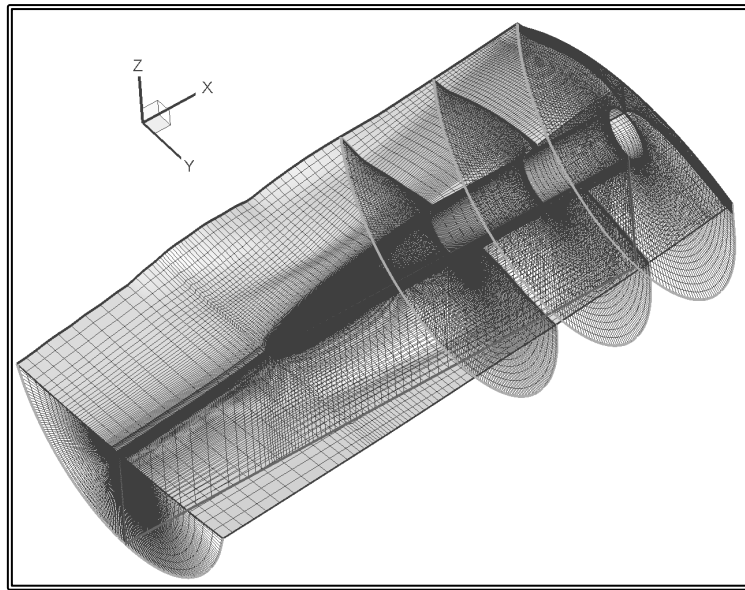**Figure 5.3.4** Numerical grid, test A, from top left to bottom right, sections K=1, K=42, K=51 and K=NK.

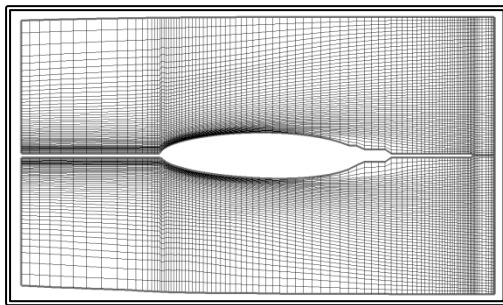**Figure 5.3.5** Perspective view of the numerical grid, test B.

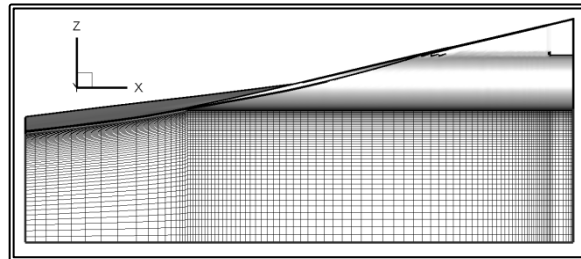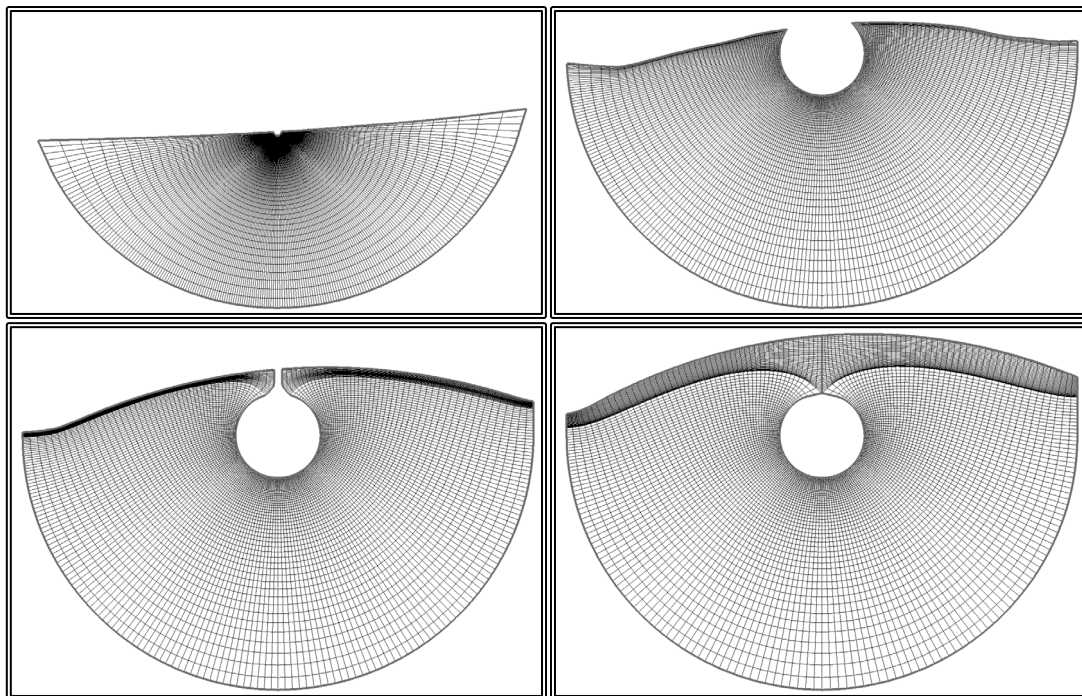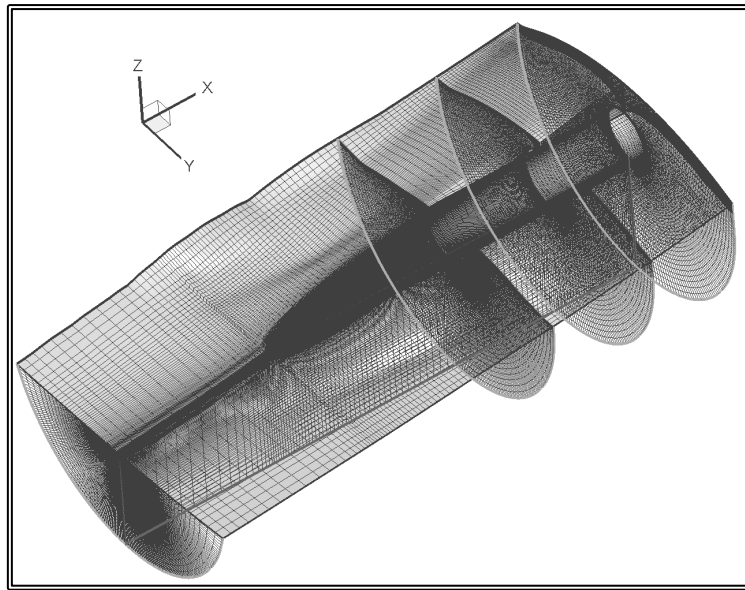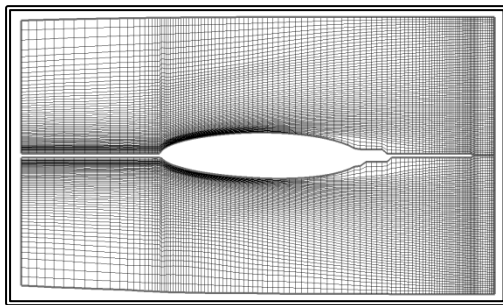**Figure 5.3.6** Numerical grid on the hull, I=1, I=NI, test B.

Figure 5.3.7 Numerical grid on the symmetry plane, I=NIM, test B.

Figure 5.3.8 Numerical grid, test B, from top left to bottom right, sections K=1, K=52, K=65 and K=NK.

Figure 5.3.9 Perspective view of the numerical grid, test C.

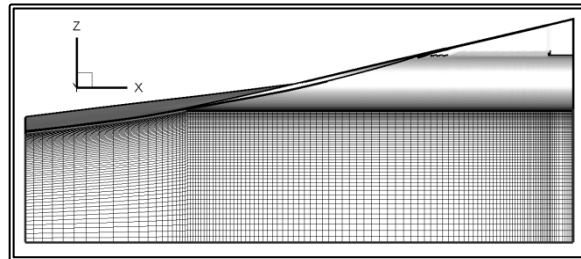**Figure 5.3.10** Numerical grid on the hull, I=1, I=NI, test C.

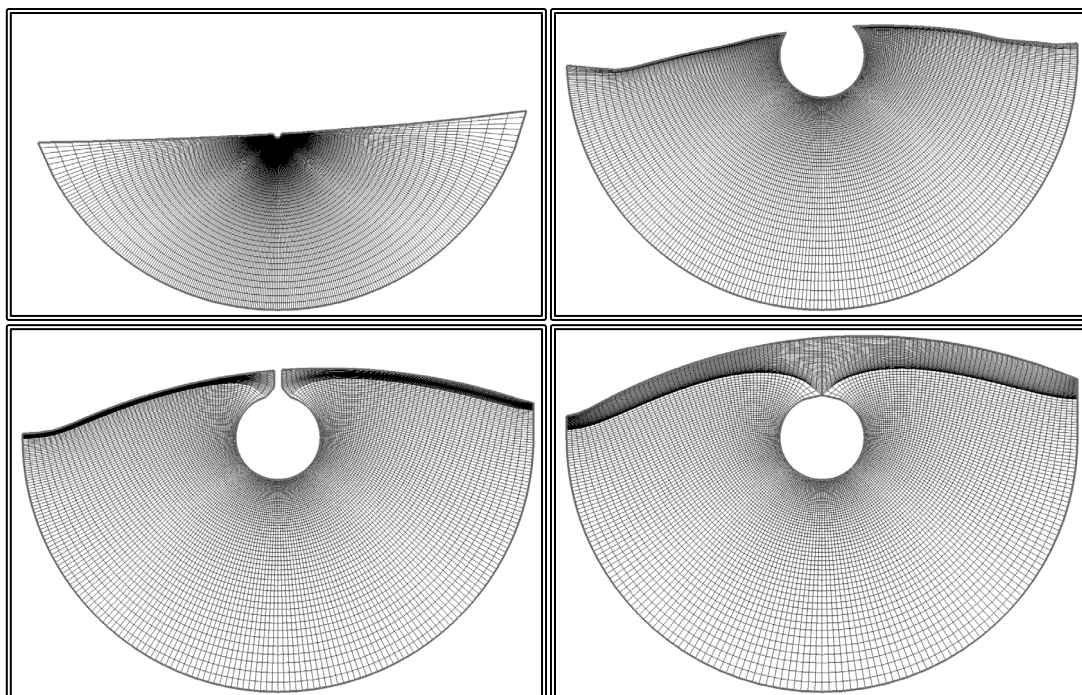**Figure 5.3.11** Numerical grid on the symmetry plane, I=NIM, test C.

Figure 5.3.12 Numerical grid, test C, from top left to bottom right, sections K=1, K=62, K=80 and K=NK.
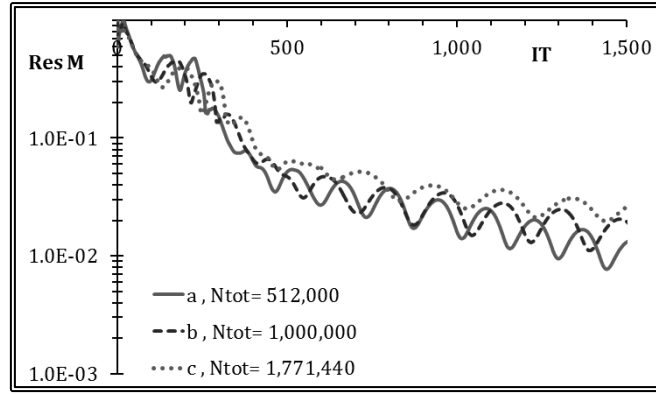
Figure 5.3.13 Mass residual convergence history, tests A, B and C.

In the presented numerical tests, the convergence level for the mass residual is quite high. This is the primarily the result of the unrealistic boundary conditions (uniform flow) especially on the outflow (downstream, K=NK) boundary.

In figures 5.3.14 to 5.3.16 the distribution of the pressure coefficient c_P is presented on the solid boundary. The pressure coefficient is calculated as:

$$c_P = \frac{p}{0.5 \cdot \rho \cdot U_\infty{}^2} (5.3.1)$$

Where p is the pressure and ρ is the fluid density.

In figures 5.3.17 to 5.3.20, the iso-wake contours are presented for the three tests. More specifically the contours for the w-velocity component, the one parallel to the shaft axis, divided by the free-stream velocity U_∞ are presented at for location along the shaft axis. The four locations are presented in figure 5.3.17, while in figures 5.3.18 to 5.3.20, the iso-wake contours are presented for the three tests.

The presented method can generate the numerical grid around various configurations of what is a rather difficult geometry, around a propeller shaft bossing. The modified RANS solver can now handle the C-H-type block with the East, West and South boundaries being handled as solid boundaries. In this paragraph it is demonstrated that the solver can produce realistic results in terms of the flow characteristics and the pressure distribution on the bossing surface. Farther examination is required though, in order to determine the required grid density and extends. Also the method requires validating in terms of the produced integrated values, such as the increase in the ship resistance.
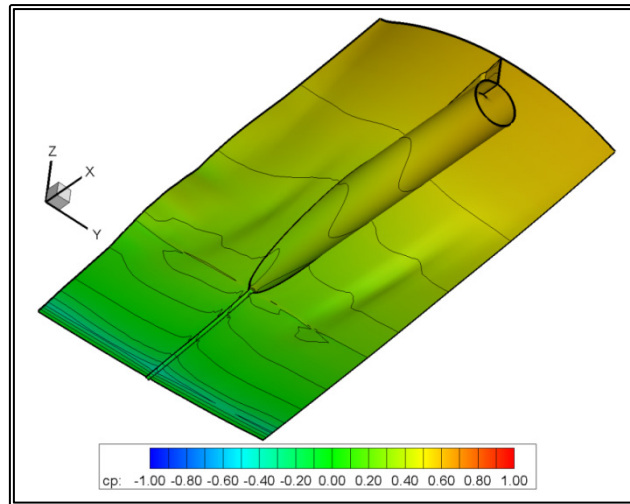
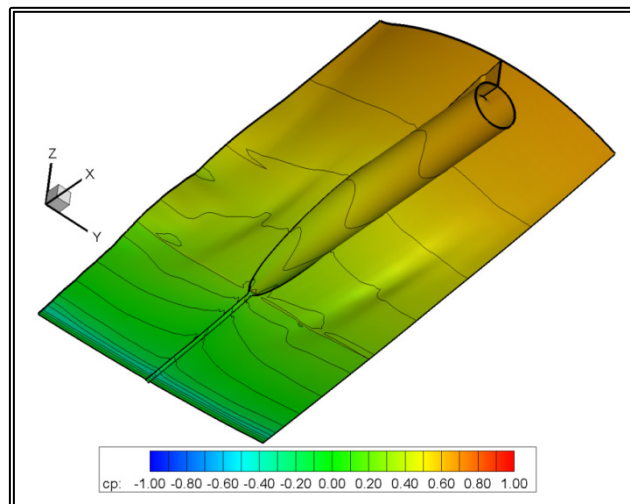**Figure 5.3.14** Pressure coefficient (c_P) contours on the solid boundary, test A.

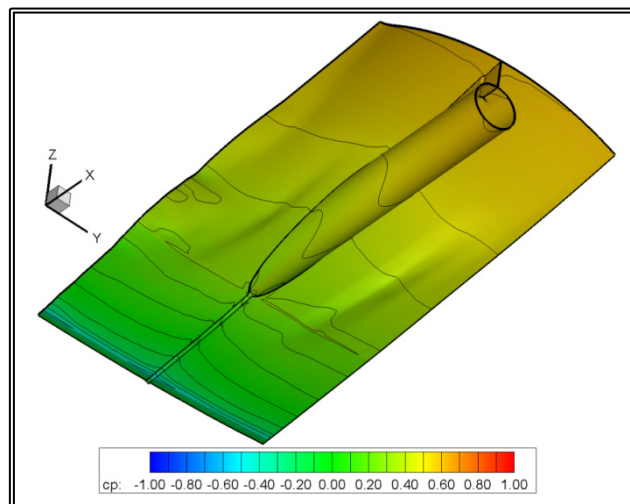**Figure 5.3.15** Pressure coefficient (c_P) contours on the solid boundary, test B.

Figure 5.3.16 Pressure coefficient (c_P) contours on the solid boundary, test C.
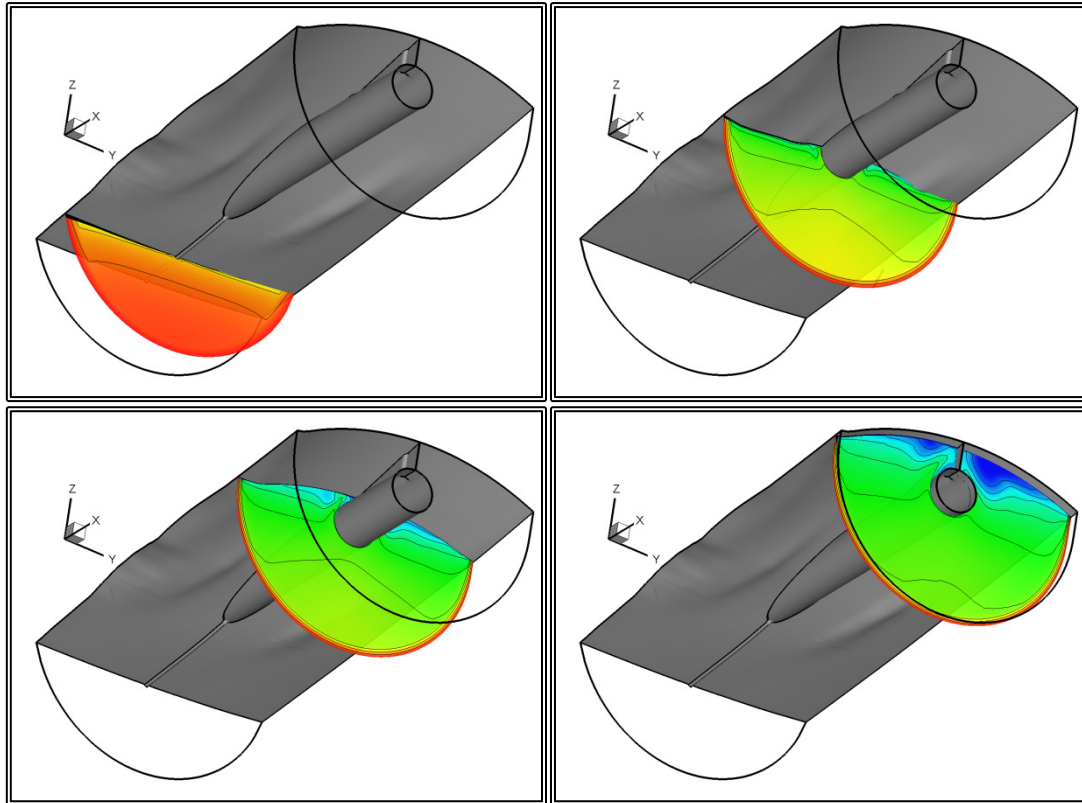
Figure 5.3.17 Iso-wake (w/ U_∞) contour locations, from top left to bottom right, x_1=-2.0, x_2=-1.0, x_3=-0.5 and x_4=-0.05, test A.

Figure 5.3.18 Iso-wake (w/ U_∞) contours, from top left to bottom right, x_1=-2.0, x_2=-1.0, x_3=-0.5 and x_4=-0.05, test A.

Figure 5.3.19 Iso-wake (w/ U_∞) contours, from top left to bottom right, x_1=-2.0, x_2=-1.0, x_3=-0.5 and x_4=-0.05, test B.
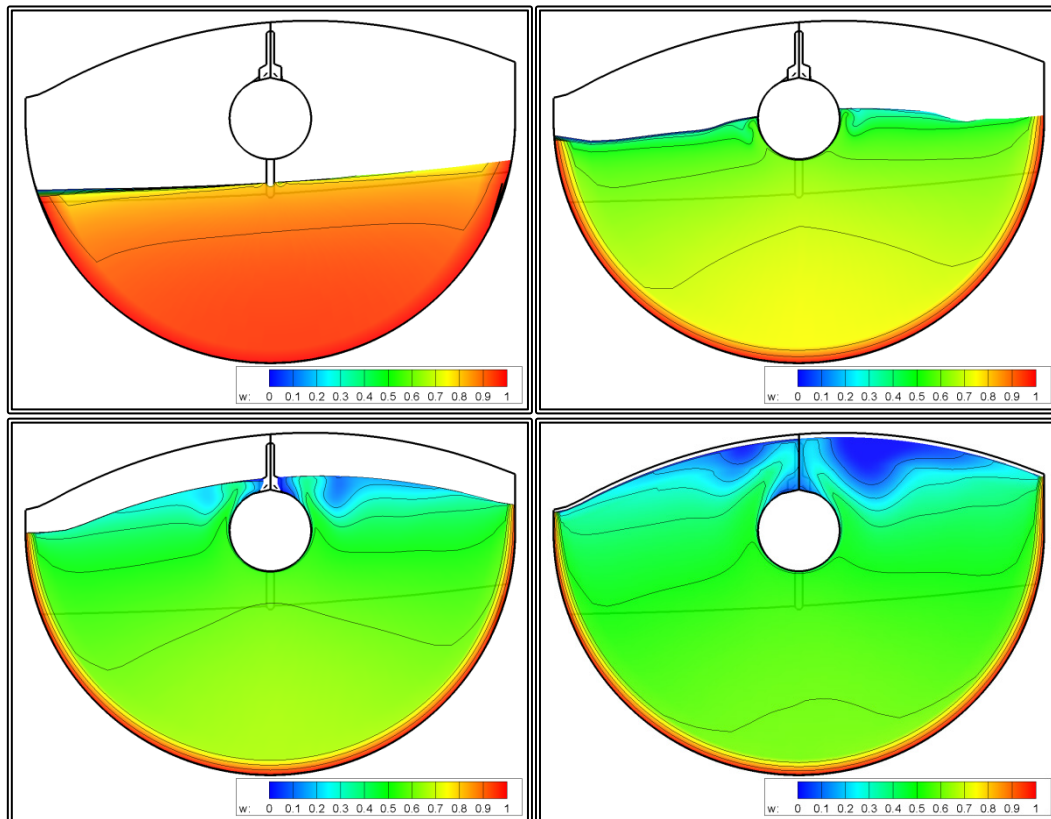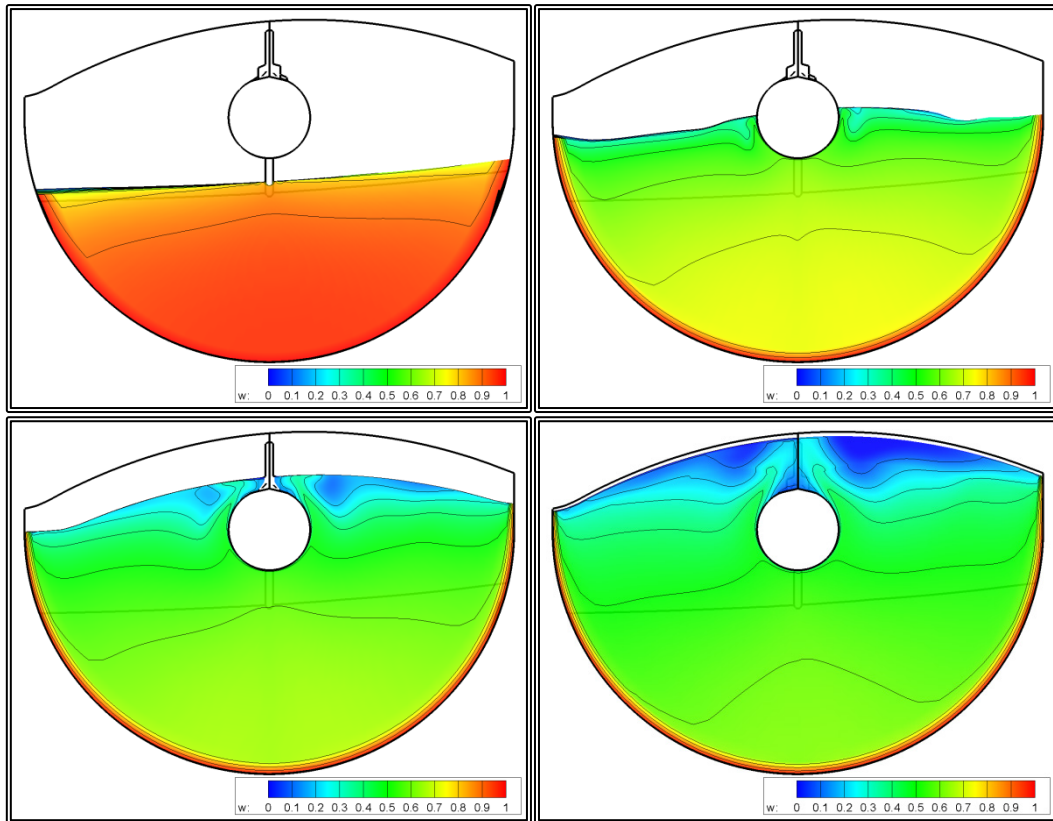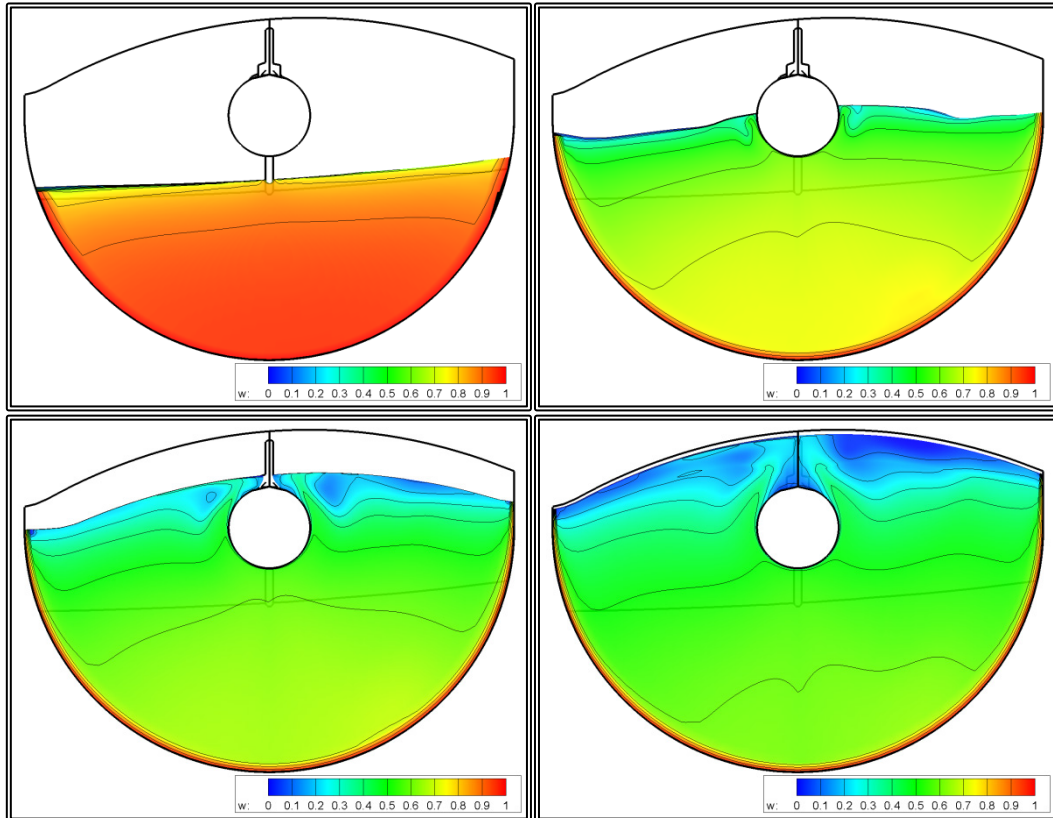

Figure 5.3.20 Iso-wake (w/ U_∞) contours, from top left to bottom right, x_1=-2.0, x_2=-1.0, x_3=-0.5 and x_4=-0.05, test C.

5.4 Flow Calculations about a Strut

In order to solve the viscous flow around a strut of the LSMH 200/08 model, a C-H-type block was generated by employing the method described in paragraph 4.8. The block consists of initially planar orthogonal curvilinear grid sections, normal to the strut axis. Near the hull, the first section is projected on the hull while a set number of sections are also deformed. Two tests were conducted, using different grid densities for the outer strut of the shaft V-bracket. The values for the main grid variables are presented in table 5.4.1, for each of the tests.

Table 5.4.1 Main grid variables for the strut tests

	A	B
NI	198	298
NIS	158	238
NJ	31	46
NK	30	45
NIxNJxNK	184,140	616,860
Upstream extend	0.5xC	
Side extend	1.0xC	
Downstream extend	1.0xC	

In the above table, NK is the number of planar sections normal to the strut axis, NI is the number of nodes in the circumferential direction and NJ is the number of nodes in the radial direction. NIS is the number of nodes in the circumferential direction that lay on the strut surface.

The upstream extend (ahead of the strut leading edge) of the grid is set equal to half a chord while the side and downstream (abaft the strut trailing edge) extends are set equal to one chord length. In figures 5.4.1 and 5.4.2, the arrangement for the strut block is presented. In figures 5.4.3 to 5.4.5 several sections of the two blocks are presented.

One numerical test was performed with each of the grids. In both tests, the external flow is considered undisturbed and at the inlet and external boundaries of the block, the velocity is set equal to the free stream velocity U_∞ which in these tests is normal to the strut axis. On the hull, solid boundary conditions are employed. The flow variables for the tests are presented in table 5.4.2. The viscous flow problem was then solved. In figure 5.4.6, the convergence history is presented. More specifically, the mass residual is depicted as a function of the pressure correction algorithm steps.

Table 5.4.2 Flow variables for the strut tests

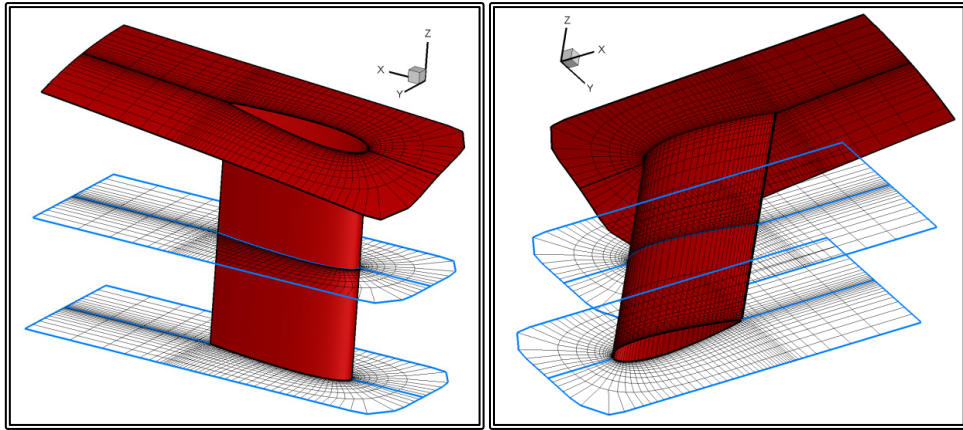|		
Free Stream Velocity, U_∞	10.000	m/s
Fluid Viscosity, ν	1.030E-06	m²/s
Reynolds's Number, Re	2.913+06	
Reference Chord, C	0.300	m

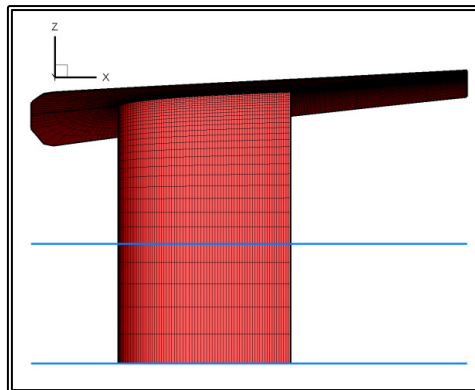**Figure 5.4.1** Perspective view of the strut grid arrangement.

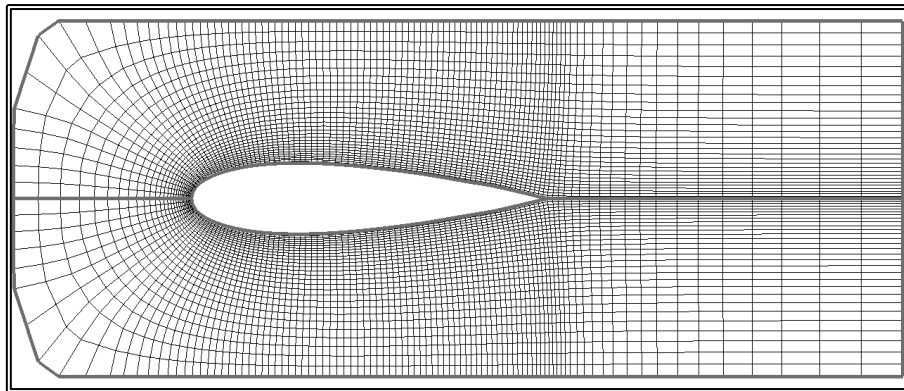**Figure 5.4.2** Side view of the strut grid arrangement.

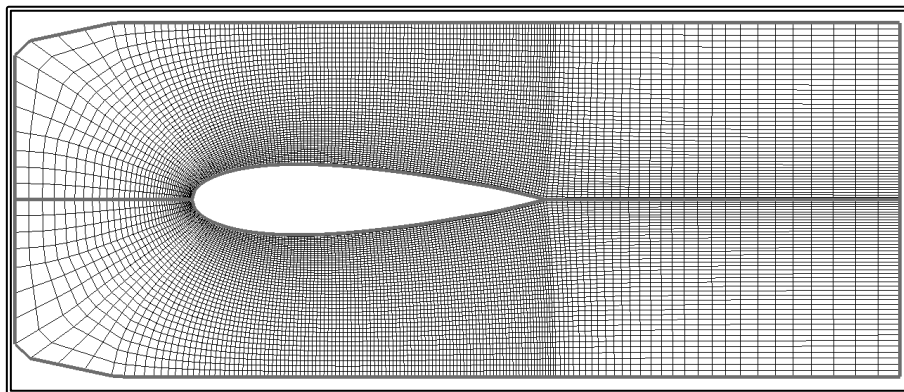**Figure 5.4.3** 2-D grid section at the strut root, test A, N_{Tot}=184,140 nodes.

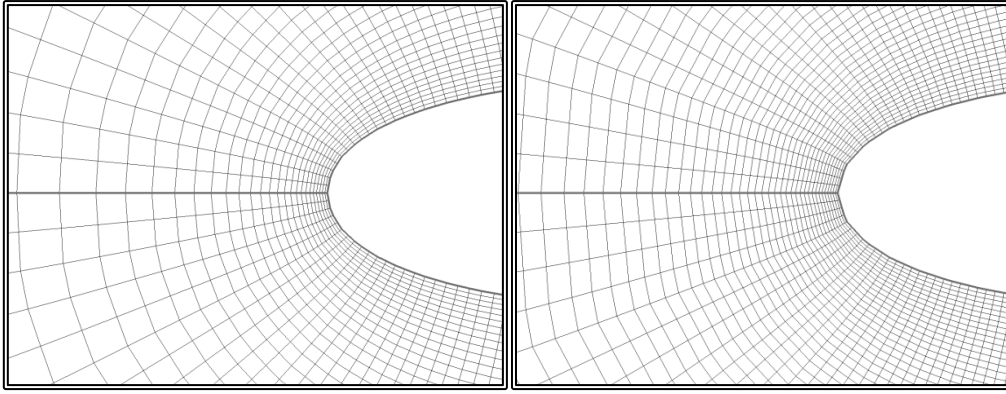**Figure 5.4.4** 2-D grid section at the strut root, test B, N_{Tot}=616,860 nodes.

Figure 5.4.5 Detail of the 2-D grid section near the leading edge, on the left test A, N_{Tot}=184,140 nodes, and on the right test B, N_{Tot}=616,860 nodes,.
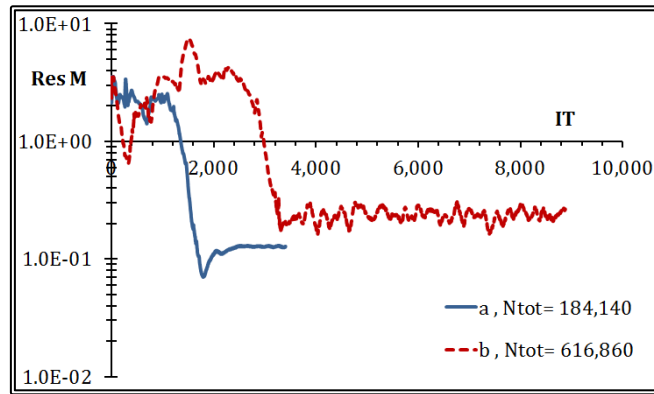

Figure 5.4.6 Mass residual convergence history, tests A, and B.

In the presented numerical tests, the convergence level for the mass residual is quite high. This is the primarily the result of the unrealistic boundary conditions (uniform flow) in conjunction with the narrow width of the strut block.

The test cases are compared in terms of the total Drag which is calculated as the sum of the skin friction R_F and the pressure drag R_P:

$$\text{Drag} = R_P + R_F \qquad (5.4.1)$$

$$R_P = \iint_{A_S} p \cdot \mathbf{n} \cdot \mathbf{i} \ ds \quad (5.4.1)$$

$$R_F = \iint_{A_S} \tau_w \cdot \mathbf{s} \cdot \mathbf{i} \ ds \quad (5.4.2)$$

Where A_S is the strut surface, p is the pressure on the strut surface, $\mathbf{n}$ is the unit vector normal to the strut surface, $\mathbf{i}$ the unit vector parallel to the strut chord, τ_w is the wall shear stress and $\mathbf{s}$ is the tangential unit vector to the strut surface.

The drag components are expressed in their respective non-dimensional form:

$$C_P = \frac{R_P}{0.5 \cdot \rho \cdot A_S \cdot U_\infty{}^2} \qquad (5.4.4)$$

$$C_F = \frac{R_F}{0.5 \cdot \rho \cdot A_S \cdot U_\infty{}^2} \qquad (5.4.5)$$

$$C_D = C_P + C_F = \frac{\text{Drag}}{0.5 \cdot \rho \cdot A_S \cdot U_\infty{}^2} \ (5.4.6)$$

In table 5.4.3, the results of the two tests are presented, in terms of the non-dimensional drag coefficients.

Table 5.4.3 Strut tests, Drag coefficients

	A	B
NIxNJxNK	184,140	616,860
C_D	5.411E-03	5.284E-03
C_F	5.013E-03	5.263E-03
C_P	1.398E-03	1.021E-03

In figure 5.4.7, the convergence history for the drag coefficient (C_D) is presented, as a function of the pressure correction algorithm steps.
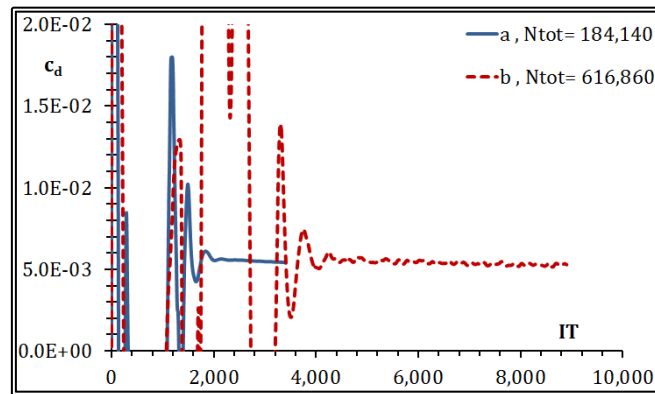

Figure 5.4.7 Drag coefficient (C_D) convergence history, tests A, and B.

The tests are also compared in terms of the values of the localized coefficients for the pressure c_p and the skin friction c_f:

$$c_P = \frac{p}{0.5 \cdot \rho \cdot U_\infty^2} \quad (5.4.7)$$

$$c_f = \frac{\tau_w}{0.5 \cdot \rho \cdot U_\infty^2} \quad (5.4.8)$$

In figures 5.4.8 and 5.4.9, the pressure coefficient contours are presented on the two sides of the strut. In figures 5.4.10 and 5.4.11, the pressure c_p and the skin friction c_f coefficients are presented on a section half-way along the length of the strut.

The presented method can generate the numerical grid around a propeller strut. The strut may have a varying chord length and twist along its length. The modified RANS solver can now handle the C-H-type block with the Upstream boundary being handled as a solid boundary, while the South boundary is handled partially as a solid boundary and partially as a symmetry line. In this paragraph it is demonstrated that the solver can produce realistic results in terms of the flow characteristics and the pressure and skin friction distribution on the strut surface. Farther examination is required though, in order to determine the required grid density and extends. Also the method requires validating in terms of the produced integrated values, such as the increase in the ship resistance.
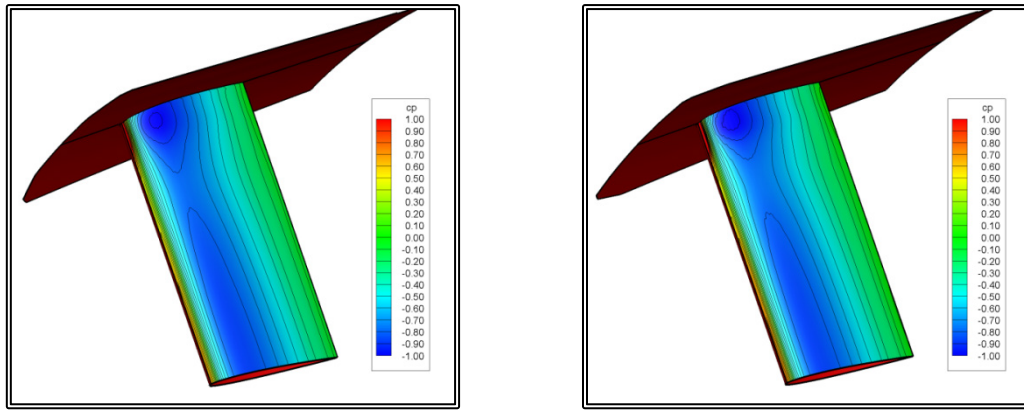
Figure 5.4.8 Pressure coefficient (c_P) contours on the outer side of the strut surface, tests A (on the left) and B (on the right).
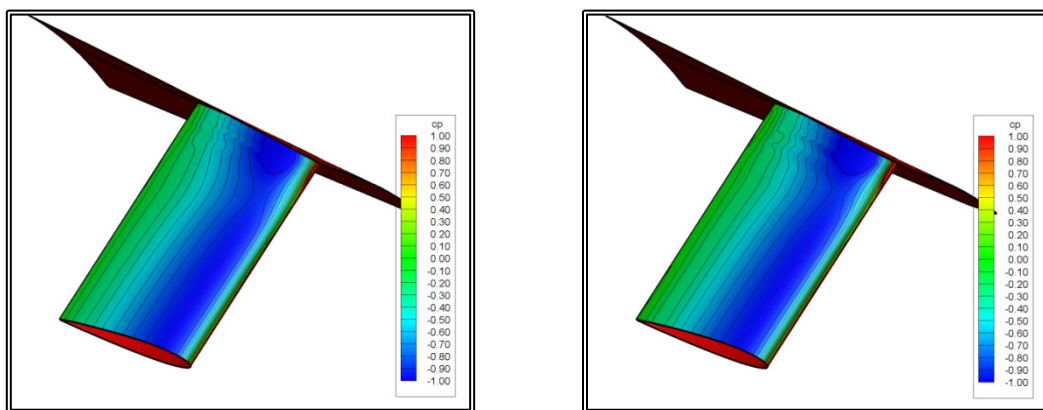
Figure 5.4.9 Pressure coefficient (c_P) contours on the inner side of the strut surface, tests A (on the left) and B (on the right).
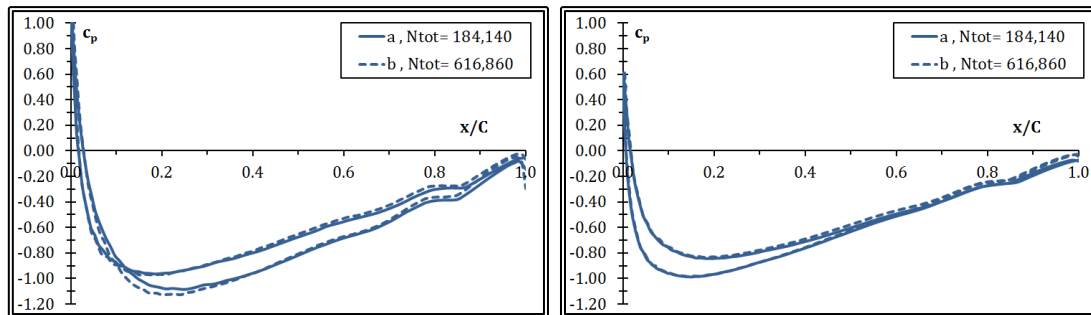

Figure 5.4.10 Pressure Drag coefficient (c_P) distribution, tests A and B, strut root (on the left) and half way along the strut length (on the right).
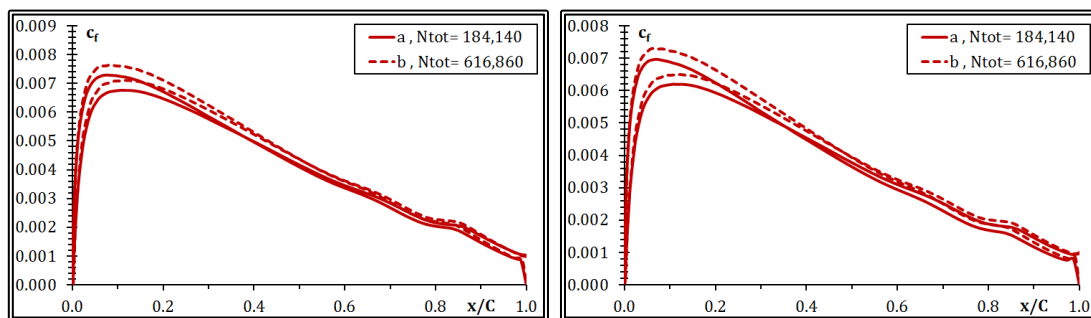

Figure 5.4.11 Skin Friction coefficient (c_f) distribution, tests A and B, strut root (on the left) and half way along the strut length.

5.5   Flow Calculations about the Rudder

In order to solve the viscous flow around one of the twin rudders of the LSMH 200/08 model, a C-H-type block was generated by employing the method described in paragraph 4.9. The block consists of initially planar orthogonal curvilinear grid sections, normal to the rudder axis. Near the hull, the first section is projected on the hull while a set number of sections are also deformed. In table 5.5.1, the values for the main grid variables are presented for two tests that were conducted.

Table 5.5.1 Main grid variables for the rudder tests

	A	B
NI	198	298
NIS	158	238
NJO	30	45
NJI	11	11
NK	58	78
NKU	20	20
NKL	30	45
NKD	10	15
NIxNJxNK	459,360	1,278,420
Upstream extend	0.5xC	
Side extend	1.0xC	
Downstream extend	1.0xC	
Extend under the tip	0.5xC	

In the above table, NKL is the number of planar sections normal to the rudder axis, NI is the number of nodes in the circumferential direction and NJO is the number of nodes in the radial direction. NIS is the number of nodes in the circumferential direction that lay on the rudder surface. NJI is the number of nodes in the radial direction that form the inner sub-grid for solving the flow below the rudder tip. Finally NKU and NKD correspond to the number of section above the rudder kink (see figure 5.5.1) and below the rudder tip respectively.

The extend of the block below the rudder tip is set equal to half a chord. The upstream extend of the grid (ahead of the rudder leading edge) is set equal to half a chord while the side and downstream (abaft the rudder trailing edge) extends are set equal to one chord length. In figures 5.5.1 (a) and (b), the arrangement for the rudder block is presented. In figures 5.5.2 and 5.5.3 two sections of the rudder block, A, are presented, at the rudder root and at the tip respectively. In figures 5.5.4 and 5.5.5 the corresponding sections are presented for block B. In figures 5.5.6 and 5.5.7, a detail of the above grids is presented, near the leading edge.

For each of the two grids, one numerical test was performed. The external flow was considered undisturbed and at the inlet and external boundaries of the block, the velocity was set equal to the free stream velocity U_∞ which in these tests is normal to the rudder axis. On the hull and the rudder surface, solid boundary conditions are employed. The flow variables for the tests are presented in table 5.5.2. The viscous flow problem was then solved. In figure 5.5.8, the convergence history is presented.

More specifically, the mass residual is depicted as a function of the pressure correction algorithm steps.

Table 5.5.2 Flow variables for the rudder tests

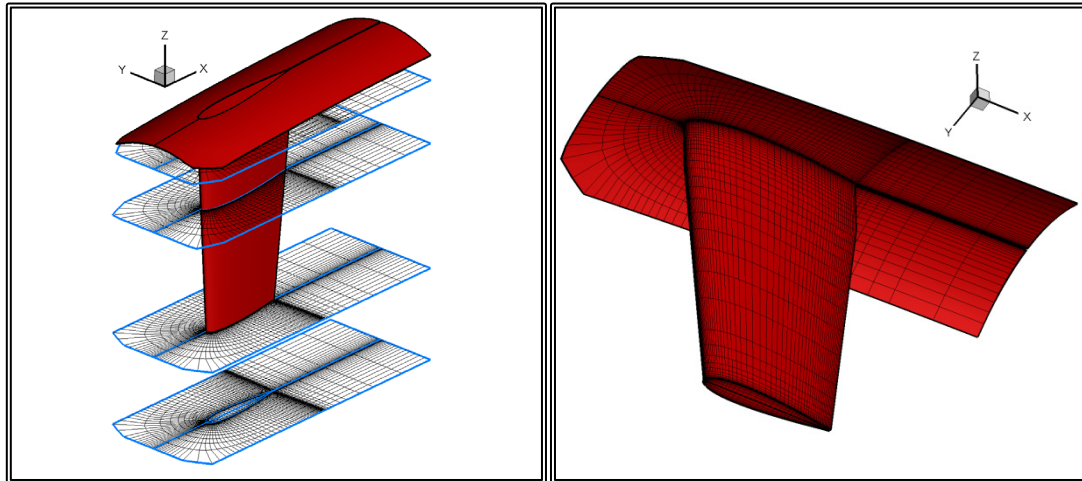| Free Stream Velocity, U_∞	10.000	m/s
Fluid Viscosity, ν	1.030E-06	m^2/s
Reynolds's Number, Re	7.087E+06	
Reference Chord, C	0.730	m

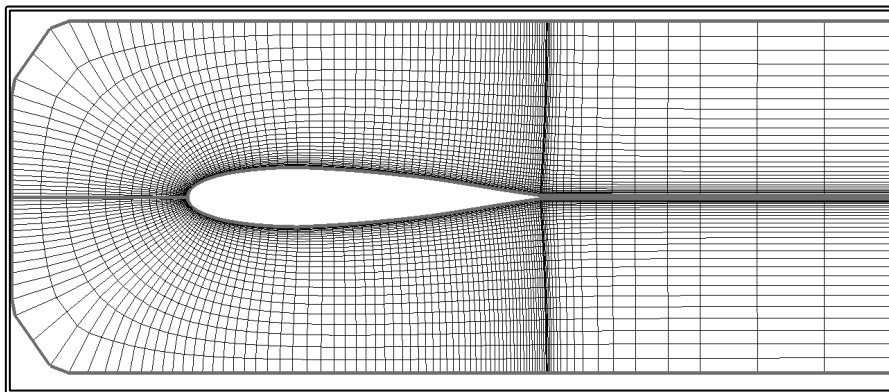**Figure 5.5.1** Perspective view of the numerical grid arrangement.

Figure 5.5.2 2-D grid section at the rudder root, test A, N_{Tot}=459,360 nodes.
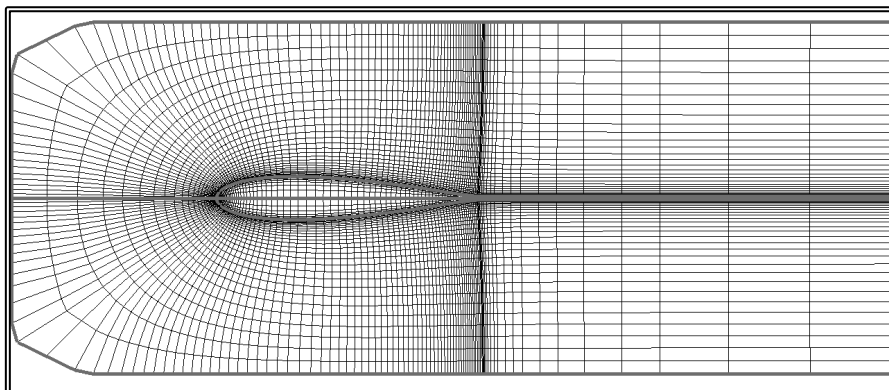
Figure 5.5.3 2-D grid section at the rudder tip, test A, N_{Tot}=459,360 nodes.
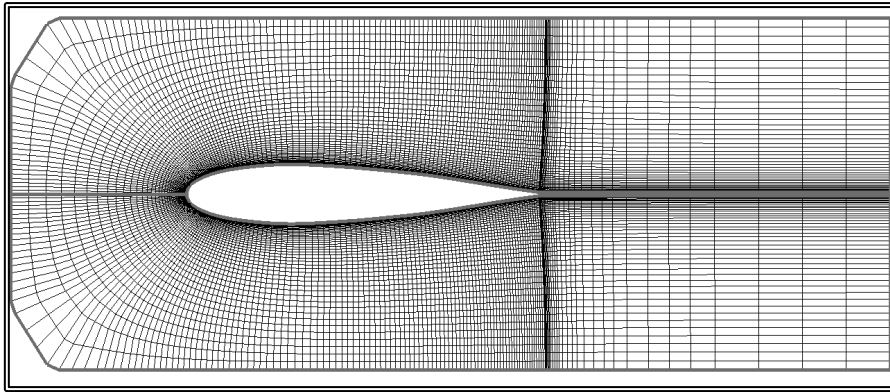
Figure 5.5.5 2-D grid section at the rudder root, test B, N_{Tot}=1,278,420 nodes.

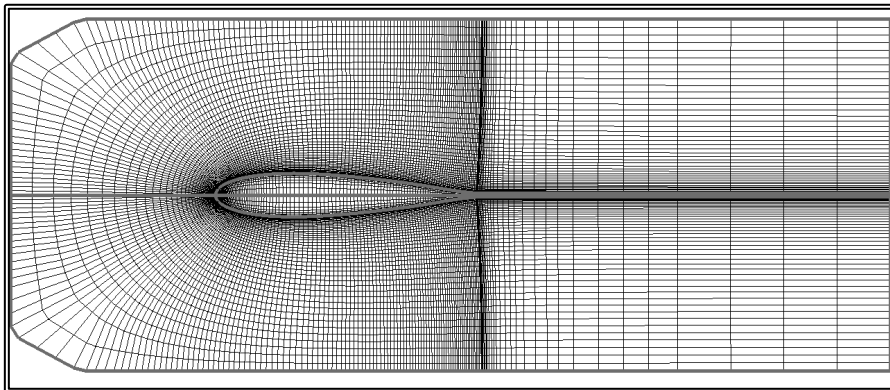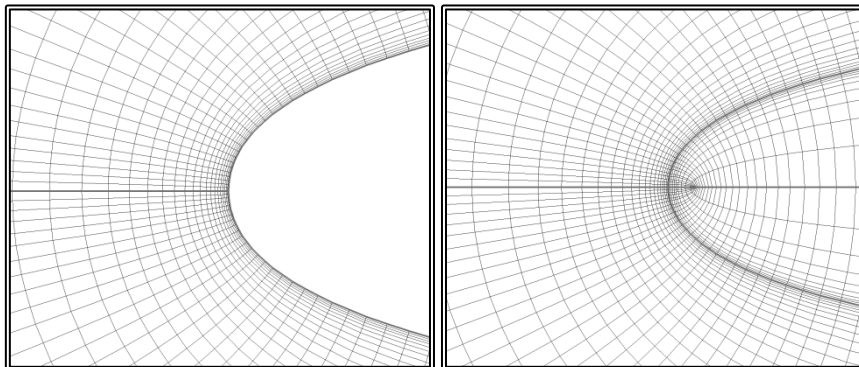**Figure 5.5.5** 2-D grid section at the rudder tip, test B, N_{Tot}=1,278,420 nodes.

Figure 5.5.6 Detail of the 2-D grid section near the leading edge, test A, N_{Tot}=459,360 nodes, rudder root on the left and rudder tip on the right.
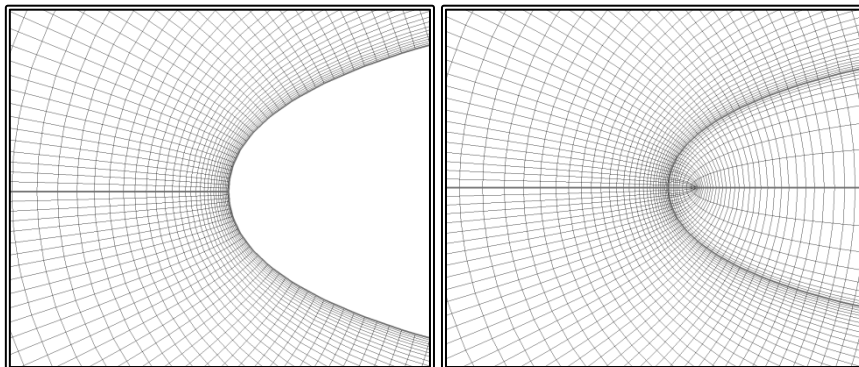

Figure 5.5.7 Detail of the 2-D grid section near the leading edge, test B, N_{Tot}=1,278,420 nodes, rudder root on the left and rudder tip on the right.
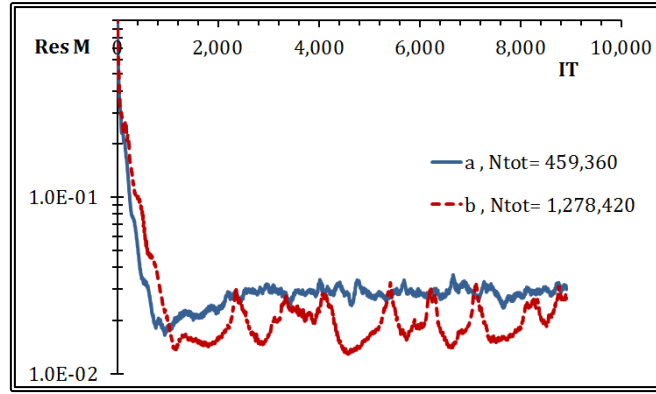
Figure 5.5.8 Mass residual convergence history, tests A, and B.

In the presented numerical tests, the convergence level for the mass residual is quite high. This is the primarily the result of the unrealistic boundary conditions (uniform flow) in conjunction with the narrow the narrow width of the rudder block.

The test cases are compared in terms of the total Drag which is calculated as the sum of the skin friction R_F and the pressure drag R_P:

$$Drag = R_P + R_F \qquad (5.5.1)$$

$$R_P = \iint_{A_R} p \cdot \mathbf{n} \cdot \mathbf{i} \ ds \quad (5.5.1)$$

$$R_F = \iint_{A_R} \tau_w \cdot \mathbf{s} \cdot \mathbf{i} \ ds \quad (5.5.2)$$

Where A_R is the rudder surface, p is the pressure on the rudder surface, $\mathbf{n}$ is the unit vector normal to the rudder surface, $\mathbf{i}$ the unit vector parallel to the rudder chord, τ_w is the wall shear stress and $\mathbf{s}$ is the tangential unit vector to the rudder surface.

The drag components are expressed in their respective non-dimensional form:

$$C_P = \frac{R_P}{0.5 \cdot \rho \cdot A_R \cdot U_\infty^2} \qquad (5.5.4)$$

$$C_F = \frac{R_F}{0.5 \cdot \rho \cdot A_R \cdot U_\infty^2} \qquad (5.5.5)$$

$$C_D = C_P + C_F = \frac{Drag}{0.5 \cdot \rho \cdot A_R \cdot U_\infty^2} (5.5.6)$$

In table 5.5.3, the results of the two tests are presented, in terms of the non-dimensional drag coefficients.

Table 5.5.3 Rudder tests, Drag coefficients

	A	B
NIxNJxNK	459,360	1,278,420
C_D	5.708E-03	5.530E-03
C_F	3.045E-03	3.013E-03
C_P	2.663E-03	1.517E-03

In figure 5.5.9, the convergence history for the drag coefficient (C_D) is presented, as a function of the pressure correction algorithm steps.
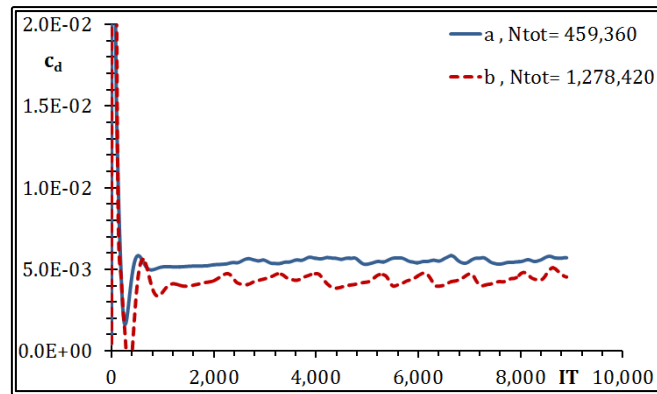
Figure 5.5.9 Drag coefficient (C_D) convergence history, tests A, and B.

The tests are also compared in terms of the values of the localized coefficients for the pressure c_p and the skin friction c_f:

$$c_P = \frac{p}{0.5 \cdot \rho \cdot U_\infty^2} (5.5.7)$$

$$c_f = \frac{\tau_w}{0.5 \cdot \rho \cdot U_\infty^2} (5.5.8)$$

In figures 5.5.10 (a) and (b), the pressure coefficient contours are presented on the rudder surface. In figures 5.5.11 and 5.5.12, the pressure c_p and the skin friction c_f coefficients are presented on a section at the kink of the rudder.
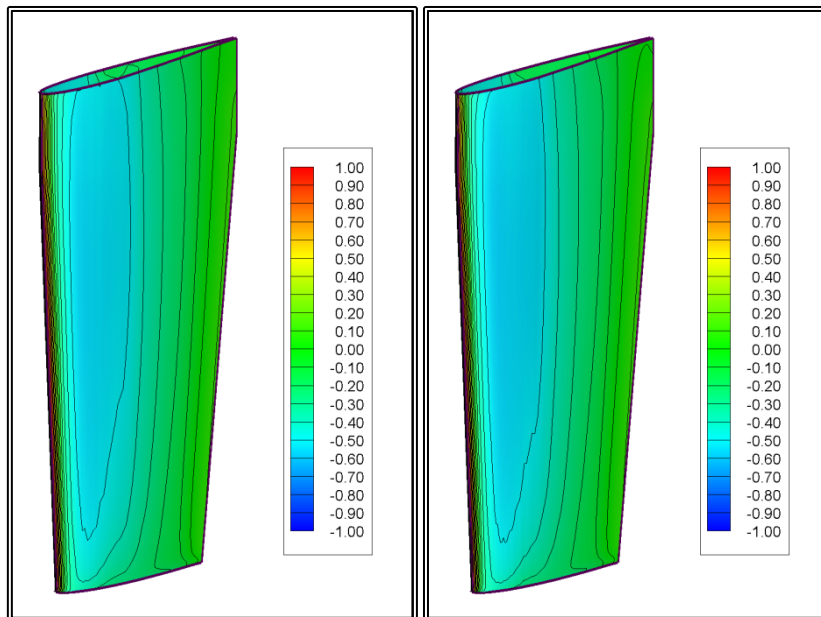
Figure 5.5.10 Pressure coefficient (c_P) contours on the rudder surface, tests A (on the left) and B (on the right).
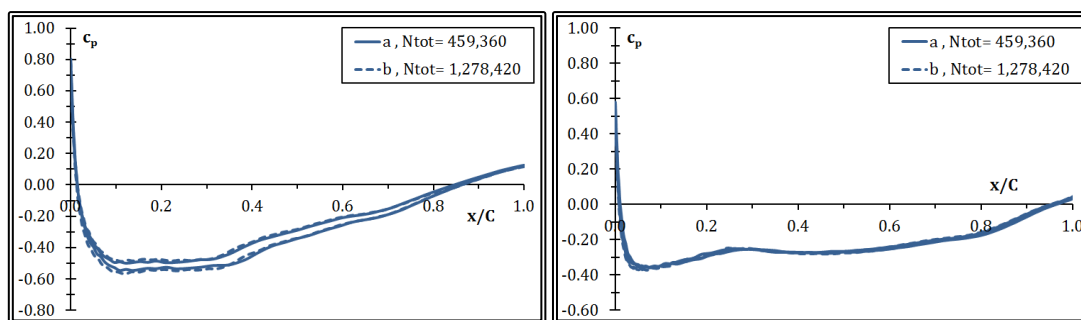
Figure 5.5.11 Pressure Drag coefficient (c_P) distribution, tests A and B, rudder kink (on the left) and rudder tip (on the right).
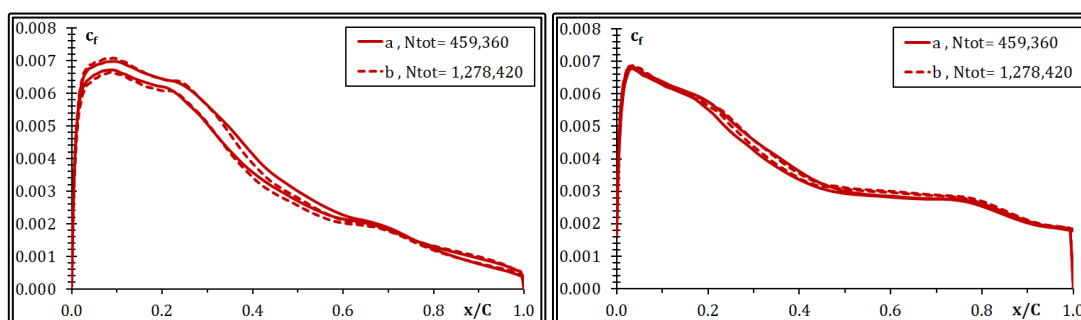
Figure 5.5.12 Skin Friction coefficient (c_f) distribution, tests A and B, rudder kink (on the left) and rudder tip (on the right).

The presented method can generate the numerical grid around a ship rudder. The rudder may have a varying chord length and twist along its length. The rudder tip may have a finite cross section, in which case a step is created in the geometry. The modified RANS solver can now handle the C-H-type block with the Upstream boundary being handled as a solid boundary, while the South boundary is handled partially as a solid boundary and partially as a symmetry line. The solver can now handle the step at the rudder tip.In this paragraph it is demonstrated that the solver can produce realistic results in terms of the flow characteristics and the pressure and skin friction distribution on the rudder surface. Farther examination is required though, in order to determine the required grid density and extends. Also the method requires validating in terms of the produced integrated values, such as the rudder drag. Such an examination is presented in the case of the "Dyne" tanker, in Chapter 6.

(This page intentionally left blank)

CHAPTER 6   FLOW CALCULATIONS ABOUT A SHIP WITH RUDDER

(This page intentionally left blank)

6.1 Introduction, the "Dyne" Test Case

In order to validate the new method for solving the flow around a ship with appendages, the case of a single propeller tanker with rudder was selected. More specifically the "Dyne" tanker model was selected (Dyne, 1995), since it was extensively tested both in the towing tank and the wind tunnel in order to provide a comprehensive data set for the validation of CFD methods. The main particulars of the "Dyne" tanker are presented in table 6.1.1, while in figure 6.1.1, the lines plan is provided.

Table 6.1.1 Main particulars of the "Dyne" model and ship

	Model	Ship	
Scale factor, λ	36		
Length between perpendiculars, L_{PP}	7.028	253.008	m
Breadth, B	1.065	38.340	m
Draught, T	0.396	14.256	m
Displacement, V	2.523	117713	m^3
Wetted surface, WS	11.450	14839.2	m^2
L/B	6.6		
B/T	2.7		
C_B	0.85		
Velocity, V	1.370		m/s
		16.000	kn
Froude number, Fn	0.165		
Reynolds number, Re	9.628×10^6	2.082×10^9	
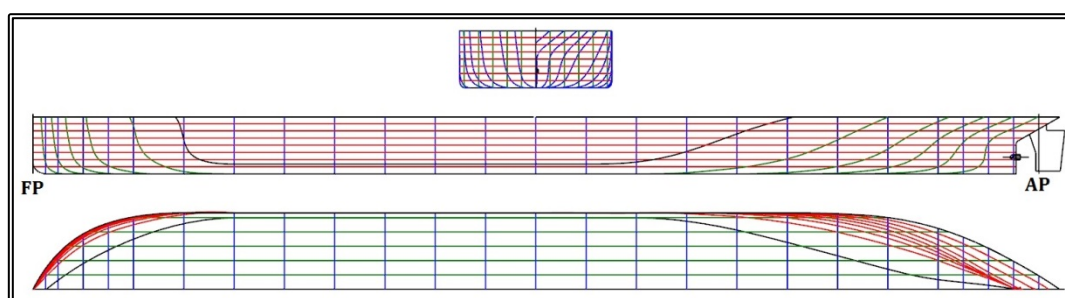
Figure 6.1.1 Lines plan for the "Dyne" model

The towing tank measurements were carried out in the SSPA towing tank, comprising resistance and self-propulsion tests, nominal wake measurements using Prandtl tubes and five-hole Pitot tubes, Prandtl tube measurements in a plane ahead of the propeller with and without working propeller (Figure 6.1.2), static pressure measurements in the propeller plane and hull pressure measurements with and without working propeller. The SSPA towing tank has a length of 260 m, a breadth of 10 m and a water depth of 5 m. A different model was tested at the HSVA windtunnel (Denker et al. 1992) having an L_{PP}=2.664 m and a scale factor λ=96. During one series of resistance measurements and throughout the self-propulsion experiments, the model was

equipped with a ruder having a NACA 18 profile. The planform of the rudder is shown in figure 6.1.2.
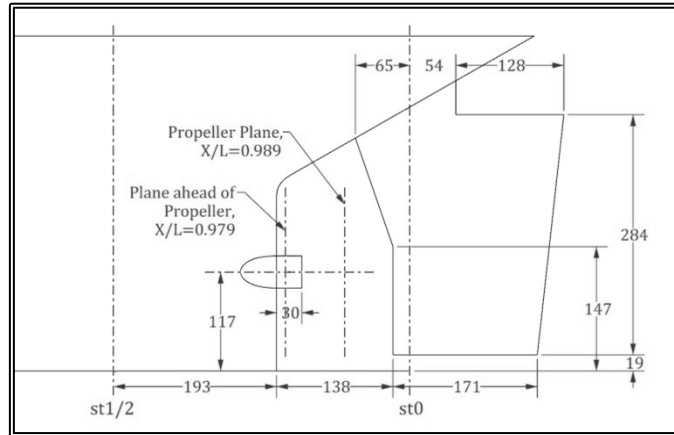
Figure 6.1.2 Wake measurement planes and Rudder planform

For the self-propulsion tests, the model was equipped with a propeller model, located at X/L_{PP}=0.989, measuring from the Fore Perpendicular. The propeller model, P1171, belongs to the SSPA standard propeller family SSPA 6.60 Its main data are:

Table 6.1.2 Main data of the P1171 propeller model

Number of blades, z	5	
Diameter, D	0.195	m
Pitch ratio, P/D	0.650	
Blade area ratio, A_D/A_0	0.600	

The open water characteristics of the P1171 propeller were measured experimentally and in the calculations can be replaced by following polynomials:

$$10 \times K_T = 3.0764 - 2.3236 \times J - 4.4347 \times J^2 + 4.5852 \times J^3 - 2.9248 \times J^4$$
$$100 \times K_Q = 3.088 - 1.490 \times J - 3.319 \times J^2 + 1.837 \times J^3 - 1.340 \times J^4$$

(6.1.1)

The above polynomials represent the propeller characteristics with an error of less than 1%. In figure 6.1.3, the propeller characteristics are graphically presented.

Figure 6.1.3 Open water characteristics of the P1171 propeller model

6.2   Free Surface Calculations

The free surface was calculated using the new hybrid potential-viscous method of paragraph 3.3. All calculations were performed at model scale and at a Froude 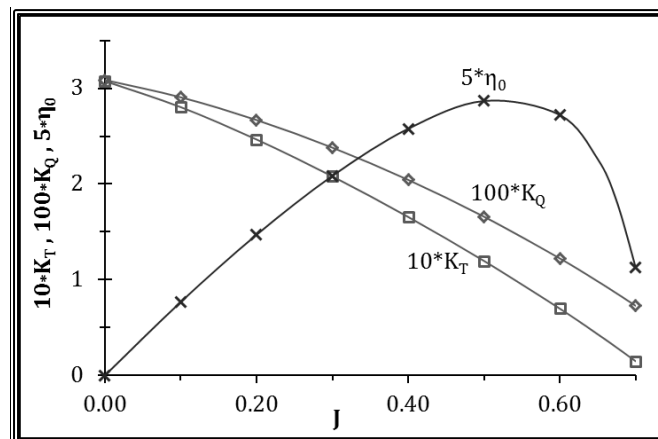number of Fn=0.165 corresponding to a full-scale velocity of 16.00 kn. The flow variables for the free surface calculations are presented in table 6.2.1.

Table 6.2.1 Flow variables for the free surface calculations.

Scale Factor, λ	36	
Ship Speed, V_S	16.0	kn
Model Speed, V_m	1.371	m/s
Fluid Viscosity, ν	1.161E-06	m²/s
Froude Number, Fn	0.165	
Reynolds's Number, Re	8.474E+06	

For the potential calculations, a total of 45,214 panels were employed.The free surface was then corrected using the hybrid method. The transition point was located at 44.1% of the waterline length, measuring from the bow of the ship. A single C-O-type block was employed with a grid size NIxNJxNK=81x180x861 where NK is the number of planar 2-D, NI is the number of grid nodes in the circumferential direction of each planar section and NJ is the number of grid nodes in the radial direction of each planar section. The total grid size was 12,553,380 nodes. In figure 6.2.1 the grid on the free surface (I=1) is presented, near the bow of the ship.

In figures 6.2.2 and 6.2.3, a perspective view of the water elevation contours are presented, as calculated by the potential solver and as corrected by means of the RANS solver respectively.

In figures 6.2.4 and 6.2.5, a top view of the water elevation contours are presented, as calculated by the potential solver and as corrected by means of the RANS solver respectively.

The water elevation contours for the potential solver free surface and the RANS corrected free surface are compared in figure 6.2.6.
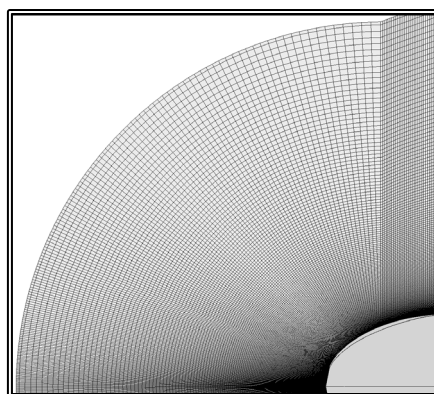
Figure 6.2.1 Numerical grid on the free-surface.
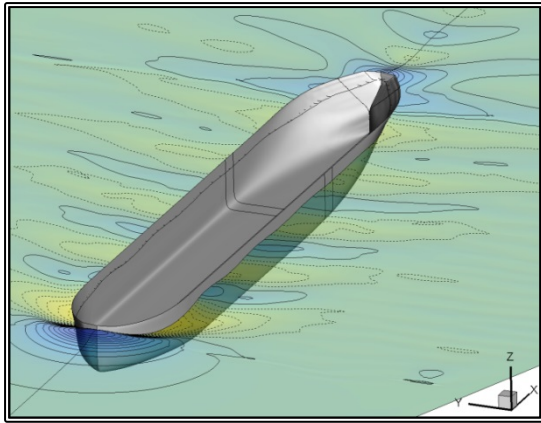
Figure 6.2.2 Perspective view of the water elevation contours, potential free surface, Froude number Fn=0.165
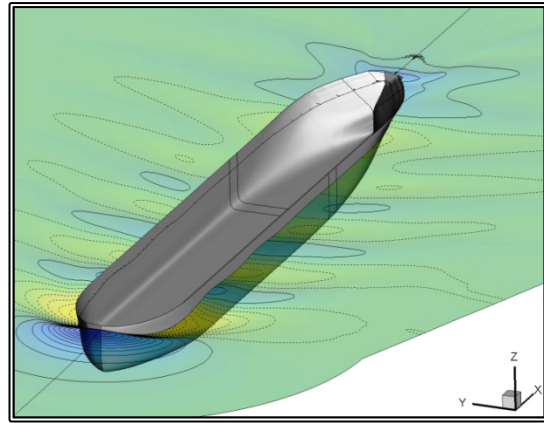
Figure 6.2.3 Perspective view of the water elevation contours, corrected free surface, Froude number Fn=0.165
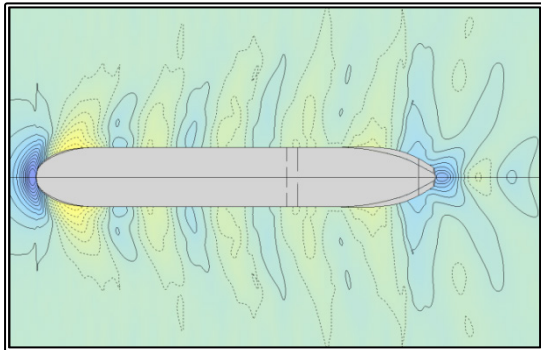
Figure 6.2.4 Top view of the water elevation contours, potential free surface, Froude number Fn=0.165
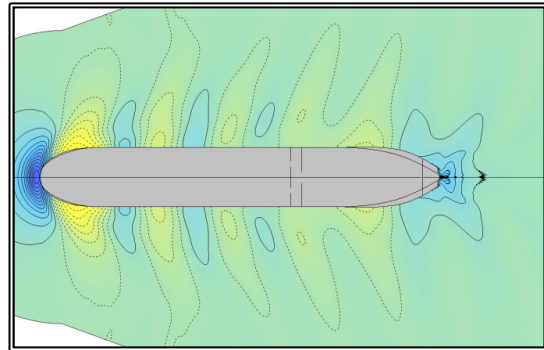
Figure 6.2.5 Top view of the water elevation contours, corrected free surface, Froude number Fn=0.165
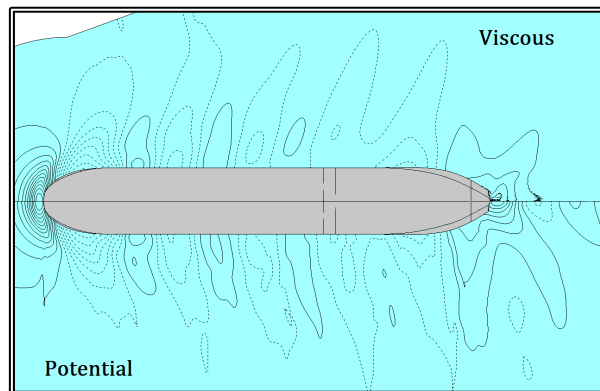
Figure 6.2.6 Top view of the water elevation contours, top: corrected free surface, bottom: potential free surface. Froude number Fn=0.165

In figures 6.2.7 to 6.2.10, longitudinal sections of the wave patter, at a fixed distance from the side of the ship are presented. The solid lines correspond to the corrected free surface, the dashed lines correspond to the potential free surface and finally the the x-marks are data measured experimentally (Lundgren & Åhman, 1994).
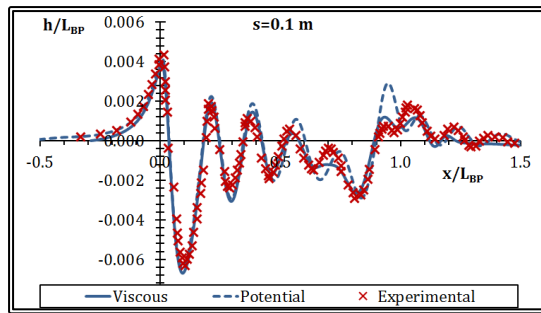
Figure 6.2.7 Wave pattern at a distance of 0.1 m from side of the model, Froude number Fn=0.166.
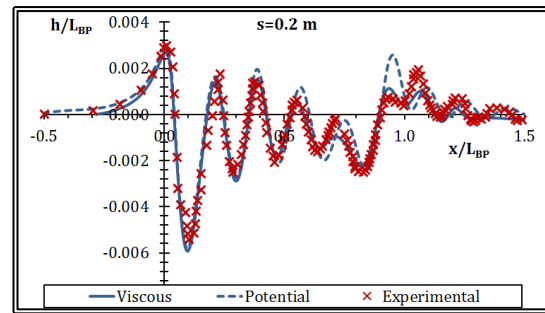
Figure 6.2.8 Wave pattern at a distance of 0.2 m from side of the model, Froude number Fn=0.166.
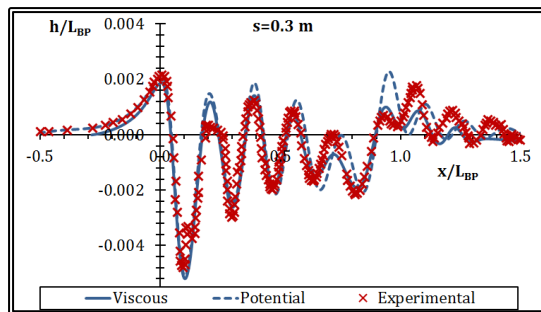
Figure 6.2.9 Wave pattern at a distance of 0.3 m from side of the model, Froude number Fn=0.166.
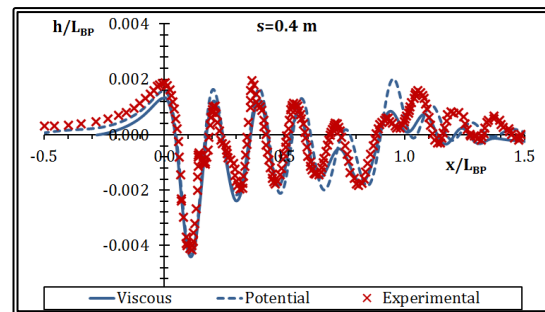
Figure 6.2.10 Wave pattern at a distance of 0.4 m from side of the model, Froude number Fn=0.166.

The calculated free-surface, using the new hybrid method, is in good agreement with the experimental data and the over-prediction of wave height near the stern of the ship, presented in the potential calculations is corrected. The differences that appear between the potential and the viscous solutions upstream the transition point should be attributed to the interpolations needed, in order to calculate the wave elevation on the viscous grid nodes, from the respective values on the panels of the potential solver.

6.3 "Bare" Hull Calculations

In order to validate the method for solving the viscous flow around a ship, a series of numerical experiments was conducted for the "Dyne" model, without the rudder. Simulations were performed at model scale and full scale, at a constant Froude number, Fn=0.165 corresponding to a full-scale velocity of 16.00 kn. The flow variables for the "bare" hull calculations are presented in table 6.3.1.

Table 6.3.1 Flow variables for the "bare" hull calculations.

	Model	Ship	
Scale Factor, λ	36		
Speed, V	-	16.0	kn
	1.371	8.226	m/s
Fluid Viscosity, ν	1.161E-06	1.431E-06	m²/s
Froude Number, Fn	0.165		
Reynolds's Number, Re	8.474E+06	1.484E+09	

The free surface was calculated at model scale, using the new hybrid method, as described in paragraph 6.2. In the following numerical experiments the free surface was treated as a fixed boundary.

The viscous flow was then solved by employing two grid blocks, one C-O-type around the bow and fore half of the ship and an H-O-type block around the aft half of the ship as well as the wake. The method for solving the viscous flow problem with multiple grid blocks is described in paragraph 2.5. In table 6.3.2, the dimensions of the grids used in the various tests are presented. The grids used for the propulsion tests were the same as in the resistance tests. For the full scale tests and the test without the use of wall functions, the grid dimensions were the same as in the other tests but the node distribution in the radial (J) direction differed. Specifically it was made finer near the solid boundary. In table 6.3.2, the average value for the y+ parameter is included for each test.

Table 6.3.2 Grid dimensions for the "bare" hull tests

| | | Model Scale | | Full Scale |
| | | Symmetric | | Asymmetric | Asymmetric |
		Wall fun's	Near wall	Wall fun's	Wall fun's
Bow Grid Block	NI	81	81	81	81
	NJ	180	180	180	180
	NK	511	511	511	511
	$N_{TOT,bow}$	7,450,380	7,450,380	7,450,380	7,450,380
Stern Grid Block	NI	81	81	160	160
	NJ	180	195	180	180
	NK	571	571	411	411
	$N_{TOT,stern}$	8,325,180	9,018,945	11,836,800	11,836,800
	N_{TOT}	15,775,560	16,469,325	19,287,180	19,287,180
	y+	60	0.5	30	260

For each numerical test, the resistance components were then calculated (Tzabiras, 2009):

$$R_P = \iint_{WS}(p^* - \rho gh) \cdot (\mathbf{n} \cdot \mathbf{i})\, ds \qquad (6.3.1)$$

$$R_F = \iint_{WS} \tau_w \cdot (\mathbf{s} \cdot \mathbf{i})\, ds \qquad (6.3.2)$$

Where R_P is the pressure resistance, R_F is the frictional resistance, WS is the actual wetted surface, p^* is the pressure on the hull, ρgh is the hydrostatic term, ρ is the water density, g is the gravitational acceleration, h is the height from a reference level, $\mathbf{n}$ is the unit vector normal to the hull, $\mathbf{i}$ is the unit vector parallel to the ship longitudinal axis, τ_w is the wall shear stress and $\mathbf{s}$ is the tangential unit vector to the hull. The total resistance is then considered equal to the sum of the pressure and frictional resistance:

$$R_T = R_P + R_F \qquad (6.3.3)$$

The resistance components are expressed in their respective non-dimensional form:

$$C_P = \frac{R_P}{0.5 \cdot \rho \cdot WS \cdot V^2} \qquad (6.3.4)$$

$$C_F = \frac{R_F}{0.5 \cdot \rho \cdot WS \cdot V^2} \qquad (6.3.5)$$

$$C_T = C_P + C_F = \frac{R_T}{0.5 \cdot \rho \cdot WS \cdot V^2} \qquad (6.3.6)$$

Where V is the ship or model speed.

Apart from the integrated values, flow variables are also presented on four sections of the ship near the stern (figure 6.3.1). The first, Section A, is located upstream the propeller plane, at a distance of $0.979 L_{BP}$ from the bow. The second section, Section B, coincides with the propeller plane, at a distance of $0.989 L_{BP}$ from the bow. The other two sections, Sections C and D, are located abaft the propeller plane, at a distance of $0.992 L_{BP}$ and $0.996 L_{BP}$ from the bow respectively.
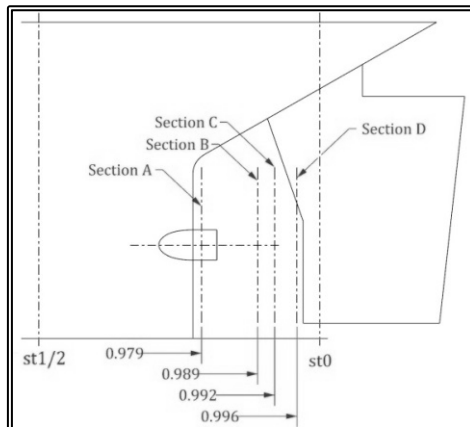

Figure 6.3.1 Location of measurement planes

On each of the four sections, three figures are presented. The first corresponds to the iso-wake contours for the longitudinal velocity components w, on the non-dimensional form w/V. In the second figure, cross flow envelop are presented on that

section, taking into account the two planar velocity components u, v but ignoring w. Finally in the third figure, the iso-bar contours are presented for the local pressure coefficient:

$$c_P = \frac{p^* - \rho gh}{0.5 \cdot \rho \cdot V^2} \quad (6.3.7)$$

In the self-propulsion numerical tests, the propeller is modeled via the actuator disk method (paragraph 2.6) and the propeller characteristics are those of the "Dyne" model as presented in paragraph 6.1. The self-propulsion algorithm is presented in figure 6.3.2. Initially the resistance problem is solved. Then, the propeller thrust is set equal to the resistance, the body forces are calculated inside the propeller disk and 30 iterations of the SIMPLE algorithm are performed and by that stage, the algorithm has only partially converged. Then the new resistance is calculated, the thrust is set equal to the new resistance and the procedure is repeated until convergence is achieved, in terms of thrust being equal to the calculated resistance. Approximately 60 iterations of the above procedure are necessary.
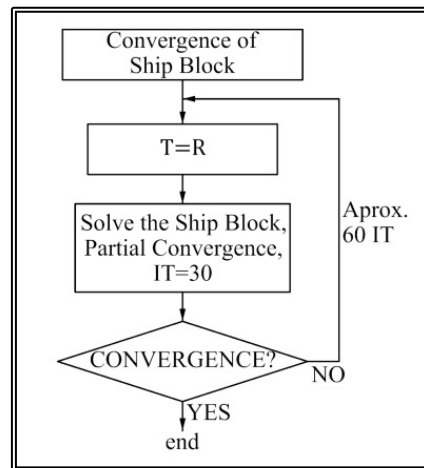
Figure 6.3.2 "Bare" hull, flow chart of the self-propulsion procedure.

In the propulsion tests the hull-propeller interaction coefficients are calculated:

$$1 - w = \frac{V_A}{V} \quad (6.3.8)$$

$$1 - t = \frac{T}{R_T} \quad (6.3.9)$$

Where w is the wake fraction, t is the augment of resistance coefficient, V_A is the wake speed, i.e. the mean velocity on the propeller disk and T is the propeller thrust.

6.3.1   Model Scale Resistance Calculations, Symmetric Flow

In the first series of tests, the problem was considered symmetric and only one-half of the computational domain was modeled. First the resistance problem was solved at model scale, using a C-O-type bow grid block measuring NIxNJxNK=81x180x511 nodes, where NK is the number of planar 2-D, NI is the number of grid nodes in the circumferential direction of each planar section and NJ is the number of grid nodes in the radial direction of each planar section. The total grid size for the bow grid was 7,450,380 nodes. The stern was modeled using an H-O-type grid measuring NIxNJxNK=81x180x571 nodes for a total of 8,325,180 nodes. The total grid size was 15,775,560 nodes. The calculated values for the resistance characteristics are presented collectively in table 6.3.1 of paragraph 6.3.8.
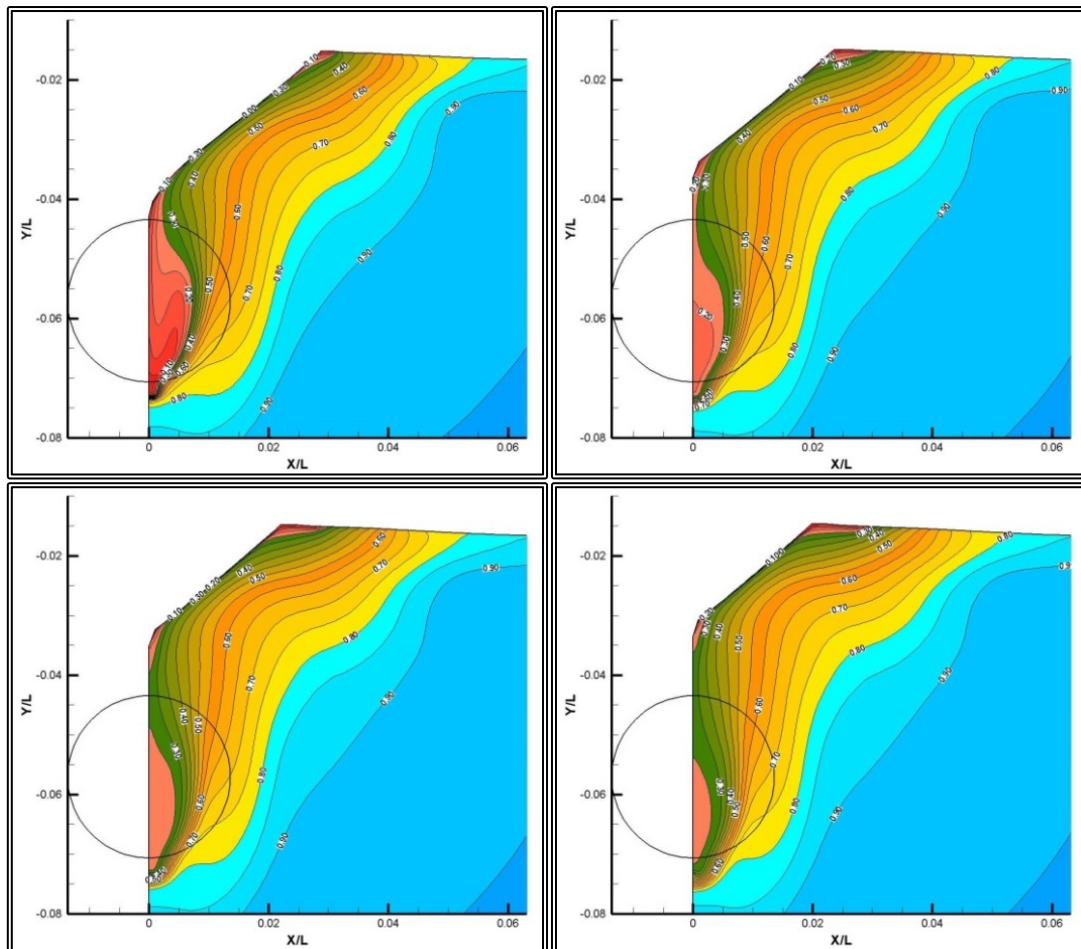
Figure 6.3.3 Isowake (w/V) contours, model scale, symmetric flow, resistance. From top right to bottom left, sections A, B, C and D.

Figure 6.3.4 Cross flow envelopes, model scale, symmetric flow, resistance. From top right to bottom left, sections A, B, C and D.

Figure 6.3.5 Isobar (c_P) contours, model scale, symmetric flow, resistance. From top right to bottom left, sections A, B, C and D.

6.3.2 Model Scale, Near Wall Treatment Resistance Calculations, Symmetric Flow

In order to evaluate the accuracy of the wall functions approach (paragraph 1.4.4) used in the previous test, the same problem was solved using this time the near-wall treatment approach. In this approach the south boundary of the numerical grid coincides with the hull surface and the no-slip condition is applied. This approach requires finer grids near the solid boundary and as a result was employed only on the stern block. The bow grid block was the same as in the case of paragraph 6.3.1, measuring NIxNJxNK=81x180x511 nodes, a total of 7,450,380 nodes. For the stern block, extra nodes were added in the J-direction: NIxNJxNK=81x195x571 nodes for a total of 9,018,945 nodes. The total grid size was 16,469,325 nodes.

Figure 6.3.6 Isowake (w/V) contours, model scale, symmetric flow, resistance, near wall treatment. From top right to bottom left, sections A, B, C and D.

Figure 6.3.7 Cross flow envelopes, model scale, symmetric flow, resistance, near wall treatment. From top right to bottom left, sections A, B, C and D.

Figure 6.3.8 Isobar (c_P) contours, model scale, symmetric flow, resistance, near wall treatment. From top right to bottom left, sections A, B, C and D.

6.3.3   Model Scale Propulsion Calculations, Symmetric Flow

The propulsion problem was then solved, considering the flow symmetric. The propeller was modeled using the actuator disk method. Since the problem is considered symmetric, the actuator disk induces body forces to the flow, only in the axial direction. The wall functions were employed for the conditions on the solid boundary and the bow and stern grid blocks were the same as in the test of paragraph 6.3.1.

Figure 6.3.9 Isowake (w/V) contours, model scale, symmetric flow, propulsion. From top right to bottom left, sections A, B, C and D.
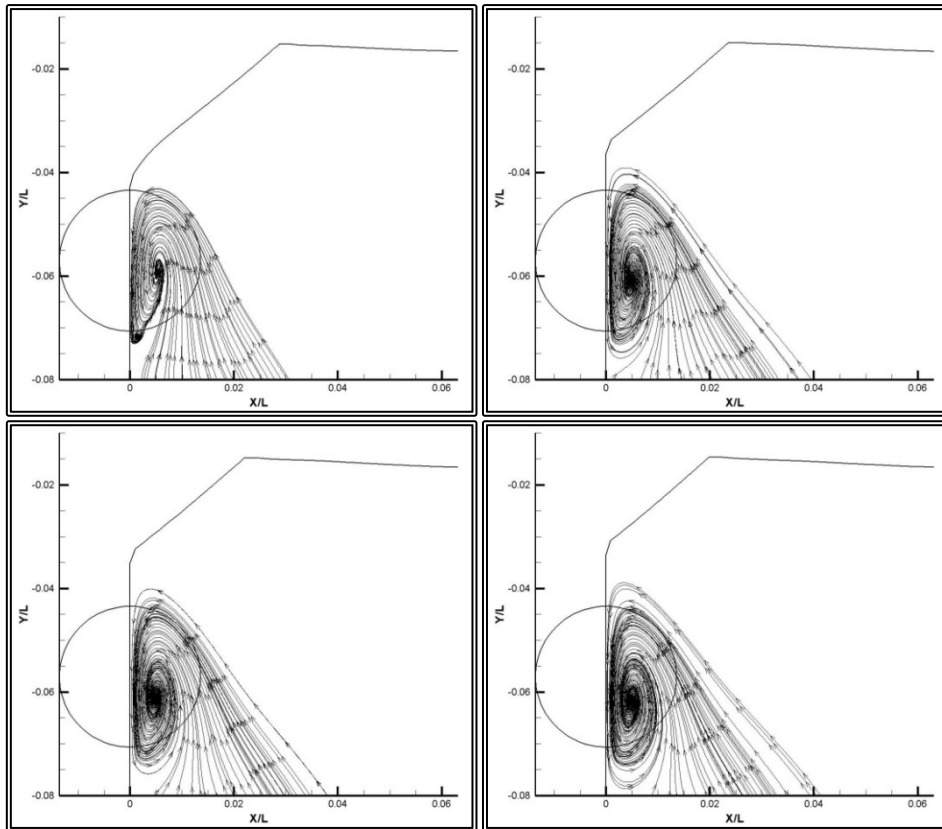
Figure 6.3.10 Cross flow envelopes, model scale, symmetric flow, propulsion. From top right to bottom left, sections A, B, C and D.
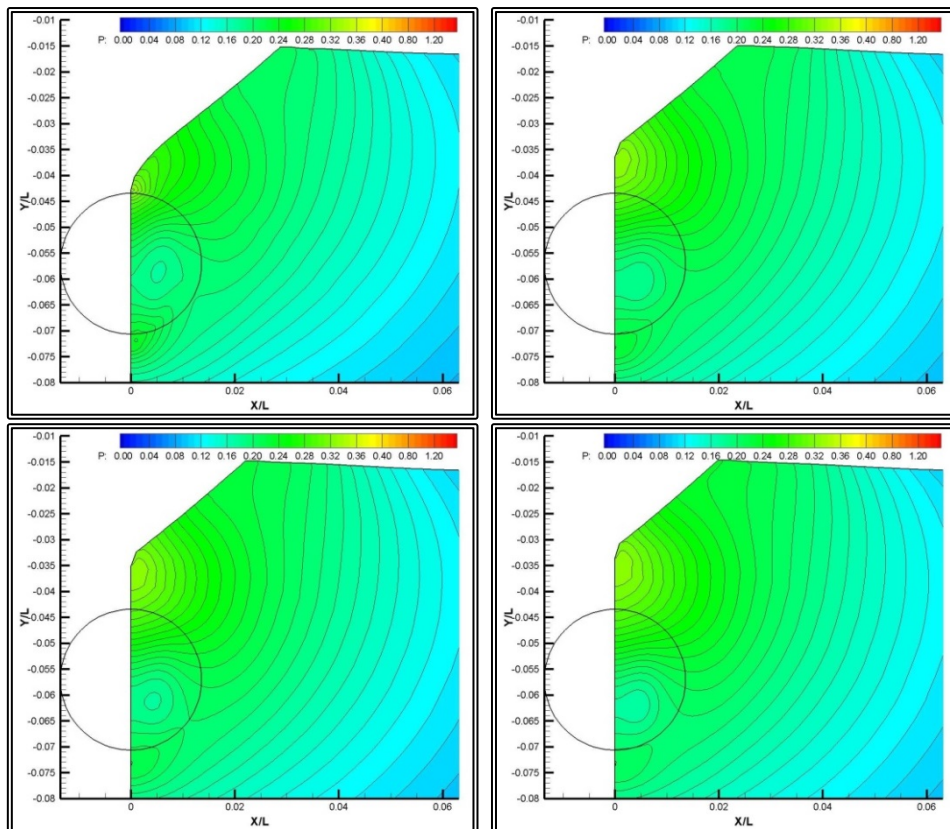

Figure 6.3.11 Isobar (c_P) contours, model scale, symmetric flow, propulsion. From top right to bottom left, sections A, B, C and D.

6.3.4 Model Scale Resistance Calculations, Asymmetric Flow

The propulsion problem is inherently asymmetrical, since the flow interacts with the rotating propeller. In order to solve an asymmetric flow problem, all of the computational has to be modeled and consequently a grid of twice the size is required. In order to reduce computational cost and since the flow becomes asymmetric near the propeller, the bow grid block covered one-half of the domain, measuring NIxNJxNK=81x180x511 nodes, a total of 7,450,380 nodes, the same as in all other tests. The H-O-type stern grid block covered all of the domain, having NIxNJxNK=160x180x371 nodes for a total of 10,684,800 nodes. The total grid size was 18,135,180 nodes. For the solid boundary conditions, the wall functions were employed.

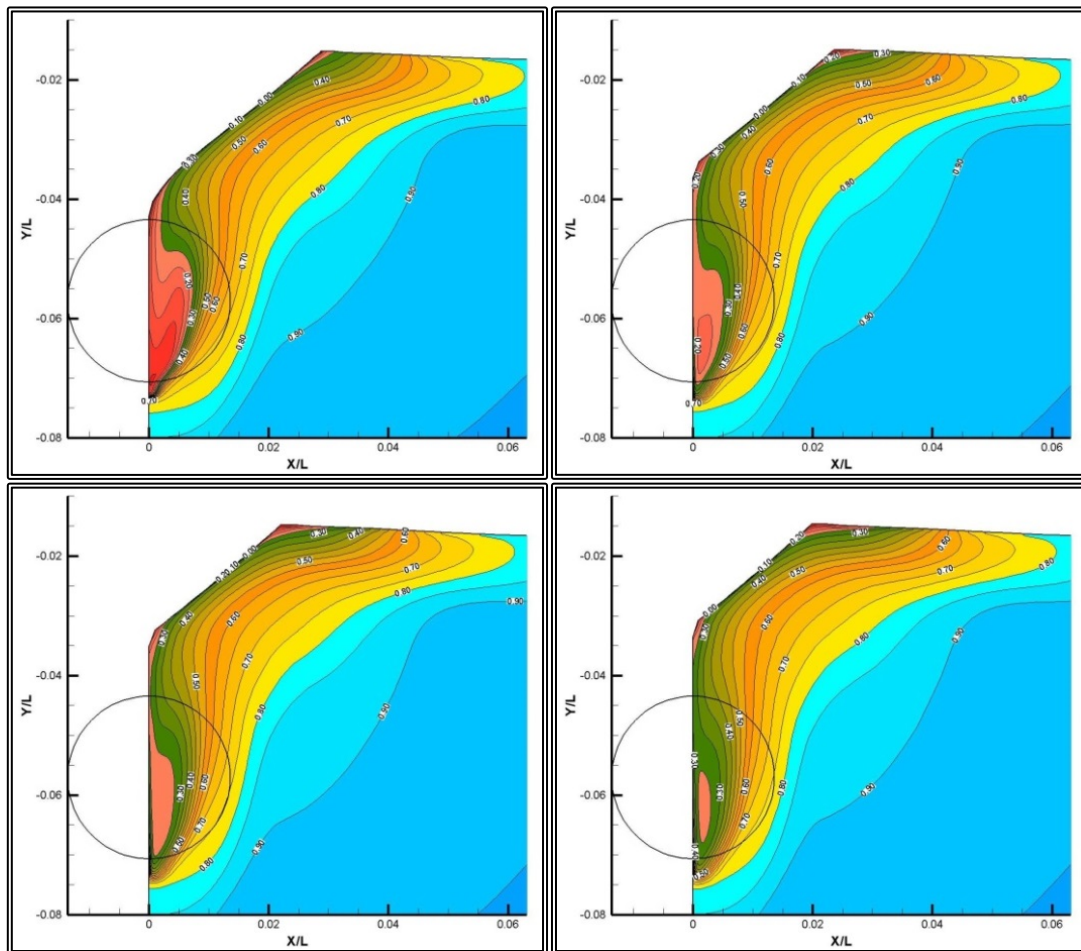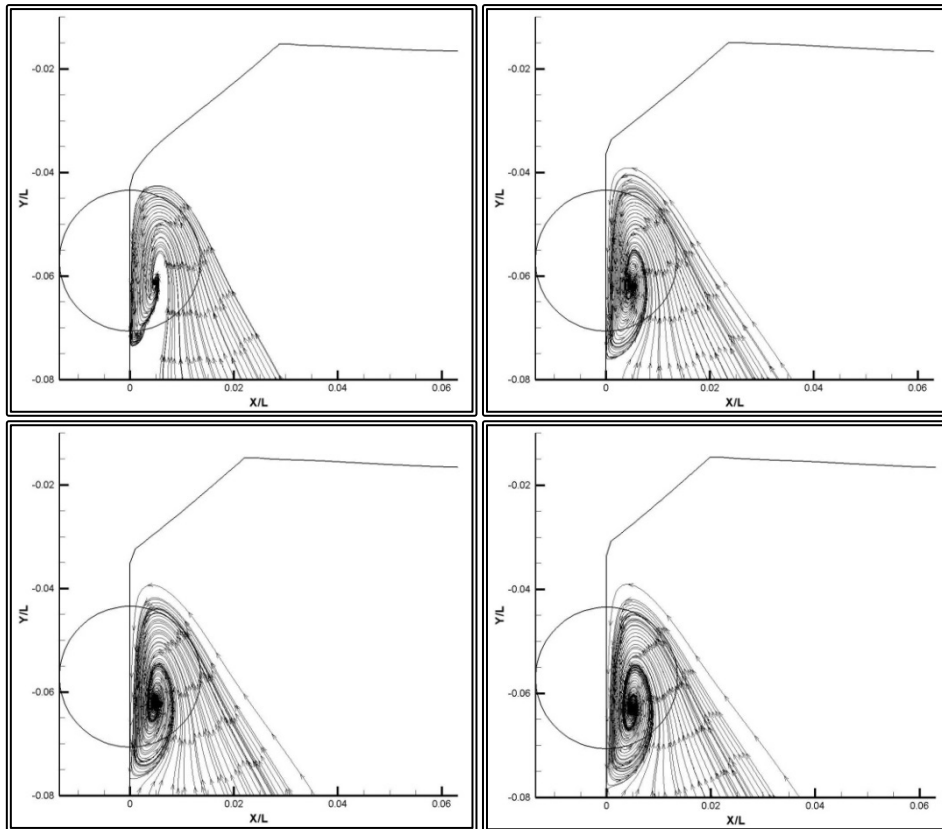**Figure 6.3.12** Isowake (w/V) contours, model scale, asymmetric flow, resistance. From top right to bottom left, sections A, B, C and D.

Figure 6.3.13 Cross flow envelopes, model scale, asymmetric flow, resistance. From top right to bottom left, sections A, B, C and D.
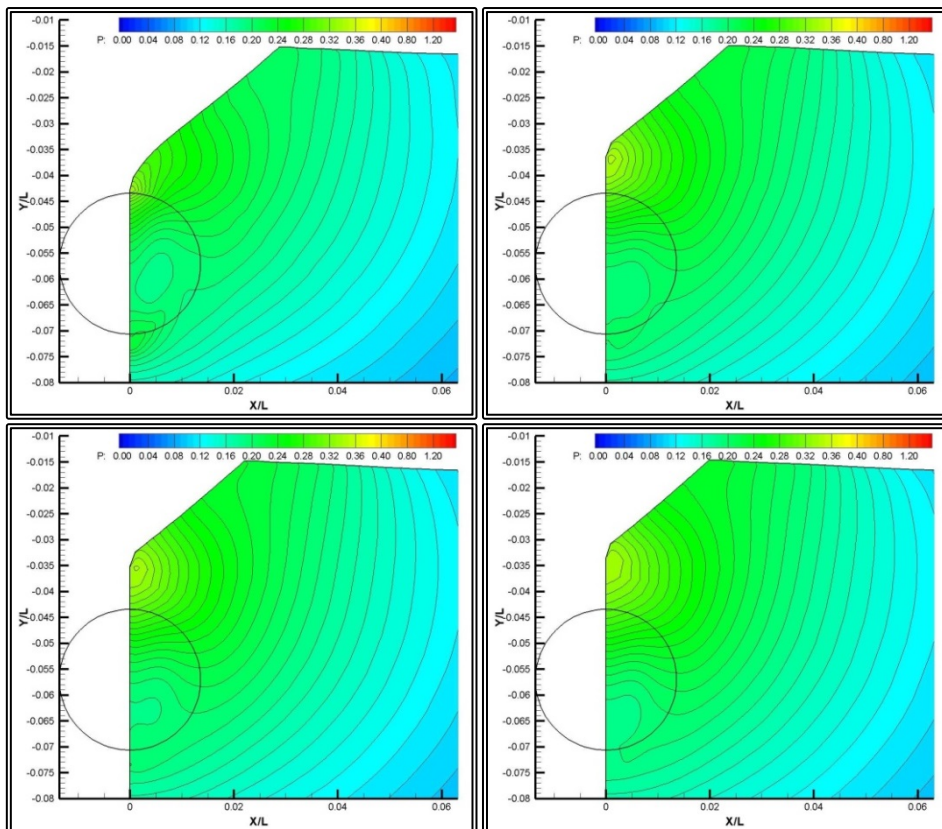

Figure 6.3.14 Isobar (c_P) contours, model scale, asymmetric flow, resistance. From top right to bottom left, sections A, B, C and D.

6.3.5 Model Scale Propulsion Calculations, Asymmetric Flow

The asymmetric propulsion problem at model scale was solved, by employing the set-up of paragraph 6.3.4. Specifically, the bow C-O-type grid block measuring NIxNJxNK=81x180x511 nodes, a total of 7,450,380 nodes, covered one half of the respective computational domain. The H-O-type stern grid block covered all of the domain, having NIxNJxNK=160x180x371 nodes for a total of 10,684,800 nodes. The total grid size was 18,135,180 nodes. The propeller action was modeled using the actuator disk method, this time incorporating the tangential and radial components of the body forces.
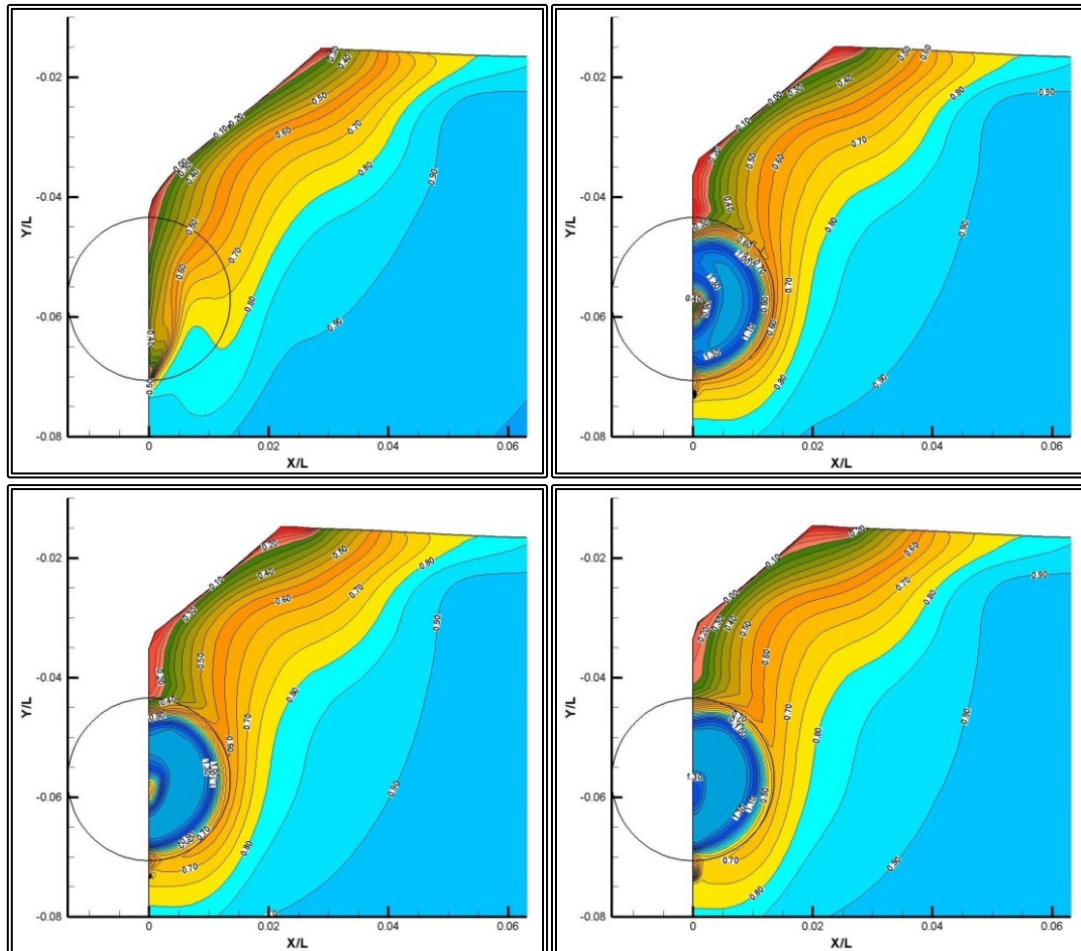

Figure 6.3.15 Isowake (w/V) contours, model scale, asymmetric flow, propulsion. From top right to bottom left, sections A, B, C and D.
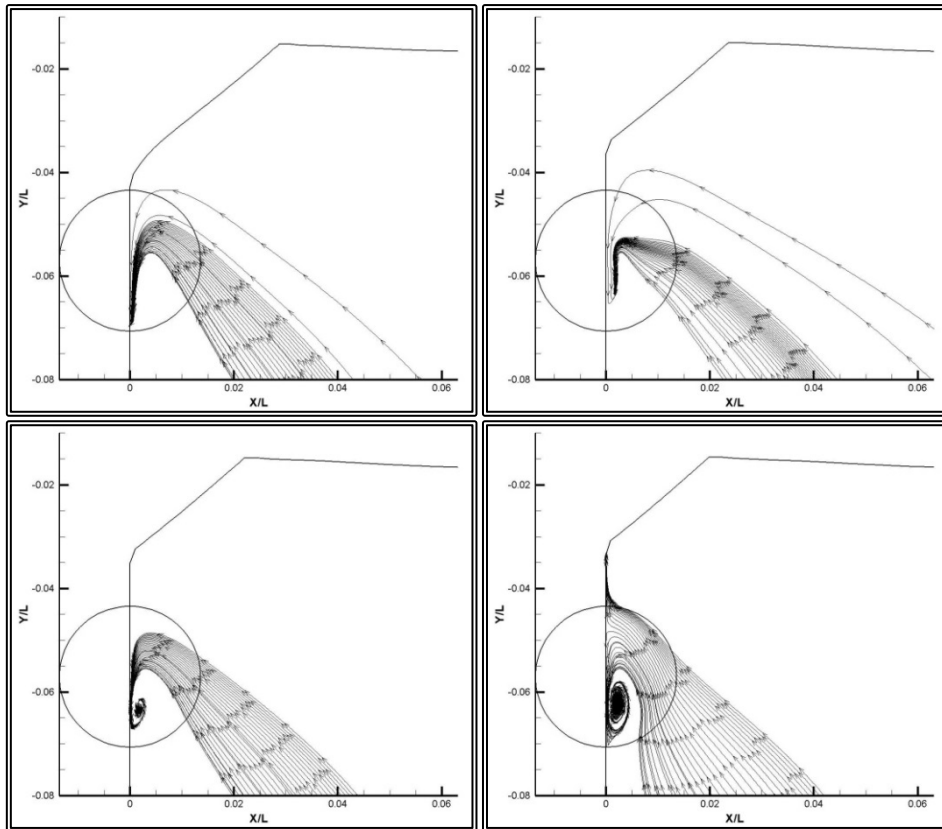
Figure 6.3.16 Cross flow envelopes, model scale, asymmetric flow, propulsion. From top right to bottom left, sections A, B, C and D.
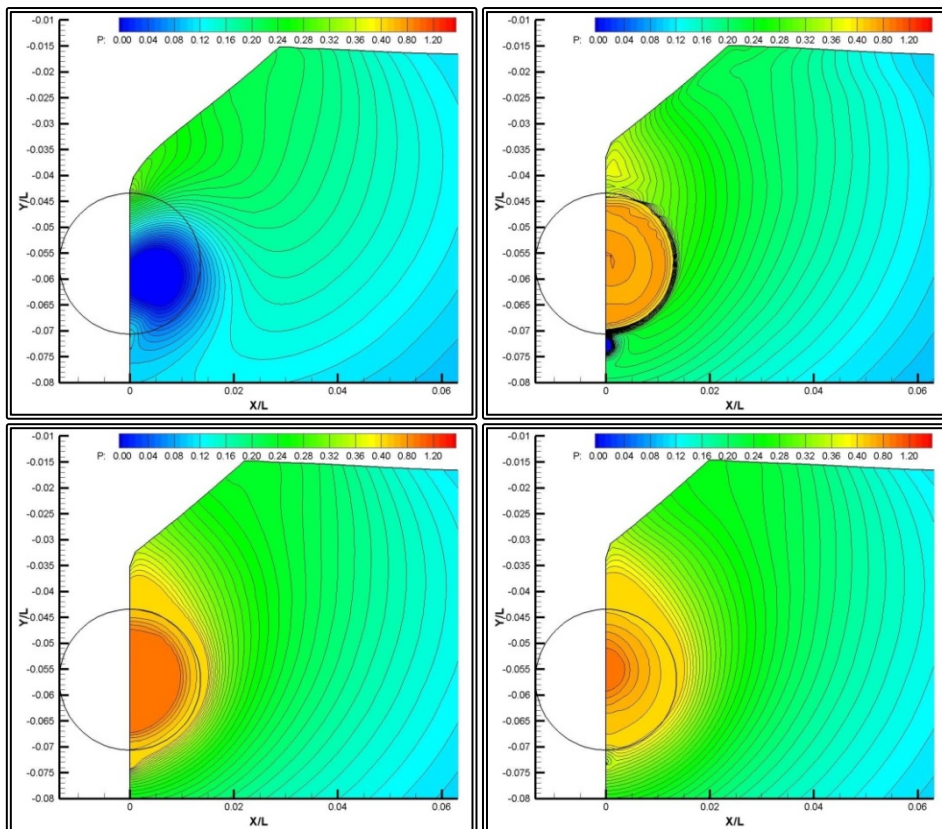

Figure 6.3.17 Isobar (c_P) contours, model scale, asymmetric flow, propulsion. From top right to bottom left, sections A, B, C and D.

6.3.6 Full Scale Resistance Calculations

For the full scale resistance problem, the problem was considered asymmetric and the set-up of paragraph 6.3.4 was employed. Specifically, the bow C-O-type grid block measuring NIxNJxNK=81x180x511 nodes, a total of 7,450,380 nodes, covered one half of the respective computational domain. The H-O-type stern grid block covered all of the domain, having NIxNJxNK=160x180x371 nodes for a total of 10,684,800 nodes. The total grid size was 18,135,180 nodes. For the solid boundary conditions, the wall functions were employed.

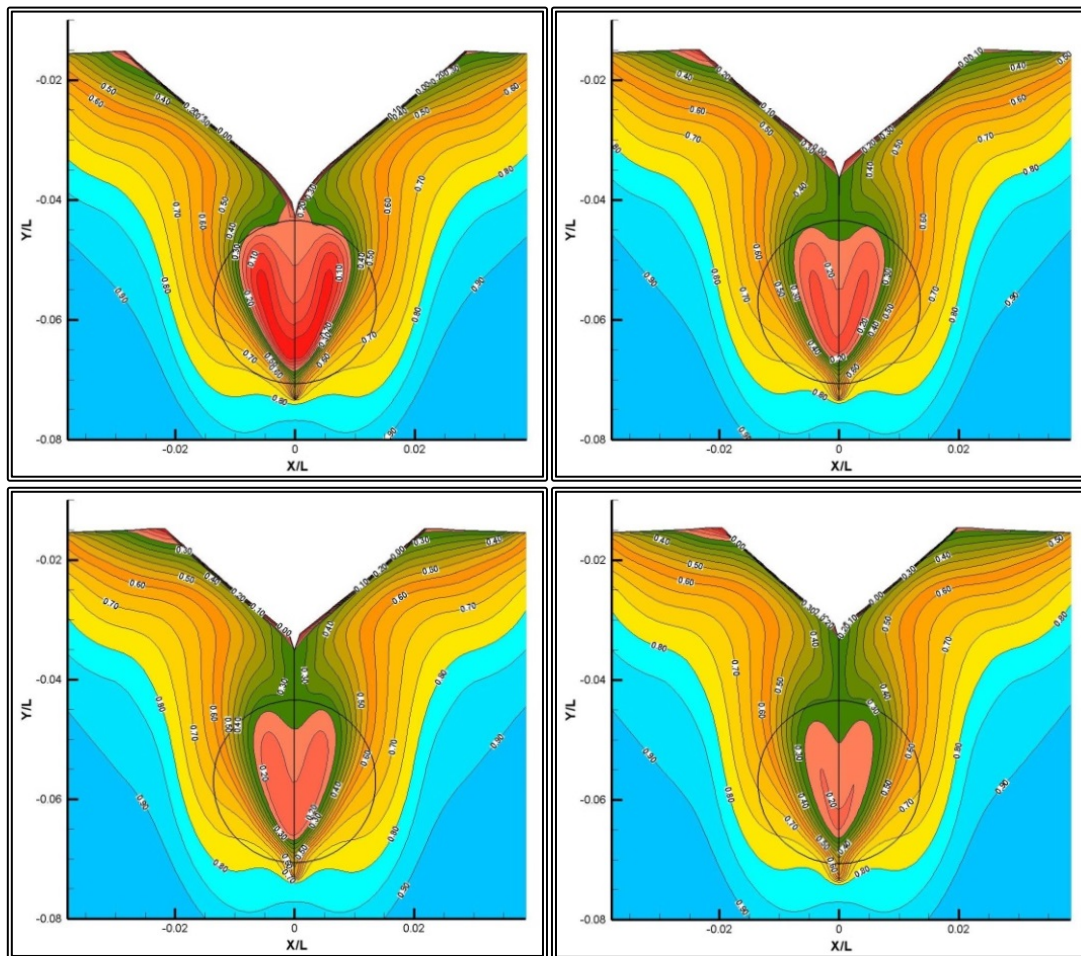**Figure 6.3.18** Isowake (w/V) contours, full scale, asymmetric flow, resistance. From top right to bottom left, sections A, B, C and D.

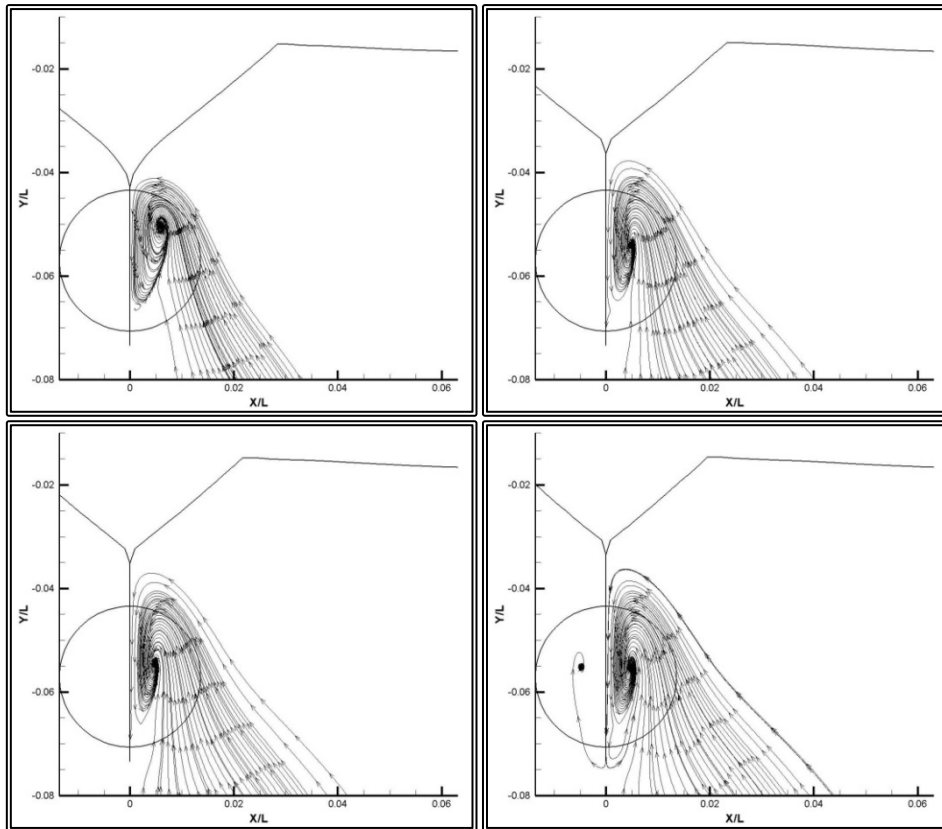**Figure 6.3.19** Cross flow envelopes, full scale, asymmetric flow, resistance. From top right to bottom left, sections A, B, C and D.
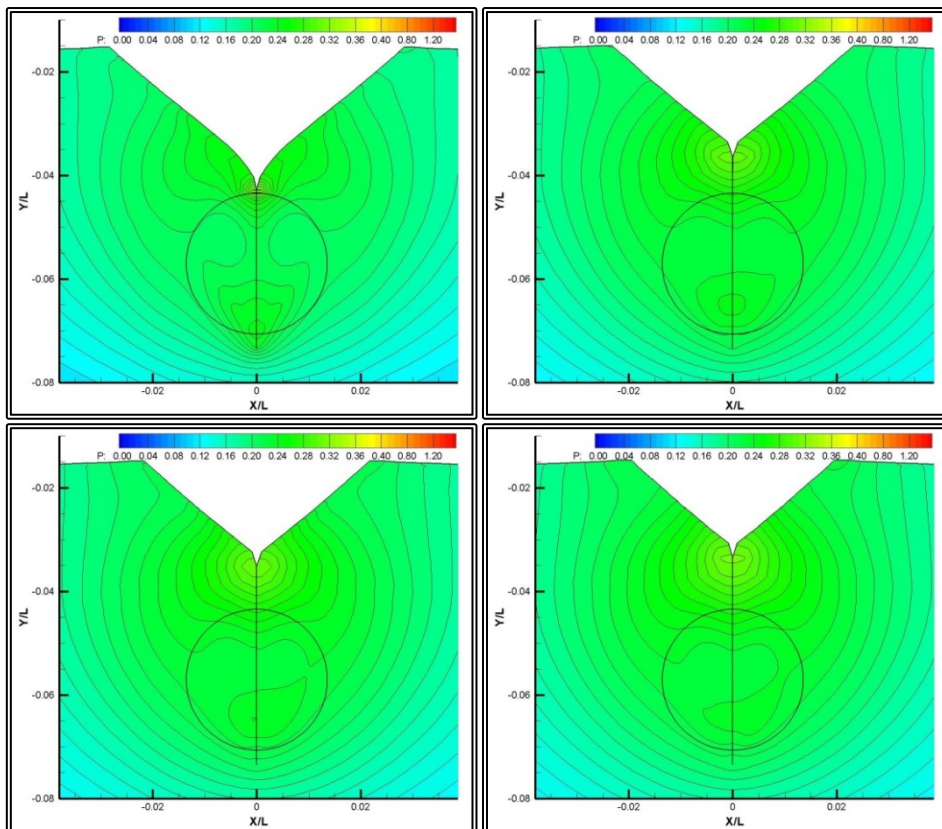

Figure 6.3.20 Isobar (c_P) contours, full scale, asymmetric flow, resistance. From top right to bottom left, sections A, B, C and D.

6.3.7 Full Scale Propulsion Calculations

The full scale propulsion problem was considered asymmetric and the set-up of paragraph 6.3.4 was employed. Specifically, the bow C-O-type grid block measuring NIxNJxNK=81x180x511 nodes, a total of 7,450,380 nodes, covered one half of the respective computational domain. The H-O-type stern grid block covered all of the domain, having NIxNJxNK=160x180x371 nodes for a total of 10,684,800 nodes. The total grid size was 18,135,180 nodes. The propeller action was modeled using the actuator disk method, this time incorporating the tangential and radial components of the body forces.
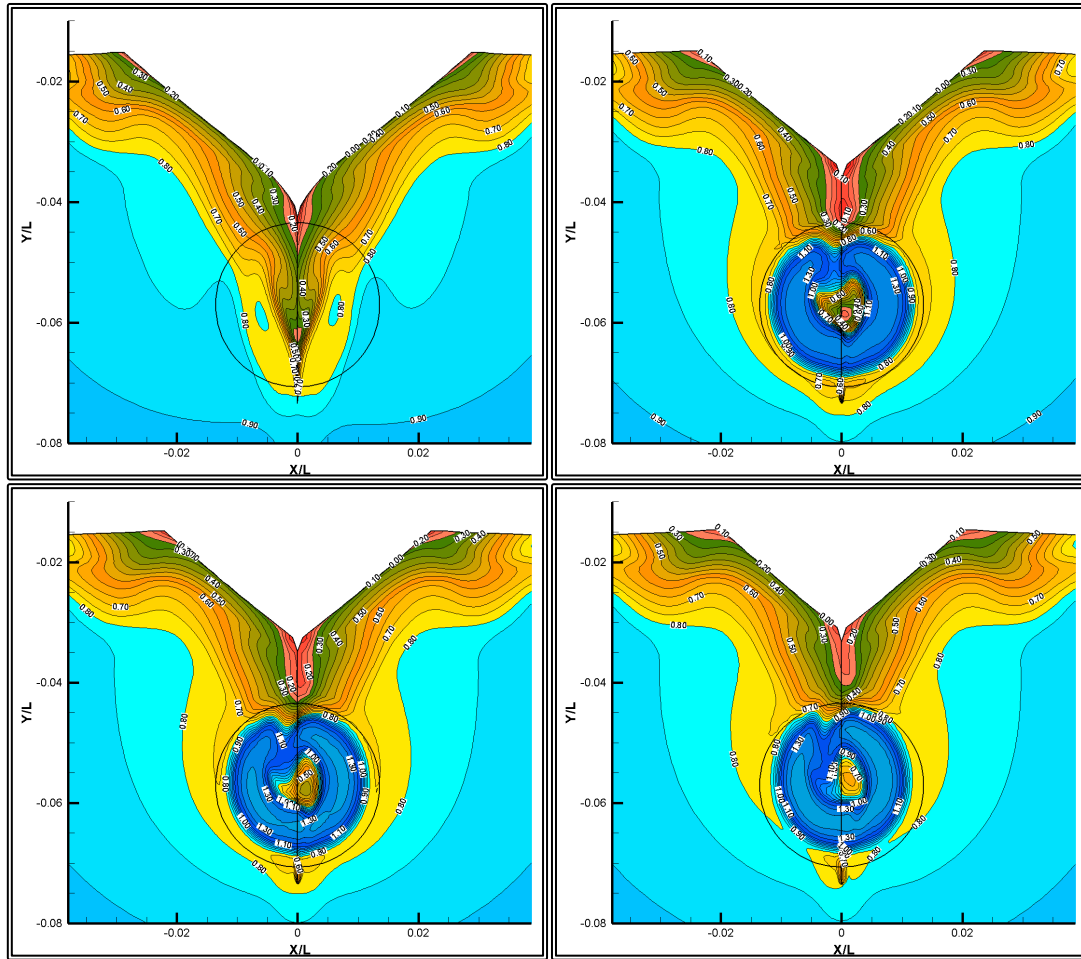
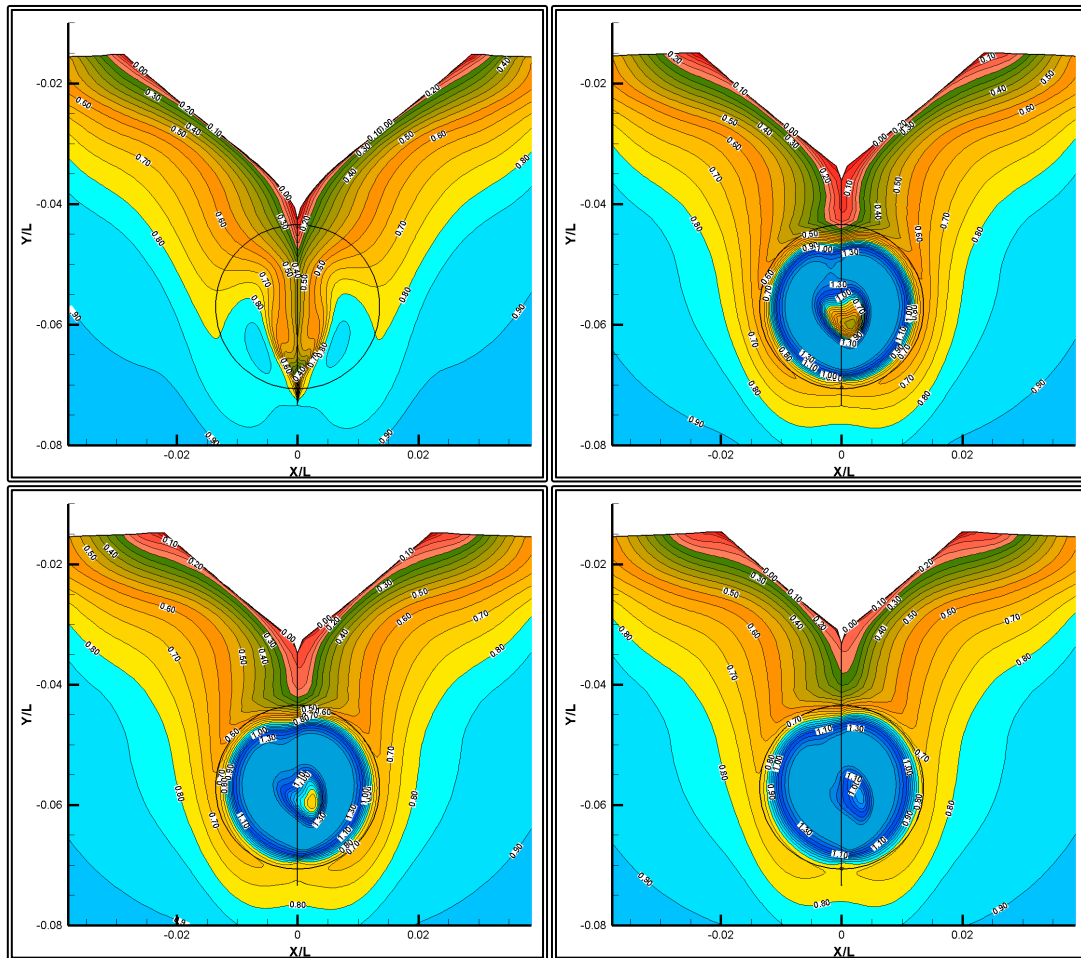**Figure 6.3.21** Isowake (w/V) contours, full scale, asymmetric flow, propulsion. From top right to bottom left, sections A, B, C and D.
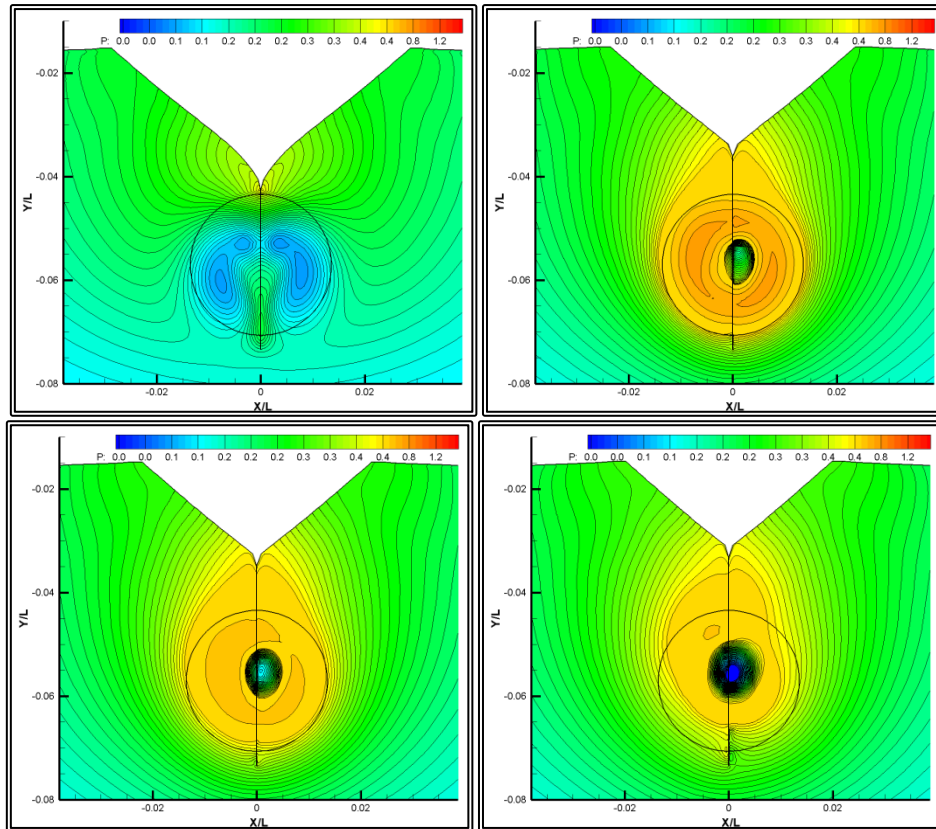
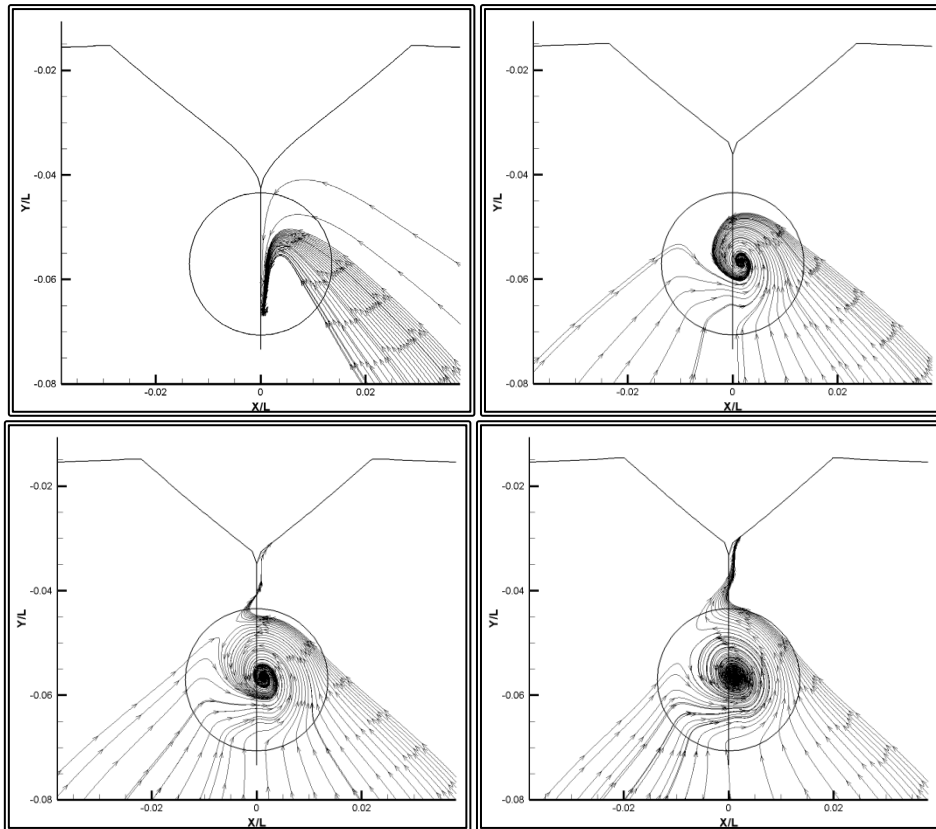**Figure 6.3.22** Cross flow envelopes, full scale, asymmetric flow, propulsion. From top right to bottom left, sections A, B, C and D.
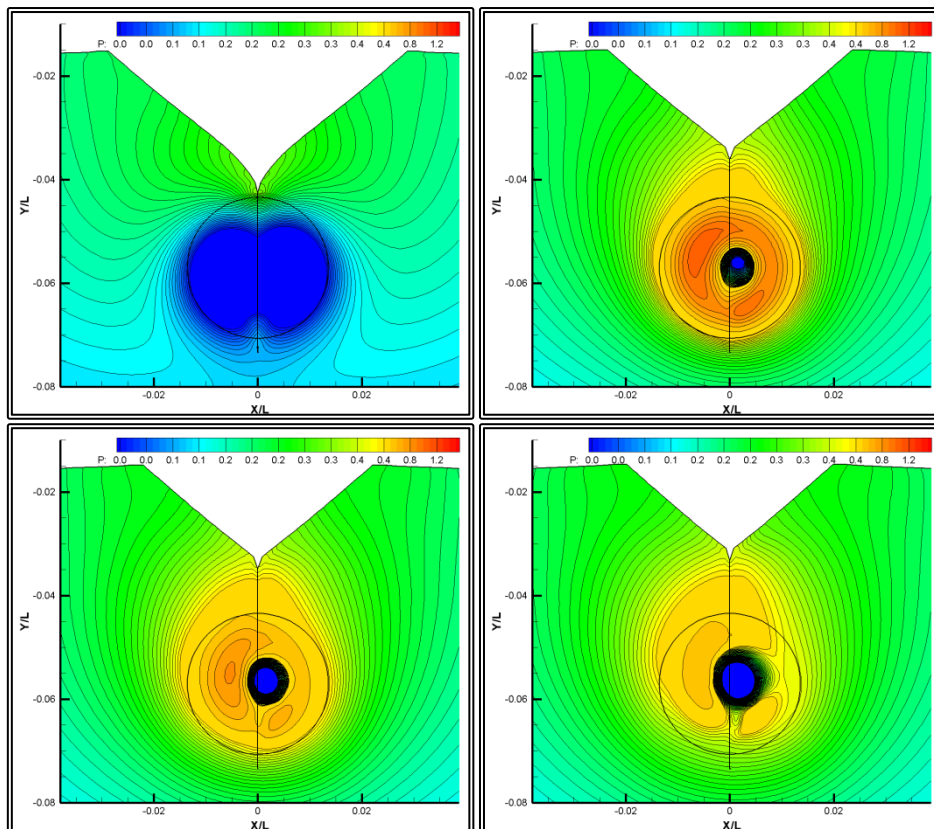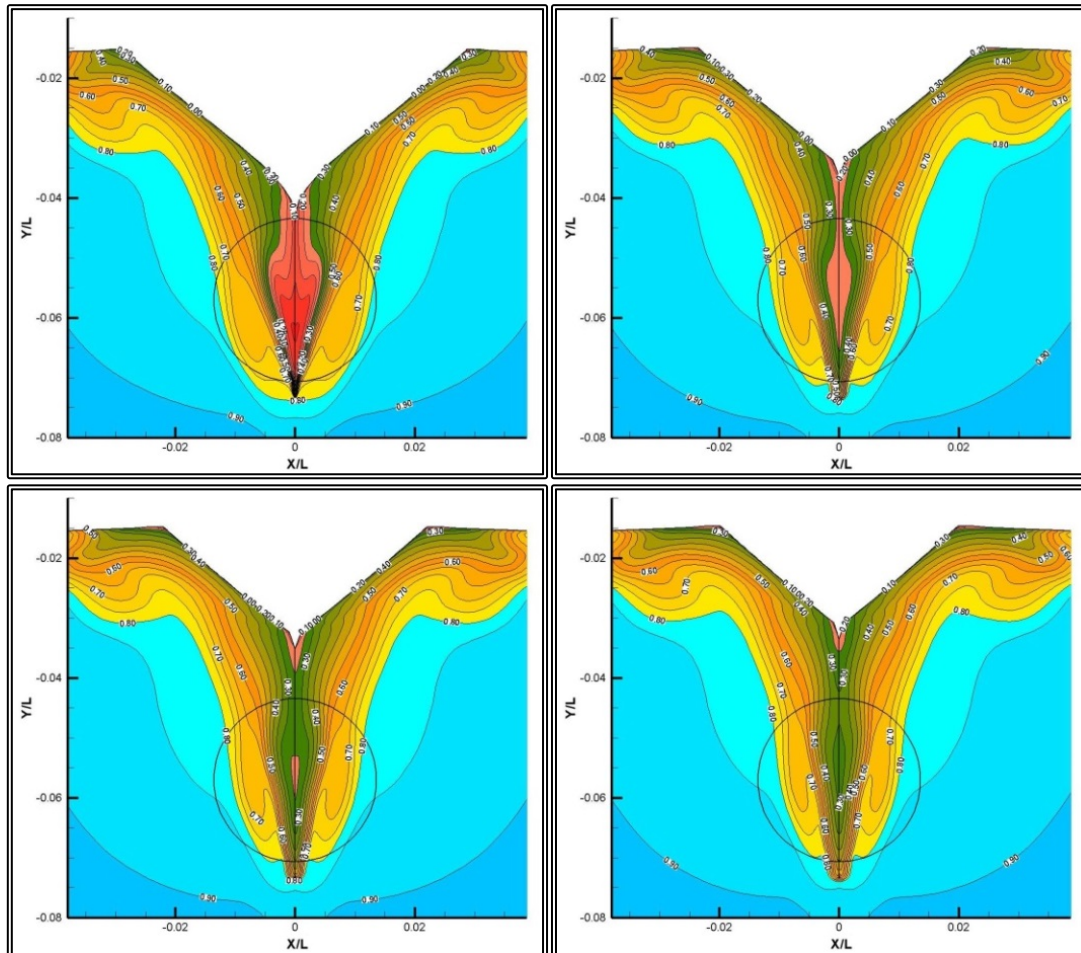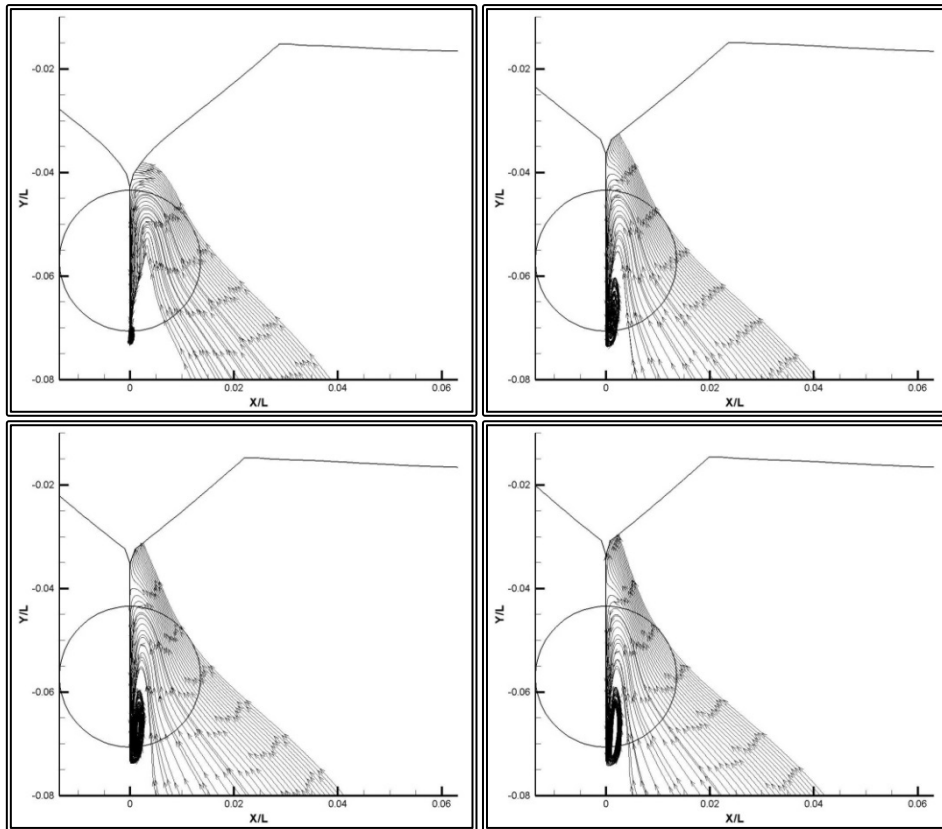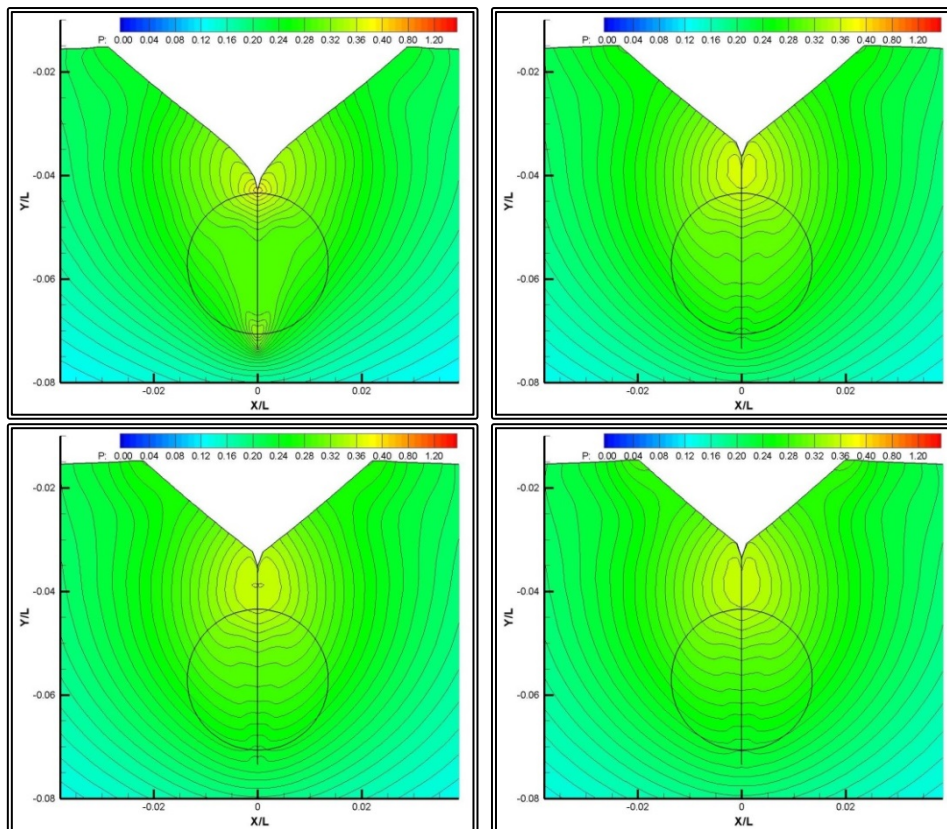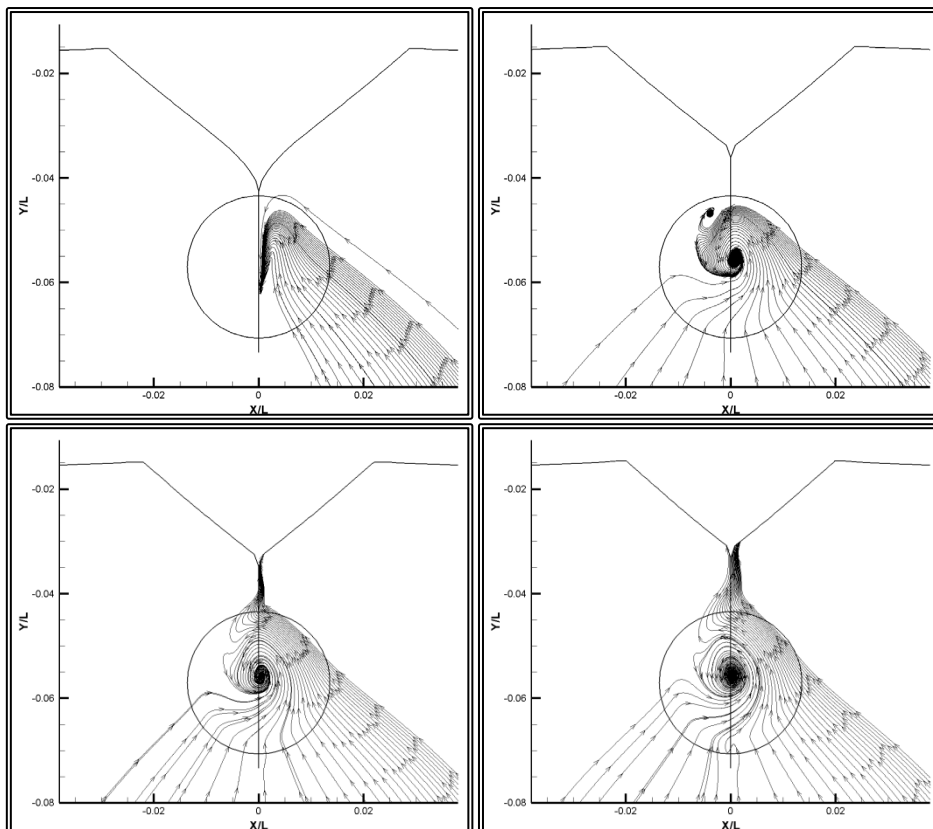

Figure 6.3.23 Isobar (c_P) contours, full scale, asymmetric flow, propulsion. From top right to bottom left, sections A, B, C and D.

6.3.8 "Bare" Hull Results Comparison

Resistance and propulsion data, obtained through the numerical tests of the previous paragraphs, are presented in tables 6.3.3 and 6.3.4. Also presented in those tables are data measured experimentally (Dyne, 1995). In figure 6.3.24, the iso-wake contours for the longitudinal velocity components are presented and compared with experimental data.

Table 6.3.5 Resistance Characteristics, "bare" hull calculations

	Experimental	Model Scale		Asymmetric	Full Scale Asymmetric
		Symmetric			
		Wall fun's	Near wall	Wall fun's	Wall fun's
WS [m²]	11.552	11.548	11.548	11.548	14,966
R_T [Nt]	46.255	47.521	47.160	46.674	1.274E+06
EHP [kW]	6.342E-02	6.515E-02	6.466E-02	6.399E-02	1.048E+04
C_T	4.293E-03	4.383E-03	4.349E-03	4.305E-03	2.455E-03
C_F	3.008E-03	3.085E-03	3.111E-03	3.046E-03	1.520E-03
C_P	1.285E-03	1.299E-03	1.238E-03	1.259E-03	9.349E-04

Table 6.3.4 Propulsion Characteristics, "bare" hull calculations

	Model Scale		Full Scale
	Symmetric	Asymmetric	Asymmetric
1-w (nom)	0.394	0.366	0.561
1-w (eff)	0.555	0.573	0.651
1-t	0.859	0.835	0.834
n [rpm]	807	806	115
T [Nt]	56.009	55.665	1.527E+06
DHP [kW]	1.040E-01	1.040E-01	1.593E+04
C_T	5.113E-03	5.134E-03	2.943E-03
C_F	3.086E-03	3.059E-03	1.523E-03
C_P	2.027E-03	2.075E-03	1.419E-03

In the asymmetric flow case, the difference between the calculated and measured R_T is 0.91%. In the symmetric flow case with wall functions, the corresponding difference is 2.74%, while in the symmetric case without wall functions, the difference is 1.96%. The effect of the wall functions, as expressed in the difference between the two symmetric flow cases, is 0.76%. When considering the fact that the uncertainty of the experimental measurement is in the region of 2% (Dyne, 1995), the numerically calculated values for the total resistance at model scale are in very satisfactory agreement with the experimental data.

By examining the wake patterns, the numerical method is able to approximate the flow structures, such as the vortex that appears in the experimental data, on either side of the shaft bossing. Regarding the intensity and extend of the vortex, the numerical results appear quite inaccurate but it should be taken into consideration the fact that even experimental data gathered using the two technics, Padtl tubes or Pitot tubes, differ significantly.
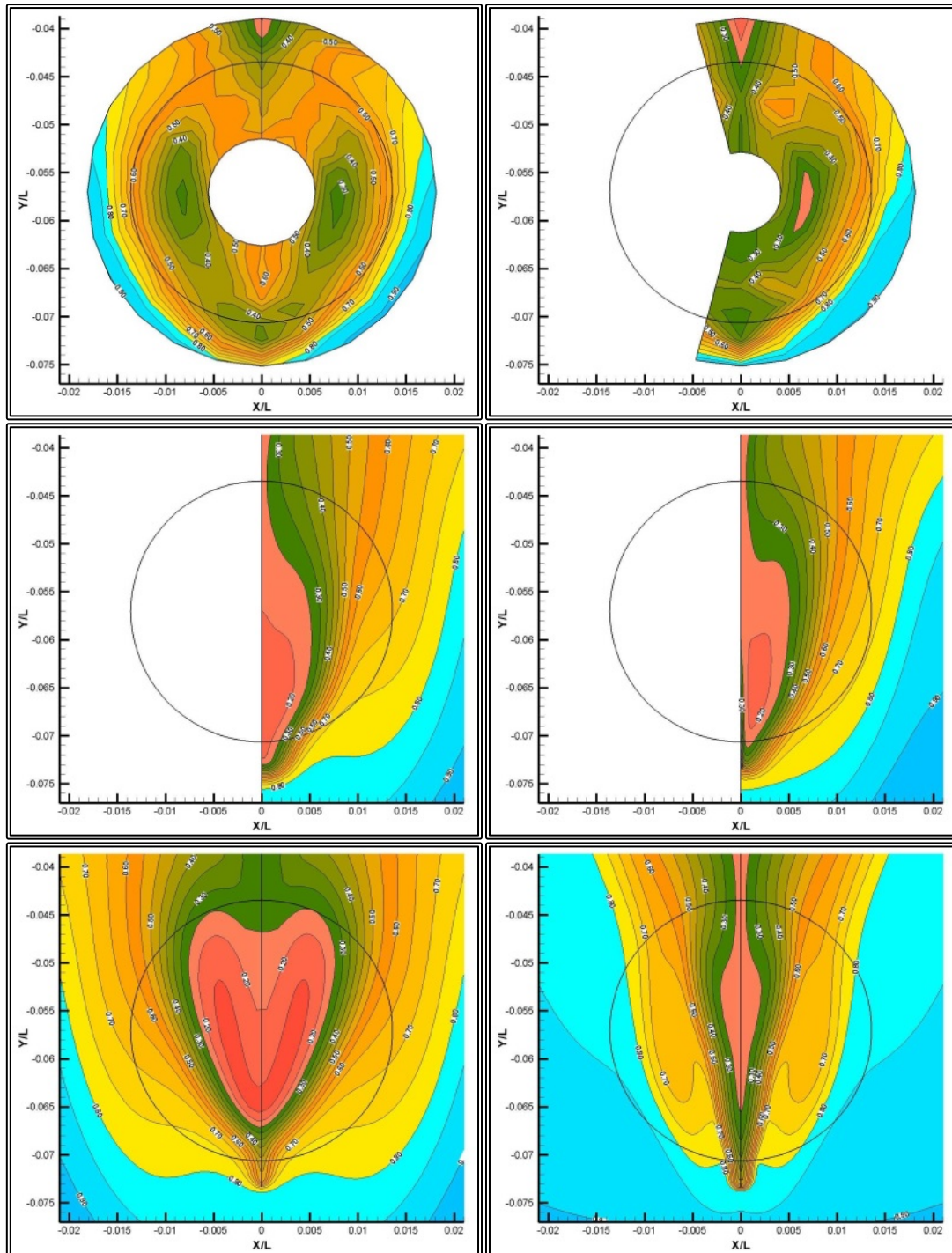
Figure 6.3.24 Comparison of isowake (w/V) contours, resistance, section B (propeller plane). From top right to bottom left, experimental Pradtl tube measurements, experimental pitot tube measurements, model scale symmetric flow, model scale symmetric flow with near wall treatment, model scale asymmetric flow, full scale.

6.4 The Overlapping Block Setup for the Rudder

6.4.1 Overview of the Overlapping Block Setup

For the flow calculations at the stern of the ship with a rudder, the overlapping grid block method is employed, as explained in Chapter 4. The planform of the rudder is presented in figure 6.1.2 while the cross section profile was that of NACA 18, i.e. the maximum thickness was equal to 0.20xC, where C is the chord length. The NACA 18 hydrofoil profile is presented in figure 6.4.1.
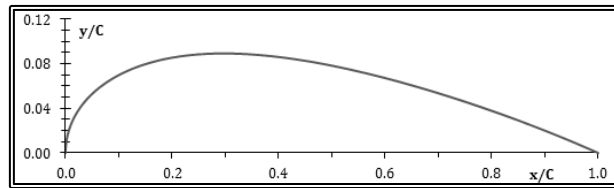
Figure 6.4.1 Profile of the NACA18 hydrofoil section

The rudder grid block was generated by employing the method presented in Paragraph 4.9. The grid comprises 2-D curvilinear orthogonal C-type grids, normal to the rudder axis. Since the chord length of each section varies along the rudder axis, the 2-D grids differ and the resulting 3-D grid is partially orthogonal. Also near the hull, the grid conforms to the hull and the water surface and as a result, the sections are not planar. In figure 6.4.2 two perspective views of the rudder block are presented, while in figure 6.4.3, a side view of the rudder block is presented.
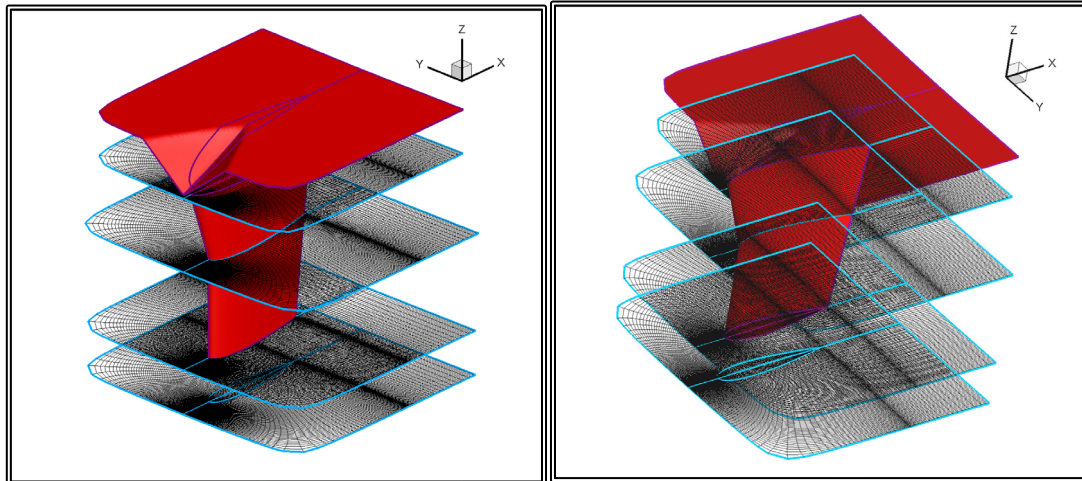
Figure 6.4.2 Perspective view of the rudder, the upstream (top) and downstream (bottom) boundaries, as well as three K-sections at the root of the rudder, the kink and the tip
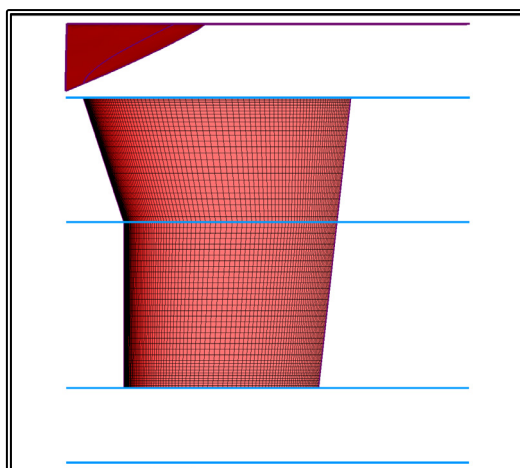
Figure 6.4.3 Side view of the rudder and the grid on the rudder surface, the upstream (top) and downstream (bottom) boundaries, as well as three K-sections at the root of the rudder, the kink and the tip

In this application, the orthogonal curvilinear 2-D grids are generated by employing both the singularity distribution method presented on paragraph 3.4 and the conformal mapping method of paragraph 1.4.3. More specifically, near the hydrofoil, the grid is generated using the conformal mapping method. Then in order for the grid to conform with the user defined boundaries, the rest of the grid is generated using the singularity distribution method.

In figure 6.4.4 the 2-D grid on section K=45, at the kink of the rudder profile, is presented. The number of grid nodes in this grid is NIxNJ=298x78, with NI the number of nodes in the circumferential direction and NJ the number of nodes in the radial direction. Out of the NI nodes, NIC=239 nodes lay on the rudder surface and NID=60 nodes are abaft the ruder trailing edge. In figure 6.4.5 a detail near the leading edge of the above grid is presented.
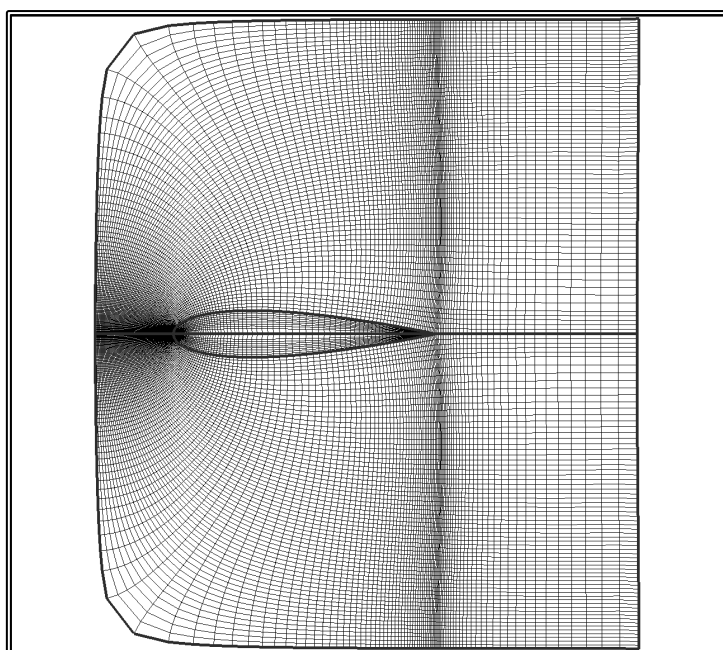
Figure 6.4.4 2-D, K=45 section (at the kink of the rudder), NIxNJ=298x78 with NIC=239 nodes on the rudder surface and NJ1=10 grid lines inside the rudder volume
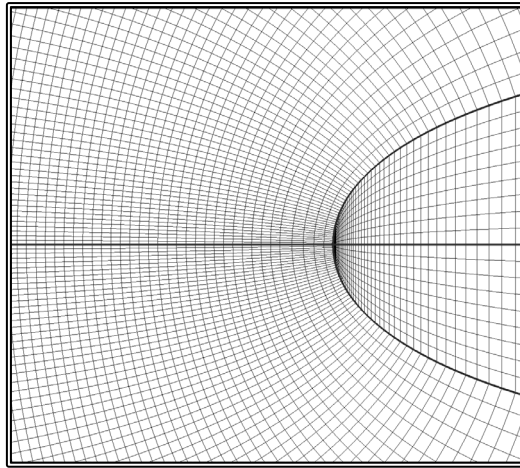
Figure 6.4.5 Detail near the leading edge of the 2-D, K=45 section (at the kink of the rudder), NIxNJ=298x78 with NIC=239 nodes on the rudder surface and NJ1=10 grid lines inside the rudder volume

Since the rudder thickness is non-zero at the rudder root and tip, the resulting geometrical discontinuity is modeled using extra grid nodes (extra iso-J lines) that form an inner sub-grid. The finite volumes that are inside the rudder, remain inactive during the solution of the problem, while those above the root and below the tip are part of the solution procedure. In the first area, where the volumes are inactive, the shape of the grid is trivial and consequently consists of one set of lines, normal to the chord and another set that is calculated through linear interpolation between the chord and the profile (Figure 6.4.6)

Above the rudder root and beneath the tip, the inner grid is solved and in order to be orthogonal curvilinear, it is generated using the singularity distribution method presented on paragraph 3.4. In figure 6.4.6, the inner grid is presented for section K=NK, having NJ1=10 grid lines inside the rudder volume.
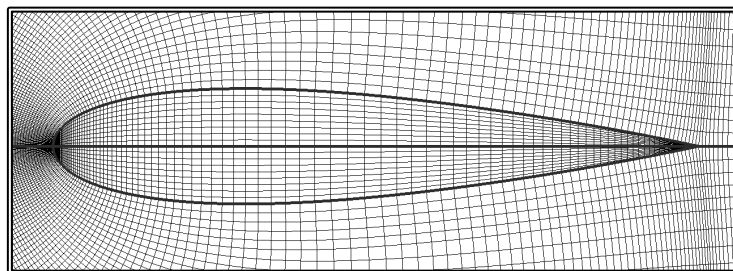
Figure 6.4.6 Inner grid of section, K=45 (at the kink of the rudder), with NICxNJ1=239x10 nodes
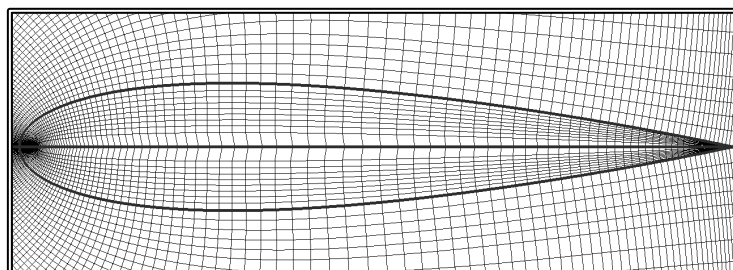
Figure 6.4.7 Inner grid of section K=NK (the downstream boundary), with NICxNJ1=239x10 nodes

In order for the grid to conform to the hull contours, the upstream section (K=1) is projected on the hull. The rest of the 2-D grids of part-A, above the rudder root, are also deformed by an amount varying linearly between zero at the rudder root and one at section K=1. In this application, the rudder block extends abaft the ship stern. In order for the rudder block to be able to use data from the ship block as boundary conditions, the location of the K=1 section is selected in such a way that it is always underneath the water surface. Then, the portion of the K=1 section that intersects the hull is deformed while the rest of the grid remains planar. In figures 6.4.8 and 6.4.9, the upstream, K=1 section is presented.
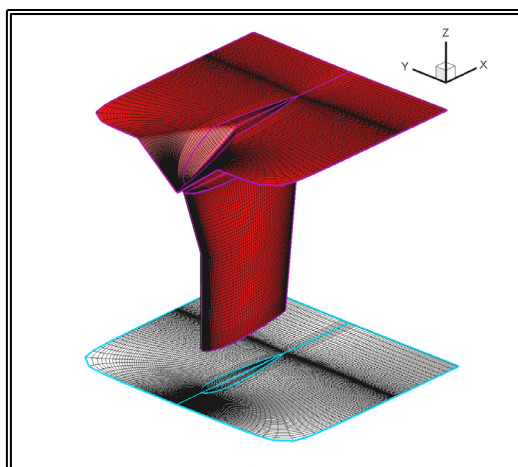
Figure 6.4.8 Perspective view of the rudder and the grid on the rudder surface, the upstream (top) K=1 grid and the downstream (bottom) K=NK grid
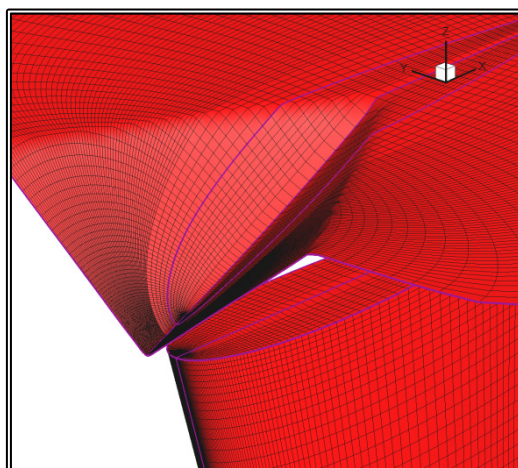
Figure 6.4.9 Detail of the upstream (top) K=1 grid and the grid on the rudder surface

The rudder block, uses the solution of the ship block as boundary condition for the upstream (K=1), the downstream (K=NK), the north (J=NJ), the west (I=1) and east (I=NI) boundaries. In figures 6.4.10 and 6.4.12 the north (J=NJ) rudder block boundary is presented in yellow.

During the solution procedure, as described in paragraph 3.11, the ship block also takes information from the rudder block solution. The transfer of information, from rudder to ship block is performed at four sections of the ship block, forming a closed volume. Two of the sections are part of iso-K planar grids, just upstream the ruder

leading edge and downstream the trailing edge. Another section is an iso-J grid section selected as close as possible to the rudder without intersection it at any point. This iso-J grid section is presented in figures 6.4.10 and 6.4.12 in red color.

In this application, the final section cannot be an iso-I grid section, rather a continuous surface described by varying values of the I-index. This final section is presented in figures 6.4.10 and 6.4.12 in green color.
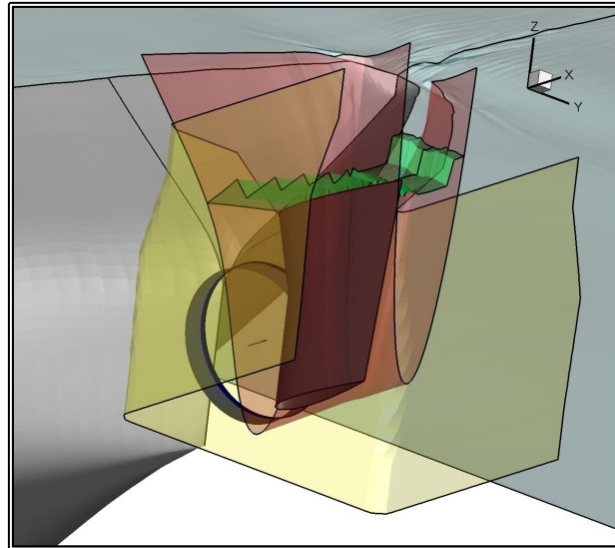
Figure 6.4.10 Perspective view of the Overlapping block setup. The North (external) boundary of the rudder block is presented in yellow. In red is the iso-J line and in green is the I-line of the ship grid block where boundary conditions are taken from the rudder block
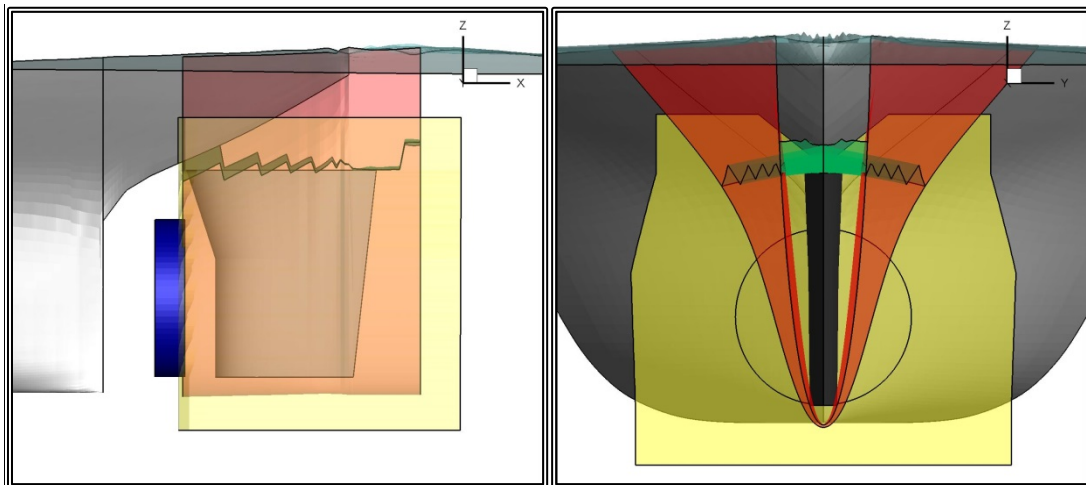
Figure 6.4.11 Side and rear view of the Overlapping block setup. The North (external) boundary of the rudder block is presented in yellow. In red is the iso-J line and in green is the I-line of the ship grid block where boundary conditions are taken from the rudder block

6.4.2 Grid Independence Tests for the Rudder Grid Block

The grid size greatly affects the numerical solution and consequently numerical tests are required in order to determine the minimum grid size in order to obtain an accurate solution. In this paragraph, the results of such a grid independence test are presented.

The tests were performed for the "Dyne" rudder at model scale. The presence of the ship was ignored and the rudder at a free flow problem was solved. The free stream fluid velocity was 1.371 m/s, corresponding to a Reynold's number Re=1.141E+05. The main flow variables are presented in table 6.4.1.

Table 6.4.1 Flow variables for the grid independence tests

Free Stream Velocity, U_∞	1.371	m/s
Fluid Viscosity, ν	1.161E-06	m^2/s
Reynolds's Number, Re	1.141E+05	
Reference Chord Length, C	0.097	m

The required grid size for a solution independent of the grid, was roughly estimated based on past experience and the tests were performed using relatively fine grids. The main grid variables are presented in table 6.4.2. In the following table, NI is the total number of nodes in the circumferential direction, NIC is the number of nodes in the circumferential direction, that lay on the rudder surface, NID is the number of nodes in the circumferential direction abaft the ruder trailing edge, NJ is the number of nodes in the radial direction, NK is the total number of nodes along the rudder axis, NKU is the number of nodes along the rudder axis, above the rudder root, NKL is the number of nodes along the rudder axis, along the rudder span and NKD is the number of nodes along the rudder axis, beneath the rudder tip. The tests were performed for different grid sizes along all three directions, but in all test, the y+ parameter was in the region of 100.

Table 6.4.2 Main grid variables for the grid independence tests

	Coarse			Medium			Fine	
	c1	c2	c3	m1	m2	m3	f1	f2
NI	698	298	698	698	498	698	698	698
NIC	599	239	599	599	419	599	599	599
NID	104	64	104	104	84	104	104	104
NJ	48	78	78	63	78	78	78	78
NK	95	95	50	95	95	72	95	95
NKU	20	20	20	20	20	20	20	10
NKL	30	62	27	62	62	44	62	77
NKD	15	15	5	15	15	10	15	10
NIxNJxNK	3,182,880	2,208,180	2,722,200	4,177,530	3,690,180	3,919,968	5,172,180	5,172,180

In figure 6.4.12 perspective views of two rudder blocks are presented, for the coarse-c2 (NIxNJxNK=298x78x95) (on the left) and the fine-f1 (NIxNJxNK=698x78x95) (on the right) test cases.

In figure 6.4.13 the 2-D grid on section K=NK, the downstream edge, is presented for the coarse-c2 (NIxNJxNK=298x78x95) (on the left) and the fine-f1 (NIxNJxNK=698x78x95) (on the right) test cases. The number of nodes on the rudder surface NIC, are respectively 239 and 599. In both case the inner grid comprises NJ1=10 lines. In figure 6.4.14 a detail near the leading edge of the above grids is presented.
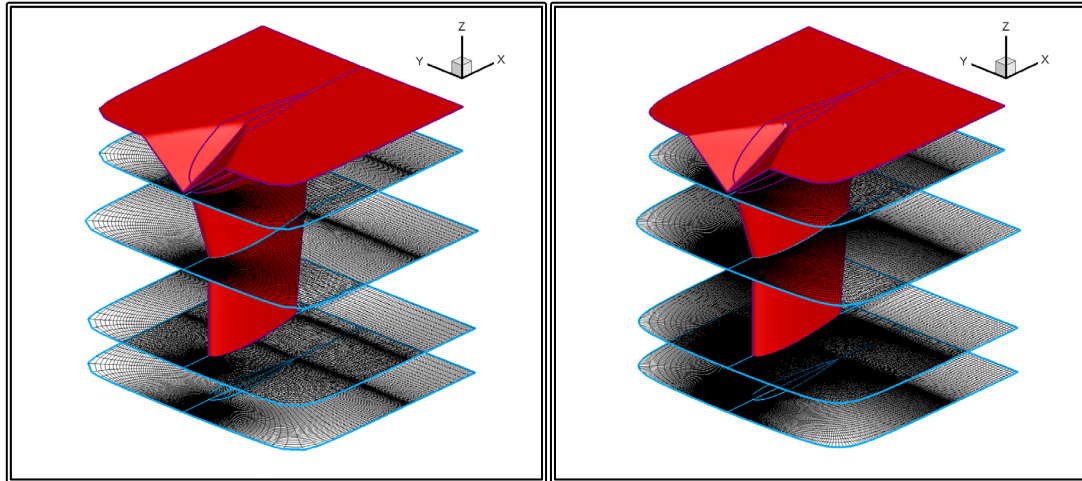
Figure 6.4.12 Perspective view of the rudder, the upstream (top) and downstream (bottom) boundaries, as well as three K-sections at the root of the rudder, the kink and the tip for the coarse-c2 (on the left) and the fine-f1 (on the right) tests
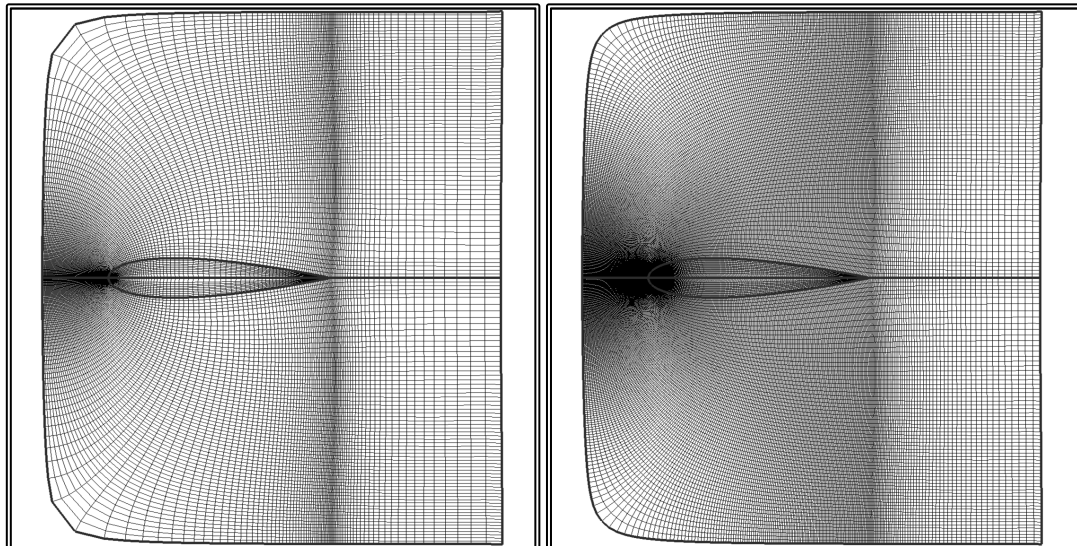
Figure 6.4.13 2-D, K=NK section (the downstream boundary), for the coarse-c2 (on the left) and the fine-f1 (on the right) tests. The coarse grid size is NIxNJxNK=298x78x95 with NIC=239 nodes on the rudder surface and NJ1=10 grid lines inside the rudder volume. The fine grid size is NIxNJxNK=698x78x95 with NIC=599 nodes on the rudder surface and NJ1=10 grid lines inside the rudder volume
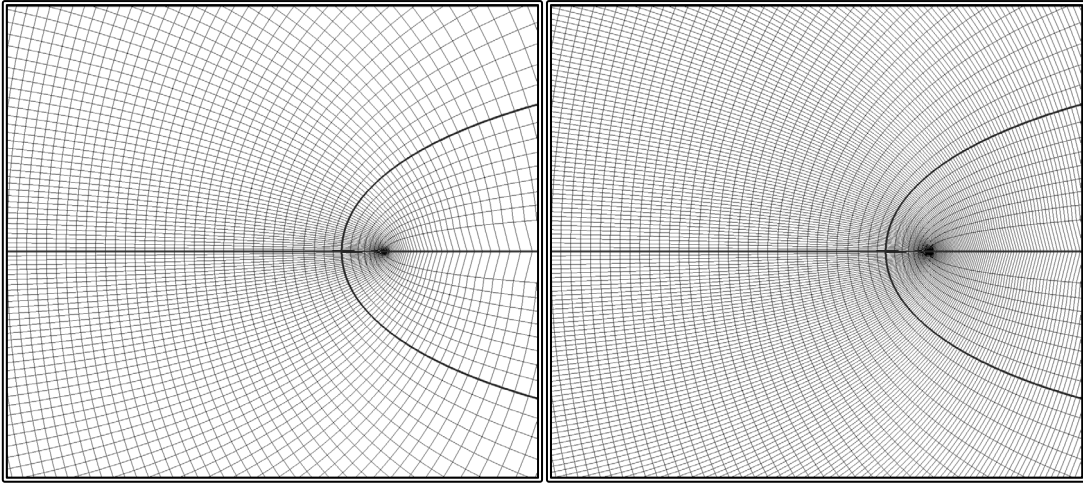
Figure 6.4.14 Detail near the leading edge of the 2-D, K=NK section (the downstream boundary), for the coarse-c2 (on the left left) and the fine-f1 (on the right) tests. The coarse grid size is NIxNJxNK=298x78x95 with NIC=239 nodes on the rudder surface and NJ1=10 grid lines inside the rudder volume. The fine grid size is NIxNJxNK=698x78x95 with NIC=599 nodes on the rudder surface and NJ1=10 grid lines inside the rudder volume

The test cases are compared in terms of the total Drag which is calculated as the sum of the skin friction R_F and the pressure drag R_P:

$$\text{Drag} = R_P + R_F \qquad (6.4.1)$$

$$R_P = \iint_{A_R} p^* \cdot \mathbf{n} \cdot \mathbf{i} \; ds \quad (6.4.1)$$

$$R_F = \iint_{A_R} \tau_w \cdot \mathbf{s} \cdot \mathbf{i} \, ds \quad (6.4.2)$$

Where A_R is the rudder surface, p^* is the pressure on the rudder surface, $\mathbf{n}$ is the unit vector normal to the rudder surface, $\mathbf{i}$ is the unit vector parallel to the rudder chord, τ_w is the wall shear stress and $\mathbf{s}$ is the tangential unit vector to the rudder surface.

The drag components are expressed in their respective non-dimensional form:

$$C_P = \frac{R_P}{0.5 \cdot \rho \cdot A_R \cdot U_\infty^2} \qquad (6.4.4)$$

$$C_F = \frac{R_F}{0.5 \cdot \rho \cdot A_R \cdot U_\infty^2} \qquad (6.4.5)$$

$$C_D = C_P + C_F = \frac{\text{Drag}}{0.5 \cdot \rho \cdot A_R \cdot U_\infty^2} (6.4.6)$$

Where U_∞ is the free stream fluid velocity.

In table 6.4.3, the results of the numerical tests are presented, in terms of the non-dimensional drag coefficients. In table 6.4.4, the same results are presented, in terms of the per cent variation between each test and the f1 test that is characterized by the highest number of nodes.

Table 6.4.3 Results of the grid independence tests

	Coarse			Medium			Fine	
	c1	c2	c3	m1	m2	m3	f1	f2
NIxNJxNK	3,182,880	2,208,180	2,722,200	4,177,530	3,690,180	3,919,968	5,172,180	5,172,180
C_D	1.503E-02	1.621E-02	1.562E-02	1.563E-02	1.574E-02	1.541E-02	1.564E-02	1.574E-02
C_F	8.019E-03	8.204E-03	8.155E-03	8.137E-03	8.187E-03	8.163E-03	8.180E-03	8.189E-03
C_P	7.006E-03	8.009E-03	7.469E-03	7.488E-03	7.552E-03	7.245E-03	7.459E-03	7.549E-03

Table 6.4.4 Comparison of the grid independence test results

	Coarse			Medium			Fine	
	c1	c2	c3	m1	m2	m3	f1	f2
NIxNJxNK	3,182,880	2,208,180	2,722,200	4,177,530	3,690,180	3,919,968	5,172,180	5,172,180
C_D	-3.93%	3.67%	-0.10%	-0.09%	0.64%	-1.48%	-	0.63%
C_F	-1.97%	0.29%	-0.31%	-0.53%	0.09%	-0.21%	-	0.10%
C_P	-6.07%	7.37%	0.13%	0.39%	1.24%	-2.87%	-	1.20%

The results are very close with a maximum deviation of 4% for the Drag. Also the deviation tends to decrease as the number of nodes increases. This is more easily understood through the graphical presentation of the results. In figures 6.4.15-6.4.17, the per cent variation of the drag coefficient, the skin friction coefficient and the pressure drag coefficient is presented respectively. The base line is the f1 test, characterized by the highest number of nodes.
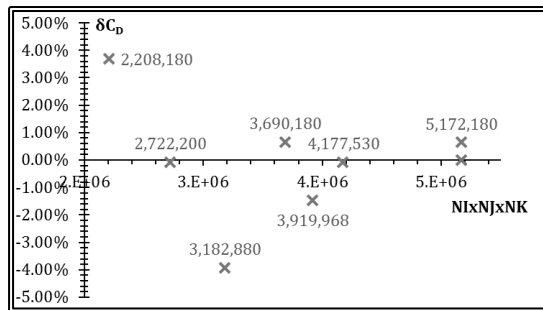
Figure 6.4.15 Per cent variation of the Drag Coefficient C_D with respect to the total number of grid nodes
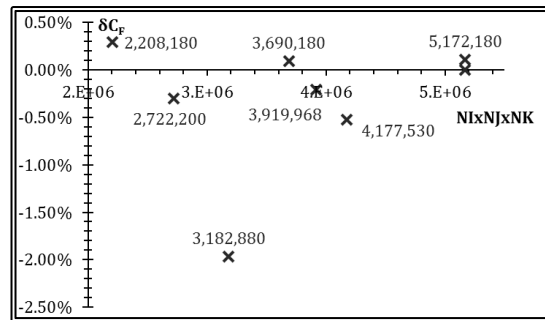
Figure 6.4.16 Per cent variation of the Skin Friction Coefficient C_F with respect to the total number of grid nodes
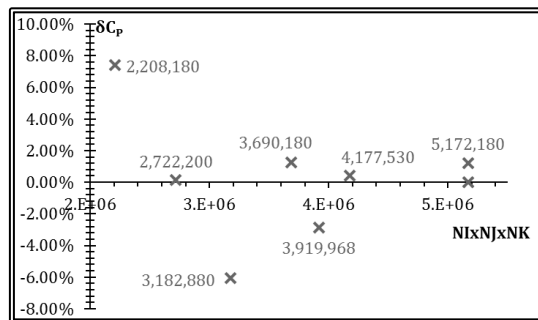
Figure 6.4.17 Per cent variation of the Pressure Drag Coefficient C_P with respect to the total number of grid nodes

Apart from the integrated quantities, the numerical solution is very similar for all tests, also in terms of the values of the localized coefficients for the pressure drag c_p and the skin friction c_f:

$$c_P = \frac{p}{0.5 \cdot \rho \cdot U_\infty^2} (6.4.7)$$

$$c_f = \frac{\tau_w}{0.5 \cdot \rho \cdot U_\infty^2} (6.4.8)$$

In figures 6.4.18 and 6.4.19, the distribution of the pressure drag c_p and the skin friction c_f coefficients is presented on section K=62, for four of the test cases. In figure 6.4.20, the pressure drag coefficient contour on the rudder surface is presented, for the same test cases
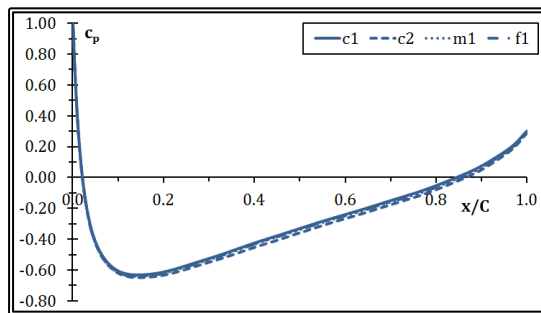
Figure 6.4.18 Pressure Drag coefficient c_p, distribution on section K=62
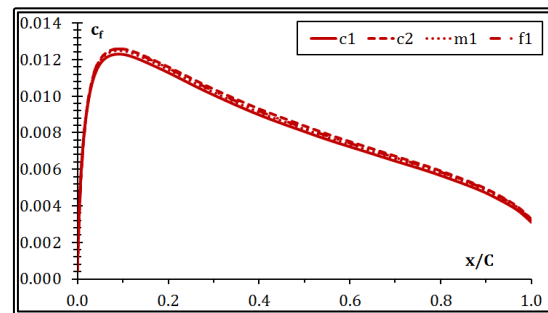
Figure 6.4.19 Skin Friction c_f, coefficient distribution on section K=62
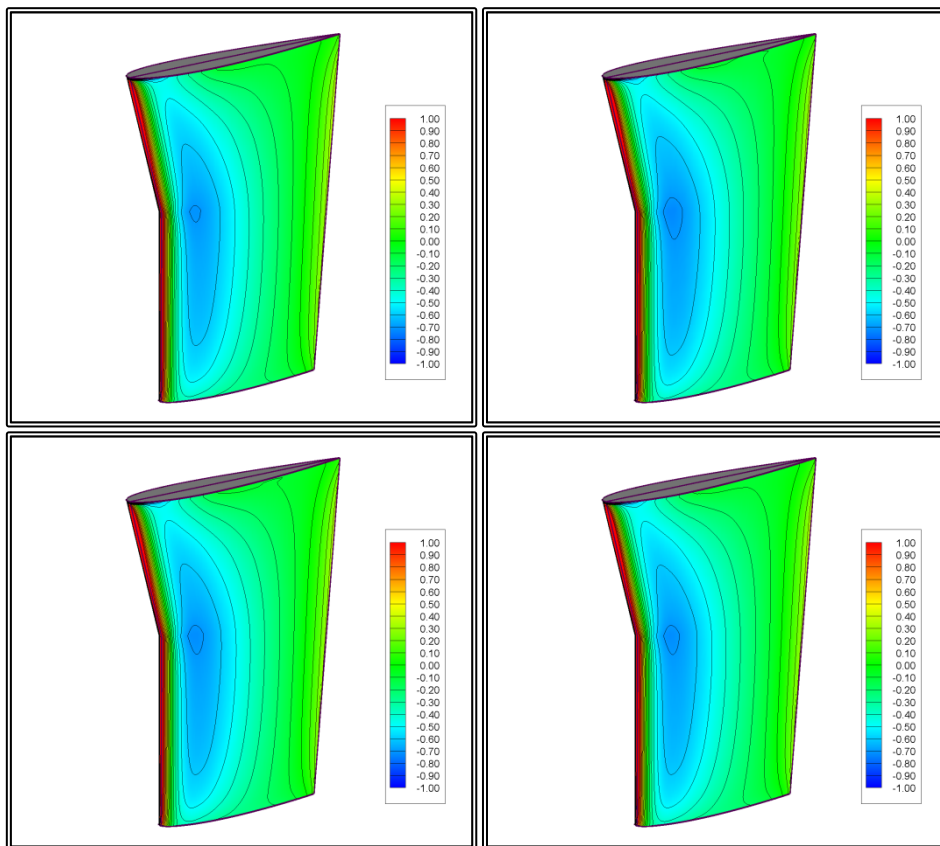
Figure 6.4.20 Pressure Drag coefficient c_p, contours on the rudder surface, test cases c1, c2, m1 and f1, from top left to bottom right,

The distributions of pressure and skin friction coefficients appear to be very similar in all tests. This indicates that the finer grid size is sufficient. A final comment on the grid independence tests is that the convergence history is also very similar. In figure 6.4.21 the convergence history of the drag coefficient C_D is presented for four of the test cases. All test cases appear to have converged after less than 1,000 iterations.
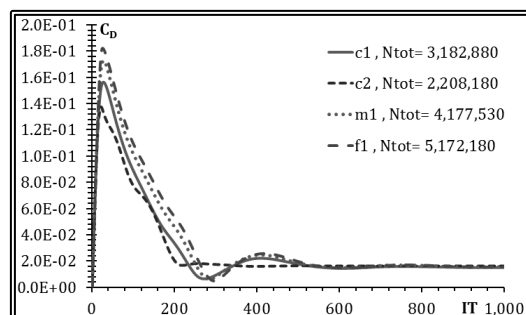
Figure 6.4.21 Convergence history for the Drag Coefficient C_D for the c1, c2, m2 and f1 tests

6.4.3 2-D Tests for the Overlapping Block Setup

Since the boundary conditions affect the numerical solution, the external boundaries of a grid need be at a distance from the solid boundary. In the case of the external flow past a hydrofoil, the grid typically extends one chord length upstream the leading edge, two chord lengths downstream the trailing edge, and one chord length to the side. In this application, the rudder grid block is significantly narrower, especial upstream, due to the presence of the propeller disk.

In order to evaluate the possible effect of the narrow block on the accuracy of the solution, a numerical comparison was conducted between two alternative setups for the solution of the 2-D flow problem past a NACA 18 hydrofoil. In the first test, a single large C-type block was generated around the hydrofoil and boundary conditions are those of undisturbed flow. In the second test a small C-type block was generated around the hydrofoil. The boundary conditions for this smaller block are provided by the solution of an external H-type block.

The extend of the inner C-type block is similar to those used in the rudder block, while the extends of the outer H-type block are similar to those of the single C-type block. In figure 6.4.22, the setup for the two test is presented with the extend of the single C-type block in blue color, the extends of the outer H-type block in green and the inner C-type block in red color.

The main variables of the grids are presented in table 6.4.5 where for the C-type grids NI is the total number of nodes in the circumferential direction, NIC is the number of nodes in the circumferential direction, that lay on the hydrofoil, NID is the number of nodes in the circumferential direction downstream the trailing edge and NJ is the number of nodes in the radial direction.

For the H-type grid, NI is the total number of nodes in the longitudinal direction, NIU is the number of nodes in the longitudinal direction upstream the leading edge, NIC is the number of nodes in the longitudinal direction, along the hydrofoil chord, NID is

the number of nodes in the longitudinal direction downstream the trailing edge and NJ is the number of nodes in the transverse direction.
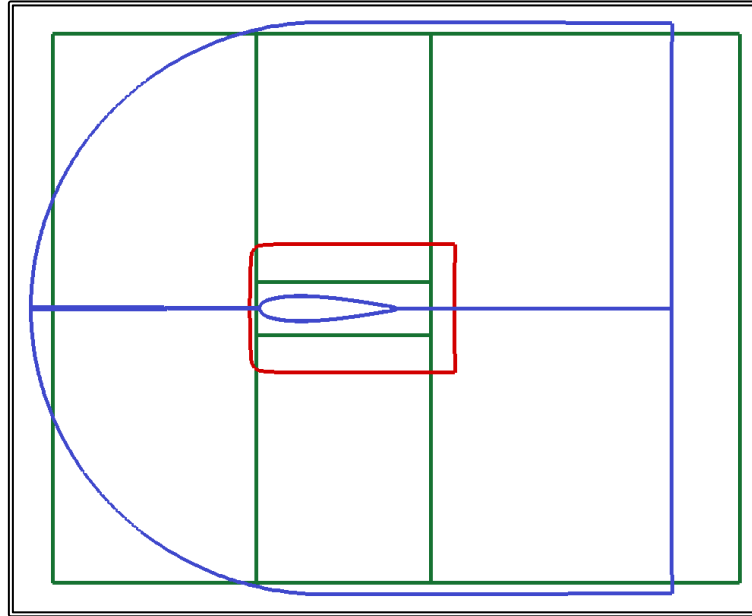
Figure 6.4.22 Overlapping block setup, with the outer and inner boundaries of the external H-type block in green, the outer boundary of the internal C-type block in red. The blue lines correspond to the boundaries of the single C-type block

Table 6.4.5 Main grid variables for the 2-D overlapping block setup tests

	Single C-type	External H-type	Internal C-type
NI	550	400	350
NIU	-	100	-
NIC	300	250	300
NID	250	50	50
NJ	350	400	80
NIxNJ	385,000	320,000	56,000
Upstream extend	1.5xC	1.5xC	0.07xC
Downstream extend	2.0xC	3.5xC	0.5xC
Side extend	2.0xC	2.0xC	0.5xC
NIxNJ$_{Tot}$	385,000	376,000	

In figure 6.4.23 the single C-type grid is presented. In figure 6.4.24, the inner C-type grid is presented. A comparison of the two C-type grids, near the hydrofoil leading edge, is presented in figure 6.4.25. Finally in figure 6.4.26 the external H-type grid is presented. In the last figure, the area missing from the H-type grid is the area that remains inactive during the numerical solution.
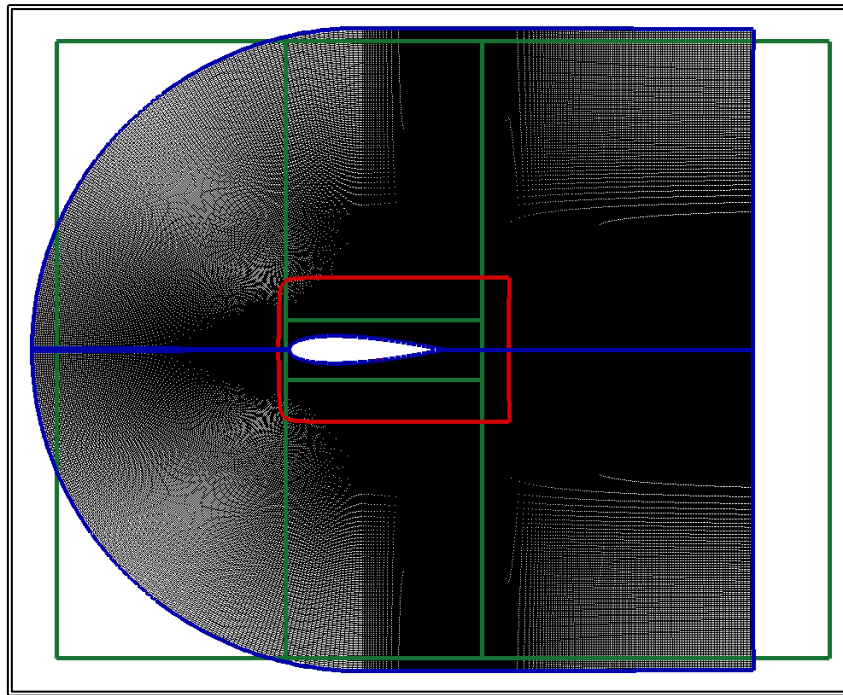
Figure 6.4.23 Single C-type block with NIxNJ=550x350 with NIC=300 nodes along the chord of the hydrofoil and NIA=250 nodes downstream the trailing edge
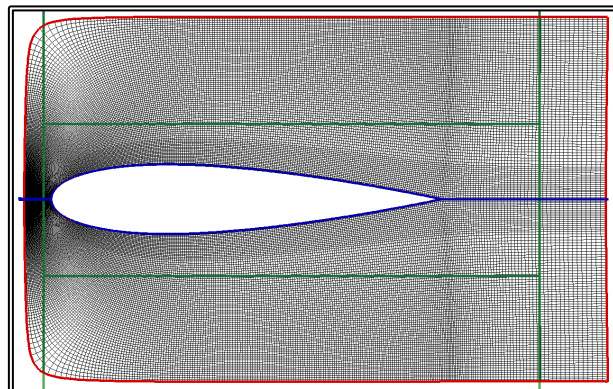
Figure 6.4.24 Internal C-type block with NIxNJ=350x80 with NIC=300 nodes along the chord of the hydrofoil and NIA=50 nodes downstream the trailing edge
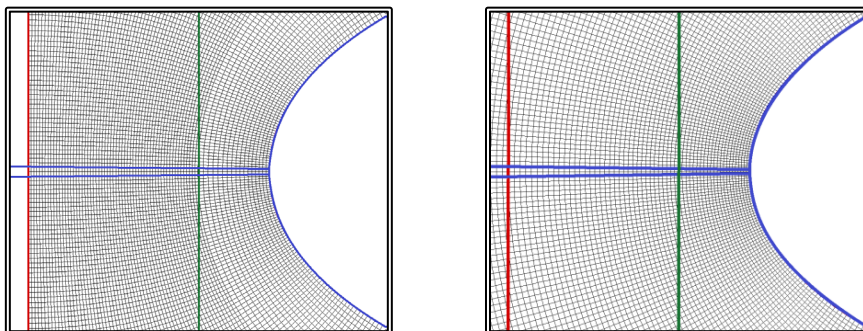
Figure 6.4.25 Detail near the leading edge of the internal (on the left left) and the single (on the right) C-type blocks with NIxNJ=350x80, NIC=300, NIA=50 and NIxNJ=550x350, NIC=300, NIA=250 nodes respectively.
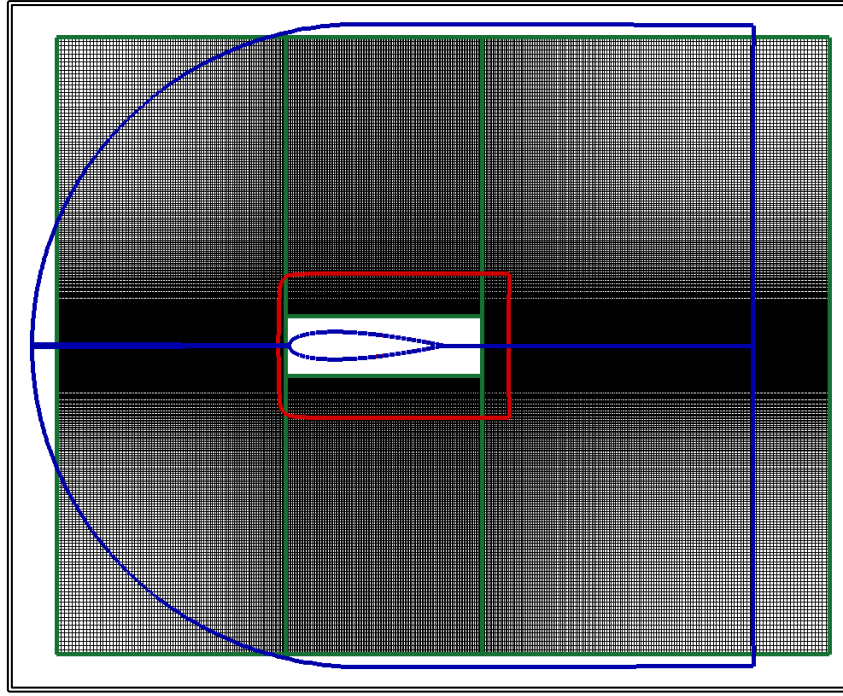
Figure 6.4.26 External H-type block with NIxNJ=400x400 with NIC=250 nodes along the chord of the hydrofoil, NIU=100 nodes upstream the leading edge and NID=50 nodes downstream the trailing edge

Both tests were performed for a free stream fluid velocity corresponding to a Reynold's number Re=1.0E+06. The main flow variables are presented in table 6.4.6.

Table 6.4.6 Flow variables for the 2-D overlapping block setup tests

Free Stream Velocity, U_∞	1.000	m/s
Fluid Viscosity, ν	1.000E-06	m^2/s
Reynolds's Number, Re	1.000E+06	
Reference Chord Length, C	1.000	m

The two cases are compared in terms of the total Drag per unit length, which is calculated as the sum of the skin friction R_F and the pressure drag R_P:

$$\text{Drag} = R_P + R_F \qquad (6.4.9)$$

$$R_P = \int_S p \cdot \mathbf{n} \cdot \mathbf{i}\, ds \quad (6.4.10) \qquad R_F = \int_S \tau_w \cdot \mathbf{s} \cdot \mathbf{i}\, ds \quad (6.4.11)$$

Where R_P is the pressure drag, R_F is the skin friction, S is the hydrofoil curve length of the hydrofoil, p is the pressure, $\mathbf{n}$ is the unit vector normal to the hydrofoil, $\mathbf{i}$ is the unit vector parallel to the chord line, τ_w is the wall shear stress and $\mathbf{s}$ is the tangential unit vector to the hydrofoil. The drag components are expressed in their respective non-dimensional form:

$$C_P = \frac{R_P}{0.5 \cdot \rho \cdot C \cdot U_\infty^2} \qquad (6.4.12) \qquad C_F = \frac{R_F}{0.5 \cdot \rho \cdot C \cdot U_\infty^2} \qquad (6.4.13)$$

$$C_D = C_P + C_F = \frac{\text{Drag}}{0.5 \cdot \rho \cdot C \cdot U_\infty^2} \quad (6.4.14)$$

Where U_∞ is the free stream velocity.

In table 6.4.7, the results of the numerical tests are presented, in terms of the non-dimensional drag coefficients. The difference between the two tests is quite small, around 3.5%. Consequently, despite the very narrow internal C-type grid, this setup produces acceptable results.

Table 6.4.7 Results of the 2-D overlapping block setup tests

	C-type	H+C-type	
IT_1	2071	3	
IT_2	-	70	
C_D	1.394E-02	1.343E-02	-3.66%
C_F	1.056E-02	1.050E-02	-0.57%
C_P	3.383E-03	2.928E-03	-13.45%

Also presented in the above table are the iterations required for convergence of the solution. IT_1 corresponds to the number of steps required for the convergence of the pressure correction algorithm, while IT_2 corresponds to the number of steps required for the convergence of the overlapping block method. The latter is also presented in graphical form, in figure 6.4.27.
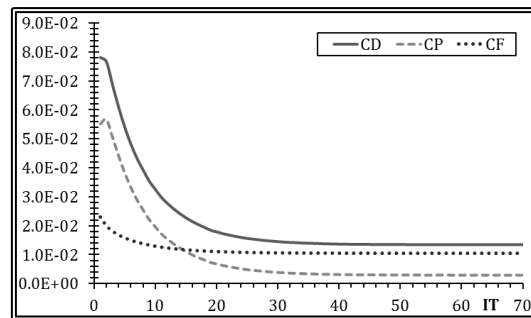
Figure 6.4.27 Convergence history of the overlapping block method, for the Drag, Pressure Drag and Skin Friction Coefficients, C_D, C_P and C_F, for the H+C-type case.

Apart from the integrated quantities, the numerical solutions should yield similar results in terms of the values of the localized coefficients for the pressure drag c_p and the skin friction c_f. In figures 6.4.28 and 6.4.29, the distribution of the pressure c_p and the skin friction c_f coefficients is presented for the two cases.
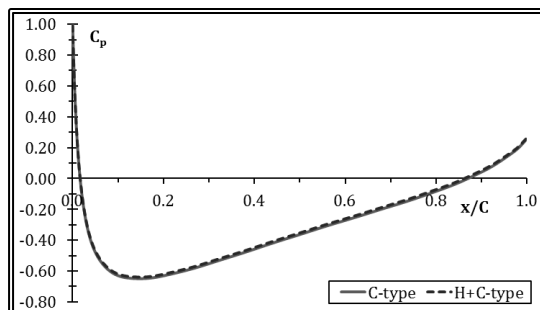
Figure 6.4.28 Comparison of the Pressure coefficient c_p, distribution on the hydrofoil
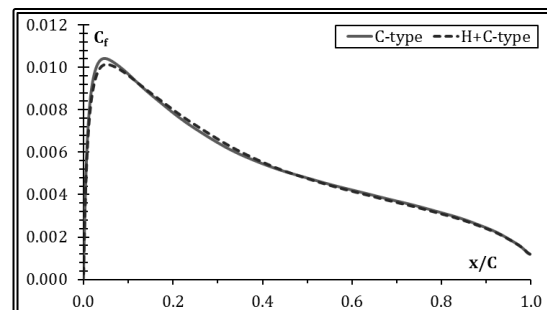
Figure 6.4.29 Comparison of the Skin Friction c_f, coefficient distribution on the hydrofoi

6.5 Hull and Rudder Calculations

The resistance and propulsion problems were solved for the "Dyne" tanker. Simulations were performed at model scale and full scale, at a constant Froude number, Fn=0.165 corresponding to a full-scale velocity of 16.00 kn. The flow variables for the hull and rudder calculations are presented in table 6.5.1.

Table 6.5.1 Flow variables for the hull and rudder calculations.

	Model Scale	Full Scale	
Scale Factor, λ	36	-	
Speed, V	-	16.0	kn
	1.371	8.226	m/s
Fluid Viscosity, ν	1.161E-06	1.431E-06	m²/s
Froude Number, Fn	0.165		
Reynolds's Number, Re	8.474E+06	1.485E+09	
Rudder Reynolds's Number, Re_C	2.2744E+05	1.998E+07	

The free surface was calculated at model scale, using the new hybrid method, as described in paragraph 6.2. In the following numerical experiments the free surface was treated as a fixed boundary. The viscous flow around the ship was then solved by employing two grid blocks, one C-O-type around the bow and fore half of the ship and an H-O-type block around the aft half of the ship as well as the wake. The method for solving the viscous flow problem with multiple grid blocks is described in paragraph 2.5. The flow around the rudder was solved using a separate C-H-type grid block, as described in paragraph 6.4. The grid dimensions and solution procedures were according to the findings of paragraphs 6.3 and 6.4. The main grid variables for each block are presented in table 6.5.2.

Table 6.5.2 Grid block dimensions for the calculations for the "Dyne" tanker with rudder

Bow Grid Block	NI	81
	NJ	180
	NK	511
	$N_{TOT,bow}$	7,450,380
Stern Grid Block	NI	160
	NJ	180
	NK	411
	$N_{TOT,stern}$	11,836,800
	y+ (model/full scale)	30/260
Rudder Block	NI	698
	NJ	78
	NK	95
	$N_{TOT,rudder}$	5,172,180
	y+ (model/full scale)	50/100
	N_{TOT}	24,459,360

The flow problem for the hull with the rudder is solved using the overlapping block methhod where boundary conditions are exchaned between the ship and rudder blocks until convergence is achieved for both blocks (paragraph 4.11). The solution algorithm is presented in figure 6.5.1. Initially the flow problem is solved for the hull without the rudder. Then, the solution of the ship block is used as boundary conditions for the rudder block. Specifically on the North (J=NJ), Upstream (K=1) and Downstream (K=NK) boundaries of the rudder block, the velcoity components are specified as Dirichlet conditions. On the East (I=NI) and West (I=1) boundaries (the outflow boundaries), the pressure is specifyied as Dirichlet condition. Then the SIMPLE algorithm is followed for the rudder block, ensuring the mass conservation. In this first step, 2750 iterations of the SIMPLE algorithm are performed ensuring a high degree of convergence.

Then, the ship block is solved again, incorporating the rudder solution. Specifically, the velocity components, as calculated in the rudder block, are imposed as fixed conditions on a closed surface, inside the rudder block, but not intersecting the rudder. On one face of this close surface, the one characterised by the maximum K-index, toward the rudder outflow boundary, the velocity components are uniformelly scaled. The scale factor is chowsen in such a way as to ensure the mass continuity through the boundary surface.

Then, 300 iterations of the SIMPLE algorithm are performed for the ship block. Another 300 iterations of the SIMPLE algorithm are then performed for the rudder block, using the new ship solution for the boundary conditions. The two above steps are repeated until the solution of the two blocks converges. Approximately 6 iterations are enough.
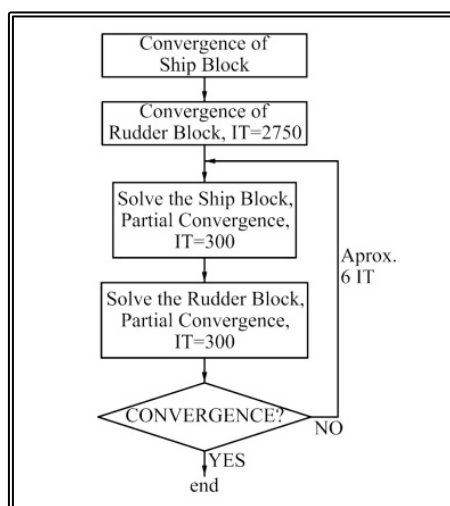
Figure 6.5.1 Hull and rudder, flow chart of the resistance calculation procedure.

In figures 6.5.2 and 6.5.3, the convergence history is presented for the first solution of the rudder block at model scale. In terms of the mass residual, approximately 2500 iterations are required for convergence. On the other hand the Drag appears to have converged after about 700 iterations. Thus, 2750 iterations for the first step and 300 iterations for the partial convergence of the following steps were selected. The level of convergence for the mass residual (4×10^{-3}) is approximately one order higher than the desired level of convergence for the mass residual for the ship (10^{-4}). This is the

result of the selected boundary conditions and the narrow extend of the rudder block. In any case it does not appear to affect the convergence of the drag.
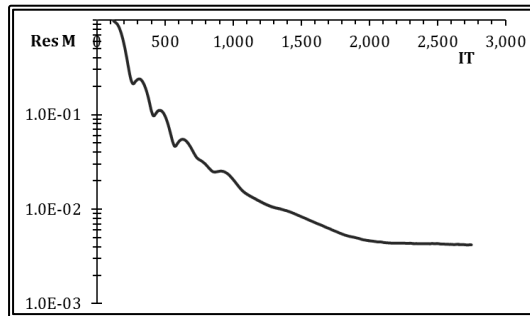
Figure 6.5.2 Mass residual convergence history.
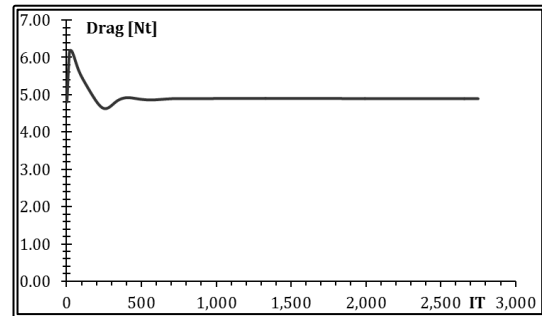
Figure 6.5.3 Drag convergence history rudder.

In the self-propulsion numerical tests, the propeller is modeled via the actuator disk method (paragraph 2.6) and the propeller characteristics are those of the "Dyne" model as presented in paragraph 6.1. The self-propulsion algorithm in the case of the ship with the rudder is presented in figure 6.5.4. Initially the flow problem is solved for the hull without the rudder. Then, the solution of the ship block is used as boundary conditions for the rudder block as described above and 2750 iterations of the SIMPLE algorithm are performed for the rudder block.

Then, the propeller thrust is set equal to the resistance of the hull, plus the rudder drag, the body forces are calculated inside the propeller disk and 30 iterations of the SIMPLE algorithm are performed for the ship block incorporating the rudder solution. The above step is repeated another nine times, each time setting the thrust equal to the new resistance. Then, 300 iterations of the SIMPLE algorithm are performed for the rudder block, using the new ship solution for the boundary conditions.

The above procedure is repeated until the problem converges, with approximately 12 iterations being enough.
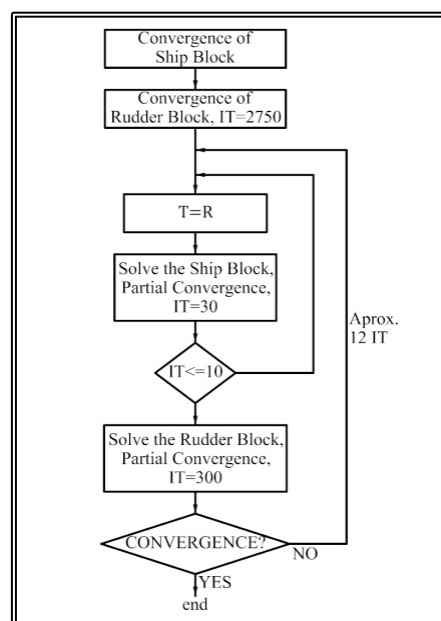
Figure 6.5.4 Hull and rudder, flow chart of the self-propulsion procedure.

Following the above procedures, the resistance and self-propulsion problems are solved, at model and at full scale, for the "Dyne" tanker with rudder. In figure 6.5.5, the Total Resistance R_T and the rudder Drag convergence histories are presented at model scale. In figure 6.5.6, the Thrust and the rudder Drag convergence histories are presented, at full scale.
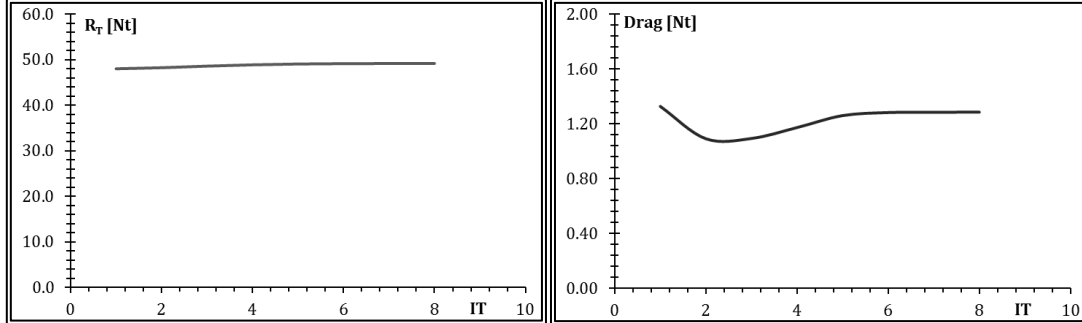
Figure 6.5.5 Convergence history for the total resistance R_T (on the left) and the rudder drag (on the right), model scale.
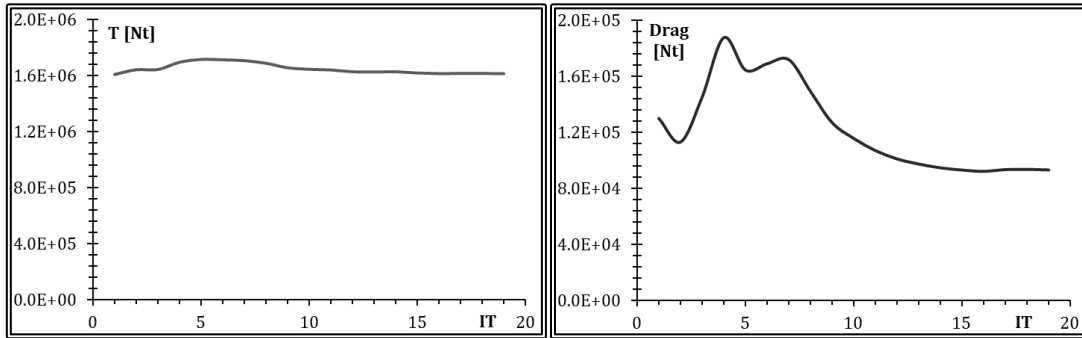
Figure 6.5.6 Convergence history for the Thrust T (on the left) and the rudder drag (on the right), full scale.

For each numerical test, the resistance components were then calculated (Tzabiras, 2009):

$$R_P = \iint_{WS} (p^* - \rho gh) \cdot (\mathbf{n} \cdot \mathbf{i}) \, ds \qquad (6.5.1)$$

$$R_F = \iint_{WS} \tau_w \cdot (\mathbf{s} \cdot \mathbf{i}) \, ds \qquad (6.5.2)$$

Where R_P is the pressure resistance, R_F is the frictional resistance, WS is the actual wetted surface, p* is the pressure on the hull, ρgh is the hydrostatic term, ρ is the water density, g is the gravitational acceleration, h is the height from a reference level, $\mathbf{n}$ is the unit vector normal to the hull, $\mathbf{i}$ is the unit vector parallel to the ship longitudinal axis, τ_w is the wall shear stress and $\mathbf{s}$ is the tangential unit vector to the hull.

The total resistance is then considered equal to the sum of the pressure and frictional resistance:

$$R_T = R_P + R_F \qquad (6.5.3)$$

The resistance components are expressed in their respective non-dimensional form:

$$C_P = \frac{R_P}{0.5 \cdot \rho \cdot WS \cdot V^2} \qquad (6.5.4)$$

$$C_F = \frac{R_F}{0.5 \cdot \rho \cdot WS \cdot V^2} \qquad (6.5.5)$$

$$C_T = C_P + C_F = \frac{R_T}{0.5 \cdot \rho \cdot WS \cdot V^2} \quad (6.5.6)$$

Where V is the ship or model speed.

In the propulsion tests the hull-propeller interaction coefficients are calculated as:

$$1 - w = \frac{V_A}{V} \quad (6.5.7)$$

$$1 - t = \frac{T}{R_T} \quad (6.5.8)$$

Where w is the wake fraction, t is the augment of resistance coefficient, V_A is the wake speed, i.e. the mean velocity on the propeller disk and T is the propeller thrust.

The rudder Drag is calculated as the sum of the skin friction $R_{F,R}$ and the pressure drag $R_{P,R}$:

$$\text{Drag} = R_{P,R} + R_{F,R} \qquad (6.5.9)$$

$$R_{P,R} = \iint_{A_R} p^* \cdot \mathbf{n} \cdot \mathbf{i} \ ds \qquad (6.5.10)$$

$$R_{F,R} = \iint_{A_R} \tau_w \cdot \mathbf{s} \cdot \mathbf{i} \ ds \qquad (6.5.7)$$

Where A_R is the rudder surface, p^* is the pressure on the rudder surface, $\mathbf{n}$ is the unit vector normal to the rudder surface, $\mathbf{i}$ is the unit vector parallel to the rudder chord, τ_w is the wall shear stress and $\mathbf{s}$ is the tangential unit vector to the rudder surface.

The drag components are expressed in their respective non-dimensional form:

$$C_{P,R} = \frac{R_{P,R}}{0.5 \cdot \rho \cdot A_R \cdot V^2} \qquad (6.5.8)$$

$$C_{F,R} = \frac{R_{F,R}}{0.5 \cdot \rho \cdot A_R \cdot V^2} \qquad (6.5.9)$$

$$C_D = C_{P,R} + C_{F,R} = \frac{\text{Drag}}{0.5 \cdot \rho \cdot A_R \cdot V^2} \qquad (6.5.10)$$

Also presented are the distributed values for the pressure drag c_p and the skin friction c_f coefficients:

$$c_{p,D} = \frac{p^*}{0.5 \cdot \rho \cdot V^2} \qquad (6.5.7)$$

$$c_{f,D} = \frac{\tau_w}{0.5 \cdot \rho \cdot V^2} \qquad (6.5.8)$$

In table 6.5.3, the calculated resistance characteristics, rudder drag included, are presented along with the corresponding experimental measurements (Dyne, 1995). In the same table, the rudder drag and the corresponding coefficients are also presented.

In table 6.5.4, the calculated propulsion characteristics are presented along with the corresponding experimental measurements. The experimental data refer to the self-

propelled model with rudder; that is the case were the external force exerted to the model by the tank carriage, is equal to zero. In the same table, the rudder drag and the corresponding coefficients are also presented.

Table 6.5.3 Resistance and rudder drag characteristics,
hull and rudder calculations

		Experimental	Model Scale	Full Scale
Resistance Characteristics	WS [m^2]	11.450	11.548	14966
	R_T [Nt]	45.716	48.158	1.347E+06
	EHP [kW]	6.268E-02	6.603E-02	1.108E+04
	C_T	4.243E-03	4.344E-03	2.478E-03
	C_F	3.008E-03	3.048E-03	1.521E-03
	C_P	1.235E-03	1.297E-03	9.563E-04
Rudder Drag Characteristics	A_R [m^2]	-	1.029E-01	1.334E+02
	Drag [Nt]	-	1.057E+00	6.095E+04
	C_D	-	1.100E-02	1.321E-02
	C_F	-	1.762E-03	9.850E-04
	C_P	-	9.234E-03	1.222E-02

Table 6.5.4 Propulsion and rudder drag characteristics,
hull and rudder calculations

		Experimental	Model Scale	Full Scale
Rudder Drag Characteristics	A_R [m^2]	-	1.029E-01	1.334E+02
	Drag [Nt]	-	2.466	8.688E+04
	C_D	-	2.557E-02	1.878E-02
	C_F	-	4.037E-03	3.243E-03
	C_P	-	2.153E-02	1.554E-02
Propulsion Characteristics	1-w (nom)	0.411	0.404	0.519
	1-w (eff)	0.543	0.511	0.568
	1-t	0.800	0.800	0.837
	n [rpm]	-	805	111
	T [Nt]	57.145	58.121	1.577E+06
	DHP [kW]	1.051E-01	1.069E-01	1.541E+04
	C_T	-	4.942E-03	2.871E-03
	C_F	-	3.057E-03	1.523E-03
	C_P	-	1.886E-03	1.349E-03

In the following figures, the results of the foure numerical tests are presented (model scale resistance, model scale propulsion, full scale resistance and full scale propulsion). The presure and skin fricktion coefficient distributions refer to four sections normal to the rudder axis. These sections are presented in figure 6.5.7. The axial wake contours and cross-flow refer to six sections along the ship length, presented in figure 6.5.8. Section "A" is a section ahead of the propeller plane, at the same location as section "A" of figure 6.1.2. Section "B" coincides with the propeller plane, also section "B" of figure 6.1.2. Finally sections "C" and "F" are located ahead of the rudder leading edge and abaft the trailing edge respectivelly, while sections "D" and "E" intersect the rudder.
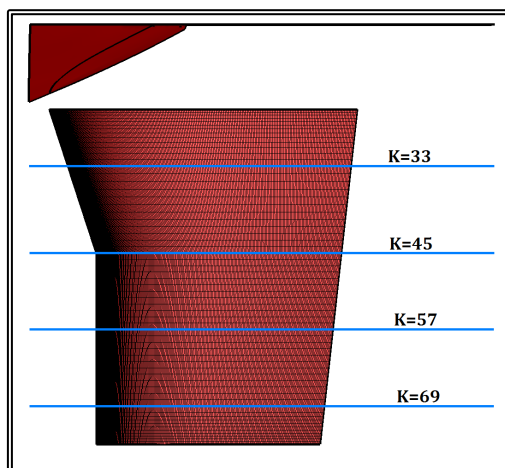
Figure 6.5.7 Locations of c_p, c_f, measurement planes.
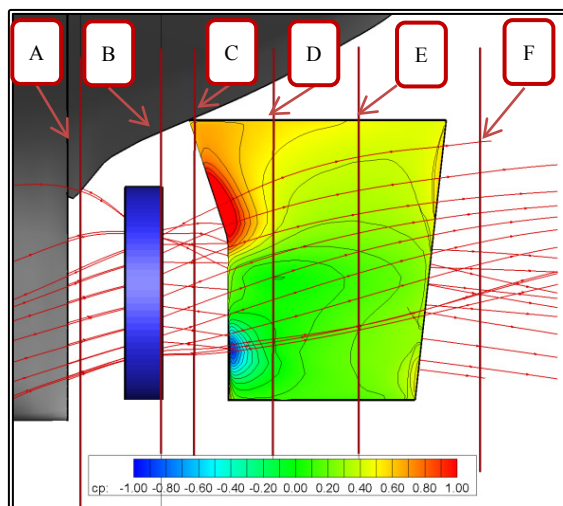
Figure 6.5.8 Location of cross-flow sections.

In figures 6.5.9 to 6.5.12 the pressure Drag coefficient (c_p) contours are presented on the rudder surface. In figures 6.5.13 to 6.5.16 the pressure coefficient (c_p) distribution on each of the sections of figure 6.5.5 is compared amongst the four test cases. In figures 6.5.17 to 6.5.20 the skin friction coefficient (c_f) distribution on each of the sections of figure 6.5.5 is compared amongst the four test cases. In figures 6.5.21 to 6.5.24, stream traces passing through the propeller disk, at a circle having a diameter equal to the mean of the propeller and propeller hub diameters. In figures 6.5.25 to 6.5.28 the cross-flow and axial velocity (w/V) contours are presented on each of the sections of figure 6.5.6.
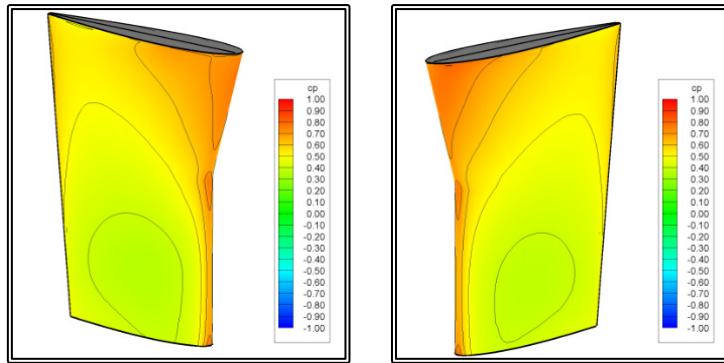
Figure 6.5.9 Pressure Drag coefficient c_p, contours on the rudder surface, model scale, resistance, starboard side on the left and port side on the right.
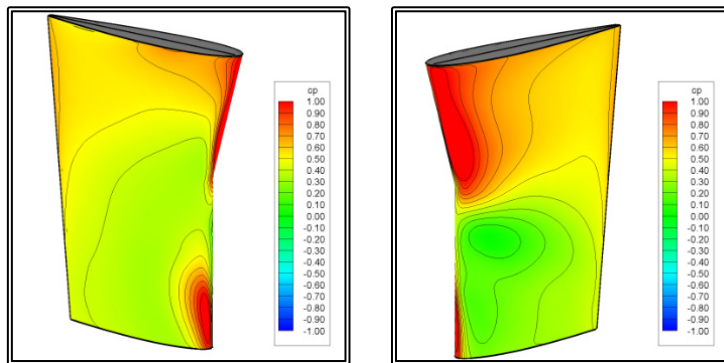
Figure 6.5.10 Pressure Drag coefficient c_p, contours on the rudder surface, model scale, starboard side on the left and port side on the right.
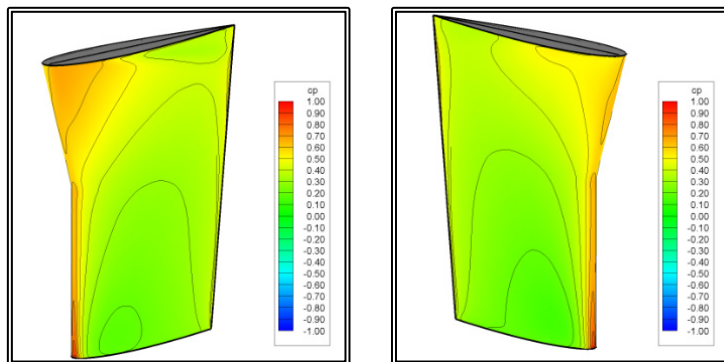
Figure 6.5.11 Pressure Drag coefficient c_p, contours on the rudder surface, full scale, resistance, starboard side on the left and port side on the right.
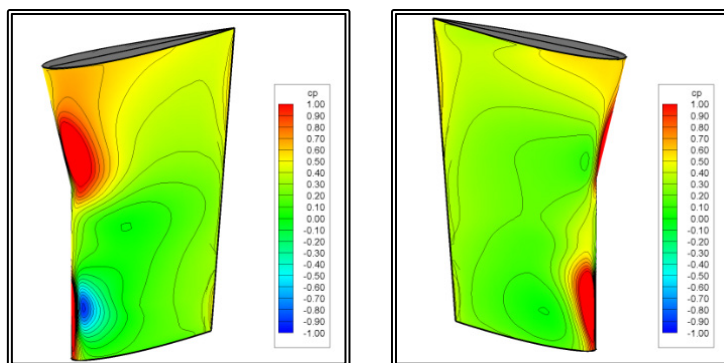
Figure 6.5.12 Pressure Drag coefficient c_p, contours on the rudder surface, full scale, propulsion, starboard side on the left and port side on the right.
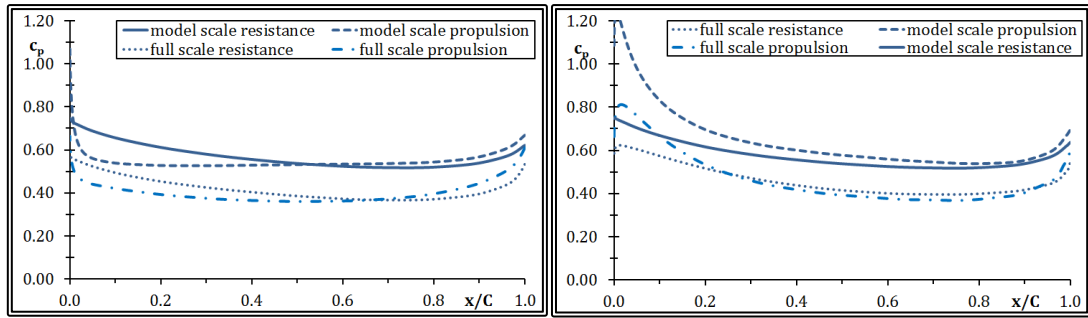
Figure 6.5.13 Comparison of the Pressure coefficient c_p, distribution on section K=33, port side on the left and starboard side on the right.
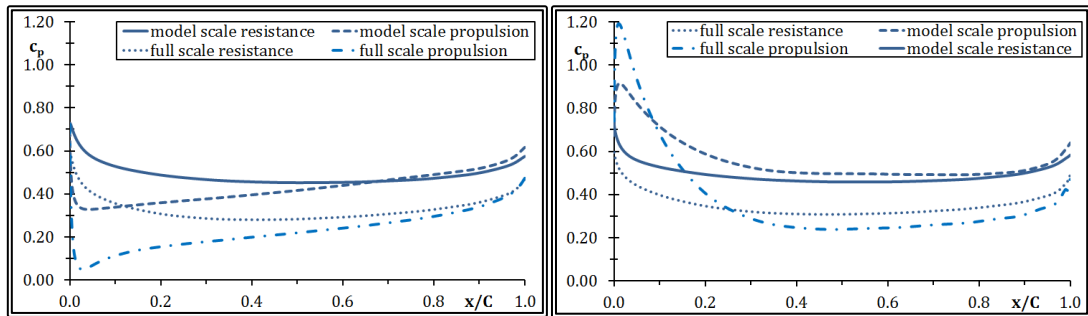
Figure 6.5.14 Comparison of the Pressure coefficient c_p, distribution on section K=45, port side on the left and starboard side on the right.
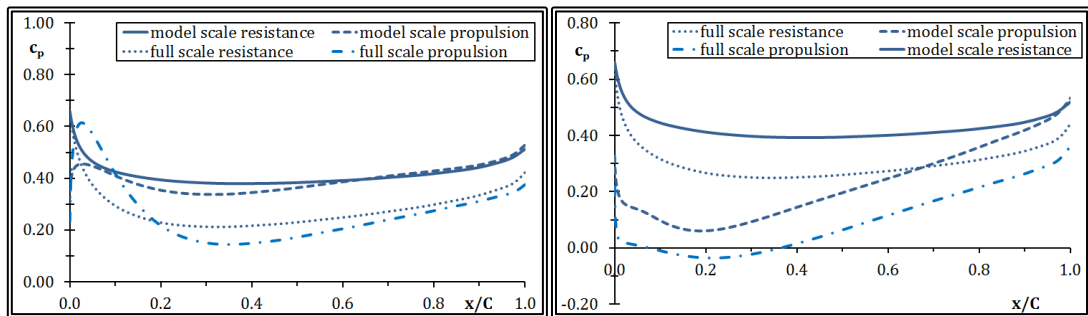
Figure 6.5.15 Comparison of the Pressure coefficient c_p, distribution on section K=57, port side on the left and starboard side on the right.
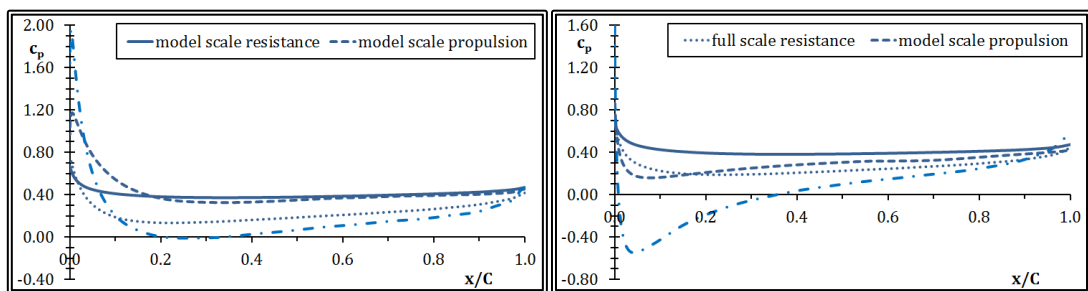
Figure 6.5.16 Comparison of the Pressure coefficient c_p, distribution on section K=69, port side on the left and starboard side on the right.
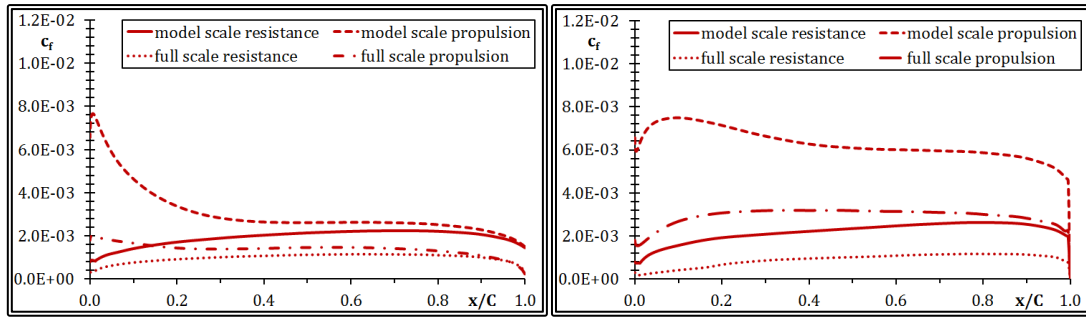
Figure 6.5.17 Comparison of the Skin Friction c_f, coefficient distribution on section K=33, port side on the left and starboard side on the right.
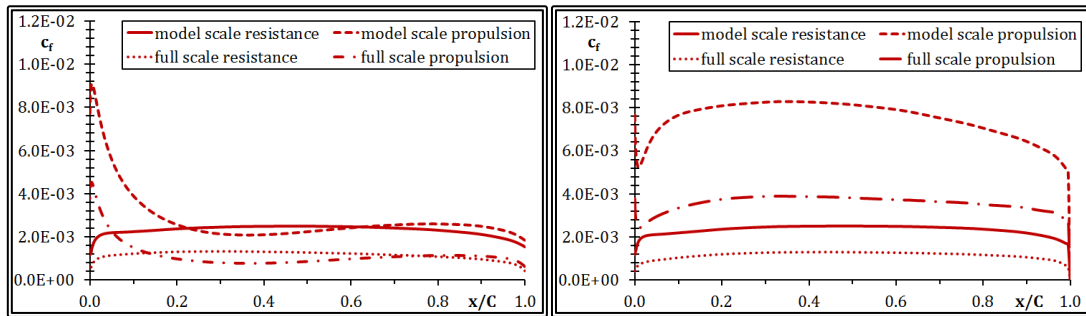
Figure 6.5.18 Comparison of the Skin Friction c_f, coefficient distribution on section K=45, port side on the left and starboard side on the right.
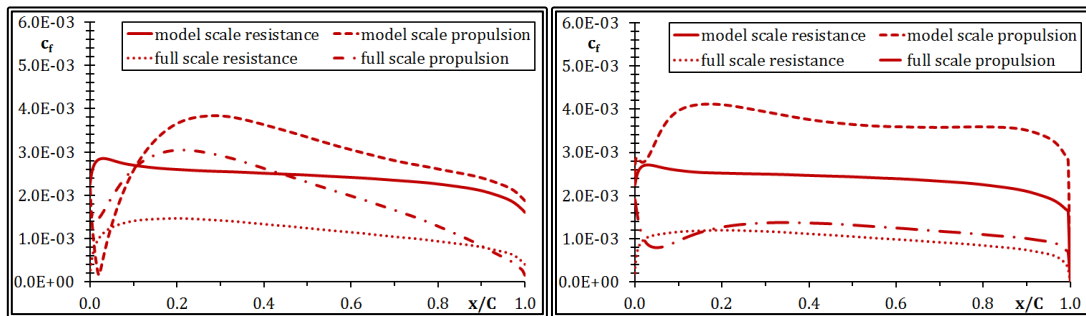
Figure 6.5.19 Comparison of the Skin Friction c_f, coefficient distribution on section K=57, port side on the left and starboard side on the right.
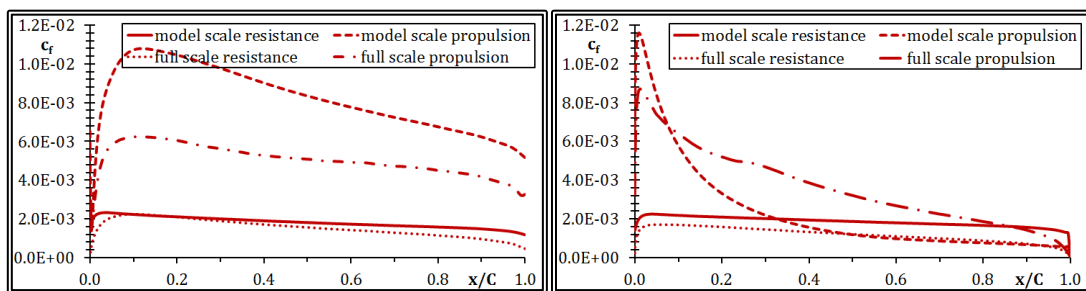
Figure 6.5.20 Comparison of the Skin Friction c_f, coefficient distribution on section K=69, port side on the left and starboard side on the right.
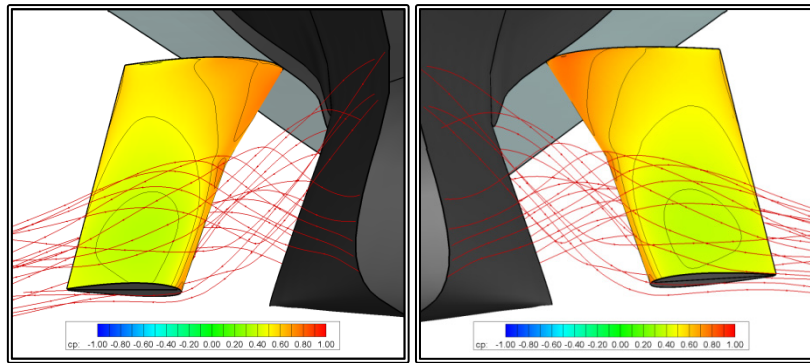
Figure 6.5.21 Stream traces at the propeller disk, model scale resistance, starboard side on the left and port side on the right.
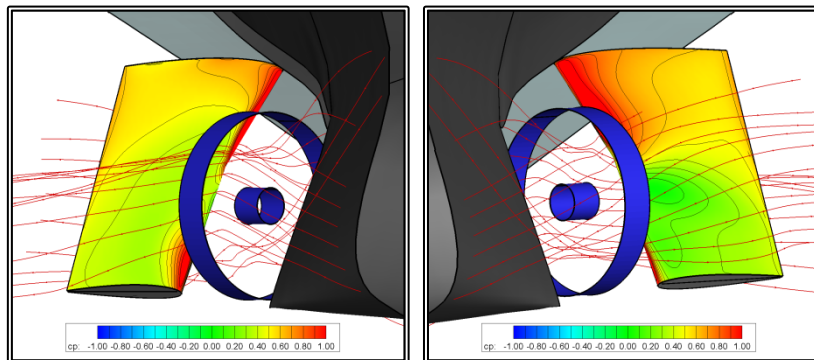
Figure 6.5.22 Stream traces at the propeller disk, model scale propulsion, starboard side on the left and port side on the right.
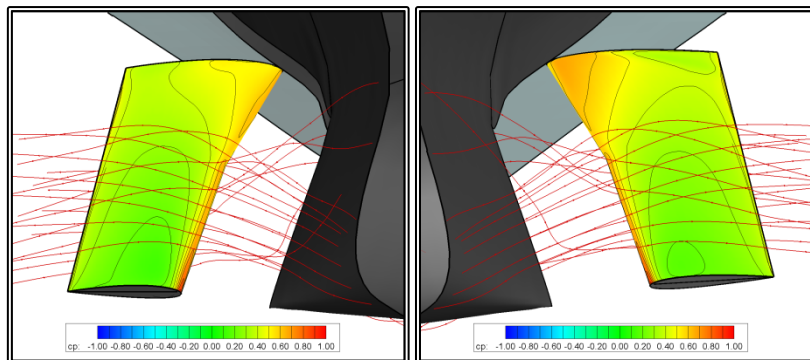
Figure 6.5.23 Stream traces at the propeller disk, full scale resistance, starboard side on the left and port side on the right.
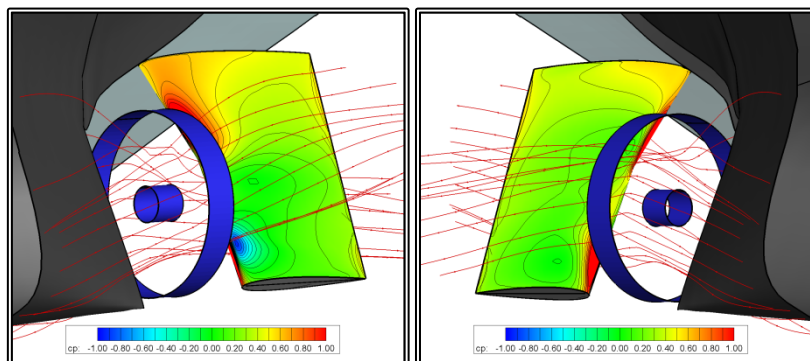
Figure 6.5.24 Stream traces at the propeller disk, full scale propulsion, starboard side on the left and port side on the right.
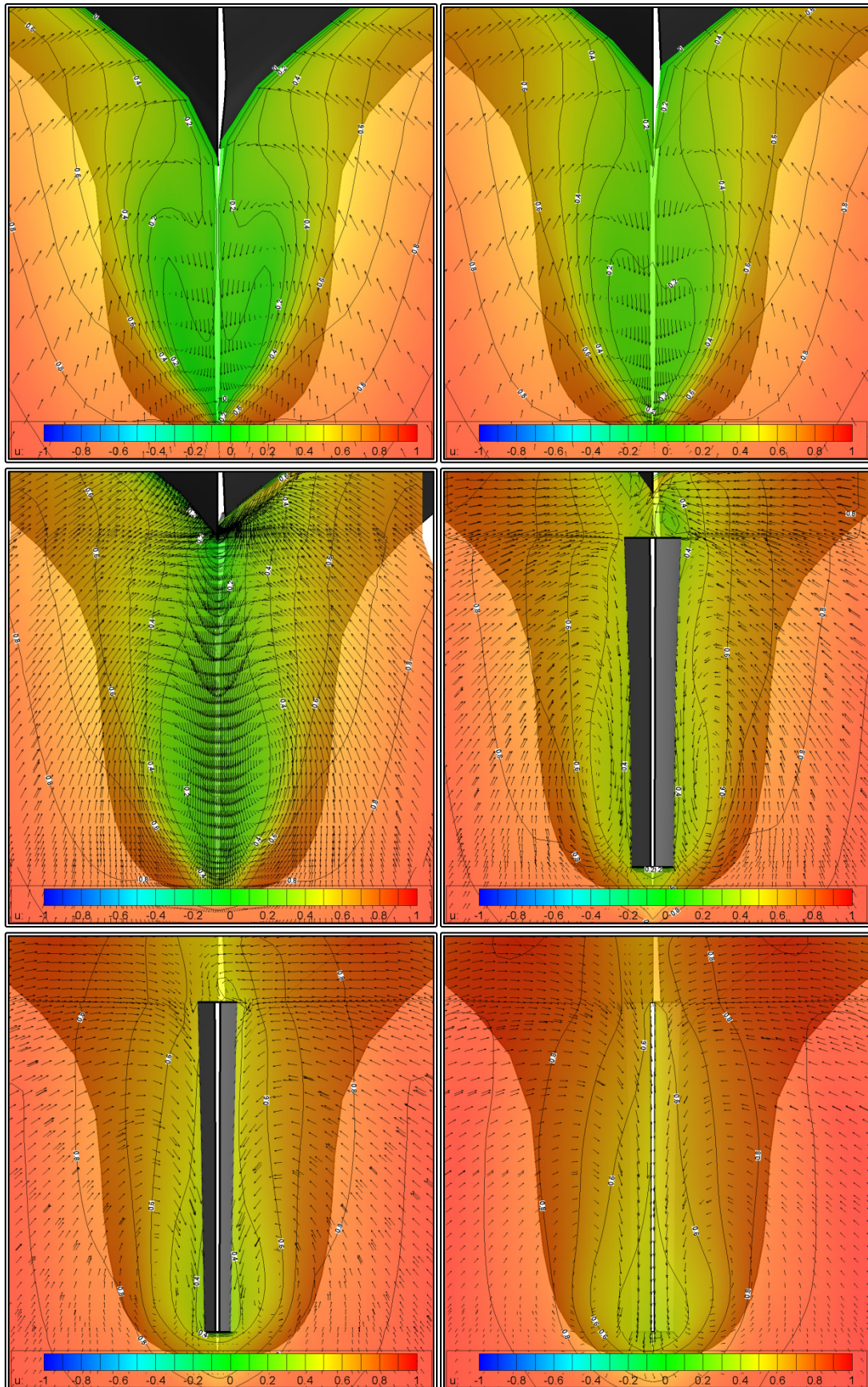
Figure 6.5.25 Cross-flow and axial velocity (w/V) contours, model scale resistance, from top left to bottom right sections A-F.
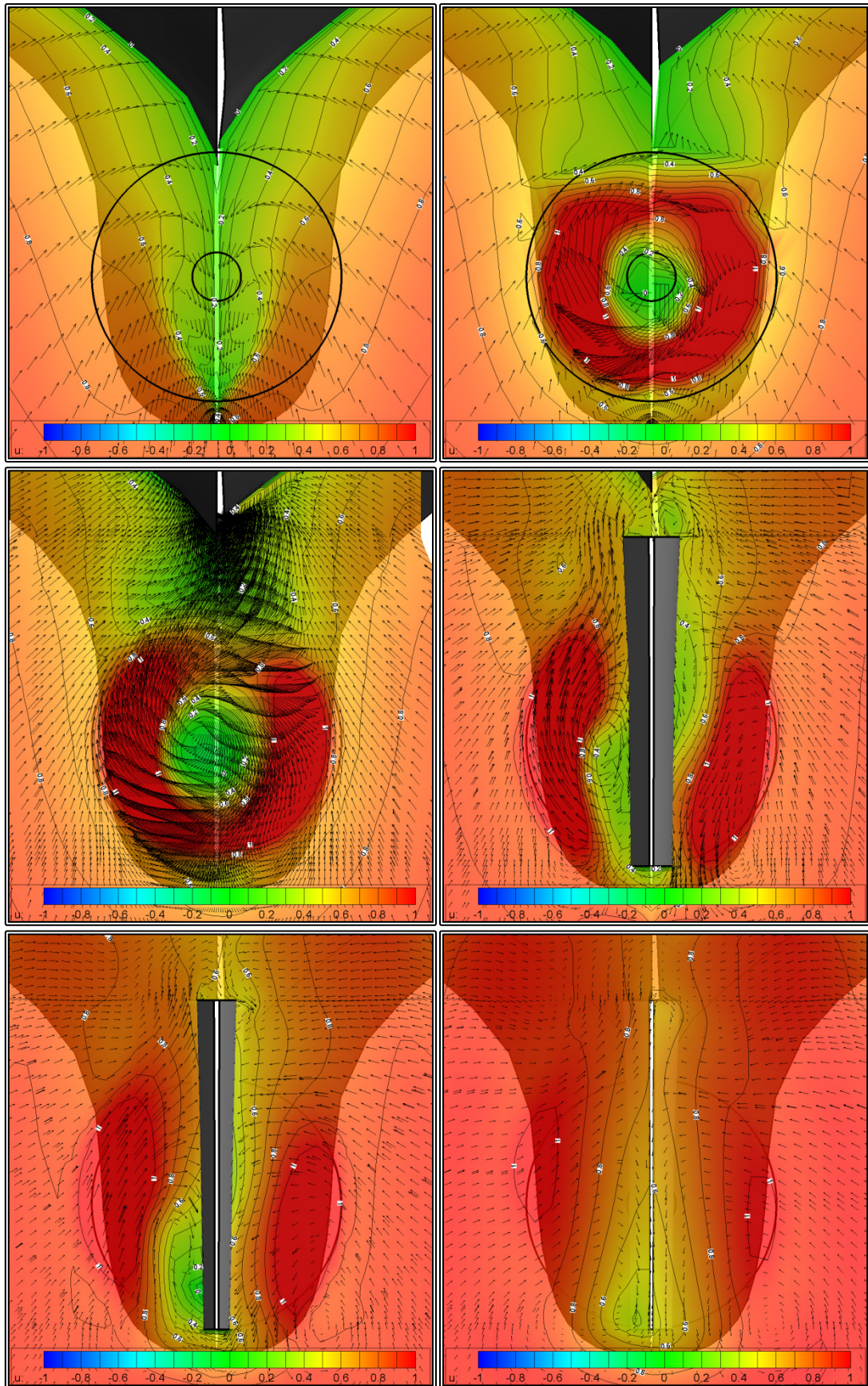
Figure 6.5.26 Cross-flow and axial velocity (w/V) contours, model scale propulsion, from top left to bottom right sections A-F.
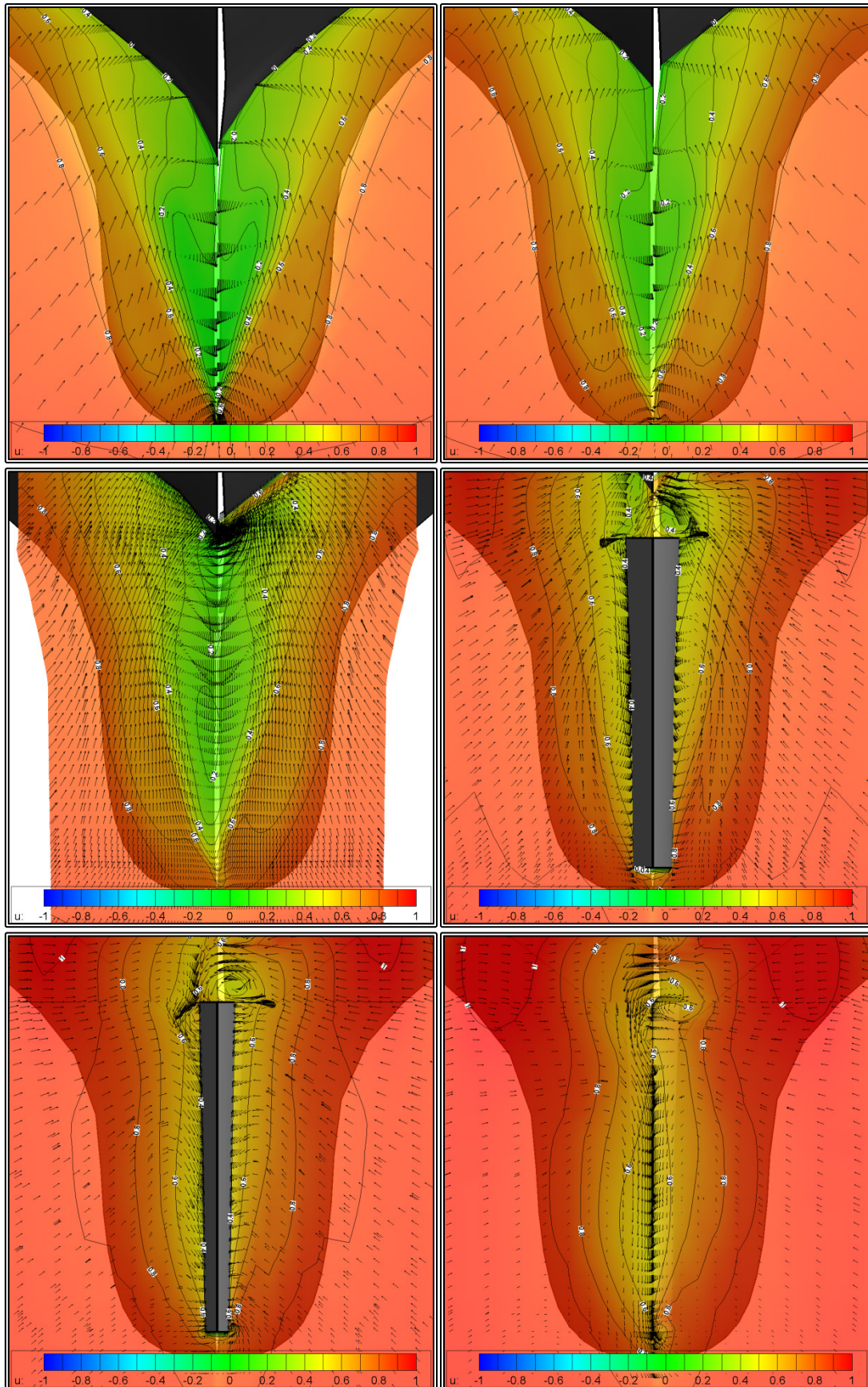
Figure 6.5.27 Cross-flow and axial velocity (w/V) contours, full scale resistance, from top left to bottom right sections A-F.
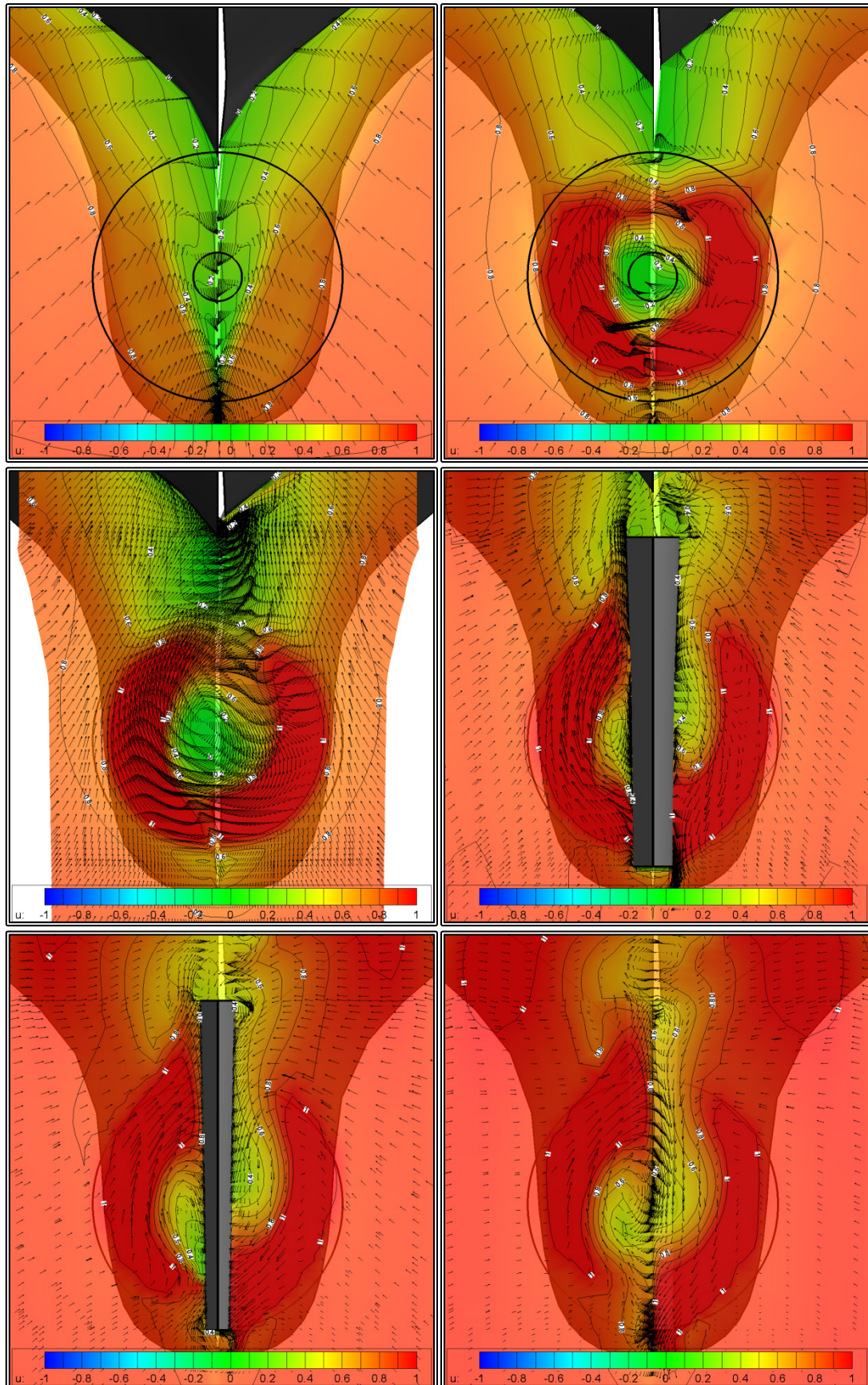
Figure 6.5.28 Cross-flow and axial velocity (w/V) contours, full scale propulsion, from top left to bottom right sections A-F.

6.6   Discussion on the "Dyne" Test Case

The data gathered in paragraphs 6.3 and 6.5, regarding the "bare" hull and the ship with the rudder are presented in the following tables and compared with experimental data.

In table 6.6.1, the total resistance R_T and the nominal wake fraction at the propeller disk are presented at model scale and compared with experimental data (EFD) for the "bare" hull case.

In table 6.6.2, the total resistance R_T, the propeller thrust T, the effective wake fraction and the thrust deduction fraction are presented at model scale and compared with experimental data, for the ship with the rudder.

Table 6.6.1 Comparison between Experimental (EFD) and Numerical (CFD) resistance data, "bare hull"

	EFD	CFD	Diff
R_T [Nt]	46.674	46.255	-0.90%
1-w (nom)	0.411	0.404	-1.72%

Table 6.6.2 Comparison between Experimental (EFD) and Numerical (CFD) resistance and propulsion data, hull with rudder

	EFD	CFD	Diff
R_T [Nt]	45.716	48.158	5.34%
T [Nt]	57.145	58.121	1.71%
1-w (eff)	0.543	0.511	-5.89%
1-t	0.800	0.829	3.57%

The numerical results are in good agreement with the experimental data, in terms of the resistance predictions (1%) for the "bare" hull, especially when considering the fact that the uncertainty of the experimental measurements is in the region of 2% for the resistance and 3% for the thrust (Dyne, 1995). In very good agreement are also the results for the nominal wake fraction (1.7%).

In the ship with the rudder case, the numerical results are also in good agreement with the experimental data, in terms of the thrust (2%) wake fraction (6%) and thrust deduction (3.5%). In terms of the total resistance with the rudder, the experimental and numerical results appear to differ significantly (5%). A closer look though, reveals something unexpected in the experimental data. The total resistance with the rudder is smaller than the resistance without it. This is clearly demonstrated in table 6.6.3, where the effect of the rudder on the resistance is presented at model scale, experimentally and numerically, as well as at full scale. In table 6.6.4, the corresponding data for the thrust are presented.

Indeed the measured resistance with the rudder is more than 1% lower than without. The numerical method predicts a more reasonable increase in the total resistance with the rudder, 3% at model and 5.7% at full scale. The latter is rather higher than

expected. For the self-propulsion case, an increase in thrust of 4% is calculated at model scale, while an increase of 3% is calculated at full scale. In any case, an uncertainty in the region of 3% is not unreasonable for RANS calculations.

Table 6.6.3 Resistance R_T [Nt], with and without rudder

		Without Rudder	With Rudder	δ
EFD		46.255	45.716	-1.16%
CFD	Model Scale	46.674	48.158	3.18%
	Full Scale	1.274E+06	1.347E+06	5.75%

Table 6.6.4 Thrust T [Nt], with and without rudder

		Without Rudder	With Rudder	δ
CFD	Model Scale	55.665	58.121	4.41%
	Full Scale	1.527E+06	1.577E+06	3.27%

Table 6.6.5 Rudder effect on the propulsion characteristics, model scale

	Without Rudder	With Rudder	Diff
1-w (eff)	0.582	0.511	-12.20%
1-t	0.814	0.829	-1.84%

In table 6.6.5, the effect of the rudder on the propulsion characteristics is presented in model scale. The results without rudder refer to a case without rudder, were the thrust was set equal to the thrust of the self-propelled model with the rudder (48.158 Nt). The significant difference observed, especially in the effective wake fraction (12%) is solely due to the presence of the rudder.

CHAPTER 7   DISCUSSION AND CONCLUSIONS

(This page intentionally left blank)

7.   Discussion and Conclusions

The present thesis aims at the formulation, programming and validation of a method for solving the viscous flow problem around the appendages on conventional vessels. The proposed method is based on the overlapping blocks approach, part of the Finite Volume family of methods. The programming and development of software was carried out using the Fortran programming language. The components of the new method were validated using available experimental data, either from past research performed at LSMH, or data taken from the scientific literature. In the next paragraphs, the new developments are presented and the conclusions drawn in each chapter are summarized.

In Chapter 2, the Total Variation Diminishing differencing scheme with the Minmod limiter function is presented. Referring to published research, the new scheme is validated by comparing the numerical results in the case of a 2-D wave tank, with corresponding experimental data.

In Chapter 3, a novel hybrid method for the calculation of the free surface is presented. The new method combines the accuracy and efficiency of a potential flow solution at the bow of ships, with the accuracy of a RANS based solution at the stern of ships. With the new method a significant reduction in computing time is achieved, when compared with RANS based methods, in the order of 75%. The method is validated by comparing the calculated wave patterns, with respective experimental measurements for two ship models. The results of the presented method are in very good agreement with the experimental data.

In Chapter 4, a method for solving the flow problem around the appendages of ships is presented. The method is based on the Overlapping Grid Block approach, where the flow around each component of the ship appendages is solved using a separate grid block. In order to obtain the solution for the overall flow problem, the blocks overlap and information is passed-on from one block to the other through the boundary conditions of the later. In the same chapter, a method is also proposed for the exchange of flow variables between blocks is detailed.

In Chapter 4, the method for generating the individual grid blocks is presented. Each block is curvilinear orthogonal in the uv-directions and non-orthogonal Cartesian in the w-direction. The method can generate the blocks around the propeller shaft, the shaft bossing, the struts, the struts' bossing and the rudder. The shaft and struts' bossing blocks are cylindrical, comprising 2-D O-type sections normal to the shaft axis. The shaft block can model steps in the shaft diameter, such at each end of a bossing or the end of the shaft itself. The sections of the struts' bossing block are not planar and are made to conform to the struts geometry as well as the bossing geometry. Despite that, the grid on each section is orthogonal curvilinear, when projected on a plane normal to the shaft axis.

The blocks around the shaft bossing, struts and rudder are C-H-type, comprising 2-D sections normal to the shaft axis, the strut axis and the rudder axis respectively. On each section an orthogonal curvilinear C-type grid is generated. The struts may have a varying chord length and twist along its length. The rudder may have a varying chord

length and twist along its length. The rudder root or tip, may have a finite cross section, in which case a step is created in the geometry.

In Chapter 5, the ability of the modified LSMH RANS solver to handle the flow past individual blocks is demonstrated. Specifically, for each of the ship appendages components, the results of a number of numerical tests are presented. The modified RANS solver can now handle the o-type shaft block with the aforementioned steps. Also it is demonstrated that the solver can produce realistic results in terms of the flow characteristics and the pressure distribution on the shaft surface.

Regarding the shaft bossing, the solver can now handle the C-H-type block with the East, West and South boundaries being handled as solid boundaries. In chapter 5 it is demonstrated that the solver can produce realistic results in terms of the flow characteristics and the pressure distribution on the bossing surface.

Also in Chapter 5, the ability of the solver to handle the C-H-type strut block, with the Upstream boundary being treated as a solid boundary, while the South boundary is handled partially as a solid boundary and partially as a symmetry line. It is demonstrated that the solver can produce realistic results in terms of the flow characteristics and the pressure and skin friction distribution on the strut surface.

Finally in Chapter 5, it is demonstrated that the modified RANS solver can handle the C-H-type rudder block, with the Upstream boundary being handled as a solid boundary, while the South boundary is treated partially as a solid boundary and partially as a symmetry line. The solver can now also handle the step at the rudder root or tip. It is demonstrated that the solver can produce realistic results in terms of the flow characteristics and the pressure and skin friction distribution on the rudder surface.

The method presented in this thesis, is validated in Chapter 6 through comparison of numerical results with available experimental data for the "Dyne" tanker. Using the proposed hybrid method the free surface was calculated in model scale and was found to be in good agreement with the experimental data. The over-prediction of wave height near the stern of the ship, presented in the potential calculations is corrected.

Then, resistance and propulsion calculations were performed for the "bare" hull, in model and full scale. The model scale calculations include symmetric and asymmetric flow calculations, as well as calculations with wall functions and near wall treatment. In the asymmetric flow case, the difference between the calculated and measured values for the Total Resistance, R_T is 0.91%. In the symmetric flow case with wall functions, the corresponding difference is 2.74%, while in the symmetric case without wall functions, the difference is 1.96%. The effect of the wall functions, as expressed in the difference between the two symmetric flow cases, is 0.76%. The above results are satisfactory in light of the fact that the uncertainty of the experimental measurements is in the region of 2%. In very good agreement are also the results for the nominal wake fraction, the difference being 1.7%. By examining the wake patterns, the numerical calculations are able to approximate the flow patterns, such as the vortex that appears in the experimental data, on either side of the shaft bossing.

The rudder of the "Dyne" tanker was modeled using a separate grid block. In Chapter 6, a series of tests to evaluate the effectiveness of the overlapping block setup are

presented. Firstly a grid independence test showed that the results are very close with a maximum deviation of 4% for the Drag. Also the deviation tends to decrease as the number of nodes increases. In order to evaluate the effect of the rudder block extends on the accuracy of the solution, a numerical comparison was conducted between two alternative setups for the 2-D flow problem past a NACA 18 hydrofoil. In the first test, a single large C-type block was generated around the hydrofoil and boundary conditions are those of undisturbed flow. In the second test a small C-type block was generated around the hydrofoil with extends similar to those of the 3-D block around the "Dyne" rudder. The boundary conditions for this smaller block are provided by the solution of an external H-type block standing for the 3-D ship block. The difference between the two tests, in terms of drag, is quite small, around 3.5%. Consequently, despite the narrow internal C-type grid, this setup produces acceptable results.

Finally in Chapter 6, the resistance and propulsion problems are solved for the ship with the rudder, in model and full scale. The numerical results are in good agreement with the experimental data, especially when considering that the uncertainty of the experimental measurements is in the region of 2% for the resistance and 3% for the thrust. The difference between the measured and the calculated resistance is 5.34%, while for the thrust, the increase is 1.71%. The difference in the resistance is quite high but it should be attributed, at least partially, ton an error in the experimental measurements. We suspect such an error exists because the measured resistance with the rudder is lower, than the measured resistance of the "bare" hull. In terms of the wake fraction and thrust deduction, the difference between the numerical results and the measured values is 5.89% and 3.57% respectively.

When comparing the "bare" hull with the ship with the rudder, the numerical method predicts a significant increase in the total resistance with the rudder, 3.18% at model and 5.75% at full scale. The latter is rather higher than expected. For the self-propulsion case, an increase in thrust of 4.41% is calculated at model scale, while at full scale the increase is 3.27%. In any case, an uncertainty in the region of 3% is not unreasonable for RANS calculations.

Another interesting result is the effect of the rudder presence, on the propulsion characteristics. When comparing the self-propelled model with the rudder with a model without rudder and with the propeller providing a thrust equal to that of self-propelled model, the difference in the wake fraction is 12% while the thrust deduction is less affected, with the difference being 1.8%.

As a conclusion, the presented method can generate the numerical grid around various setups for the appendages of a ship. The method yields good results in the case of a ship with rudder, both in model and full scale. All calculations are in good agreement with the available experimental data. Furthermore the new hybrid method for the calculation of the free surface, combines the efficiency of a potential surface tracking method, with the accuracy of a RANS based method.

7.1   Novel Contributions and Relevant Publications

The novel contributions of this PhD thesis are summarized below:

- The Total Variation Diminishing differencing scheme in conjunction with the Minmod Limiter function is introduced to the LSMH RANS solver.

- A three grid block setup is introduced to the LSMH RANS solver. The new setup comprises a C-O-type around the bow, an H-O-type around the mid and stern of the ship and finally an H-H-type abaft the transom stern. With this configuration, an increase in the accuracy of the resistance predictions is achieved, for ships with full lines at the bow area and ships with a "wetted" transom stern.

- A novel hybrid method is introduced for the calculation of the free surface. The new method combines the advantages of the existing surface tracking methods, that consider the flow either inviscid and irrotational (potential flow), or solve the RANS equations. In this new method, the free surface is initially calculated using the potential flow solver and is then corrected, using a RANS surface tracking method. The correction is applied only at the aft half and the wake of the ship, while boundary conditions on the free surface are specially treated, to avoid convergence problems

- A method is introduced, for the parametric representation of ship appendages and the generation of grid blocks around the components of the appendages. The grid blocks are orthogonal curvilinear in the uv-directions, thus increasing the accuracy.

- The LSMH RANS solver is modified, in order to handle the new blocks and the exchange of flow variables according to the overlapping block approach.

- A method is developed for the exchange of flow variables between the overlapping blocks. The new method is characterized by fast and accurate exchange of flow variables.

- The new overlapping grid method is validated by comparing available experimental data with numerical calculations, in the case of a ship with rudder. The validation concerns both the resistance and the propulsion problem, at model and full scale.

Journal publications and conference papers, thus far, from the research carried out in this thesis are listed below:

Journal Publications:

- Tzabiras, G.D., Polyzos, S.P., Sfakianaki, K., Diafas, V., Villiotis, A.D., Chrisikopoulos K., Kaloupsis S., 2010. Experimental and Numerical Study of the Flow past Olympic Class K-1 Flat Water Racing Kayak at Steady Speed. The Sport Journal, 4 (13).

- Polyzos, S.P., Tzabiras, G.D., 2016. Generation of Overlapping Structured Grid Blocks about a Ship's Appendages. Progress in Computational Fluid Dynamics, An International Journal (PCFD), **Under Review**

Conference Papers:

- Tzabiras, G.D., Polyzos, S.P., Papakonstantinoy, V.K., 2009. On a numerical method for generating harmonic waves in a finite 2D tank. 13th Congress of Int. Maritime Assoc. of Mediterranean, Istanbul 2009 (IMAM 2009).

- Tzabiras, G.D., Zarafonitis, G.N., Polyzos, S.P., 2011. Numerical prediction of the resistance characteristics of catamaran cargo ships. 14th Congress of Int. Maritime Assoc. of Mediterranean, Genoa 2011 (IMAM 2011).

- Pallas, G., Nikas, K., Polyzos, S.P., Tzabiras, G.D., Zarafonitis, G.N., 2013. Investigation of various parameters affecting the resistance characteristics of two catamaran cargo ships. 15th Congress of Int. Maritime Assoc. of Mediterranean, A Coruna 2013 (IMAM 2013).

- Tzabiras, G.D., Polyzos, S.P., 2015. A Hybrid Numerical Method for Calculating Self-Propulsion Characteristics of Ships. 16th Congress of Int. Maritime Assoc. of Mediterranean, Pula 2015 (IMAM 2015).

- Τζαμπίρας, Γ, Πολύζος, Σ., 2016. Εφαρμογή μεθόδου CFD για τον υπολογισμό των χαρακτηριστικών πρόωσης ενός tanker. Ετήσιο Συνέδριο Ελληνικού Ινστιτούτου Ναυτικής Τεχνολογίας, Αθήνα 2016 (ΕΛΙΝΤ 2016).

7.2   Future Work

- Incorporate in the method other types of ship appendages such as turning vanes ahead of the propeller or other energy saving devices such as Mewis ducts etc.

- Currently the strut grid generator can handle strut whose reference line is strait. A useful addition to the software is be the ability to handle curved struts or struts with one or more kinks.

- The rudder currently can be modeled using a single block. The use of two rudder blocks, one for the fixed portion of the rudder and another for the rotating part, will allow the solution of problems with non-zero rudder angle of attack.

- Making the software run in parallel, on multiple processors requires extensive modifications but will allow for faster convergence and increased grid sizes. The later will allow for the solution of more complex appendages arrangements.

(This page intentionally left blank)

BIBLIOGRAPHY

General Bibliography on CFD

[1]   Tzabiras, G. "*Numerical simulation of hydrodynamic flows*" (in Greek), NTUA, Athens (1998).

[2]   Bergeles, G. "*Computational fluid Dynamics*", Symeon, Athens (1995).

[3]   Ferziger, J. H., Peric, M. "*Computational Methods for Fluid Dynamics*" Springer, Berlin (1999).

[4]   Demirdzic, I., Gosman, A.D., Issa, R.I., Peric, M., 1987. A calculation procedure for turbulent flow in complex geometries. Computers & Fluids, Vol.15, 3, pp.251-273

[5]   Hess, J.L. Smith, A.M.O. 1968. Calculations of potential flow about arbitrary bodies. Prog. Aeraunaut. Sci., 8, 1-136

[6]   Launder, B.E., Spalding, D.B. 1974. The numerical computation of turbulent flows. Comp. Methods Appl. Mech. Eng., 3:269-289.

[7]   Patankar, S.V. *"Numerical Heat Transfer and Fluid Flow"*. Taylor & Francis (1980)

[8]   Versteeg, H. K., Malalasekera, W. "*An Introduction to Computational Fluid Dynamics, the Finite Volume Method*" Pearson, Edinburgh Gate (2007).

TVD Differencing Schemes

[9]   Lien F. S., Leschziner M. A., 1994. Upstream monotonic interpolation for scalar transport with application to complex turbulent flows. Int. J. for Numerical Meth. in Fluids, Vol.19, pp.527-548.

[10] Sweby P. K., 1984. High Resolution Schemes Using Flux Limiters for Hyperbolic Conservation Laws. SIAM J. on Numerical Anal. Vol.21, pp.995-1011.

[11] Roe P. L., 1985. Some Contributions to the Modelling of Discontinuous Flows. Lectures in Applied Mechanics, Vol.22, Springer-Verlag, Berlin, pp.163-193.

[12] Van Leer B., 1973. Towards the Ultimate Conservative Difference Scheme I, The quest of monotonicity. 3rd Int. Conf. on Numerical Meth. in Fluid Mech, pp.163-168.

[13] Van Leer B., 1974. Towards the Ultimate Conservative Difference Scheme II, Monotonicity and conservation combined in a second order scheme. J. Comp. Phys., 14, p361-70.

[14] Van Leer B., 1977a. Towards the Ultimate Conservative Difference Scheme III, Upstream-Centered Finite-Difference Schemes for Ideal Compressible Flow. J. for Comp. Phys, Vol.23, pp.263-275.

[15] Van Leer B., 1977b. Towards the Ultimate Conservative Difference Scheme IV, A new approach to Numerical Convection. J. for Comp. Phys, Vol.23, pp.276-299.

[16] Van Leer B., 1979. Towards the Ultimate Conservative Difference Scheme V, A second-order Sequel to Gudunov's method. J. for Comp. Phys, Vol.32, pp.101-136.

The Method for Solving the Viscous Flow around a Ship

[17] Bram S., Jaap W., Hoyte C., 2006. Validation of viscous flow and wake field predictions for ships at full scale. Proc. 26th Symp. on Naval Hydrodynamics.

[18] von Kerczek, C., Tuck, E.O., 1969. The Representation of ship hulls by conformal mapping functions. *Journal of Ship Research*, 19, 284–298.

[19] Kerczek, von C, Stern, F., 1983. The representation of ship hulls by conformal mapping functions: Fractional maps. Journal of Ship Reasearch;27:158-9.

[20] Mizine I., Karafiath G., Queutey PP., Visonneau M., 2009. Interference phenomenon in design of trimaran ship. Proc. 10th Int. Conf. on Fast Sea Transportation (2009).

[21]   Triperinas, D., Papakonstantinou, V.K., Tzabiras, G.D., 2008. Calm water resistance experiments and flow visualization for a bare hulled firefighting vessel. LMSH Technical report NAL-299-F-2008.

[22]   Tzabiras, G.D., Loukakis, T.A., 1983. A method for predicting the flow around the stern of double ship hulls. Int. Shipbuilding Progress, 2, pp.94-105.

[23]   Tzabiras , G.D., Vafiadou, M., Nassos, G., 1986. A numerical method for the generation of 2D orthogonal curvilinear grids. 1st Int. Conf. on Numerical Grid Generation, Landshut, W. Germany, 1986.

[24]   Tzabiras, G.D., Dimas, A., Loukakis, T.A., 1986. A numerical method for the calculation of incompressible, steady, separated flows around aerofoils. International Journal for Numerical Methods in Fluids, 6, 789-809.

[25]   Tzabiras, G.D., 1987. A numerical investigation of the turbulent flow-field at the stern of a body of revolution. Journal of Applied Mathematical Modelling, 11, pp.45-61.

[26]   Tzabiras, G., Garofallidis, D., Ventikos, Y., 1989. On the numerical solution of the Reynolds equations around aerofoils by various orthogonal curvilinear coordinate systems. 2nd National Congress on Mechanics, E.E.Th.E.M. (HSTAM, IUTAM member), Athens, pp.702-711.

[27]   Tzabiras, G.D., 1990a. Stern flow calculations for two double ship models. SSPA-CTH-IIHR Workshop on Ship Viscous Flow, Goteborg, 1990.

[28]   Tzabiras, G., Loukakis, T. and Garofallidis, D., 1990b. On the numerical solution of the total ship resistance problem under a predetermined free surface. 18th Symposium on Naval Hydrodynamics, ONR, Ann-Arbor, Mitchigan, 1990, pp.1-17.

[29]   Tzabiras, G.D., 1991a. A numerical study of the turbulent flow around the stern of ship models. Int. J. for Numerical Methods in Fluids, 9, pp.1179-1204.

[30]   Tzabiras, G.D., 1991b. Numerical calculation of resistance and propulsion characteristics of a body of revolution. Technica Chronica Sc. Journal of the Tech. Chamber of Greece, 11, pp.85-118.

[31]   Tzabiras, G.D., 1992. A numerical investigation of the Reynolds scale effect on the resistance of bodies of revolution. Ship Technology Research, 39, pp.28-44.

[32]   Tzabiras, G.D., 1993. Resistance and self propulsion numerical experiments on two tankers at model and full scale. Ship Technology Research, 40, pp.20-38.

[33]   Tzabiras, G.D., 1995a. On the calculation of the viscous flow around bulbous or U-shaped bows at zero Froude number. Ship Technology Research, 42, pp.31-44.

[34]   Tzabiras, G.D., 1995b. Numerical and experimental study of the pressure field around a double ship model. Technica Chronica Sc. Journal of the Tech. Chamber of Greece, 15, pp.41-51.

[35]   Tzabiras, G.D., 1995c. Numerical prediction of self-propulsion characteristics of full ship forms. STG-Yearbook, vol. 89, pp.322-326.

[36]   Tzabiras, G., Politis, G., Loukakis, T., 1995d. Calculation of propulsion characteristics of a tanker using different propeller models. First International Conference on Marine Technology ODRA-95, Szczecin, Poland, 1995, pp.65-72.

[37]   Tzabiras, G.D., Prifti, A.C., Grigoropoulos, G.J., Loukakis, T.A., 1995e. An advanced CFD method for predicting the propulsive performance of traditional fishing vessels. Proc. CADAP-95 RINA conference, 17.1-17.16.

[38]   Tzabiras, G.D., 1996a. A numerical study of actuator disk parameters affecting the self-propulsion of a tanker, International Shipbuilding Progress, April 1996, pp. 5-47

[39]   Tzabiras, G.D., 1996b. Numerical study of the viscous flow past a ship's model with asymmetric stern. Proc. MARIND-96 conference, III.41-III.57.

[40]   Tzabiras, G.D., 1997a. Numerical evaluation of Reynolds scale effects on the resistance and propulsion characteristics of ships. In: Schmitt, H. (editor). Flows at large Reynolds numbers, advances in fluid mech. series. CMEM pub, 251-290.

[41]   Tzabiras, G., 1997b, A numerical study of additive bulb effects on the resistance and self-propulsion characteristics of a full ship form, Ship Technology Research, 44, pp. 98-108

[42]   Tzabiras, G.D., 2004. Resistance and Self-Propulsion Simulations for a Series-60, CB=0.6 Hull at Model and Full Scale. Ship Technology Research, 51, pp. 21-34.

[43] Tzabiras , G.D., Kontogiannis K., 2009. An integrated method for predicting the hydrodynamic resistance of low-Cb ships. JCAD, Vol.1568, pp.1-16.

[44] Tzabiras, G.D., Polyzos S.P., Papakonstantinoy V.K., 2009. On a numerical method for generating harmonic waves in a finite 2D tank. Proc. IMAM 2009.

[45] Tzabiras, G.D ., Polyzos S.P., Zarafonitis G.N., 2009. Self propulsion simulations of passenger-ferry ships with bow and stern propulsor. Proc. NuTTS'09.

[46] Tzabiras, G., Papakonstantinou, V., Voutsinas, S., 2013. A numerical study of the flow past a wind generator. Proc. ERCOFTAC 2013.

[47] Tzabiras, G.D., Psaras, K.G., 2014. Numerical Simulation of Self-Propulsion Tests of a Product-Carrier at Various Conditions. Proc. HIPER 2014

[48] Tzabiras, G.D., Polyzos S. P., 2015. A hybrid numerical method for calculating self-propulsion characteristics of ships. Proc. IMAM 2015.

[49] Tzabiras, G.D., Polyzos S. P., 2016. Application of a CFD Method for the Calculation of the Propulsion Characteristics of a Tanker (in Greek lang.). Proc. HIMT 2016.

[50] Zhang Z. H., Liu H., Zhu S. P., Zhao F., 2006. Application of CFD in ship engineering design practice and ship hydrodynamics. Proc. Conf. of Global Chinese Scholars on Hydrodynamics, pp.315-322 (2006).

Methods for calculating the Free Surface

[51] Albadawia, A., Donoghueb, D.B., Robinsonb, A.J., Murrayb, D.B., Delauré, Y.M.C., 2014. On the assessment of a VOF based compressive interface capturing scheme for the analysis of bubble impact on and bounce from a flat horizontal surface. Int. J. of Multiphase Flow, 65, pp.82–97.

[52] Araki, M., Sadat-Hosseini, H., Sanada, Y., Tanimoto, K., Umeda, N., Stern, F., 2012. Estimating maneuvering coefficients using system identification methods with experimental, system-based, and CFD free-running trial data. Ocean Engineering, 51, pp.63–84.

[53] Carrica, P., Wilson, R., Stern, F., 2006. Unsteady RANS simulation of the ship forward speed diffraction problem. Computers & Fluids, 35, pp.545–570.

[54] Irkal, A.R., Nallayarasu, S., Bhattacharyya, S.K., 2016. CFD approach to roll damping of ship with bilge keel with experimental validation. Applied Ocean Research, 55, pp.1–17.

[55] Queutey, P., Visonneau, M., 2007. An interface capturing method for free-surface hydrodynamic flows. Computers & Fluids, 36, pp.1481–1510.

[56] Shi, A., Wu, M., Yang, B., Wang, X., Wang, Z., 2012. Resistance Calculation and Motions Simulation for Free Surface Ship Based on CFD. Procedia Engineering, 31, pp.68 – 74.

[57] Tzabiras, G., Ventikos, Y., 1991. Calculation of the wave pattern generated by a 2D submerged hydrofoil: A Navier-Stokes approach. First Int. Conference on Mathematical and Numerical Aspects of Wave Propagation Phenomena, INRIA-SIAM, Strasbourg, 1991, pp.406-416.

[58] Tzabiras, G.D., 1995f. On the calculation of the free surface flow above an arbitrary 2D topography. Foutrh National Conference on Mechanics, E.E.Th.E.M. (HSTAM, IUTAM member), Xanthi, Greece, 1995, pp.938-945

[59] Tzabiras, G.D., 1997c. A numerical investigation of 2D, steady free surface flows. Int. J. for Numerical Methods in Fluids, 25, pp.567-598.

[60] Tzabiras, G.D., 1997d. Numerical calculation of 2D free surface flows. Proc. Computational Methods and Experimental Measurements VIII (CMEM-97), 1997, Rhodes, Greece, pp.361-370

[61] Tzabiras, G.D. 2008. A method for predicting the influence of an additive bulb on ship resistance. Proc. 8th International conference on hydrodynamics, 53-60.

[62] Papakonstantinou V., Tzabiras, G.D., 2002. Wave resistance calculations of a series 60, c_B=0.6 hull using commercial codes. IMAM Conference, 2002, Crete, Greece.

[63] Wilson R.V., Nichols D.S., Mitchell B., Karman S.L., Hyams D.G., Sreenivas K., Taylor L.K., Briley W.R., Whitfield, D.L., 2006. Application of an Unstructured Free Surface Flow Solver for High Speed Transom Stern Ships. Proc. 26th Symp. on Naval Hydrodynamics (2006).

[64] Wilson, R.V., Carrica, P.M., Stern, F., 2006. Unsteady RANS method for ship motions with application to roll for a surface combatant. Computers & Fluids, 35, pp.501–524.

Ship Appendages

[65] Campana, E.F., Peria, D., Taharab, Y., Stern, F., 2006. Shape optimization in ship hydrodynamics using computational fluid dynamics. Computer Methods in Applied Mechanics and Engineering, Vol. 196, 1–3, pp.634–651

[66] Choi, J.E., Min, K.-S., Kim, J.H., Lee, S.B., Seo, H.W., 2010. Resistance and propulsion characteristics of various commercial ships based on CFD results. Ocean Engineering, 37, pp.549–566

[67] Deng G.B., Queutey P., Visonneau M, 2006. Turbulent Flow Predictions around Appended Hulls. Proc. Conf. of Global Chinese Scholars on Hydrodynamics, pp.225-231.

[68] Huang, Z., Zhou, L., 2001. Numerical Simulation of Flows Over Underwater Axisymmetric Bodies With Full Appendages. Proc. 8th Int. Symposium on Practical Design of Ships and Other Floating Structures, Vol. I, pp.429–435

[69] Jang, H., Lee, H., Joo, Y., Kim, J., Chun, H., 2009. Some practical design aspects of appendages for passenger vessels. International Journal of Naval Architecture and Ocean Engineering, Vol. 1, 1, pp.50–56

[70] Lewis, E., ed. "*Principles of naval Architecture*", 2nd ed. The Society of Naval Architects and Marine Engineers, Jercey City, NJ, USA (1988).

[71] Park, S., Oh, G., Rhee, S., Koo, B., Lee, H., 2015. Full scale wake prediction of an energy saving device by using computational fluid dynamics. Ocean Engineering, 101, pp.254–263.

[72] Pinard J.C. "*Etude Experimentale et Numerique du Sillage en Amont d' une Helice*". PhD Thesis (in French), Nantes, France (1997).

[73] Rhee S. H., Kim H., 2008. A suggestion of gap flow control device for the suppression of rudder cavitation. J. Mar. Sci. Technol, Vol.13, pp.356-370 (2008).

[74] Shen, Z., Wan, D., Carrica, P.M., 2015. Dynamic overset grids in OpenFOAM with application to KCS self-propulsion and maneuvering. Ocean Engineering, 108, pp.287–306.

[75] Simonsen C.D. "*Rudder, Propeller and Hull Interaction by RANS*". PhD Thesis, Kongens Lyngby, Denmark (2000).

[76] Stern, F., Wang, Z., Yang, J., Sadat-Hosseini, H., Mousaviraad, M., Bhushan, S., Diez, M., Yoon, S.-H., Wu, P.-C., Yeon, S., Dogan, T., Kim, D.-H., Volpi, S., Conger, M., Michael, T., Xing, T., Thodal, R., Grenestedt, J., 2015. Recent progress in CFD for naval architecture and ocean engineering. Journal of Hydrodynamics, Ser. B, Vol. 27, 1, pp.1-23

[77] Visonneau M., Deng G. B., Queutey P., 2006a. Computation of model and full scale flows around fully-appended ships with an unstructured RANSE solver. Proc. 26th Symp. on Naval Hydrodynamics (2006).

[78] Visonneau, M., Queutey, P., Deng, G.B., 2006b. Model and Full-Scale Free-Surface Viscous Flow around Fully-Appended Ships. European Conference on Computational Fluid Dynamics, ECCOMAS CFD 2006.

[79] Zaghia, S., Di Masciob, A., Brogliaa, R., Muscaria, R., 2015. Application of dynamic overlapping grids to the simulation of the flow around a fully-appended submarine. Mathematics and Computers in Simulation, Vol. 116, pp.75–88

[80] Zorn T., Schmode D., Bertram V., El Moctar O., 2009. Selected hydrodynamic problems at appendages solved by CFD. Proc. 10th Int. Conf. on Fast Sea Transportation (2009).

Overlapping Grid Blocks

[81] Anwera, S., Hasana, N., Sanghib, S., Mukherjee, S., 2009. Computation of unsteady flows with moving boundaries using body fitted curvilinear moving grids. Computers and Structures, 87, pp.691–700

[82] Badcock, K.J., Richards, B.E., Woodgate, M.A., 2000. Elements of computational fluid dynamics on block structured grids using implicit solvers. Progress in Aerospace Sciences, 36, pp.351-392

[83] Brezzi, F., Lions, J.L., Pironneau, O., 2001. Analysis of a Chimera method. C. R. Acad. Sci. Paris, 332, I, 655 – 660.

[84] Borazjani, I., Ge, L., Le, T., Sotiropoulos, F., 2013. A parallel overset-curvilinear-immersed boundary framework for simulating complex 3D incompressible flows. Computers & Fluids, 77, pp.76–96.

[85] Brounswig J., Manzke M., Rung T., 2009. 2D RANS Simulations on Overset Grids. Proc. NuTT'09.

[86] Carrica, P.M., Wilson, R.V., Noak, R., Stern, F., 2007. Ship motions using single-phase level set with dynamic overset grids. Comput. Fluids, 36, 1415-1433.

[87] Carrica, P.M., Castro, A.M., Stern, F., 2010. Self-propulsion computations using a speed controller and a discretized propeller with dynamic overset grids. J Mar Sci Technol, 15, 316-330.

[88] Chan, W.M., 2009. Overset grid technology development at NASA Ames Research Center Computers & Fluids, 38, 496 – 503.

[89] Chicheportiche, J., Gloerfelt, X., 2012. Study of interpolation methods for high-accuracy computations on overlapping grids. Computers & Fluids, 68, pp.112–133.

[90] Darbandi, M., Naderi, A., 2006. Multiblock hybrid grid finite volume method to solve flow in irregular geometries. Comput. Methods Appl. Mech. Engrg., 196, pp.321–336.

[91] Desquesnes, G., Terracol, M., Manoha, E., Sagaut, P., 2006. On the use of a high order overlapping grid method for coupling in CFD/CAA. Journal of Computational Physics, 220, pp.355–382

[92] Djomehri, M., Biswas,R., 2003. Performance enhancement strategies for multi-block overset grid CFD applications. Parallel Computing, 29, pp.1791–1810

[93] Dougherty, F.C., Benek, J.A., Steger, J.L., 1985. On applications of Chimera grid schemes to store separation NASA TM-88193.

[94] Gilmanov A., Sotiropoulos F, 2005. A hybrid Cartesian-immersed boundary method for simulating flows with 3D, geometrically complex, moving bodies. J. of Comp. Phys, Vol.207, pp.457-492.

[95] Jinsheng, C., Her Mann, T., Feng. L., 2006. A parallel viscous flow solver on multi-block overset grids. Computers & Fluids, 35, pp.1290–1301.

[96] Kim, K.S., Kim, J., Park, I.R., Kim, G.D., Van, S.H., 2007. RANS analysis for hull-propeller-ruder interaction of a commercial ship using an overset grid scheme. Proc. 9th Int. Conf. on numerical ship hydrodynamics, Ann Arbor, MI, USA, 5-8 Aug 2007.

[97] Li, Y., Castro, A.M., Sinokrot, T., Prescott, W., Carrica, P.M., 2015. Coupled multi-body dynamics and CFD for wind turbine simulation including explicit wind turbulence. Renewable Energy, 76, pp.338-361.

[98] Lia, Y., Paika, K.J., Xingb, T., Carrica, P.M., 2012. Dynamic overset CFD simulations of wind turbine aerodynamics. Renewable Energy, Vol. 37, 1, pp.285–298

[99] Lilek Z., Muzaferija S., Peric M., Seidl V, 1997. An implicit finite-volume method using nonmatching blocks of structured grid. Numerical Heat Transfer, Part B: Fundamentals, Vol.32, Issue 4, pp.385- 401.

[100] Lin, C.W., Percival, S., Gotimer, E.H., 1995. Application of Chimera composite grid scheme to ship appendages. David Taylor Model Basin Report No.0704-0188.

[101] Nini, M., Motta, V., Bindolino, G., Guardone, A., 2014. Three-dimensional simulation of a complete Vertical Axis Wind Turbine using overlapping grids. Journal of Computational and Applied Mathematics, 270, pp.78–87

[102] Regnstrom, B., Bathfield, N., 2006. Drag and wake prediction for ships with appendages using an overlapping grid method. Proc. 26th Symp. on Naval Hydrodynamics.

[103] Panahi, R., Shafieefar, M., 2010. Towards a numerical hydrodynamics laboratory by developing an overlapping mesh solver based on a moving mesh solver; verification and application. Applied Ocean Research, 32, pp.308-320.

[104] Salcudean, P., Gartshore, I., Nowak, P., 1996. Multigrid Calculation of Fluid Flows in Complex 3D Geometries using Curvilinear Grids. Computers & Fluids, Vol.25, 4, pp.395-419.

[105] Simonsen, C.D., Stern, F., 2005. Flow pattern around an appended tanker hull form in simple maneuvering conditions. Computers & Fluids, 34, 169 – 198.

[106] Steger, J.L., Benek, J.A., 1987. On the use of composite grid schemes in computational aerodynamics. Comp. Meth. in App. Mech. and Eng, 64, 301 – 320.

[107] Steger, J.L., 1991. Thoughts on the Chimera method of simulation of three-dimensional viscous flow. NASA, Lewis Research Center, CFD Symposium on Aeropropulsion, 1-10.

[108] Talukdar, P., Steven, M., Issendorff, F.V., Trimis, D., 2005. Finite volume method in 3-D curvilinear coordinates with multiblocking procedure for radiative transport problems. Int. J. of Heat and Mass Transfer, 48, pp.4657–4666.

[109] Tarhan, E., Oktay, E., 2002. Solution of airfoil-flap configurations by using Chimera grid system Proc. ICAS 2002 Congress.

[110] Tu, J.Y., Fuchs, L., 1992. Overlapping grids and multigrid methods for three-dimensinal unsteady flow calculations in IC engines. Int. J. for Numerical Methods in Fluids, 15, 693 – 714.

[111] Wang, Z.J., 1995. A fully conservative interface algorithm for overlapped grids. J. of Comp. Phys., 122, 96 – 106.

[112] Zhang, X, Ni, S., He, G., 2008. A pressure-correction method and its applications on an unstructured Chimera grid. Computers & Fluids, 37, pp.993–1010.

[113] Zhang, Z.-R., Liu, H., Zhu, S.-P., Zhao, F. Applications of CFD in ship engineering design practice and ship hydrodynamics. Conference of Global Chinese Scholars on Hydrodynamics.

[114] Zhang, Z.R., Hong, F.W., Kasilnikov, V., Tang, D.H., 2008. Progress in analysis of viscous flow around podded propulsor. Proc. Int. Conf. on Hydrodynamics.

The "Dyne" case study

[115] Dyne, G. *"An experimental investigation of the tanker model "Dyne" in a towing tank"*. Charlmers University of Technology, Goteborg, Sweden (1995).

[116] Denker, J., Knack, T. Kux, J., 1992. Experiments and Numerical Investigations of the HSVA2 Tanker: Flowfield (Second Test Case of 19900 SSPA-CTH-IIHR Workshop). Inst. Schiffbau, Univ. Hamburg, Report 521.

[117] Lundgren, H., Åhman, M., 1994. *"Experimentell och numerisk bestämning av vågmotstand för ett tankfartyg (Dynetankern)"*. Report No. X-94/58, Dept. Naval Architecture and Ocean Engineering, Chalmers Univ. Techn., Gothenburg, Sweden, 1994. (In swedish).

[118] Bram, S., 2004. The prediction of scale effects on ship wave systems using a steady iterative RANS method. 7th Numerical Towing Tank Symposium, NuTTs'04, Hamburg, GERMANY, 3-5 October 2004

The "Nawigator" case study

[119] Bugalski, T., 2004. Basic model test results for Nawigator XXI. European Full-Scale Flow Research and Technology – EFFORT Deliverable D2.3.